

Master of Science Thesis

---

# **Aeroacoustic investigation of a stridor patient's upper respiratory system**

**A Lattice Boltzmann Method simulation using Exa PowerFLOW®**

**Michel Foucart**

---

August 10, 2015





# **Aeroacoustic investigation of a stridor patient's upper respiratory system**

**A Lattice Boltzmann Method simulation using Exa PowerFLOW®**

Master of Science Thesis

For obtaining the degree of Master of Science in Aerospace Engineering  
at Delft University of Technology

Michel Foucart

August 10, 2015



**Delft University of Technology**

Copyright © Aerospace Engineering, Delft University of Technology  
All rights reserved.

DELFT UNIVERSITY OF TECHNOLOGY  
DEPARTMENT OF AERODYNAMICS

The undersigned hereby certify that they have read and recommend to the Faculty of Aerospace Engineering for acceptance the thesis entitled “**Aeroacoustic investigation of a stridor patient’s upper respiratory system**” by **Michel Foucart** in fulfillment of the requirements for the degree of **Master of Science**.

Dated: August 10, 2015

Supervisors:

---

Prof. Dr. S. Hickel

---

Dr. Ir. A.H. van Zuijlen

---

Ir. W. van der Velden

---

Dr. Ir. D. Ragni

---

Dr. H.L.J. Hoeve



---

# Preface

This thesis represents the final stage in obtaining my Master's degree in Aerodynamics at the Faculty of Aerospace Engineering of the Delft University of Technology. The work deals with the aeroacoustic analysis of the fluid flow through a human upper airway as the first step towards establishing a non-intrusive diagnostic technique for upper airway disorders. Although this report can be read as a standalone document, it is preceded by a literature review [Foucart \(2014\)](#). The most relevant topics from this accompanying text have been copied here, but the interested reader can always turn to it for additional background information.

The path to this thesis is paved with the most wondrous of experiences, not in the least my repeated stay in Asia. I would therefore like to express my sincere gratitude to my parents for offering me the opportunity to pursue this degree. To my father, thank you for the many discussions we had over the past years concerning the 'optimal' career decisions. In hindsight, I may not have made all the right choices, but they certainly appeared to be so at the time, and I do not regret a single one. To my mother, thank you for the unconditional support, encouragement, and patience, and thank you for the many trips we made to Delft, especially during the first three years of my study. Also, I would like to thank all my friends for making my time in Delft into something extraordinary; together we experienced truly remarkable moments, some of which will be relived for many years to come! A special thanks to my dearest friends Marijn, Jakob, Yoeri, Wolf, Ward, Arne, and Stefan, for together we had the vision and the perseverance to built something of true and lasting value here! I wish you all the best of luck in any future endeavours.

To my partner Valentine, thank you for your loving and caring support, especially during the course of the recent challenges I exposed myself to. Your careful proof-reading of my writings was much appreciated. Also, I would like to emphasize that your assistance in the relentless 'casing' trials proved to be invaluable for my future career. As much as you supported and still support my personal and professional decisions, I want you to know that I will unconditionally support yours, and that I sincerely hope that you may successfully fulfill all your pending goals.

I greatly appreciate the support from my supervisor dr. ir. A. H. van Zuijlen, not in the least for granting me the opportunity to study such fascinating, multidisciplinary topic with a strong potential for future practical application. During the course of the thesis his many insightful comments proved to be valuable additions to my work. Finally, I wish to thank ir. W. van der Velden for helping me out with all my PowerFLOW-related questions.

I profoundly hope that my efforts may prove to be of any value for researchers who are furthering the development of a potentially life-saving diagnostic technique for upper airway obstructions.

Thank you all ever so much!

Michel Foucart

Delft

August 10, 2015

---

# Summary

Children and adults suffering from Upper Airway Obstructions (UAOs) are nowadays examined using an invasive endoscopy. Because this diagnostic technique unavoidably exposes the patient to certain health risks, there exists a clear need for a non-intrusive diagnostic tool. Several research programs have been initiated that aim at the development of such a tool. One of these initiatives attempts to determine the nature of the obstruction based on an analysis of the patient's stridor, a characteristic high-pitched breathing sound that often accompanies UAOs.

This research project contributed to the development of this non-invasive tool by assessing the potential value of the Lattice Boltzmann Method (LBM) in the aeroacoustic simulation of the airflow within the upper airways. As opposed to conventional schemes, this numerical methodology models the movement and collision of individual particle collections in such a way that they reflect the macroscopic flow behavior. Due to the mathematical simplicity of the method it can be efficiently parallelized, which was one of the main reasons to initiate an investigation into its usefulness for application in the time-sensitive simulation of respiratory airflows.

The generation of acoustic sources and their subsequent propagation was modeled simultaneously within a direct acoustic simulation. While this is uncommon in conventional numerical techniques, the LBM scheme has low dispersion and dissipation capabilities that are particularly suited for this kind of simulations.

Validation studies on a periodic hill configuration and a single diaphragm model were carried out in order to assess the capabilities of Exa PowerFLOW (the unique commercial software that was used for all simulations). They confirmed that the turbulence model can accurately resolve the process of flow separation from a smooth surface, but failed to provide a decisive conclusion regarding the accuracy of the wall model. Furthermore, they proved that nonreflecting boundary conditions are a vital part of the aeroacoustic simulations, and that these simulations should preferably be carried out at the experimental Mach number.

Investigations of simplified and realistic upper airway models, with and without subglottic stenosis, indicated that the LBM is able to model the wide variety of complex flow phenomena that are present within the upper airway. Subsequent comparisons between healthy and stridorous acoustic spectra revealed that the latter have an overall increase in broadband pressure levels that is especially pronounced in more realistic models. This implies that knowledge of these spectra alone is sufficient to distinguish between the underlying models. A thorough validation of the acoustic spectra was not carried out due to the systematic lack of either numerical, experimental or patient-derived benchmark data.

Overall, this research proved that the LBM offers a viable alternative for conventional Computational Fluid Dynamics techniques in the simulation of respiratory airflows. Following an in-depth study of related literature it was concluded that modeling the interaction between the airflow and the airway walls (thereby accounting for the effects of monopole noise sources) is an important first step towards obtaining fully accurate acoustic spectra.



---

# Table of Contents

<b>Preface</b>	<b>v</b>
<b>Summary</b>	<b>vii</b>
<b>List of Figures</b>	<b>xv</b>
<b>List of Tables</b>	<b>xxvii</b>
<b>Nomenclature</b>	<b>xxix</b>
<b>1 Introduction</b>	<b>1</b>
1.1 Research Objectives . . . . .	2
1.2 Thesis Outline . . . . .	3
<b>I Background: Medical Terminology, Airway Models and Numerical Methodologies</b>	<b>5</b>
<b>2 Medical Background</b>	<b>7</b>
2.1 Anatomy of the Upper Airway . . . . .	7
2.1.1 Nasal Cavity . . . . .	7
2.1.2 Oral Cavity . . . . .	8
2.1.3 Pharynx . . . . .	10

2.1.4	Larynx . . . . .	11
2.1.5	Anatomy of the Lower Respiratory Tract . . . . .	12
2.2	The Pediatric Airway . . . . .	14
2.3	Breathing Mechanics . . . . .	17
2.4	Stridor . . . . .	19
2.4.1	Causes . . . . .	19
2.4.2	Diagnostic Techniques . . . . .	23
<b>3</b>	<b>Upper Respiratory System Models</b>	<b>29</b>
3.1	From Medical Imaging Data to Computational Model . . . . .	30
3.2	Model Types . . . . .	30
<b>4</b>	<b>Fluid Model: Lattice Boltzmann Method</b>	<b>35</b>
4.1	Lattice Boltzmann Method . . . . .	36
4.1.1	Basic Principles . . . . .	37
4.1.2	Lattice Bhatnagar-Gross-Krook: PowerFLOW Collision Model . . . . .	38
4.2	PowerFLOW Software . . . . .	41
4.2.1	Turbulence Model . . . . .	41
4.2.2	Wall Model . . . . .	42
4.2.3	PowerFLOW Actions . . . . .	43
<b>5</b>	<b>Acoustics Modeling</b>	<b>47</b>
5.1	Aeroacoustics and the Lattice Boltzmann Method . . . . .	48
5.2	Acoustic Sources and Propagation Models . . . . .	49
5.3	PowerACOUSTICS Software . . . . .	54
5.3.1	From Pressure Signal to Sound Pressure Level . . . . .	54
5.3.2	Extraction of Quadrupole Sources . . . . .	55

---

<b>II</b>	<b>PowerFLOW Validation</b>	<b>57</b>
<b>6</b>	<b>Validation of PowerFLOW Turbulence and Wall Models</b>	<b>59</b>
6.1	Case Geometry . . . . .	60
6.2	Boundary Conditions . . . . .	61
6.3	Description of the Reference Data . . . . .	63
6.4	Turbulence Model . . . . .	63
6.5	Wall Model . . . . .	69
6.6	Quintuple Hill Geometry . . . . .	72
6.7	Alternative Turbulence Model . . . . .	76
6.8	Conclusions . . . . .	77
<b>7</b>	<b>Validation of PowerFLOW Acoustic Model</b>	<b>79</b>
7.1	Case Geometry . . . . .	79
7.2	Boundary Conditions . . . . .	80
7.3	Description of the Reference Data . . . . .	80
7.4	Fluid Simulations . . . . .	81
7.5	Aeroacoustic Simulations . . . . .	90
7.5.1	Mach Number: Chosen by PowerFLOW versus Same as Experiment . . . . .	90
7.5.2	Description of Aeroacoustic Test Cases . . . . .	96
7.5.3	Aeroacoustic Results . . . . .	98
7.6	Conclusions . . . . .	110
<b>III</b>	<b>Upper Airway Simulations</b>	<b>113</b>
<b>8</b>	<b>Simplified Upper Airway Model</b>	<b>115</b>
8.1	Case Geometry . . . . .	116
8.2	Boundary Conditions . . . . .	118
8.3	Description of the Reference Data . . . . .	119

8.4	Fluid Simulations . . . . .	120
8.4.1	Grid Convergence Study: Healthy Model . . . . .	120
8.4.2	Healthy versus Stridorous Flow Patterns . . . . .	129
8.5	Aeroacoustic Simulations . . . . .	134
8.5.1	Mach Number: Chosen by PowerFLOW versus Same as Experiment . .	134
8.5.2	Aeroacoustic Results . . . . .	137
8.6	Conclusions . . . . .	144
<b>9</b>	<b>Realistic Upper Airway Model</b>	<b>145</b>
9.1	Model Geometry . . . . .	146
9.2	Boundary Conditions . . . . .	147
9.3	Fluid Flow Results . . . . .	148
9.4	Aeroacoustic Simulations . . . . .	153
9.4.1	Pioneering Work . . . . .	153
9.4.2	Mach Number: Chosen by PowerFLOW versus Same as Experiment . .	155
9.4.3	Aeroacoustic Results . . . . .	155
9.5	Conclusions . . . . .	162
<b>IV</b>	<b>Project Close-Out</b>	<b>163</b>
<b>10</b>	<b>Conclusion</b>	<b>165</b>
<b>11</b>	<b>Recommendations</b>	<b>167</b>
11.1	Towards a Non-Invasive Diagnostic Tool: Next Steps . . . . .	167
11.2	Upper Airway Model . . . . .	172
11.3	Numerical Methodology . . . . .	173
	<b>Bibliography</b>	<b>175</b>
<b>A</b>	<b>Hill Geometry</b>	<b>187</b>

<b>B</b>	<b>Influence of Window Functions on Acoustic Spectrum</b>	<b>189</b>
<b>C</b>	<b>Coarsest Mesh: Instantaneous Flow Fields</b>	<b>191</b>
<b>D</b>	<b>SUAM - Possible Implementation of NRBC</b>	<b>193</b>
<b>E</b>	<b>SUAM - Fluid Flow Results</b>	<b>195</b>
E.1	Mach Number Chosen by PowerFLOW: Acoustic Mesh . . . . .	195
E.2	Mach Number Same as Experiment: Acoustic Mesh . . . . .	197
E.3	Mach Number Same as Experiment: Fine Mesh . . . . .	198
E.4	Mach Number Same as Experiment: Acoustic Mesh, Seeded . . . . .	199
E.5	Mach Number Chosen by PowerFLOW: Acoustic Mesh, Seeded . . . . .	200
<b>F</b>	<b>RUAM - Fluid Flow Results</b>	<b>201</b>
F.1	Boundary-Layer Resolution . . . . .	201
F.2	Instantaneous Flow Fields . . . . .	202
F.3	Temporal Evolution of Pressure Signal . . . . .	205



---

## List of Figures

2.1	Overview of the upper airway system Drake et al. (2009). . . . .	8
2.2	Internal anatomy of the nasal cavity Drake et al. (2009). . . . .	9
2.3	Internal anatomy of the oral cavity Drake et al. (2009). . . . .	9
2.4	Internal anatomy of the pharynx Snell (2011). . . . .	10
2.5	Internal anatomy of the larynx Standing et al. (2009). . . . .	11
2.6	Internal anatomy of the lower respiratory system: Trachea and main bronchi Standing et al. (2009). . . . .	12
2.7	Internal anatomy of the lower respiratory system: Bronchioles and alveoli Standing et al. (2009). . . . .	13
2.8	Comparison between the upper anatomy of an infant and an older child Brodsky (2011). . . . .	14
2.9	Area change of airway components in terms of percentage. Graph based on results from Xi et al. (2012). V & V = Vestibule & Valve, TR = Turbinate Region, NP = Nasopharynx. . . . .	15
2.10	The respiratory pump muscles McConnell (2013). . . . .	17
2.11	Laryngomalacia (A) before and (B) after surgery Thompson et al. (2012). . . . .	21
2.12	Myer-Cotton grading system for subglottic stenosis de Alarcon et al. (2012). . . . .	22
2.13	Subglottic hemangioma (A) before and (B) after treatment Thompson et al. (2012). . . . .	22
2.14	Laryngeal papillomas just below the vocal cords Jardine et al. (2011). . . . .	23
2.15	Example of foreign body in the trachea Jardine et al. (2011). . . . .	23
2.16	Exhaled aerosol profiles at the mouth for airway with (a) normal condition, (b) carina tumor, (c) left bronchial tumor, and (d) asthma Xi et al. (2013). . . . .	24

2.17	Lossless tube model of the upper airway <a href="#">Leiberman et al. (1986)</a> . . . . .	25
2.18	Spectrogram of multiple inspiratory breath sounds of a 15-month-old boy with subglottic stenosis. Picture taken from <a href="#">Zwartenkot (2010)</a> . . . . .	26
3.1	(a) CT image projected in the coronal plane, corresponding to slice middle cavity, with user-defined segmentation. Detail of the middle meatus section with (b) step-like segmentation as selected by the user and (c) reduced model <a href="#">Gambaruto et al. (2009)</a> . . . . .	30
3.2	Relevant cross-sectional dimensions of the extrathoracic oral airway model <a href="#">Jayaraju et al. (2008)</a> . . . . .	31
3.3	Relevant geometrical dimensions of the extrathoracic oral airway model seen in a side view (left) and back view (right) <a href="#">Krause et al. (2013)</a> . . . . .	32
3.4	Realistic CT-scan derived upper airway model of a patient suffering from subglottic stenosis (left) and the adapted version to represent a healthy person (right) <a href="#">Lynch (2012)</a> . . . . .	33
4.1	Illustration of the streaming process. . . . .	37
4.2	Illustration of the collision process of two distribution functions. Note that this is only one of many possible collision outcomes. . . . .	38
4.3	Definition of the microscopic velocities for the D2Q9 lattice. . . . .	40
4.4	Definition of the microscopic velocities for the D3Q15 lattice. . . . .	40
4.5	Comparison of three different means to extract fluid profiles from PowerFLOW: command line vs. PowerVIZ Line Graph with(out) tri-linear interpolation. . . . .	44
5.1	(a)(c) Dispersion, and (b)(d) dissipation error with $Ma = 0.2$ . (-) LBM, ( $\Delta$ , $\nabla$ ) 2nd order finite-difference, (+, $\times$ ) 3rd order optimized finite-difference, ( $\star$ , $\star$ ) 6th order optimized finite-difference <a href="#">Marié et al. (2009)</a> . . . . .	48
5.2	(a) Dispersion, and (b) dissipation error with $Ma = 0.0$ . (-) LBM, ( $\Delta$ ) 2nd order finite-difference, (+) 3rd order optimized finite-difference, ( $\star$ ) 6th order optimized finite-difference <a href="#">Marié et al. (2009)</a> . . . . .	49
5.3	Radiation patterns of monopoles, dipoles, and quadrupoles <a href="#">Norton and Karczub (2007)</a> . . . . .	50
6.1	Two-dimensional view of the periodic hill geometry. The dashed lines indicate the measurement locations. . . . .	60
6.2	Instantaneous vorticity component $\omega_z$ normal to the cross-section at an arbitrarily chosen instant in time <a href="#">Breuer et al. (2009)</a> . . . . .	62



6.3	Selection of grids used in the periodic hill grid convergence study. . . . .	64
6.4	Instantaneous values of $y^+$ , a measure of the position of the first off-wall voxel position, at the lower boundary, mid-span. The bracketed values represent the non-dimensional smallest voxel size. . . . .	65
6.5	Averaged values of $u$ at the first off-wall voxel position, lower boundary, mid-span. The zero-crossings (transition to/from backflow) yield an indication to the separation and reattachment locations. The bracketed values represent the non-dimensional smallest voxel size. . . . .	66
6.6	Comparison of the averaged streamwise-velocity profiles with those obtained by Breuer et al. (2009) at six streamwise positions, mid-span. . . . .	67
6.7	Averaged values of $u$ at the first off-wall voxel position, lower boundary, mid-span, for different inlet turbulence settings. The zero-crossings (transition to/from backflow) yield an indication to the separation and reattachment locations. Medium mesh ( $\Delta/h = 0.0136$ ). . . . .	69
6.8	Instantaneous values of $y^+$ at the lower boundary, mid-span, for different boundary-layer resolutions. The bracketed values represent the non-dimensional smallest voxel size. . . . .	70
6.9	Averaged values of $u$ at the first off-wall voxel position, lower boundary, mid-span, for different boundary-layer resolutions. The zero-crossings (transition to/from backflow) yield an indication to the separation and reattachment locations. . . . .	71
6.10	Comparison of the averaged streamwise-velocity profiles for the different boundary-layer resolutions with those obtained by Breuer et al. (2009) at six streamwise positions, mid-span. . . . .	71
6.11	Snapshot of the average streamwise velocity $u$ (levels between -0.3 and 0 m/s), quintuple hill geometry, medium mesh, mid-span. . . . .	73
6.12	Snapshot of the average streamwise velocity $u$ (levels between -0.3 and 0 m/s) superimposed with a selection of streamlines, quintuple hill geometry, medium mesh, mid-span. . . . .	73
6.13	Averaged values of $u$ at the first off-wall voxel position, lower boundary, mid-span, quintuple hill geometry. The zero-crossings (transition to/from backflow) yield an indication to the separation and reattachment locations. . . . .	74
6.14	Comparison of the streamwise-velocity profiles downstream of the third hill in the quintuple hill geometry with those obtained by Breuer et al. (2009) at six streamwise positions, mid-span. . . . .	75
6.15	Comparison of the streamwise-velocity profiles downstream of the fourth hill in the quintuple hill geometry with those obtained by Breuer et al. (2009) at six streamwise positions, mid-span. . . . .	76
6.16	Snapshot of the average streamwise velocity $u$ (levels between -0.3 and 0 m/s), quintuple hill geometry, medium mesh, ILES turbulence model, mid-span. . . . .	78

6.17	Snapshot of the average streamwise velocity $u$ (levels between -0.3 and 0 m/s) superimposed with a selection of streamlines, quintuple hill geometry, medium mesh, ILES turbulence model, mid-span. . . . .	78
7.1	Three-dimensional view of the simulated diaphragm model. The additional outlet is designated in <b>red</b> , while the acoustic measurement plane is shown in <b>blue</b> . The $(-\cdot-)$ lines indicate the streamwise position of the measurement locations. . . .	80
7.2	Grids used in the diaphragm grid convergence study. . . . .	82
7.3	Comparison of the instantaneous longitudinal velocity $u$ (levels between -15 and 28 m/s), mid-span. From top to bottom: <b>Gloerfelt and Lafon (2008)</b> , coarse mesh, medium mesh, fine mesh. . . . .	83
7.4	Comparison of the averaged streamwise-velocity profiles at six streamwise positions, mid-span. <b>Red</b> : coarse mesh, <b>blue</b> : medium mesh, <b>green</b> : fine mesh, black: reference data <b>Piellard and Bailly (2010)</b> . . . . .	83
7.5	Comparison of the instantaneous crossflow velocity $v$ (levels between -10 and 10 m/s), mid-span. From top to bottom: <b>Gloerfelt and Lafon (2008)</b> , coarse mesh, medium mesh, fine mesh. . . . .	84
7.6	Comparison of the averaged crossflow-velocity profiles at six streamwise positions, mid-span. <b>Red</b> : coarse mesh, <b>blue</b> : medium mesh, <b>green</b> : fine mesh, black: reference data <b>Piellard and Bailly (2010)</b> . . . . .	84
7.7	Comparison of the instantaneous spanwise velocity $w$ (levels between -10 and 10 m/s), mid-span. From top to bottom: <b>Gloerfelt and Lafon (2008)</b> , coarse mesh, medium mesh, fine mesh. . . . .	85
7.8	Comparison of the averaged spanwise-velocity profiles at six streamwise positions, mid-span. <b>Red</b> : coarse mesh, <b>blue</b> : medium mesh, <b>green</b> : fine mesh, black: reference data <b>Piellard and Bailly (2010)</b> . . . . .	85
7.9	Comparison of the instantaneous vorticity magnitude $\ \omega\ $ (levels between -5,000 and 5,000 $s^{-1}$ ), mid-span. From top to bottom: <b>Gloerfelt and Lafon (2008)</b> , coarse mesh, medium mesh, fine mesh. . . . .	86
7.10	Comparison of the averaged streamwise-velocity profiles at six streamwise positions, medium mesh, mid-span. <b>Red</b> : TF 9 - 12 (0.083 s), <b>blue</b> : TF 9 - 16 (0.193 s), <b>green</b> : TF 9 - 20 (0.303 s), <b>cyan</b> : TF 9 - 27 (0.495 s), black: reference data <b>Piellard and Bailly (2010)</b> . . . . .	88
7.11	Comparison of the averaged crossflow-velocity profiles at six streamwise positions, medium mesh, mid-span. <b>Red</b> : TF 9 - 12 (0.083 s), <b>blue</b> : TF 9 - 16 (0.193 s), <b>green</b> : TF 9 - 20 (0.303 s), <b>cyan</b> : TF 9 - 27 (0.495 s), black: reference data <b>Piellard and Bailly (2010)</b> . . . . .	88
7.12	Comparison of the averaged streamwise-velocity profiles at six streamwise positions, medium mesh, mid-span. <b>Red</b> : $k - \epsilon$ , <b>blue</b> : ILES, black: reference data <b>Piellard and Bailly (2010)</b> . . . . .	89

7.13	Comparison of the instantaneous vorticity magnitude $\ \omega\ $ (levels between $-5,000$ and $5,000\text{s}^{-1}$ ) as simulated by the $k - \epsilon$ (top) and ILES (bottom) turbulence model, mid-span. . . . .	90
7.14	Comparison of the instantaneous longitudinal velocity $u$ (levels between $-15$ and $28\text{ m/s}$ ), mid-span. From top to bottom: medium mesh (CbP), medium mesh (SaE), fine mesh (SaE), finest mesh (SaE). . . . .	92
7.15	Comparison of the instantaneous crossflow velocity $v$ (levels between $-10$ and $10\text{ m/s}$ ), mid-span. From top to bottom: medium mesh (CbP), medium mesh (SaE), fine mesh (SaE), finest mesh (SaE). . . . .	92
7.16	Comparison of the instantaneous spanwise velocity $w$ (levels between $-10$ and $10\text{ m/s}$ ), mid-span. From top to bottom: medium mesh (CbP), medium mesh (SaE), fine mesh (SaE), finest mesh (SaE). . . . .	93
7.17	Comparison of the instantaneous vorticity magnitude $\ \omega\ $ (levels between $-5,000$ and $5,000\text{s}^{-1}$ ), mid-span. From top to bottom: medium mesh (CbP), medium mesh (SaE), fine mesh (SaE), finest mesh (SaE). . . . .	93
7.18	Comparison of the instantaneous dimensionless eddy viscosity $\mu_t/\mu$ (levels between $0$ and $10$ ), mid-span, medium mesh. From top to bottom: Chosen by PowerFLOW, Same as Experiment. . . . .	94
7.19	Comparison of the instantaneous swirl $S = \mathbf{u} \cdot (\nabla \times \mathbf{u})$ (levels between $-100$ and $100$ ), mid-span, medium mesh. From top to bottom: Chosen by PowerFLOW, Same as Experiment. . . . .	94
7.20	Comparison of instantaneous dimensionless eddy viscosity $\mu_t/\mu$ profiles for different Mach number settings along the central longitudinal axis, medium mesh. . . . .	95
7.21	Comparison of instantaneous dimensionless eddy viscosity $\mu_t/\mu$ profiles for different Mach number settings at six streamwise positions, mid-span, medium mesh. <b>Red:</b> medium mesh (CbP), <b>blue:</b> medium mesh (SaE), <b>green:</b> finest mesh (SaE). . . . .	95
7.22	Location of acoustic probes relative to the diaphragm model, $x = 595\text{ mm}$ (with the exception of one simulation used in the directivity analysis). . . . .	97
7.23	Pressure perturbation determined from the pressure signal at Probe # 8, fine mesh, Mach Number Same as Experiment. Note the transient start-up prior to $t \approx 0.05\text{ s}$ . . . . .	98
7.24	Sound Pressure Levels at selected horizontal probe locations for different grid resolutions, $f_s \approx 24\text{ kHz}$ , $\Delta f \approx 16.4\text{ Hz}$ . Comparison with results from <b>Gloerfelt and Lafon (2008)</b> . . . . .	99
7.25	Sound Pressure Levels at selected vertical probe locations for different grid resolutions, $f_s \approx 24\text{ kHz}$ , $\Delta f \approx 16.4\text{ Hz}$ . Comparison with results from <b>Gloerfelt and Lafon (2008)</b> . . . . .	100

7.26	Sound Pressure Levels at selected horizontal and vertical probe locations for test cases with(out) NRBC, $f_s \approx 24$ kHz, $\Delta f \approx 16.4$ Hz. Comparison with results from Gloorfelt and Lafon (2008). . . . .	102
7.27	Directivity analysis at the diaphragm outlet ( $x = 595$ mm), fine mesh. . . . .	104
7.28	Directivity analysis at the inner diaphragm ( $x = 300$ mm), fine mesh. . . . .	105
7.29	Pressure perturbation determined from the pressure signal at Probe # 8, fine mesh. Mach Number Chosen by PowerFLOW. Note the transient start-up prior to $t \approx 0.1$ s. 106	
7.30	Sound Pressure Levels at selected horizontal and vertical probe locations for different grid resolutions, Mach Number Chosen by PowerFLOW, sampling frequencies given in Table (7.4), $\Delta f \approx 16.4$ Hz. Comparison with results from Gloorfelt and Lafon (2008). . . . .	108
7.31	Comparison between CbP and SaE Sound Pressure Levels at selected horizontal and vertical probe locations, $f_{s,CbP} \approx 11.4$ kHz, $f_{s,SaE} \approx 11.9$ kHz, $\Delta f_{CbP,SaE} \approx 16.4$ Hz. Comparison with results from Gloorfelt and Lafon (2008). . . . .	109
8.1	Three-dimensional view of the simulated SUAM (developed by Brouns et al. (2006)), including a 75% constriction in the tracheal lumen at the level of the vocal cords, which has been introduced by Lynch (2012) as a means to investigate the acoustic characteristics of stridor. . . . .	117
8.2	Computational grid of the SUAM geometry in the central sagittal plane, every second grid line is shown, fine mesh ( $39.65 \times 10^6$ voxels). . . . .	121
8.3	Instantaneous snapshot of $y^+$ (levels between 0 and 5), a measure for the near-wall resolution, healthy model. From left to right: medium mesh, fine mesh. . . . .	121
8.4	Comparison of the instantaneous vertical velocity $u_z$ (levels between -7 and 3 m/s) in the central sagittal plane, healthy model. From left to right: van der Velden (2012), coarse mesh, medium mesh, fine mesh, DNS. . . . .	123
8.5	Comparison of the instantaneous velocity magnitude $\ \mathbf{u}\ $ (levels between 0 and 7.5 m/s) in the central sagittal plane, healthy model. From left to right: van der Velden (2012), coarse mesh, medium mesh, fine mesh, DNS. . . . .	123
8.6	Comparison of the instantaneous vorticity magnitude $\ \boldsymbol{\omega}\ $ (levels between -7,500 and $7,500 \text{ s}^{-1}$ ) in the central sagittal plane, healthy model. From left to right: van der Velden (2012), coarse mesh, medium mesh, fine mesh, DNS. . . . .	124
8.7	Comparison of the instantaneous pressure deficit $p'$ (levels between -5 and 40 Pa) in the central sagittal plane, healthy model. From left to right: van der Velden (2012), coarse mesh, medium mesh, fine mesh, DNS. . . . .	124
8.8	Snapshot of the instantaneous horizontal velocity $u_x$ (levels between -7 and 3 m/s) in the central sagittal plane, healthy model. From left to right: medium mesh, fine mesh, DNS. . . . .	125

8.9	Comparison of normalized 2-component ( $u_x$ and $u_z$ ) velocity magnitude in the central sagittal plane with reference data from Jayaraju et al. (2008), healthy model. The specified locations (C, H - J) coincide with those of Figure (3.2). The fluid profiles are measured from the posterior to the anterior wall of the airway. . . . .	126
8.10	Comparison of normalized 3-component turbulent kinetic energy $k$ in the central sagittal plane with reference data from Jayaraju et al. (2008), healthy model. The specified locations (C, H - J) coincide with those of Figure (3.2). The fluid profiles are measured from the posterior to the anterior wall of the airway. . . . .	127
8.11	Snapshot of the instantaneous vertical velocity $u_z$ (levels between -7 and 3 m/s) in the central sagittal plane, fine mesh. From left to right: healthy model, 50 % constriction, 75 % constriction. . . . .	131
8.12	Snapshot of the average vertical velocity $u_z$ (levels between -7 and 0 m/s) in the central sagittal plane, superimposed with a selection of streamlines, fine mesh. Areas in pink correspond to regions with positive vertical velocity. From left to right: healthy model, 50 % constriction, 75 % constriction. . . . .	131
8.13	Snapshot of the instantaneous velocity magnitude $\ \mathbf{u}\ $ (levels between 0 and 7.5 m/s) in the central sagittal plane, fine mesh. From left to right: healthy model, 50 % constriction, 75 % constriction. . . . .	132
8.14	Comparison of the averaged velocity magnitude $\ \mathbf{u}\ $ at the end of the constriction in the central sagittal plane, fine mesh. . . . .	132
8.15	Snapshot of the instantaneous vorticity magnitude $\ \omega\ $ (levels between -7,500 and 7,500 s <sup>-1</sup> ) in the central sagittal plane, fine mesh. From left to right: healthy model, 50 % constriction, 75 % constriction. . . . .	133
8.16	Snapshot of the instantaneous pressure deficit $p'$ (levels between -5 and 40 Pa) in the central sagittal plane, fine mesh. From left to right: healthy model, 50 % constriction, 75 % constriction. . . . .	133
8.17	Comparison of the averaged pressure deficit $p'$ in the pharyngeal-laryngeal-tracheal region, fine mesh. Positions are measured from the start of the oropharynx (Section B'-B in Figure (3.2)). . . . .	134
8.18	Temporal evolution of the averaged velocity magnitude $\ \mathbf{u}\ $ (levels between 0 and 45 m/s), Mach Number Same as Experiment, healthy model, acoustic mesh. The front views are taken within 1 mm from the inlet boundary. Note the development of the erroneous jet at the inlet. From left to right: 0.05 s, 0.1 s, 0.29 s. . . . .	135
8.19	Temporal evolution of the averaged horizontal velocity $u_x$ (levels between -40 and 10 m/s), Mach Number Same as Experiment, healthy model, acoustic mesh. The front views are taken within 1 mm from the inlet boundary. Note the strong backflow in the cylindrical inlet region. From left to right: 0.05 s, 0.1 s, 0.29 s. . . . .	135
8.20	Pressure perturbation as measured by the acoustic probes, healthy model, Mach Number Chosen by PowerFLOW. Note the transient start-up prior to $t = 0.25$ s. . . . .	138
8.21	Sound Pressure Levels at inlet probes for the healthy and constricted models, $f_s \approx 35.1$ kHz, $\Delta f \approx 8$ Hz. . . . .	139

8.22	Sound Pressure Levels at outlet probes for the healthy and constricted models, $f_s \approx 35.1$ kHz, $\Delta f \approx 8$ Hz. . . . .	139
8.23	Snapshot of the instantaneous divergence of the Lighthill tensor $\nabla T_{ij}$ (levels between 0 and $7,500 \text{ kg}^2/(\text{m}^6\text{s})$ ), a measure for the strength of quadrupole sound sources, in the central sagittal plane, acoustic mesh. From left to right: healthy model, 50 % constriction, 75 % constriction. . . . .	141
8.24	Snapshot of the instantaneous force magnitude $\ \mathbf{F}\ $ (levels between 0 and $1.5 \times 10^{-6}$ N), a measure for the strength of dipole sound sources, acoustic mesh. From left to right: healthy model, 50 % constriction, 75 % constriction. . . . .	141
8.25	Comparison of turbulent kinetic energy ( $k$ ) profiles in the central sagittal plane, 20 mm downstream of constriction, with reference data from van der Velden et al. (2015). . . . .	142
8.26	Power spectrum of infantile stridor, acquired from a one-year-old boy who suffers from subglottis stenosis (SGS). Figure taken from Gray et al. (1985). Note that Gray et al. (1985) refer to the power scale as 'arbitrary'. . . . .	143
9.1	Three-dimensional view of the Realistic Upper Airway Model, which has been built from Computed Tomography images. Picture taken from van der Velden (2012). . . . .	146
9.2	Computational grids of the RUAM geometry in the central sagittal plane, every second grid line is shown, acoustic mesh ( $\sim 7.5 \times 10^6$ voxels). . . . .	148
9.3	Snapshot of the instantaneous vertical velocity $u_z$ (levels between -13 and 3 m/s) in the central sagittal plane, acoustic mesh. From left to right: healthy model, stridorous model. . . . .	150
9.4	Snapshot of the average vertical velocity $u_z$ (levels between -13 and 0 m/s) in the central sagittal plane, superimposed with a selection of streamlines, acoustic mesh. Areas in pink correspond to regions with positive vertical velocity. From left to right: healthy model, stridorous model. . . . .	150
9.5	Snapshot of the instantaneous velocity magnitude $\ \mathbf{u}\ $ (levels between 0 and 15 m/s) in the central sagittal plane, acoustic mesh. From left to right: healthy model, stridorous model. . . . .	151
9.6	Comparison of the averaged velocity magnitude $\ \mathbf{u}\ $ at the end of the constriction in the central sagittal plane, acoustic mesh. . . . .	151
9.7	Snapshot of the instantaneous vorticity magnitude $\ \omega\ $ (levels between -15,000 and $15,000 \text{ s}^{-1}$ ) in the central sagittal plane, acoustic mesh. From left to right: healthy model, stridorous model. . . . .	152
9.8	Snapshot of the instantaneous pressure deficit $p'$ (levels between 0 and 230 Pa) in the central sagittal plane, acoustic mesh. From left to right: healthy model, stridorous model. . . . .	152

9.9	Sound pressure results versus frequency from the inlet probe of the RUAM compared with actual patient data from Zwartenkot (2010). Graph taken from van der Velden (2012). . . . .	154
9.10	Monopole source sound pressure measured at the outlet probe. Figure taken from van der Velden et al. (2015). . . . .	154
9.11	Pressure perturbation as measured by the acoustic probes, healthy model, Mach Number Chosen by PowerFLOW. Note the transient start-up prior to $t = 0.25$ s. . . . .	156
9.12	Sound Pressure Levels at inlet probes for the healthy and stridorous patient, Mach Number Chosen by PowerFLOW, $f_s \approx 70.1$ kHz, $\Delta f \approx 8$ Hz. . . . .	158
9.13	Sound Pressure Levels at bifurcation probes for the healthy and stridorous patient, Mach Number Chosen by PowerFLOW, $f_s \approx 70.1$ kHz, $\Delta f \approx 8$ Hz. . . . .	158
9.14	Snapshot of the instantaneous divergence of the Lighthill tensor $\nabla T_{ij}$ (levels between 0 and $15,000 \text{ kg}^2/(\text{m}^6\text{s})$ ), a measure for the strength of quadrupole sound sources, in the central sagittal plane, Mach Number Chosen by PowerFLOW, acoustic mesh. From left to right: healthy patient, stridorous patient. . . . .	159
9.15	Snapshot of the instantaneous force magnitude $\ \mathbf{F}\ $ (levels between 0 and $1.5 \times 10^{-6}$ N), a measure for the strength of dipole sound sources, Mach Number Chosen by PowerFLOW, acoustic mesh. From left to right: healthy patient, stridorous patient. . . . .	159
9.16	Sound Pressure Levels at inlet probes for the healthy and stridorous patient, Mach Number Same as Experiment, $f_s \approx 69.9$ kHz, $\Delta f \approx 20.2$ Hz. . . . .	160
9.17	Sound Pressure Levels at bifurcation probes for the healthy and stridorous patient, Mach Number Same as Experiment, $f_s \approx 69.9$ kHz, $\Delta f \approx 20.2$ Hz. . . . .	160
9.18	Snapshot of the instantaneous divergence of the Lighthill tensor $\nabla T_{ij}$ (levels between 0 and $15,000 \text{ kg}^2/(\text{m}^6\text{s})$ ), a measure for the strength of quadrupole sound sources, in the central sagittal plane, Mach Number Same as Experiment, acoustic mesh. From left to right: healthy patient, stridorous patient. . . . .	161
9.19	Snapshot of the instantaneous force magnitude $\ \mathbf{F}\ $ (levels between 0 and $2 \times 10^{-6}$ N), a measure for the strength of dipole sound sources, Mach Number Same as Experiment, acoustic mesh. From left to right: healthy patient, stridorous patient. . . . .	161
11.1	Overview of the sequence of steps that should be taken in the development of a noninvasive diagnostic tool for Upper Airway Obstructions. . . . .	170
11.1	Overview of the sequence of steps that should be taken in the development of a noninvasive diagnostic tool for Upper Airway Obstructions. (cont.) . . . . .	171
B.1	Comparison of four different window functions used to calculate the acoustic spectrum of Probe # 8, fine mesh, Mach Number Same as Experiment. . . . .	189



C.1	Overview of the instantaneous flow fields obtained with the coarsest mesh. From top to bottom: longitudinal velocity $u$ (levels between -15 and 28 m/s), crossflow velocity $v$ (levels between -10 and 10 m/s), spanwise velocity $w$ (levels between -10 and 10 m/s), vorticity magnitude $\ \omega\ $ (levels between -5,000 and 5,000 s <sup>-1</sup> ).	191
D.1	Possible implementation of a Nonreflecting Boundary Condition in the Simplified Upper Airway Model. The colors indicate regions of increased voxel size. . . . .	193
E.1	Snapshot of the instantaneous vertical velocity $u_z$ (levels between -7 and 3 m/s) in the central sagittal plane, acoustic mesh (6 cells/mm). From left to right: healthy model, 50 % constriction, 75 % constriction. . . . .	195
E.2	Snapshot of the instantaneous velocity magnitude $\ \mathbf{u}\ $ (levels between 0 and 7.5 m/s) in the central sagittal plane, acoustic mesh (6 cells/mm). From left to right: healthy model, 50 % constriction, 75 % constriction. . . . .	196
E.3	Snapshot of the instantaneous vorticity magnitude $\ \omega\ $ (levels between -7,500 and 7,500 s <sup>-1</sup> ) in the central sagittal plane, acoustic mesh (6 cells/mm). From left to right: healthy model, 50 % constriction, 75 % constriction. . . . .	196
E.4	Snapshot of the instantaneous pressure deficit $p'$ (levels between -5 and 40 Pa) in the central sagittal plane, acoustic mesh (6 cells/mm). From left to right: healthy model, 50 % constriction, 75 % constriction. . . . .	197
E.5	Snapshot of the averaged velocity magnitude $\ \mathbf{u}\ $ (levels between 0 and 45 m/s) in the central sagittal plane, acoustic mesh (6 cells/mm). The front views are taken within 1 mm from the inlet boundary. From left to right: 50 % constriction (0.29s), 75 % constriction (0.19s). . . . .	197
E.6	Temporal evolution of the averaged velocity magnitude $\ \mathbf{u}\ $ (levels between 0 and 45 m/s), Mach Number Same as Experiment, healthy model, fine mesh (8 cells/mm). The front views are taken within 1 mm from the inlet boundary. From left to right: 0.05 s, 0.1 s. . . . .	198
E.7	Temporal evolution of the averaged horizontal velocity $u_x$ (levels between -40 and 10 m/s), Mach Number Same as Experiment, healthy model, fine mesh (8 cells/mm). The front views are taken within 1 mm from the inlet boundary. Note the strong backflow in the cylindrical inlet region. From left to right: 0.05 s, 0.1 s. . . . .	198
E.8	Effect of CbP initial condition on the temporal evolution of the averaged velocity magnitude $\ \mathbf{u}\ $ (levels between 0 and 15 m/s), Mach Number Same as Experiment, healthy model, acoustic mesh (6 cells/mm). The front views are taken within 1 mm from the inlet boundary. From left to right: 0 s, 0.1 s, 0.15 s. . . . .	199
E.9	Effect of CbP initial condition on the temporal evolution of the averaged velocity magnitude $\ \mathbf{u}\ $ (levels between 0 and 15 m/s), Mach Number Same as Experiment, 75 % constriction, acoustic mesh (6 cells/mm). The front views are taken within 1 mm from the inlet boundary. From left to right: 0 s, 0.1 s, 0.15 s. . . . .	199



E.10	Effect of SaE initial condition on the temporal evolution of the averaged velocity magnitude $\ \mathbf{u}\ $ (levels between 0 and 15 m/s), Mach Number Chosen by PowerFLOW, healthy model, acoustic mesh (6 cells/mm). The front views are taken within 1 mm from the inlet boundary. From left to right: 0.026 s, 0.133 s, 0.24 s.	200
F.1	Instantaneous snapshot of $y^+$ (levels between 0 and 5), a measure for the near-wall resolution, acoustic mesh, Mach Number Chosen by PowerFLOW. From left to right: healthy model, stridorous model. . . . .	201
F.2	Snapshot of the instantaneous vertical velocity $u_z$ (levels between -13 and 3 m/s) in the central sagittal plane, Mach Number Same as Experiment, acoustic mesh (6 cells/mm). From left to right: healthy model, stridorous model. . . . .	202
F.3	Snapshot of the instantaneous vorticity magnitude $\ \omega\ $ (levels between -15,000 and 15,000 $s^{-1}$ ) in the central sagittal plane, Mach Number Same as Experiment, acoustic mesh (6 cells/mm). From left to right: healthy model, stridorous model.	202
F.4	Snapshot of the instantaneous velocity magnitude $\ \mathbf{u}\ $ (levels between 0 and 15 m/s) in the central sagittal plane, Mach Number Same as Experiment, acoustic mesh (6 cells/mm). From left to right: healthy model, stridorous model. . . .	203
F.5	Comparison of the averaged velocity magnitude $\ \mathbf{u}\ $ at the end of the constriction in the central sagittal plane, Mach Number Same as Experiment, acoustic mesh (6 cells/mm). . . . .	203
F.6	Snapshot of the instantaneous pressure deficit $p'$ (levels between 0 and 230 Pa) in the central sagittal plane, Mach Number Same as Experiment, acoustic mesh (6 cells/mm). From left to right: healthy model, stridorous model. . . . .	204
F.7	Pressure perturbation as measured by the acoustic probes, healthy model, Mach Number Same As Experiment. Note the transient start-up prior to $t = 0.05$ s. .	205



---

## List of Tables

2.1	Nasal airway dimension of the four airway models of different ages <a href="#">Xi et al. (2012)</a> . . . . .	16
2.2	Nostrils and upper trachea dimension of the four airway models of different ages <a href="#">Xi et al. (2012)</a> . . . . .	16
2.3	Respiratory parameters under quiet breathing conditions at various ages <a href="#">Xi et al. (2012)</a> . The Reynolds numbers ( $Re$ ) are calculated using the hydraulic diameter data from Table (2.2). The value for the kinematic viscosity was taken to be $1.568 \times 10^{-5} \text{ m}^2/\text{s}$ , which corresponds to a temperature of 300 K. . . . .	18
2.4	Differential diagnoses of stridor <a href="#">Muñiz (2008)</a> . . . . .	20
3.1	Overview of upper airway models available in literature. . . . .	34
4.1	Overview of the LBM as used in the simulation of upper airway flow. Note that <a href="#">Ball et al. (2008)</a> are the only group of researchers in the list who applied PowerFLOW (version 3.4) for their simulations. . . . .	35
4.2	The magnitude and the number of velocity directions for lattice models D2Q9, D3Q15, D3Q19 and D3Q27 and their corresponding weights $w_i$ <a href="#">Aidun and Clausen (2010)</a> . . . . .	39
5.1	Results of a dimensional analysis performed separately on each of the source terms of the Ffowcs-Williams Hawkins acoustic analogy <a href="#">Norton and Karczub (2007)</a> . . . . .	54
6.1	Voxel sizes (in mm) associated with the VR regions used in the periodic hill meshes. . . . .	65
6.2	Comparison of approximated separation and reattachment locations with those obtained by <a href="#">Breuer et al. (2009)</a> . . . . .	67
6.3	Comparison of approximated separation and reattachment locations for different inlet turbulence settings with those obtained by <a href="#">Breuer et al. (2009)</a> . . . . .	68
6.4	Comparison of approximated separation and reattachment locations for different boundary-layer resolutions with those obtained by <a href="#">Breuer et al. (2009)</a> . . . . .	70

---

6.5	Comparison of approximated separation and reattachment locations for the quintuple hill geometry with those obtained by Breuer et al. (2009). The single hill data is repeated from Table (6.2) for the reader's convenience. . . . .	75
7.1	Voxel sizes (in mm) associated with the VR regions used in the diaphragm meshes.	81
7.2	Streamwise velocity magnitudes in m/s at six streamwise positions as simulated by the $k - \epsilon$ and ILES turbulence models. . . . .	89
7.3	Average OASPL-values in the upper (10 - 170°) and lower (190 - 350°) diaphragm.	103
7.4	Overview of the timesteps, sampling frequencies and maximum frequencies of the CbP simulations. . . . .	107
8.1	Overview of averaged velocity magnitude $\ \mathbf{u}\ $ (levels between 0 and 5.2 m/s) with superimposed secondary velocity streamlines, healthy model. The specified locations (A, C - D, G - H, J) coincide with those of Figure (3.2). . . . .	128
11.1	Overview of most important physical and biological processes that are active in the upper airway. . . . .	172

---

# Nomenclature

## Abbreviations

BE	<i>Boltzmann Equation</i>
CbP	<i>Chosen by PowerFLOW</i>
CFD	<i>Computational Fluid Dynamics</i>
CT	<i>Computed Tomography</i>
DES	<i>Detached Eddy Simulation</i>
DNC	<i>Direct Noise Computation</i>
DNS	<i>Direct Numerical Simulation</i>
LBGK	<i>Lattice Bhatnagar Gross Krook</i>
LBM	<i>Lattice Boltzmann Method</i>
(I)LES	<i>(Implicit) Large Eddy Simulation</i>
LS	<i>Turbulent Length Scale</i>
MRI	<i>Magnetic Resonance Imaging</i>
NRBC	<i>Nonreflecting Boundary Condition</i>
NSE	<i>Navier-Stokes Equations</i>
OASPL	<i>Overall Sound Pressure Level</i>
PIV	<i>Particle Image Velocimetry</i>
PSD	<i>Power Spectral Density</i>
RANS	<i>Reynolds-Averaged Navier-Stokes</i>
RNG	<i>Renormalization Group</i>
RUAM	<i>Realistic Upper Airway Model</i>
SaE	<i>Same as Experiment</i>
SGS	<i>Subglottic Stenosis</i>
SPL	<i>Sound Pressure Level</i>
SUAM	<i>Simplified Upper Airway Model</i>
TF	<i>Timeframe</i>
TI	<i>Turbulence Intensity</i>
UAO	<i>Upper Airway Obstruction</i>
VR	<i>Variable Resolution</i>

## Symbols

### Roman

$\mathbf{a}$	Acceleration
$C$	Collision operator
$c$	Speed of sound
$c_{0,ph}$	Physical speed of sound
$c_s, c_{0,la}$	Lattice speed of sound
$D$	Typical acoustic source dimension
$\mathbf{e}$	Microscopic velocity
$f$	Frequency
$f(\cdot)$	Distribution function
$f^{eq}(\cdot)$	Equilibrium distribution function
$f_s$	Sampling frequency
$f_T$	Breathing frequency
$I$	Sound Intensity
$k$	Wavenumber
	Turbulent kinetic energy
$M$	Mach number
$N$	Number of grid points
$N_{ppw}$	Number of points per wavelength
$Pr$	Prandtl number
$p$	Macroscopic pressure
$p'$	Pressure perturbation
$Q$	Airflow rate
$Re$	Reynolds number
$r$	Distance between noise source and observer
$S$	Swirl
$T$	Absolute temperature
$T_{ij}$	Lighthill's turbulence stress tensor
$t$	Time
$\mathbf{u}$	Macroscopic velocity
$u$	Streamwise velocity
$u_x$	Horizontal velocity (in conjunction with airway models)
$u_z$	Vertical velocity (in conjunction with airway models)
$u^+$	Mean velocity normalized by friction velocity
$u_{char}$	Characteristic velocity, PowerCASE variable
$u_\tau$	Friction velocity
$v$	Crossflow velocity
	Wave propagation speed
$V_T$	Tidal volume
$w$	Spanwise velocity
$w_i$	Weights corresponding to lattice velocities $\mathbf{e}_i$
$y^+$	Normalized (by viscous length scale) distance between wall and first off-wall voxel

**Greek**

$\Delta$	Grid spacing
$\Delta f$	Frequency band
$\Delta t$	Simulation time step
$\Delta x$	Local voxel size
$\Delta P$	Pressure drop
$\epsilon$	Turbulent dissipation
$\lambda$	Wavelength
$\mu_t$	Eddy viscosity
$\nu$	Kinematic viscosity
$\tau$	Relaxation parameter
$\tau_{turb}$	Turbulent relaxation time scale
$\tau_w$	Wall shear stress
$\omega$	Vorticity





---

# Chapter 1

---

## Introduction

Upper Airway Obstructions (UAOs) are a common disorder in both children and adults. While these constrictions often remain harmless, they can cause serious and potentially lethal health risks once they grow to a critical size. Often associated with more severe obstructions is the presence of a characteristic breathing sound known as stridor, a high-pitched noise caused by the vibration of airway tissue and/or turbulent flow in the vicinity of the obstruction. This stridor is often the impulse to seek medical consultation and a cause of extreme anxiety in concerned parents.

Indeed, an important realization is that neonates and infants are especially susceptible to severe health risks due to a smaller diameter of their airway lumen. As an example, a homogeneous edema of 1 mm at the airway walls would decrease the airway lumen by 75 % in children and 44 % in adults, leading to a corresponding 16-fold and 3-fold increase in airway resistance, respectively [Wheeler et al. \(2009\)](#).

The current ‘golden’ standard in diagnosing the location and size of UAOs is an invasive endoscopy, even though this procedure poses additional health risks [Claes et al. \(2005\)](#). Most importantly, the intervention often requires full sedation in junior patients. Besides, the endoscope blade might damage the airway tissue, possibly leading to new obstructions. Therefore, several non-invasive techniques are being developed that might be able to determine the nature of the obstruction. Within this range of potential diagnostic tools, one of the possibilities is to use the acoustical spectrum of the patient’s stridor to determine the size and location of the obstruction. The incentive for this particular research is the belief that every UAO has a unique acoustic ‘footprint’ in terms of tonal frequencies and broadband sound pressure levels, independent of their physiological inter-subject variabilities [Zwartenkot \(2010\)](#); [Gray et al. \(1985\)](#).

In its simplest version, the acoustic diagnostic technique only relies on the attentive ear of a medical expert. Thoughtful consideration of the stridor sound in combination with their vast empirical expertise is applied to pinpoint the obstruction as being pharyngeal, laryngeal,

tracheal or intrathoracic. This approach has been shown to be fairly reliable for common obstructions such as laryngomalacia, but it is nonetheless insufficiently accurate to be used as a decisive means to determine the size and type of UAOs [Zwartenkot et al. \(2010\)](#).

Recently more importance is attached to Computational Fluid Dynamics (CFD) as a means to simulate the fluid flow through the upper respiratory tract as well as the associated acoustic field. Once this numerical methodology is shown to be a reliable tool it might be used in two ways to determine the location and dimensions of any UAO. When it is confirmed that stridor is indeed largely independent of patient-specific anatomy, efforts can be aimed at the development of a look-up table which unambiguously relates acoustic features to upper airway disorders. This approach would not require physicians to have knowledge of the underlying numerical methodologies. On the other hand, when patient-specific anatomical detail does play a role of importance in the simulation results, this information should be used in the attempt to solve the inverse numerical problem. Following this approach, a combination of in vivo acoustic measurement data and imaging data of the patient's upper airway anatomy would be used to determine the type of fluid flow, and hence the type of obstruction, which might have caused the stridor. This requires a study of time-reversal methods and causes an additional burden for physicians. Moreover, computational time becomes of crucial importance due to the required urgency of the diagnosis.

Independent research has been conducted into the numerical simulation of airflow patterns of the upper respiratory system, the fluid-structure interaction of different airway components, and the experimental analysis of acoustic characteristics of stridor. It has however, to this author's knowledge, never been attempted to combine all these aspects in a single simulation of the human airway tract, an indisputably essential feature of the aforementioned goal. Two exceptions are the theses by [Lynch \(2012\)](#) and [van der Velden \(2012\)](#), the results of which have been recently compiled and extended in a paper by [van der Velden et al. \(2015\)](#). These researchers applied finite-volume methods with Large Eddy Simulation turbulence modeling to a single realistic upper airway model. While [Lynch \(2012\)](#) laid the foundation for accurate simulations, [van der Velden \(2012\)](#) put more emphasis on the resulting acoustic spectrum, thereby accounting for the contributions of both turbulence and solid surfaces. Results were promising but as yet inconclusive, in part due to the required 1-month simulation time.

In this thesis it will be investigated whether the Lattice Boltzmann Method (LBM) can provide a worthy alternative for the conventional CFD methods. Since the LBM is widely praised for its simplicity of implementation, inherent parallelism, and easy handling of complex boundaries, it was deemed appropriate to investigate its usefulness and potential superiority in the aeroacoustic simulation of fluid flow through the upper respiratory system.

## 1.1 Research Objectives

The main objective of this research project is to contribute to the development of a non-intrusive diagnostic technique that can accurately and efficiently determine the cause of stridor as well as the approximate location, dimensions and nature of the obstruction(s). It is

envisioned that the proposed method could serve as a safe alternative for the current intrusive and possibly harmful endoscopy. As a first step towards reaching this goal, the research project will assess whether it is feasible to adopt the LBM as a means to predict the noise generated by the obstruction and the propagation of this noise through the airways.

Since the LBM is a relatively new approach to the modeling of complex flow phenomena, making its first appearance in the late 1980s, the amount of open-source models and documentation concerning its implementation is limited [McNamara and Zanetti \(1988\)](#); [Higuera and Jiménez \(1989\)](#). Combined with the fact that this thesis intends to utilize this numerical methodology as a means to an end, rather than performing an in-depth theoretical study of its characteristics, it was decided to carry out the simulations using the commercial software package PowerFLOW, developed by Exa Corporation. Because this software has been designed primarily for use in automotive engineering, it is questionable whether it can also be applied for internal aeroacoustic simulations at low Reynolds- and Mach numbers. This issue called for a subdivision in the primary research objective, with the first objective being the following: Investigate whether the PowerFLOW-LBM is capable of simulating internal flow fields at low Mach- and Reynolds numbers, as well as their associated acoustic fields. It is envisioned that this validation procedure is not only essential to attain a certain level of experience in working with the program, but that it will also set out best practices that can be applied in the upper airway simulations.

## 1.2 Thesis Outline

In accordance with the aforementioned two-fold research objective this thesis is split in four distinct parts:

- I Medical terminology and numerical methodologies;
- II Validation of the PowerFLOW software for use in internal aeroacoustic simulations;
- III Simulation of stridor in simplified and realistic upper airway models;
- IV Conclusions and recommendations.

The first part includes all background information that is required to fully comprehend the terminology that is used throughout subsequent parts, as well as to gain maximal insight in the implications of the simulation results. It starts with an anatomical description of the human airway and an explanation of the stridor phenomenon in Chapter 2. Chapter 3 then elaborates on how the intricate geometrical features of the airway can be converted to working computational models. The basic principles of the all-important Lattice Boltzmann Method are discussed in Chapter 4, while Chapter 5 provides an overview of the aerodynamic noise-generating mechanisms that are encountered in the airway. Readers who are already familiar with these topics can skip this first part and return to it whenever necessary (clear references are included in later parts). Nonetheless, it is advised to read through Sections 4.2 and 5.3 as these include essential details concerning the PowerFLOW software.

The combined second and third part constitute the research portion of this thesis and are directly linked to the objectives that have been put forward in Section 1.1. First, the second part addresses the steps that have been taken in order to validate the PowerFLOW software. Chapter 6 deals with a periodic hill configuration and is mainly focused on the validation of the wall and turbulence models. Afterwards, Chapter 7 concentrates on an analysis of the aeroacoustic characteristics of the PowerFLOW-LBM. Based on a diaphragm test case a thorough discussion is provided concerning all parameters that might influence the acoustic spectrum. Once reassured that PowerFLOW is indeed capable of performing aeroacoustic simulations of the fluid flow through internal geometries at low Reynolds- and Mach numbers, part three switches attention to the main research objective. Over the course of two chapters (8 and 9) it elaborates on the aeroacoustic flow fields through a simplified and a realistic upper airway model, respectively.

Finally, the fourth part concludes the thesis by providing the reader with a conclusion concerning the potential value of the results in Chapter 10, and by listing possible improvements over the methodologies applied throughout this thesis in Chapter 11.

## **Part I**

# **Background: Medical Terminology, Airway Models and Numerical Methodologies**



---

## Chapter 2

---

# Medical Background

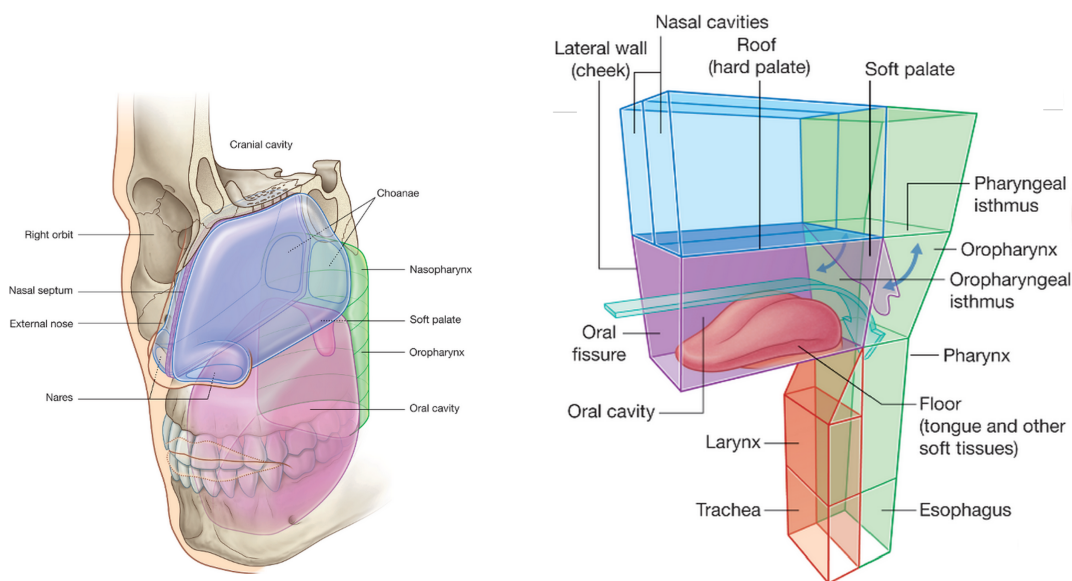
This chapter gives a brief overview of the anatomy of the upper airway system, as well as the medical terminology often used in relation to stridor. Detailed anatomical descriptions can be found in the monographs by [Standring et al. \(2009\)](#), [Drake et al. \(2009\)](#) and [Snell \(2011\)](#). Section 2.1 elaborates on the anatomy of each of the four clinical regions that together comprise the upper airway. For the sake of completeness, a brief overview of the lower respiratory system anatomy is also included. Next, the differences between an adult and a pediatric airway are highlighted in Section 2.2, while Section 2.3 discusses how airflow is created inside the airways. Finally, Section 2.4 is dedicated to an explanation of the most common causes of stridor, additionally providing an overview of well-established and recently proposed diagnostic techniques.

### 2.1 Anatomy of the Upper Airway

A general overview of the upper airway system is shown in Figure (2.1). Air enters the body through the external nares and the mouth after which it is led successively through the pharynx and the larynx on to the lower respiratory system. The larynx, situated in the anterior part of the neck, runs parallel with the laryngopharynx. Each of these components will be discussed in the following subsections.

#### 2.1.1 Nasal Cavity

The nasal cavity consists of two nasal fossae which start at the flexible external nares and extend for approximately 10 to 14 cm to the rigid choanae which open into the nasopharynx. The fossae are separated medially by the nasal septum and bounded at the apex by the cribriform plate and at the bottom by the hard palate. The lateral walls consist of the inferior,



**Figure 2.1:** Overview of the upper airway system Drake et al. (2009).

middle and superior turbinate bones (conchae). These conchae run inwards and downwards into the nasal fossa and divide it into five spaces, see Figure (2.2). The regions enclosed by the conchae are referred to as the inferior, middle and superior meatuses. The space above the superior concha is called the sphenoidal recess, which contains an opening to the sphenoidal sinus. It is this small region situated in the apex of the nasal cavity that enables olfaction. Finally, the medial passage is found between the nasal septum and the conchae.

The nasal septum as well as the conchae are covered with mucous membrane, formed by mucins secreted by epithelial goblet cells. Underneath this mucous membrane, the cribriform plate is perforated to allow a connection with the cranial cavity.

### 2.1.2 Oral Cavity

The oral cavity runs from the oral fissure to the oropharyngeal isthmus which opens into the oropharynx. A pair of dental arches separate the oral cavity into two regions: the oral vestibule on the outside and the proper oral cavity on the inside. The oral vestibule is bounded laterally by the internal walls of the cheeks which are covered with oral mucosa.

The floor of the proper oral cavity consists mainly of the tongue. An important aspect of the oral part of the tongue is its irregular structure due to the presence of papillae, see Figure (2.3(a)). Posteriorly, one third of the tongue, i.e., the pharyngeal part, extends outside the oral cavity where it forms part of the anterior wall of the oropharynx. Even though the pharyngeal part of the tongue is also irregular it does not exhibit papillae, nor does the inferior surface of the oral part of the tongue. The division line between the two parts is



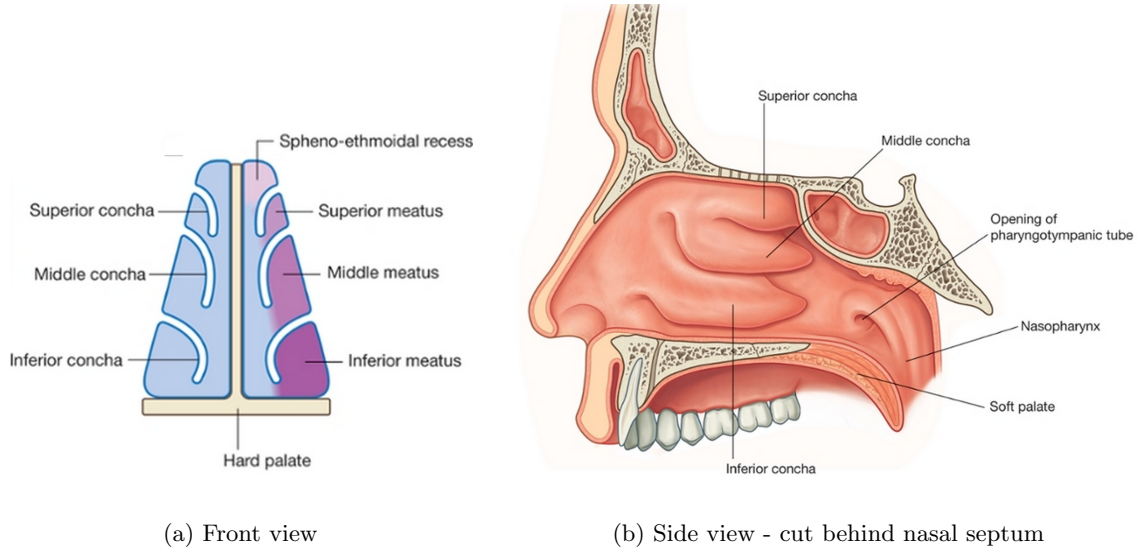


Figure 2.2: Internal anatomy of the nasal cavity Drake et al. (2009).

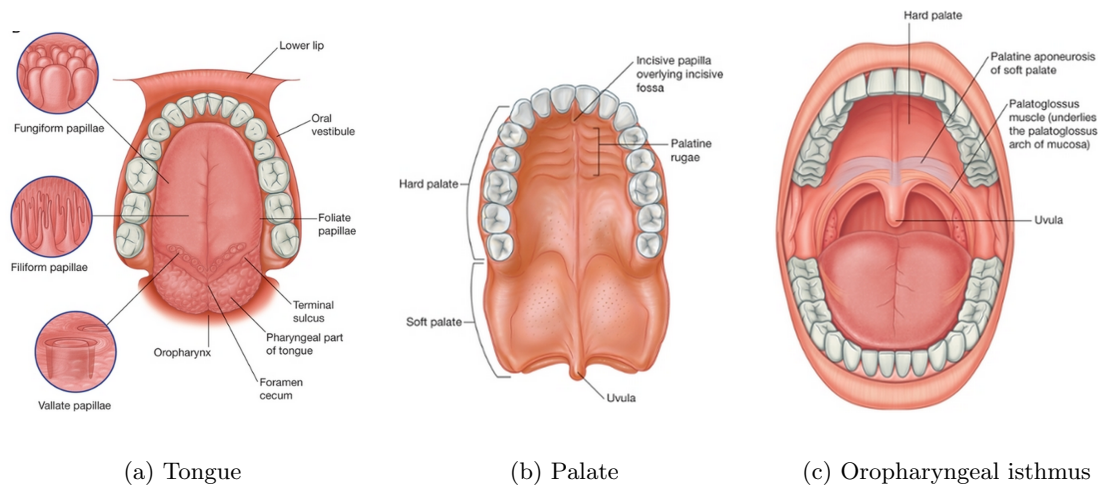


Figure 2.3: Internal anatomy of the oral cavity Drake et al. (2009).

called the terminal sulcus. The central depression in the tongue is caused by the genioglossus muscle.

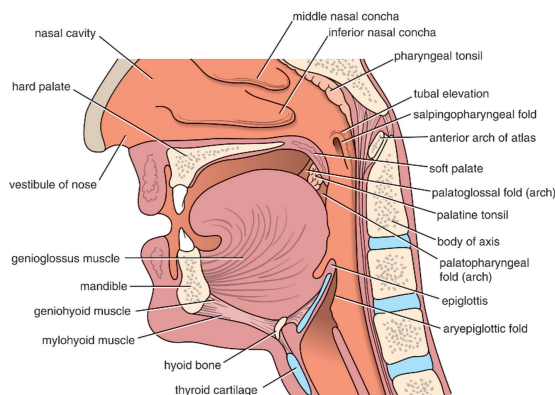
The hard and soft palate form the apex of the proper oral cavity and are also covered with mucosa, see Figure (2.3(b)). These surfaces are in general smooth, with the exception of the anterior part of the hard palate, which is covered by palatine rugae. While the hard palate, which forms the separation between the oral and nasal cavity, is rigid, the soft palate is flexible and plays an important role in closing the oropharyngeal isthmus to separate the oral cavity from the oropharynx. This is necessary to allow nasal breathing whilst chewing. Also the palatoglossus muscle ensures that this can be achieved, see Figure (2.3(c)). Whilst contracting, it elevates the back of the tongue and pulls the soft palate towards the center.

### 2.1.3 Pharynx

The pharynx is 12 to 15 cm in length and lies behind the nasal cavity, the oral cavity and the larynx, where it extends from the cranial base to the cricoid cartilage (at the level of the sixth cervical vertebra), see Figure (2.4). Its width varies constantly though it is narrowest at the entrance to the esophagus ( $\approx 1.5$  cm) and widest at the level of the hyoid bone ( $\approx 5$  cm).

The pharynx can be subdivided into the nasopharynx, oropharynx and laryngopharynx (hypopharynx). The rigid nasopharynx starts at the termination of the choanae and runs until the inferior side of the soft palate. Here the flexible oropharynx starts, which extends to the superior side of the epiglottis. The flexible laryngopharynx starts at the superior side of the epiglottis and runs until the esophagus.

The posterior side of the pharynx consists of mucous membrane. Underneath this membrane are two muscle layers, each with three paired muscles, which play an important role in deglutition. The external circular layer advances the food from the oral cavity to the esophagus, while the internal longitudinal layer elevates the pharynx and shortens the larynx during deglutition - to avoid food entering the trachea.

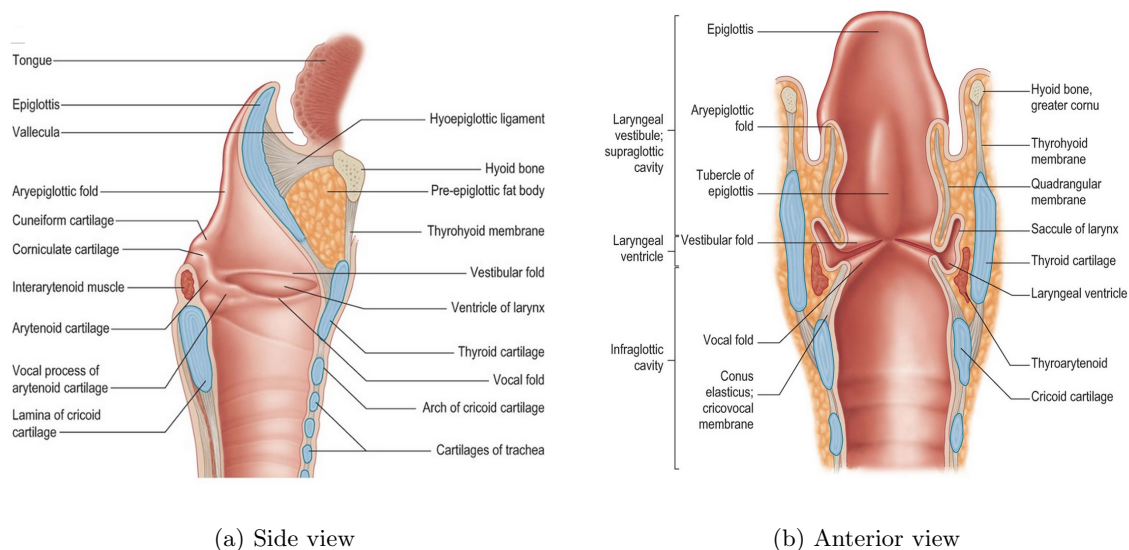


**Figure 2.4:** Internal anatomy of the pharynx Snell (2011).

### 2.1.4 Larynx

The larynx starts at the level of the third cervical vertebra and extends to the inferior part of the cricoid cartilage. Air enters it through the laryngeal inlet (aditus), which lies at the anterior wall of the laryngopharynx and is bounded superiorly by the superior side of the epiglottis, inferiorly by the fold of mucous membrane between the arytenoid cartilages and laterally by the aryepiglottic folds.

The larynx can be subdivided in the supraglottic larynx, laryngeal ventricle and infraglottic larynx, see Figure (2.5). The supraglottic larynx extends from the laryngeal inlet to the vestibular folds (ventricular or false vocals). The area that runs from the vestibular folds to the vocal folds (vocal cords) is called the laryngeal ventricle. At the vocal folds the infraglottic larynx starts from where it runs until the inferior part of the cricoid cartilage where it connects with the trachea.



**Figure 2.5:** Internal anatomy of the larynx [Strandring et al. \(2009\)](#).

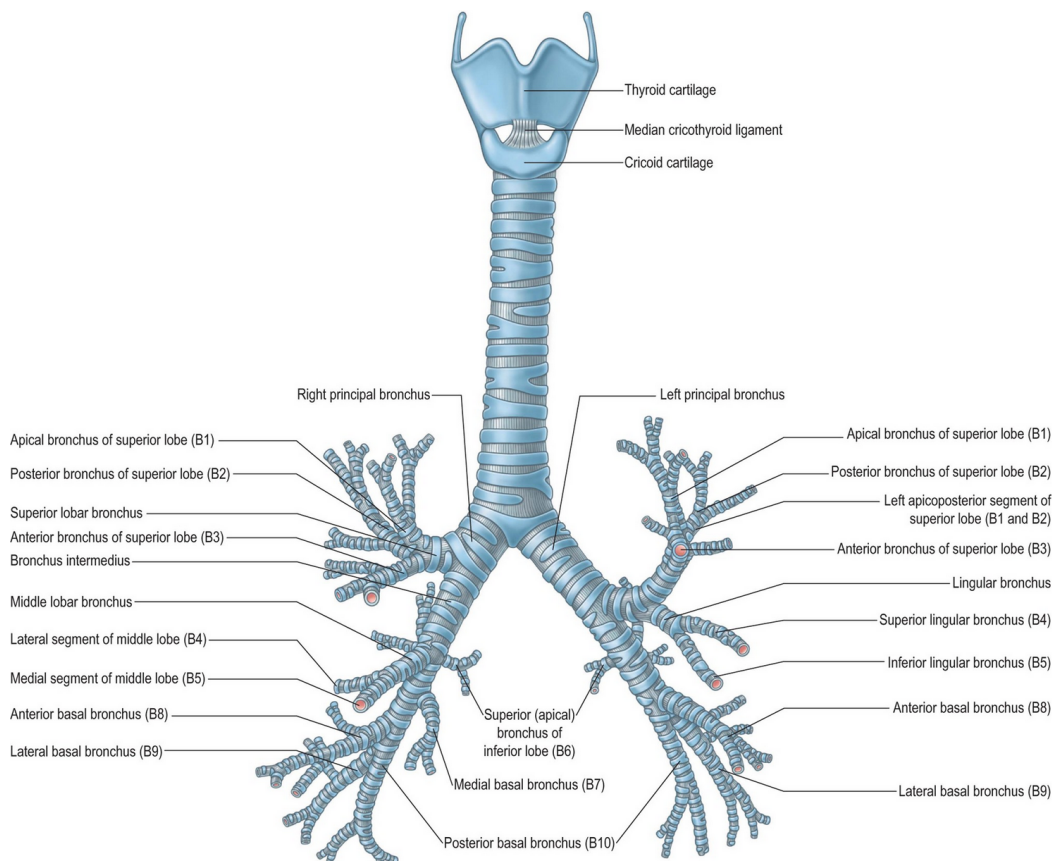
Its structure is provided by a framework of nine cartilages, of which the thyroid, cricoid and epiglottis are the most interesting. The thyroid cartilage causes the greater laryngeal prominence (Adam's apple) with men, which results in larger vocal folds and a deeper voice compared to women. At the lower limit of the larynx, the circular cricoid cartilage forms the connection with the trachea. Food and liquids are diverted from the larynx by the concave anterior surface of the epiglottis.

Next to its respiratory function, the larynx is also an organ of phonation. The phonation occurs at the level of the glottis (rima glottidis), which is confined between the vocal cords and the arytenoid cartilages, and which is the narrowest part of the larynx (sagittal diameter of  $\pm 23$  mm for men and  $\pm 17$  mm for women). Opening and closing of the glottis due to

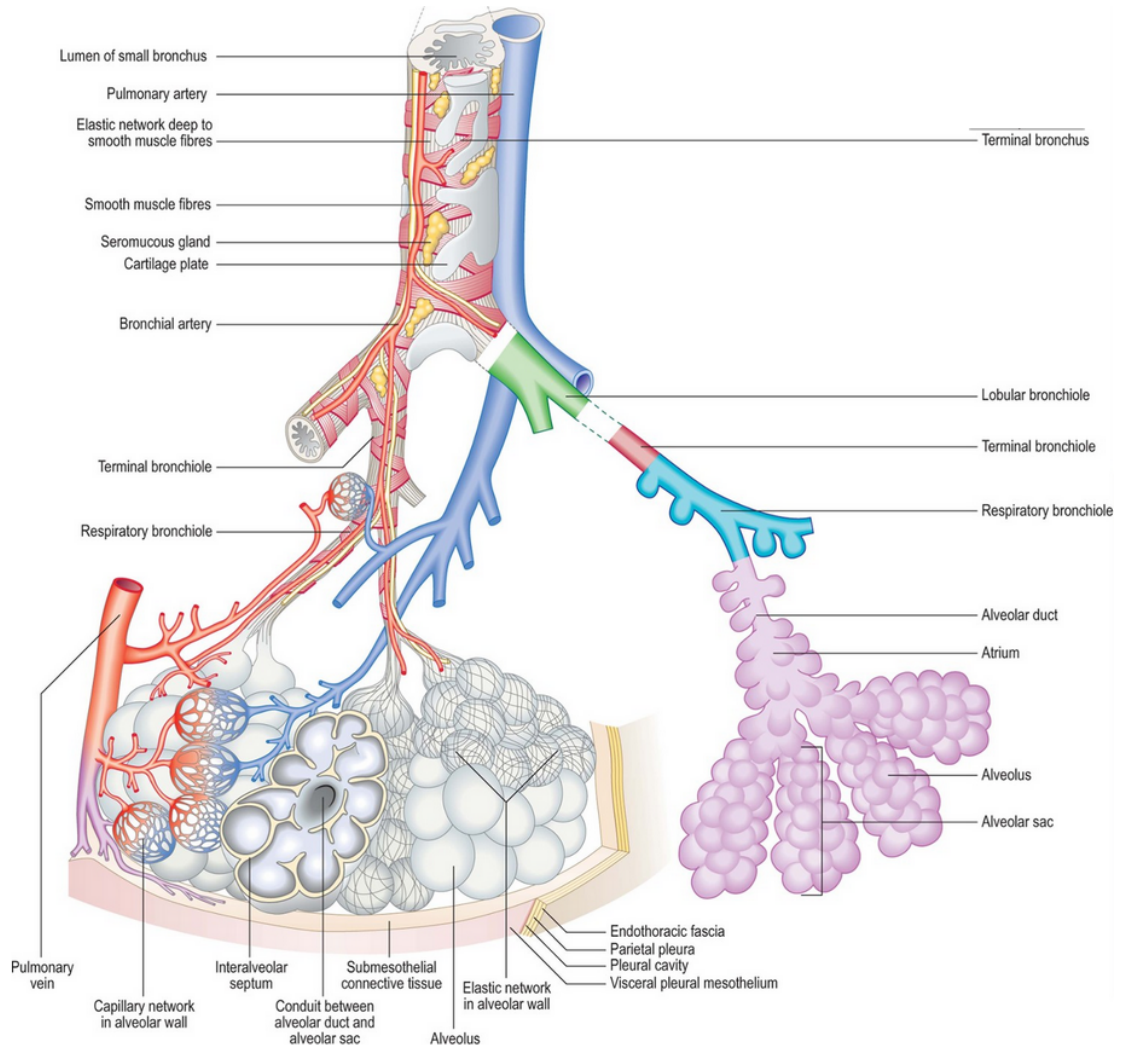
differences in subglottal pressure causes the vocal cords to vibrate with sound production as result.

### 2.1.5 Anatomy of the Lower Respiratory Tract

Since the lower respiratory tract will not be implemented in the simulations (the outlet boundary condition will be specified at the level of the trachea), a brief account of its anatomy is merely included for the sake of completeness. The lower airway system starts at the trachea which extends for approximately 10 to 11 cm to the level of the superior border of the fifth thoracic vertebra. Here the trachea splits into the right and left principal bronchi, which subsequently split into segmental (lobar) bronchi, each of which runs through a separate bronchopulmonary segment, see Figure (2.6). After several subdivisions the bronchi arrive at the respiratory bronchioles which have walls of alveolar sacs, see Figure (2.7). These alveolar sacs contain the alveoli responsible for gas exchange ( $O_2$  and  $CO_2$ ) and are thus essential for the respiratory function.



**Figure 2.6:** Internal anatomy of the lower respiratory system: Trachea and main bronchi [Stranding et al. \(2009\)](#).



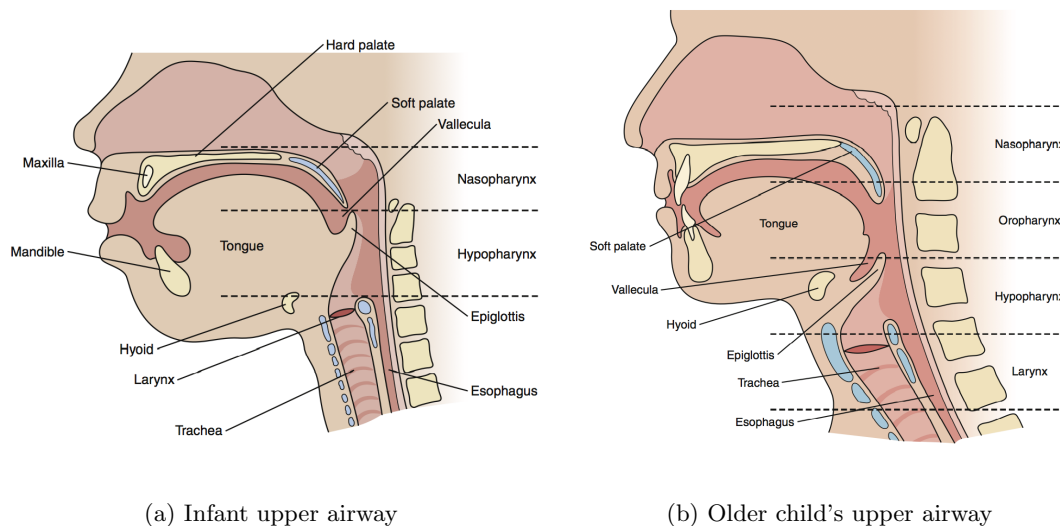
**Figure 2.7:** Internal anatomy of the lower respiratory system: Bronchioles and alveoli **Standing et al. (2009)**.



## 2.2 The Pediatric Airway

The thesis will be aimed at the simulation of an adult airway because medical image-data of a children's airway is not readily available nor easily obtainable as a result of the health risks associated with common imaging techniques, see Chapter 3. Since stridor is predominantly present in children, it is important to study the anatomic differences between the adult and pediatric airway in order to allow sensible recommendations regarding the extrapolation of simulation data from adults to children.

[Wheeler et al. \(2009\)](#) described five major morphologic anatomic differences between the pediatric and adult airway, most of which are visualized in Figure (2.8):



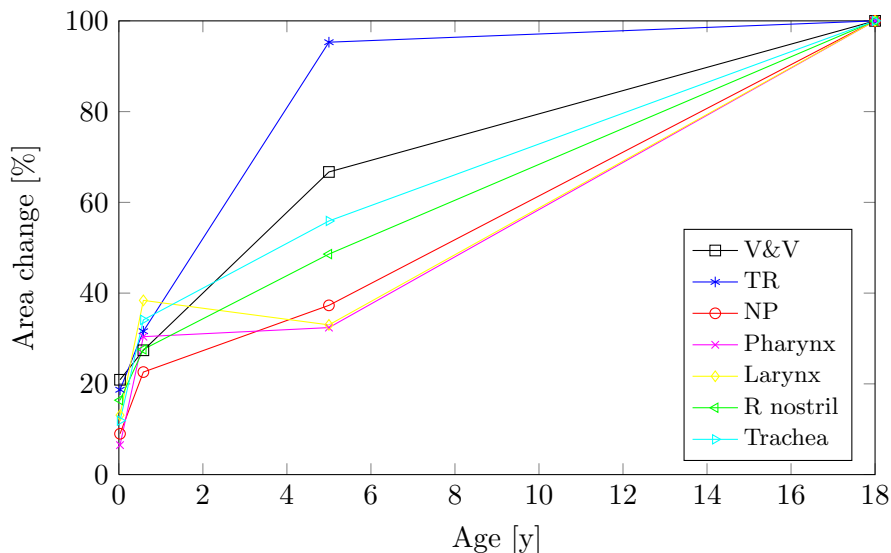
**Figure 2.8:** Comparison between the upper anatomy of an infant and an older child [Brodsky \(2011\)](#).

- The tongue occupies the majority of the oral cavity in infants.
- The position of the larynx shifts throughout childhood. The glottic opening of neonates lies at the level of the third or fourth cervical vertebra, after which it descends to the adult level at the fourth or fifth cervical vertebra by the age of two. During later childhood the larynx still moves more caudal in relation to the face and skull, but its position with respect to the vertebral column remains unchanged [Lieberman et al. \(2001\)](#). It should be noted that the more cephalad position of the larynx causes a closer proximity of the oropharyngeal structures (note the position of the epiglottis with respect to the soft palate in Figure (2.8)), which contributes to the fact that infants are obligate nasal breathers until the age of 3 - 5 months.
- Compared to the adult's epiglottis, the infant's epiglottis tends to be omega ( $\Omega$ ) shaped, narrower, and more inclined in relation to the glottic opening [Adewale \(2009\)](#).

- The attachment of the infant's vocal cords is lower anteriorly than posteriorly.
- The infant's larynx is generally funnel-shaped with its narrowest part situated in the subglottic region or at the level of the circular cricoid cartilage, while the adult's larynx is more cylindrical with its narrowest part at the glottis.

Next to these general differences it can also be observed that the change in flow direction from the nasal cavity to the nasopharynx becomes more acute with age, approaching  $90^\circ$  in adults [Brodsky \(2011\)](#). Also, the relative size of the adenoids (pharyngeal tonsils, see Figure (2.4)) in relation to the nasopharyngeal space is larger in children than in adults because the adenoids grow until their maximum size by the age of 4 - 6 years and start to involute again at the age of 8 - 9 years [Haapaniemi \(1995\)](#).

Developmental changes in upper airway dimensions are described accurately by [Xi et al. \(2012\)](#) for a 10-day-old girl, a 7-month-old girl, a 5-year-old boy and a 53-year-old adult. Their measurements are listed in Tables (2.1) - (2.2), while the area change of the different components is displayed in Figure (2.9). Based on these results, [Xi et al. \(2012\)](#) concluded that '*younger subjects have smaller sized nostrils, shorter turbinate regions, slender nasopharynx and thinner pharynx-larynx*'. Figure (2.9) additionally indicates that the growth of the different components is strongest during the first year of life (largest slope). Furthermore, the turbinate region appears to be completely developed by the age of 5, while the nasopharynx matures much slower as compared to other components. Given the area (or volume) decrease of the larynx and pharynx between the ages of 7 months and 5 years, it is reasonable to question the measurement validity of these two components.



**Figure 2.9:** Area change of airway components in terms of percentage. Graph based on results from [Xi et al. \(2012\)](#). V & V = Vestibule & Valve, TR = Turbinate Region, NP = Nasopharynx.

**Table 2.1:** Nasal airway dimension of the four airway models of different ages [Xi et al. \(2012\)](#). V & V = Vestibule & Valve, TR = Turbinate Region, NP = Nasopharynx.

Anatomy	Volume, $V$ (cm <sup>3</sup> )					Surface Area, $A$ (cm <sup>2</sup> )					Effective diam., $d_e$ (cm)				
	10 day	7 month	5 year	Adult	Adult	10 day	7 month	5 year	Adult	Adult	10 day	7 month	5 year	Adult	
V & V	0.79	1.25	3.37	5.50	7.45	9.75	23.74	35.58	0.43	0.52	0.57	0.62	0.62	0.62	
TR	1.57	2.83	11.03	12.63	21.09	35.63	107.34	112.59	0.30	0.32	0.41	0.45	0.45	0.45	
NP	0.48	1.74	3.95	16.33	3.72	9.27	15.27	40.93	0.52	0.75	1.03	1.60	1.60	1.60	
Pharynx	0.31	3.19	2.64	13.89	2.96	13.71	14.59	45.10	0.42	0.93	0.72	1.23	1.23	1.23	
Larynx	0.36	1.32	1.22	6.70	2.87	8.37	7.20	21.81	0.50	0.63	0.68	1.23	1.23	1.23	
Total	3.51	10.33	22.21	55.05	38.09	76.73	168.14	256.01	0.37	0.54	0.53	0.86	0.86	0.86	
Ratio (%)	6.40	18.80	40.30	100.00	22.70	30.00	65.70	100.00	43.00	62.80	61.60	100.00	100.00	100.00	

**Table 2.2:** Nostrils and upper trachea dimension of the four airway models of different ages [Xi et al. \(2012\)](#).

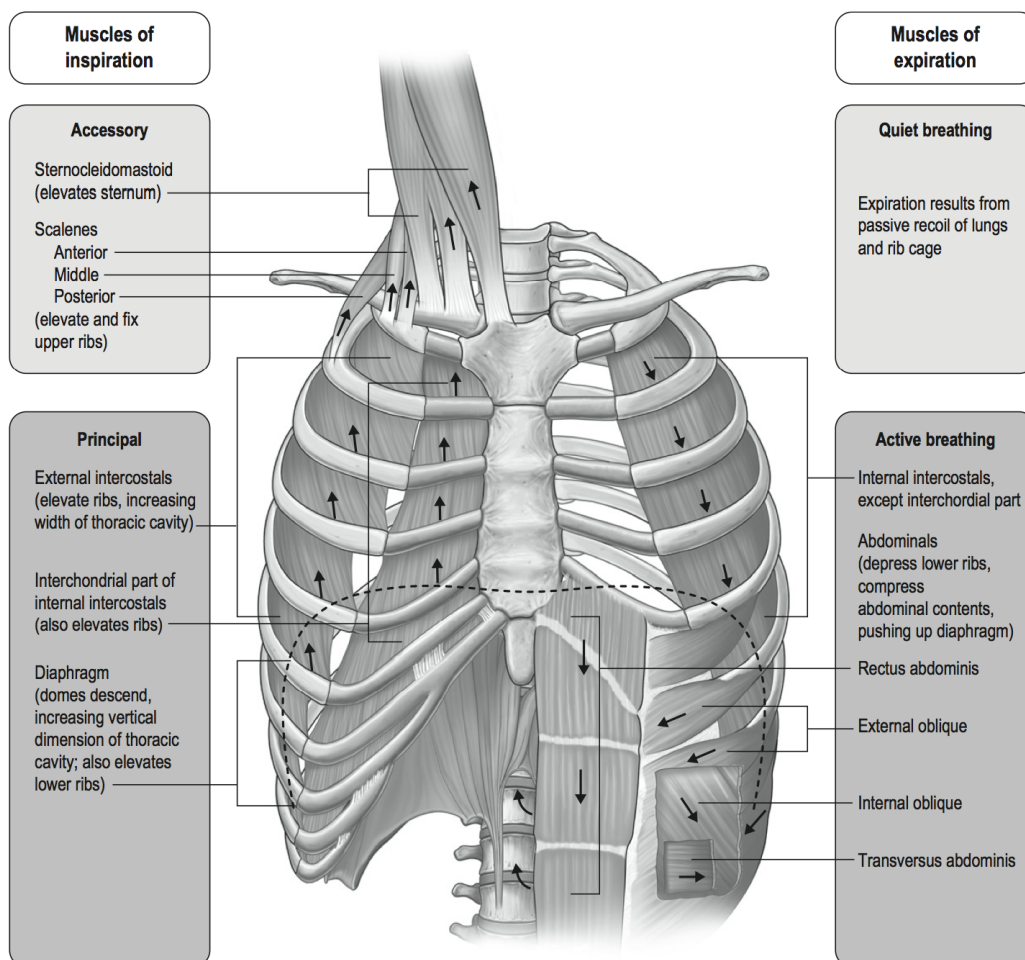
Anatomy	Coronal Area, $A$ (mm <sup>2</sup> )					Perimeter, $P$ (mm)					Hydr. diam., $d_h$ (mm)				
	10 day	7 month	5 year	Adult	Adult	10 day	7 month	5 year	Adult	Adult	10 day	7 month	5 year	Adult	
R nostril	16.59	27.98	49.20	101.27	14.46	19.92	25.61	44.53	4.59	5.62	7.68	9.10	9.10	9.10	
L nostril	16.59	31.48	43.73	101.27	14.46	20.49	24.89	44.53	4.59	6.15	7.03	9.10	9.10	9.10	
Trachea	17.77	50.64	83.23	148.66	15.33	25.59	33.59	45.66	4.64	8.01	9.91	13.02	13.02	13.02	



## 2.3 Breathing Mechanics

Since the emphasis of this thesis will be on the simulation of the airflow through the upper respiratory system as a means to determine the acoustic spectrum of the stridor, it is worthwhile to briefly investigate the mechanical means by which this airflow is created.

Essentially, respiration is brought about by a pressure change in the thoracic cavity. During inspiration the contraction of both the diaphragm and external intercostal muscles (i.e., muscles between the ribs) causes the thoracic cavity to expand, which results in a negative intrathoracic pressure. Quiet expiration, on the other hand, happens under the influence of a positive intrathoracic pressure and is mainly due to the elastic recoil of the lungs and the rib cage. Additional muscle activity simplifies expiration during exercise breathing conditions [McConnell \(2013\)](#). An overview of the muscle activity during respiration is shown in Figure (2.10).



**Figure 2.10:** The respiratory pump muscles [McConnell \(2013\)](#).

More important are the typical respiratory airflow rates as they will determine both the inlet boundary conditions and Reynolds number ( $Re$ ), and therefore also the general flow conditions. Quiet airflow rates (i.e., not considering breathing conditions during physical exercise) are influenced by a number of factors including anatomy, figure, gender, age, ethnicity and presence/absence of disease [McConnell \(2013\)](#). The breathing type, i.e., nasal/oral/combined, potentially also plays a role given the larger flow resistance encountered during nasal breathing as a result of the nasal cavity's intricate geometry. This inter- and intra-subject variability clearly indicates that the results of a numerical simulation can only be correctly validated with experimental data when the airflow rates (next to the anatomy) are obtained directly from the patient. Nevertheless, it remains instructive to present some general values and definitions.

Airflow rate is defined as the product of tidal volume  $V_T$  times breathing frequency  $f_T$ , where  $V_T$  is the amount of air inhaled during a single respiratory cycle. It is clear that both variables are likely to depend on the aforementioned factors. [Hooper \(2001\)](#) experimentally demonstrated nasal airflow rates in adults to range between 5 - 12 L/min for calm breathing with an increase up to 40 L/min during physical exercise. Typical values for the associated  $Re$  lie between 400 - 12,000 (as based on the hydraulic diameter of the nostrils). With respect to age [Xi et al. \(2012\)](#) assessed that there exists a strong correlation between tidal volumes and nasal-laryngeal volumes. They also showed that  $f_T$  rapidly diminishes with age, with the steepest decline occurring in the first two years of age [Fleming et al. \(2011\)](#). Interestingly, this decrease in breathing frequency does not necessarily affect the nostril inlet velocities as these are similar for all ages. The results of [Xi et al. \(2012\)](#) are summarized in Table (2.3), although it should be noted that most of the values are based on previously published parameters. A calculation of  $Re$ , based on the hydraulic diameter of both the right nostril and the trachea, showed that it increases with age and is generally higher in the tracheal region. Unfortunately, a quantitative discussion on the influence of factors other than age is not readily available in literature.

**Table 2.3:** Respiratory parameters under quiet breathing conditions at various ages [Xi et al. \(2012\)](#). The Reynolds numbers ( $Re$ ) are calculated using the hydraulic diameter data from Table (2.2). The value for the kinematic viscosity was taken to be  $1.568 \times 10^{-5} \text{ m}^2/\text{s}$ , which corresponds to a temperature of 300 K.

Respiratory variable		10 day	7 month	5 year	Adult
Frequency	$[\text{min}^{-1}]$	44	25	21	12
Tidal volume	$[\text{mL}]$	22	87	177	500
Flow rate	$[\text{L}/\text{min}]$	3.8	6.5	11.2	18.0
Inlet velocity	$[\text{m}/\text{s}]$	1.91	1.84	1.84	1.48
$Re_{\text{Rnostril}}$	$[-]$	559	659	901	859
$Re_{\text{trachea}}$	$[-]$	1,055	1,093	1,417	1,676

## 2.4 Stridor

Stridor is the characteristic high-pitched noise produced by turbulent airflow in a partially obstructed airway and/or vibration of the surrounding tissue. It is important to note that stridor is not a disease itself, but rather a reflection or symptom of a disease. A distinction is made between inspiratory stridor, expiratory stridor and biphasic stridor. Assessment of the respiratory phase in which stridor occurs might be an indication as to what the underlying cause might be. Subsection 2.4.1 gives an overview of the possible causes of stridor. Subsection 2.4.2 describes the different diagnostic techniques that are currently applied to confirm the cause of the stridor, as well as those that might be applied in the future.

### 2.4.1 Causes

A comprehensive list of the possible causes of stridor is given by [Muñiz \(2008\)](#) and printed here in Table (2.4). Detailed analysis of these causes is outside the scope of this thesis, though it is interesting to study the most common causes of stridor in more depth.

#### Laryngotracheobronchitis (Croup)

Laryngotracheobronchitis is the most common etiology in acute stridor, and is mostly observed in children between 6 months and 3 years of age [Claes et al. \(2005\)](#). It is a viral infection which may cause severe constriction of the subglottic and tracheal lumen due to inflammation and the formation of edema. In 60 % of the cases the infection is induced by the *Parainfluenza virus type 1*.

Another disease with similar symptoms, i.e., luminal narrowing of the subglottis and trachea, is bacterial tracheitis. This is a bacterial infection primarily induced by the *S. aureus* organism.

#### Supraglottitis

Supraglottitis, more commonly referred to as epiglottitis, is a bacterial infection that causes inflammation of the supraglottic structures including the epiglottis, aryepiglottic folds, arytenoidal soft tissue and occasionally the uvula. Since it is caused by the *Haemophilus influenzae type b* in 90 % of the cases, its occurrence declined due to the availability of a vaccine. Consequently, it occurs more often in adults than in children.

#### Retropharyngeal Abscess

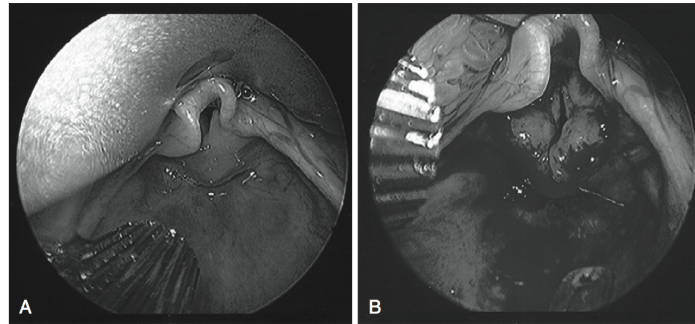
Retropharyngeal abscesses form behind the posterior pharyngeal wall. They are uncommon and typically due to the spread of an upper respiratory infection to the lymph nodes, which then inflame and eventually suppurate [Grisaru-Soen et al. \(2010\)](#). The clinical presentation is similar to supraglottitis but the swelling progresses slower.

**Table 2.4:** Differential diagnoses of stridor **Muñiz (2008)**.

<b>Location</b>	<b>Etiology</b>
<b><i>Nose and pharynx</i></b>	
Congenital anomalies	Lingual thyroid, choanal atresia, craniofacial anomalies (Apert's, Down syndrome, Pierre Robin syndrome), cysts (dermoid, thyroglossal)
Inflammatory/infectious	Abscess (peritonsillar, retropharyngeal, parapharyngeal), allergic polyps, diphtheria, uvulitis, infectious mononucleosis
Other	Adenotonsillar hyperplasia, foreign body, decreased muscle coordination from neurologic syndrome
<b><i>Larynx</i></b>	
Congenital anomalies	Laryngomalacia, laryngeal web, laryngeal cyst, laryngocele, cartilage dystrophy, subglottic stenosis, cleft larynx, hemangioma
Inflammatory/infectious	Croup, epiglottitis, tracheitis, angioneurotic edema, tuberculosis, diphtheria, sarcoidosis
Vocal cord paralysis	Congenital or traumatic
Neoplasm	Subglottic hemangioma, laryngeal papilloma, cystic hygroma, malignant (rhabdomyosarcoma), neurofibromas
Laryngospasm	Hypocalcemic tetany, irritant, drug effect, spasmodic croup
Foreign body	Laryngeal or upper esophageal
Trauma	Laryngeal fracture or dislocation, hematoma, inhalation injury
<b><i>Trachea and bronchi</i></b>	
Congenital	Vascular anomalies, webs, cysts, tracheal stenosis, tracheoesophageal fistula
Neoplasm	Tracheal, compression from adjacent tumors (thyroid, thymus, esophageal)
Inflammatory/infectious	Bacterial tracheitis
Foreign body	Tracheal or esophageal
<b><i>Other</i></b>	
	Psychogenic stridor, hemophilia (hematoma), cervical spinal trauma, caustic ingestion

### Laryngomalacia

Laryngomalacia is the most common etiology in congenital stridor, accounting for about 75% of the cases, and the most common cause of stridor in infants [Claes et al. \(2005\)](#). The disease usually resolves itself by 12 - 24 months of age. It is characterized by soft laryngeal tissue which collapses into the laryngeal cavity upon inspiration (inspiratory stridor), thereby constricting the airway, see Figure (2.11). Possible causes include delay in neuromuscular control and anatomic abnormalities [Thompson et al. \(2012\)](#).



**Figure 2.11:** Laryngomalacia (A) before and (B) after surgery [Thompson et al. \(2012\)](#).

A similar cause is tracheomalacia, i.e., collapse of the trachea during respiration due to weak cartilage or extrinsic compression [Thompson et al. \(2012\)](#). Since most defects are intrathoracic, the disorder is the predominant cause of expiratory stridor [Muñiz \(2008\)](#).

### Vocal Cord Paralysis

Vocal cord immobility accounts for 10 to 20% of congenital laryngeal disorders, which makes it the second most important cause of congenital stridor [Ahmad and Soliman \(2007\)](#). Hereby, partial or total absence of vocal cord abduction/adduction restricts the size of the glottic opening. The etiology can be either neurological or mechanical (fixation of the cricoarytenoid joint), and the disease can either be unilateral or bilateral. Unilateral vocal cord immobility usually induces dysphonia and feeding difficulties but is only rarely associated with stridor, while bilateral vocal cord immobility mostly causes biphasic stridor. In some cases the immobility resolves spontaneously but surgical treatment is more common [Garcia-Lopez et al. \(2013\)](#).

### Subglottic Stenosis

Subglottic stenosis causes a narrowing of the subglottic lumen in the cricoid region. It is diagnosed when the airway diameter is smaller than 4mm in full-term infants or 3mm in a premature infant [Claes et al. \(2005\)](#). Its etiology can be congenital or acquired and a distinction is made between membranous (soft) and cartilaginous (hard) stenosis. The latter is usually more critical though the actual severity is determined using the Myer-Cotton grading system, see Figure (2.12) [Thompson et al. \(2012\)](#). Typical for this affliction is biphasic and primarily inspiratory stridor, which usually resolves itself at later age as the larynx grows.

PERCENTAGE OF OBSTRUCTION BY ACTUAL ENDOTRACHEAL TUBE SIZE											
Patient age	Normal ID (mm)	Normal OD (mm)	Percentage of obstruction with actual endotracheal tube size								
			ID = 2.0	ID = 2.5	ID = 3.0	ID = 3.5	ID = 4.0	ID = 4.5	ID = 5.0	ID = 5.5	ID = 6.0
Premature	2.0	2.8	0%								
	2.5	3.6	40%	0%							
	3.0	4.3	58%	30%	0%						
0-3 mo	3.5	5.0	68%	48%	26%	0%					
3-9 mo	4.0	5.6	75%	59%	41%	22%	0%				
9 mo to 2y	4.5	6.2	80%	67%	53%	38%	20%	0%			
2y	5.0	7.0	84%	74%	62%	50%	35%	19%	0%		
4y	5.5	7.6	86%	78%	68%	57%	45%	32%	17%	0%	
6y	6.0	8.2	89%	81%	73%	64%	54%	43%	30%	16%	0%







Grade I		Grade II		Grade III		Grade IV
						No detectable lumen
No obstruction	50% obstruction	51% obstruction	70% obstruction	71% obstruction	99% obstruction	

Figure 2.12: Myer-Cotton grading system for subglottic stenosis de Alarcon et al. (2012).

A similar disorder might occur at the level of the trachea and is referred to as tracheal stenosis. In this case, the tracheal lumen is obstructed usually by the presence of complete cartilaginous tracheal rings or extrinsic compression. It causes biphasic stridor Claes et al. (2005).

### Laryngeal Hemangioma

Laryngeal hemangiomas account for 1.5% of congenital abnormalities of the larynx Ahmad and Soliman (2007). They are benign, soft tumors which grow rapidly in the first months of life, thereby causing asymmetric narrowing of the subglottic region and progressive biphasic or inspiratory stridor, see Figure (2.13). By the age of 2 - 3 they usually self-involute Claes et al. (2005).

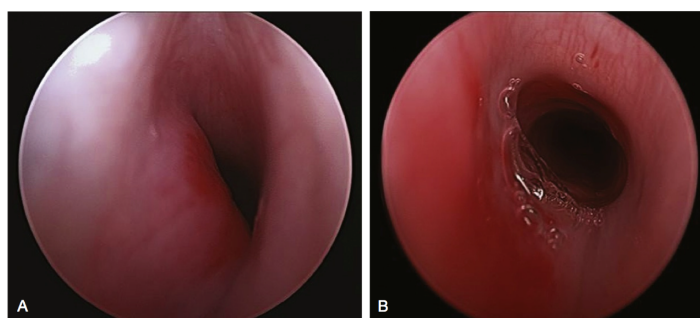


Figure 2.13: Subglottic hemangioma (A) before and (B) after treatment Thompson et al. (2012).

### Laryngeal Papillomatosis

Laryngeal papillomatosis is the most common benign laryngeal tumor in children and is caused predominantly by the *human papillomaviruses type 6 and 11*, see Figure (2.14) Gillison et al. (2012). The papillomas grow and they have a tendency to return after surgical removal in children. Associated with the infection is the presence of inspiratory stridor Claes et al. (2005).

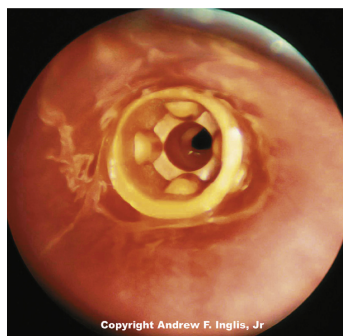




**Figure 2.14:** Laryngeal papillomas just below the vocal cords [Jardine et al. \(2011\)](#).

### Foreign Body Aspiration

A final, relatively uncommon cause of stridor is the presence of a foreign body in the airway system, see Figure (2.15). Note that a foreign body that was redirected to the esophagus may also cause airway obstruction due to tracheal compression [Claes et al. \(2005\)](#).

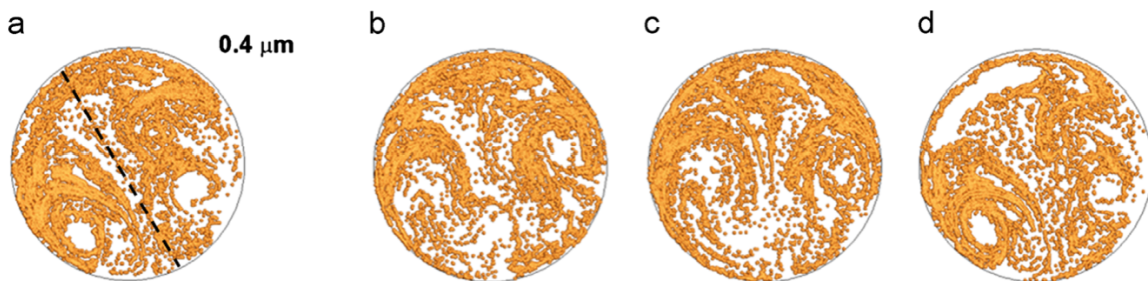


**Figure 2.15:** Example of foreign body in the trachea [Jardine et al. \(2011\)](#).

### 2.4.2 Diagnostic Techniques

**Endoscopy** is currently the most widely applied technique in the diagnosis of Upper Airway Obstruction (UAO) [Zwartenkot et al. \(2010\)](#); [Claes et al. \(2005\)](#). It is an invasive technique which requires the insertion of a laryngoscope or bronchoscope in the respiratory tract. Since this tube causes an additional narrowing of the airway lumen, careful pre-operative clinical assessment of the patient should be performed as to avoid complications during the intubation. Besides, the surgical intervention often requires general anesthesia of the patient, especially in children [Jain and Rabb \(2012\)](#); [Wheeler et al. \(2009\)](#). Since endoscopy imposes additional risks on the patient, several researchers have investigated the reliability of diverse non-invasive techniques in the assessment of UAOs. Some of those efforts will be addressed in this section.

Recently, [Xi et al. \(2013\)](#) tested the hypothesis that the **exhaled pattern of tracer aerosols** holds information on the location and severity of an UAO. They simulated the aerosol patterns, referred to as **Aerosol Fingerprint (AF)**, of four different airways and showed that they can indeed be uniquely associated with a particular airway condition, see Figure (2.16). The rather large discrepancies are caused by changes in local flow patterns due to the presence of the obstruction, which then propagate through the respiratory tract and induce different aerosol deposition patterns. Moreover, [Xi et al. \(2013\)](#) showed that the uniqueness of the AF extends to different particle sizes in the range  $0.4 - 10 \mu\text{m}$ , indicating the robustness of the method. Further research is required to establish a database that includes the AFs of a large set of UAOs, and to assess the effects of intra- and intersubject variability on the patterns. Once these criteria are fulfilled, the inverse problem can be solved using the numerical approach suggested by [Xi et al. \(2011\)](#).



**Figure 2.16:** Exhaled aerosol profiles at the mouth for airway with (a) normal condition, (b) carina tumor, (c) left bronchial tumor, and (d) asthma [Xi et al. \(2013\)](#).

[Leboulanger et al. \(2014\)](#) reviewed the use of the **Acoustic Reflection Method (ARM)** in the assessment of UAOs. This technique allows the clinician to derive the longitudinal cross-sectional area and resistance of the respiratory tract from the reflection profile of an acoustic wave. Based on these profiles it is then possible to determine the location and size of the UAO. The feasibility of the method has been tested in healthy children by [Leboulanger et al. \(2011\)](#) and used, e.g., by [Leboulanger et al. \(2012\)](#) to detect cystic fibrosis in children. Current shortcomings of the method, both of which are under investigation, are the required cooperation of the patient and the inability to acquire reliable results from nasal breathing. The latter might prove to be a problem when performing the analysis in neonates, who are obligate nasal breathers.

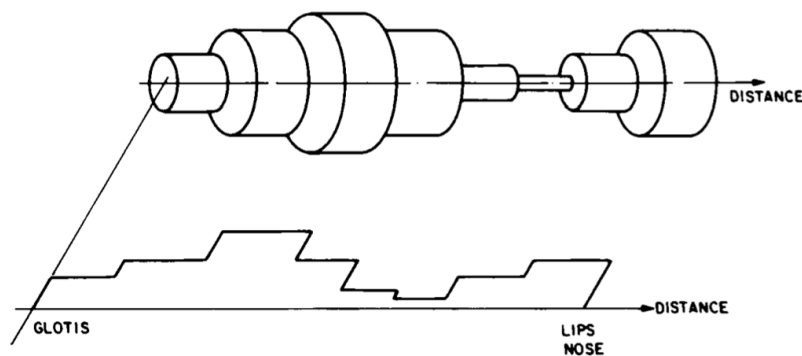
**Spirometry** results have been used frequently as a complementary technique to diagnose UAOs [Miller et al. \(2005\)](#). In view of this, [Modrykamien et al. \(2009\)](#) analyzed the reliability of both quantitative and visual criteria in the assessment of UAOs from flow-volume loops. Visual criteria included the presence of a plateau, biphasic shape, and oscillations in the inspiratory or expiratory curve. They showed that the individual criteria should not be relied upon as their predictive value ranges between 5.5 % and 47.2 %. Moreover, they include a large number of false positive tests. An aggregate criterion which combines all quantitative measures performs better with a predictive value of 69.4 %, but is still considered insufficient as a diagnostic tool for UAOs.



Yet another detection technique proposed by [Verbanck et al. \(2010\)](#) is based on the findings of [Brouns et al. \(2007\)](#), who concluded that resistance is dependent on the flow rate in patients with tracheal stenosis. [Verbanck et al. \(2010\)](#) validated these findings in practice by comparing the results of a **forced oscillation test** at different flow rates on 10 healthy patients and 10 patients with tracheal stenosis. Since this measurement method is capable of determining airway resistance, they were able to confirm the results as previously obtained by [Brouns et al. \(2007\)](#): patients suffering from tracheal stenosis have a higher airway resistance, which increases further with increasing flow rate above a critical level of stenosis.

Several researchers also investigated techniques that determine the size and/or location of an UAO from **acoustic measurements**, provided that the patient presents with stridor. [Zwartenkot et al. \(2010\)](#) examined the ability of otorhinolaryngology residents, academic specialists and non-academic consultants to localize the UAO based on recordings of the patient's stridor. This research derived from the fact that the phase (inspiratory, expiratory or biphasic) and type (voiced or fricative) of the stridor is linked to the location and etiology of the UAO [Claes et al. \(2005\)](#); [Hirschberg \(1980\)](#). Nevertheless, the average score was 29.6 % and increased only slightly when the participants were allowed access to the patient's medical history.

[Leiberman et al. \(1986\)](#) tried to localize the UAO by examining the Power Spectral Density (PSD) of the acoustic signal and estimating the cross-sectional area based on a simple model of the respiratory tract, i.e., a rigid cylindrical tube divided in  $n$  sections with varying diameter, see Figure (2.17). From the PSD curves they concluded that each UAO exhibits a specific type of stridor, while the area curves provided an estimation of the size and location of the UAO.

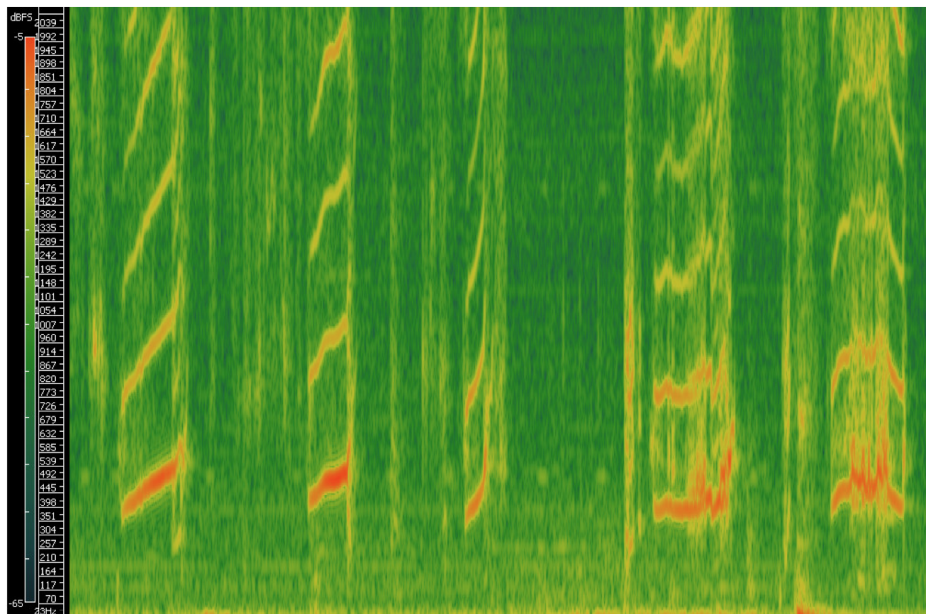


**Figure 2.17:** Lossless tube model of the upper airway [Leiberman et al. \(1986\)](#).

Another potential means to identify the underlying cause of stridor based only on acoustic measurements is to construct a **spectrogram**. Such spectrogram conveys information on the temporal evolution of the frequency content of a signal by plotting time versus frequency with the overlaying colors indicating the respective intensity levels. [Hirschberg \(1980\)](#) was the first to apply this technique during the course of an extensive study that involved 180 infants suffering from 40 different diseases or anomalies. The spectrograms allowed him to make a top-level differentiation between four different stridor types with the following characteristics:

- *Pharyngeal*: always noise-like, interrupted frequently, may occur both during in- and expiration;
- *Laryngeal*: mostly phonation-like;
- *Subglottic/Tracheal*: either stridor with a hollow timbre or a continuous breathing noise that is mainly inspiratoric;
- *Bronchial*: noise-like, appearing in the expiration phase, often spastic, with an intensive noise-zone at about 2,000 Hz.'

More recently [Zwartenkot \(2010\)](#) applied the same technique, in combination with Fourier analysis, to 12 infants with varying diseases. An example of a spectrogram from this study is shown in Figure (2.18). Although he was unable to unambiguously correlate the spectrograms with a particular UAO, the results clearly emphasize the potential of the method and the urgent need for further research on this topic.



**Figure 2.18:** Spectrogram of multiple inspiratory breath sounds of a 15-month-old boy with subglottic stenosis. Picture taken from [Zwartenkot \(2010\)](#).

A detailed study of the acoustical characteristics of stridor was also performed by [Slawinski and Jamieson \(1990\)](#), the conclusions of which are repeated here because of their valuable insights:

1. *The location of the constriction*: constrictions placed close to the nostrils emphasize higher frequencies and maintain similar values of murmur duration and intensity in both respiration cycles. Constrictions close to bifurcation increase the amplitude of lower frequencies and prolong the expiration cycle.

2. *The mass and elasticity of the tissue surrounding the constriction:* large mass and low elasticity tend to result in a fricative source, reflected in the murmur as a noise with formants corresponding to natural frequencies of the respiratory tract. Smaller mass and higher elasticity tend to result in a voiced source, which appears in the murmur as a tone.
3. *The shape of the constriction:* long constrictions tend to generate fricative sources, while short constrictions tend to generate voiced sources (if the pressure drop is sufficiently large).
4. *The cross-sectional area of the constriction* (for fricative sources): lower frequencies dominate the signal spectrum when the airway is relatively large, while higher frequencies emerge as the airway narrows.
5. *The tissue tension* (for voiced sources): high tension gives a high-frequency tonal quality to the murmur, while lower tension shifts the fundamental frequency (pitch) of the murmur to lower values.
6. *The mobility of the constriction:* with stable constrictions, resistance to airflow is equivalent in both cycles of respiration and stridor is produced in both cycles. Unstable constrictions produce changes in the spectrum from one cycle to the next and within each cycle.
7. *The ratio of the duration of the constriction opening to the period of tissue vibration* (for voiced sources): a small value of ratio (much lower than 1) is reflected in the spectrum of a murmur by many harmonics of fundamental frequency, while an appearance of only a few harmonics indicates that a constriction lumen is open much longer.'



---

## Chapter 3

---

# Upper Respiratory System Models

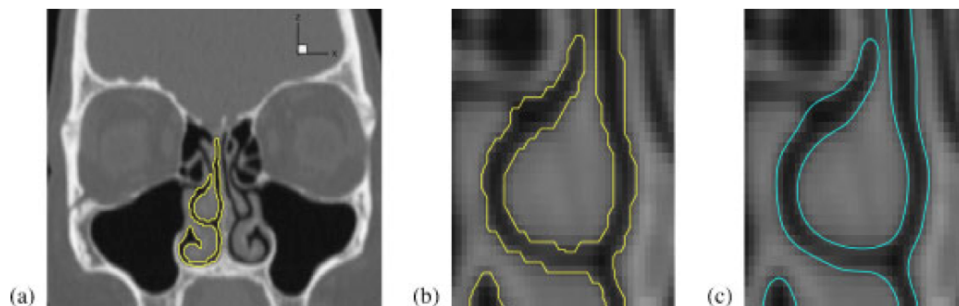
This chapter explains how the upper airway, with its intricate anatomical details as described in Chapter 2, can be converted into a suitable computational model. First of all, it should be realized that the anatomical accurateness of the model is determined by the type of research and its inherent restrictions, e.g., patient-specific versus general simulations, determination of general flow patterns versus local aerosol deposition, and experimental versus numerical investigations.

There exist several methods to acquire a working model of the upper respiratory tract, though [Doorly et al. \(2008\)](#) makes an upper-level distinction between *ex vivo* and *in vivo* models. The former are acquired from cadavers and either used directly or replicated from casting or plastination techniques. It is fairly easy to produce these models but they are generally inaccurate due to post-mortem shrinkage. *In vivo* models, on the other hand, are based on Computed Tomography (CT) or Magnetic Resonance Imaging (MRI) data which is then processed into computational models or Computer-Aided Design (CAD) models that can be used to create a physical model by, e.g., rapid prototyping [Hopkins et al. \(2000\)](#). These models are generally more representative of the airway anatomy compared to *ex vivo* models, though there are also disadvantages. Most importantly, a CT-scan subjects patients to potentially harmful ionizing radiation. In terms of effective organ dose this radiation becomes a larger issue when working with children or neonates [Brenner and Hall \(2007\)](#). An advantage of CT is the limited examination time compared to MRI, generally in the order of seconds. This reduces the risk of decreased image quality due to patient movement and avoids the necessity of sedation in children [De Backer et al. \(2008b\)](#).

Section 3.1 describes how the medical images obtained with either CT or MRI can be processed into computational models. Section 3.2 then gives an overview of the upper airway models currently available in literature.

### 3.1 From Medical Imaging Data to Computational Model

CT-images are built from a limited number of pixels which are assigned a particular grayscale, expressed in Hounsfield units (HU), according to their attenuation coefficient. As a result air appears black ( $HU = -1000$ ), tissue gray ( $HU = 40 - 80$ ) and bone white ( $HU = 400 - 1000$ ) on the CT-images [Seeram \(2009\)](#). This section summarizes the series of steps that transform a limited number of medical images into a workable 3D computational model, a procedure which is outlined in detail by [Gambaruto et al. \(2009\)](#).



**Figure 3.1:** (a) CT image projected in the coronal plane, corresponding to slice middle cavity, with user-defined segmentation. Detail of the middle meatus section with (b) step-like segmentation as selected by the user and (c) reduced model [Gambaruto et al. \(2009\)](#).

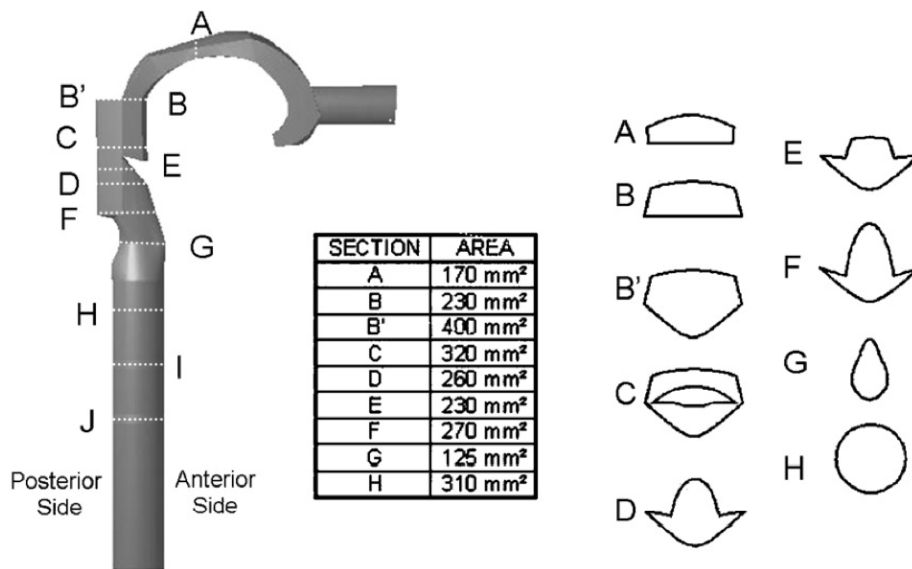
The first step is to extract the airway boundary from the surrounding bone and tissue following a method that is commonly referred to as segmentation. Here, a certain threshold value of the HU is assigned below which all pixels are removed. This segmentation is then followed by a manual revision, preferably carried out by an expert, during which irregularities are eliminated and unwanted airways removed (e.g., sinuses). Fortunately, [Doorly et al. \(2008\)](#) showed that the small geometric differences that inevitably arise from subjective assessment during this step have a negligible impact on the eventual flow patterns. The final result of these two segmentation steps is a rough, pixellated, airway boundary that needs smoothing, see Figure (3.1b). [Gambaruto et al. \(2009\)](#) used a bi-Laplacian smoothing technique, the result of which can be seen in Figure (3.1c). The final step is to connect the 2D images with a radial basis function interpolation to arrive at the 3D model, details of which can be found in [Peiró et al. \(2007\)](#). It should be noted that the images should be in close proximity for the reconstruction to be successful. Values for the required image spacing as stipulated in literature vary between 1 and 2 mm [Wang et al. \(2012\)](#); [Chung and Kim \(2008\)](#); [Bailie et al. \(2006\)](#).

### 3.2 Model Types

Prior to the analysis of a Realistic Upper Airway Model (RUAM), the numerical schemes should be validated on simplified models to gain insight in the accuracy of the methods and to filter potential coding errors. Not only will this facilitate the interpretation of results in

more complicated geometries, it will also avoid unnecessary and time-consuming debugging in later stages of the project.

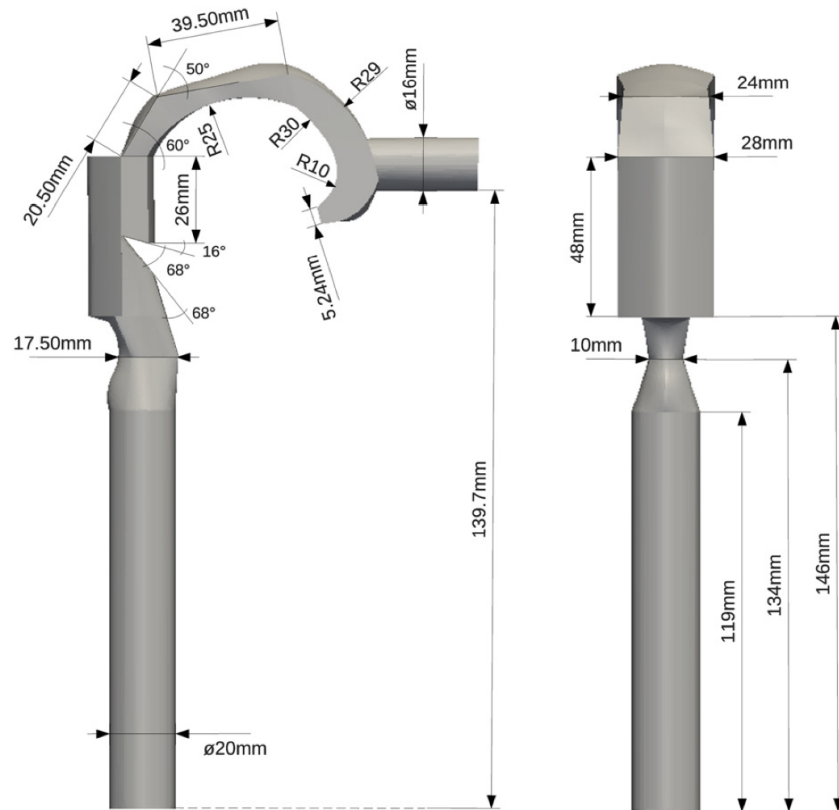
Lynch (2012) validated the numerical methodologies applied in his thesis on a reed instrument and a diaphragm, respectively. van der Velden (2012) also used a diaphragm to validate the acoustic analogies used in his thesis, primarily because this geometry is closely related to the internal flow through the glottis. Numerical and experimental validation data for both geometries is readily available in literature Miyamoto et al. (2010); Piellard and Bailly (2010); Gloerfelt and Lafon (2008); Piellard and Bailly (2008); Bailly et al. (1996).



**Figure 3.2:** Relevant cross-sectional dimensions of the extrathoracic oral airway model Jayaraju et al. (2008).

In the next step towards the simulation of a RUAM, Lynch (2012) and van der Velden (2012) simulated the airflow through a Simplified Upper Airway Model (SUAM) as seen in Figures (3.2) and (3.3). This simplified geometry closely resembles the flow through a real airway tract and has been used in the past for both numerical and experimental purposes, which implies that a large amount of validation data is available for this model. The model was created by Brouns et al. (2006), who used it to study flow patterns using Particle Image Velocimetry. In a follow-up study, Brouns et al. (2007) assessed the effects of tracheal stenosis using Computational Fluid Dynamics with a  $k - \epsilon$  turbulence model, which showed that the model can be easily adapted to reflect certain airway obstructions. Next, Jayaraju et al. (2008) applied Large Eddy Simulation and Detached Eddy Simulation analysis to the model. Later still, the model was used successively by Verbanck et al. (2011), Agnirothi et al. (2012) and Krause et al. (2013) to determine particle deposition in the upper airways.

As a final step, Lynch (2012) and van der Velden (2012) simulated the flow through two RUAMs as shown in Figure (3.4). The left model was obtained directly from a CT-scan of a stridorous patient who suffered from subglottic stenosis. Conversion of the scan data to a CAD model was conducted by Wim Vos at FLUIDDA (www.fluidda.com), a Belgian



**Figure 3.3:** Relevant geometrical dimensions of the extrathoracic oral airway model seen in a side view (left) and back view (right) Krause et al. (2013).

company specialized in functional respiratory imaging. The right model shows the same patient without subglottic stenosis and was created by Lynch (2012), in consultation with surgeon L.J.H. Hoeve from the Erasmus Medical Center in Rotterdam.

Due to the increasing interest in particle deposition and virtual surgery simulations, an increasing number of both realistic and simplified upper airway models are available in literature. An incomplete overview of the latest models is given in Table (3.1). Besides, also lower respiratory system models exist and an excellent review of those is given in Hofmann (2011). Generally, a distinction is made between symmetric (typical) and asymmetric (multi-path) bifurcation models, where the latter more closely resemble the actual geometry. Due to the limited resolution of CT- and MRI-scans, most models are based on large sets of post-mortem data and patient-specific simulations are as yet impossible. Advancements are ongoing, however, and Rosell and Cabras (2013) recently proposed a new method to extract the tracheobronchial tree from CT-images.





**Figure 3.4:** Realistic CT-scan derived upper airway model of a patient suffering from subglottic stenosis (left) and the adapted version to represent a healthy person (right) [Lynch \(2012\)](#).

**Table 3.1:** Overview of upper airway models available in literature. N = numerical, E = experimental, OC = oral cavity, NC = nasal cavity.

Article	Type	Origin	Study	OC	NC	Notes
Chen and Gutmark (2014)	SUAM	N/A	N	x		
Shinneeb and Pollard (2012)/Stapleton et al. (2000)	SUAM	CT/MRI	E/N	x		PIV measurements with special attention to turbulence structures around the epiglottis
Zhang and Kleinstreuer (2011)Heenan et al. (2003)/Johnstone et al. (2004)	SUAM	CT/MRI	N	x	x	Effect of different breathing routes, model also includes three generations of the tracheobronchial tree
Ball et al. (2008)/Stapleton et al. (2000)	SUAM	CT/MRI	N/N	x		Lattice Boltzmann Method
Mylavarapu et al. (2013)	RUAM	CT	N			Virtual surgery
Inthavong et al. (2013)	RUAM	CT	N		x	Deposition of glass and carbon composite fibers
Nicolaou and Zaki (2013)/Grgic et al. (2004)	RUAM	MRI	N/E	x		Deposition studies with emphasis on intra- and inter-subject variations
Huang et al. (2013)/Cheng et al. (1999)	RUAM	Cadaver cast	N/E	x		Effect of realistic moving boundary outlet on flow patterns
Ghalati et al. (2012)	RUAM	CT	N		x	Deposition study
Huang et al. (2011)/Cheng et al. (1999)/Zhang et al. (2002a)	RUAM	Cadaver cast	N/E/N	x		Effect of including tracheobronchial tree in model on tracheal flow
Powell et al. (2011)	RUAM	CT	N			Airflow studies in patients with sleep-disordered breathing
Sandeau et al. (2010)	RUAM	CT	N	x		Effect of using helium-oxygen mixtures in inhalation therapies
Ma and Lutchen (2009)	RUAM	CT/MRI	N	x		Deposition study
Mylavarapu et al. (2009)	RUAM	MRI	N		x	Comparison of turbulence models
Wang et al. (2009)	RUAM	CT	N		x	Model includes three generations of tracheobronchial tree, differences between inspiratory and expiratory flow
Mihaescu et al. (2008)	RUAM	MRI	N			Investigation of obstructive sleep apnea
Nithiarasu et al. (2008)	RUAM	CT	N			Detailed pressure and wall shear stress data
Lin et al. (2007)	RUAM	CT	N	x		Model includes six generations of tracheobronchial tree, detailed analysis of laryngeal jet

---

## Chapter 4

---

# Fluid Model: Lattice Boltzmann Method

There have already been numerous attempts towards the investigation and comprehension of flow patterns in the upper airway system. Most of the numerical investigations were carried out with conventional Computational Fluid Dynamics (CFD) methods, in particular using the finite-volume approach. Recently, however, some researchers focused their attention on the Lattice Boltzmann Method (LBM) as an alternative means to simulate the airflow through the respiratory tract. An (incomplete) overview of the efforts is given in Table (4.1).

**Table 4.1:** Overview of the LBM as used in the simulation of upper airway flow. Note that [Ball et al. \(2008\)](#) are the only group of researchers in the list who applied PowerFLOW (version 3.4) for their simulations.

Article	Method	$Re$	$Re$ (component)	Turbulence	Simulated airway
<a href="#">Wang and Elghobashi (2014)</a>	LBGK	-	-	DNS	Nasal cavity - trachea
<a href="#">Lintermann et al. (2013b)</a>	TLBGK	1,900	Nasopharynx	-	Nasal cavity
<a href="#">Lintermann et al. (2013a)</a>	LBGK	710	Nostrils	-	Nasal cavity
<a href="#">Miki et al. (2012)</a>	LBGK	1,500	Trachea	-	Pulmonary airways
<a href="#">Lintermann et al. (2012)</a>	LBGK	766	Nostrils	DNS	Nasal cavity
<a href="#">Eitel et al. (2010)</a>	LBGK	600	Nasopharynx	-	Nasal cavity
<a href="#">Hörschler et al. (2010)</a>	LBGK	2,500	Nasopharynx	DNS	Nasal cavity
<a href="#">Ball et al. (2008)</a>	LBGK	780	Trachea	DNS	Oral cavity - trachea
<a href="#">Freitas and Schröder (2008)</a>	LBGK	1,250	Trachea	-	Pulmonary airways
<a href="#">Finck et al. (2007)</a>	LBGK	1,000	Nasopharynx	-	Nasal cavity

The LBM is widely praised for its simplicity of implementation, inherent parallelism and easy handling of complex boundaries. Mainly due to these features [Finck et al. \(2007\)](#) decided to apply the method in the simulation of nasal airflow. Comparison of the results with those obtained using a finite-volume method showed good agreement at a much lower computational cost. The promising results were attributed to the following combined effects:

- *‘Fast grid generation even for complex geometries due to Cartesian-like grids (lattices).*
- *Easy implementation of boundary conditions on the molecular level, even for different types.*
- *Simple, granular algorithm, well suited for parallelization, enables high resolution at moderate computational effort.*
- *Local grid refinement and acceleration strategies are developed and available.*
- *Coupling with additional transport equations e.g. for temperature, humidity or aerosols is proved in other applications.’*

Finck et al. (2007) failed however to conduct a definitive validation of the method by comparing the results with experimental benchmark data. Besides, the quantitative advantage of the LBM in terms of computational speed remained unknown because the data sets were obtained from different computers. Shortly thereafter, Ball et al. (2008) simulated the airflow through a Simplified Upper Airway Model (SUAM) using the commercial solver PowerFLOW 3.4 and concluded that LBM results compare reasonably well with experimental data. More recently Chen and Gutmark (2014) showed that a second-order finite-volume scheme with a Large Eddy Simulation (LES) turbulence model generally performs better than the LBM, but they only considered the time-averaged flow field. Given that the most important consideration in the assessment of the acoustic characteristics of the flow field are the unsteady flow fluctuations, the results of Chen and Gutmark (2014) should not lead to an immediate disregard of the LBM.

Based on these promising yet indecisive preliminary results it is deemed appropriate to investigate the usefulness of the LBM in the aeroacoustic simulation of fluid flow through the upper airway. Since the commercial software package PowerFLOW will be used for all simulations, only those aspects of the LBM that are incorporated in the package will be discussed here. Section 4.1 describes the basic properties of this LBM, while Section 4.2 elaborates on those features of the PowerFLOW commercial solver that will prove to be of importance in future simulations.

## 4.1 Lattice Boltzmann Method

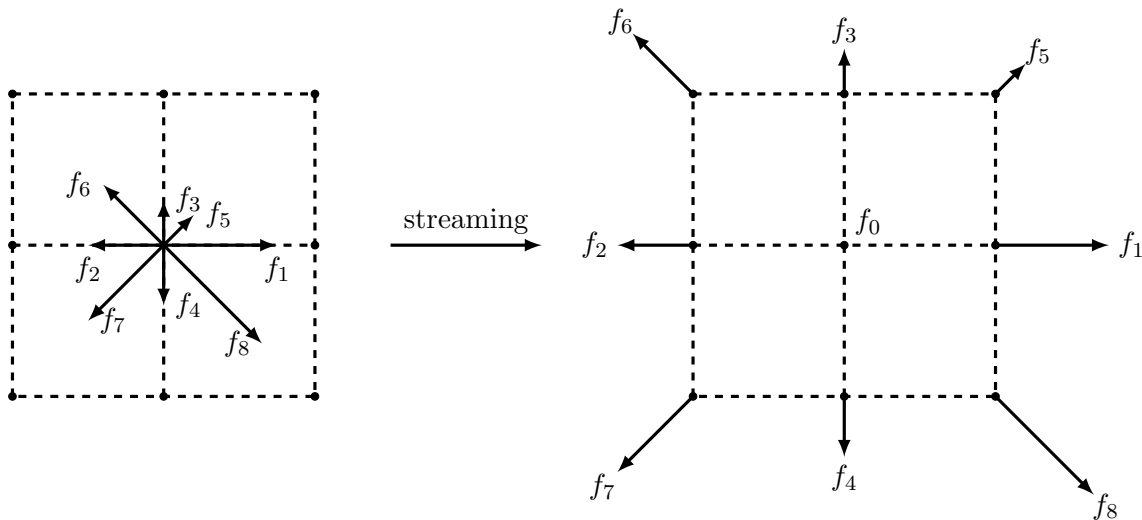
This section discusses the fundamentals of the LBM given that it will be applied in the simulation of the airflow through the upper respiratory system. Subsection 4.1.1 describes the general principles of the method and indicates the main difference with respect to conventional CFD methods. Subsequently, Subsection 4.1.2 introduces the LBM implementation type that is incorporated in PowerFLOW.

### 4.1.1 Basic Principles

The LBM is an alternative method to simulate fluid dynamics. It was proposed in 1988 as a brainchild of the Lattice Gas Cellular Automata, with the goal to do away with several shortcomings of this method [McNamara and Zanetti \(1988\)](#); [Higuera and Jiménez \(1989\)](#). This goal has been achieved to a certain extent, although the departure from the underlying microdynamics gave rise to different problems, especially nonlinear instabilities.

Instead of modeling the fluid flow at a macroscopic level like conventional CFD methods, the LBM determines the movement of collections of particles at the mesoscopic scale. In this framework the computational grid is divided into a finite number of cells with a predefined structure, which together comprise the so-called lattice. Particles, or rather collections of particles with a certain distribution function (the two will be used interchangeably), are allowed to move between lattice nodes but only along  $n$  specified directions (linkages). This process is called *streaming* or simply, advection. Whenever two particles are positioned at the same lattice node a *collision* process is activated. Hence, the evolution of the LBM in time occurs in two steps:

1. Streaming: advection of the particle distribution functions to surrounding lattice nodes - this step should be performed simultaneously on the entire lattice, see Figure (4.1).

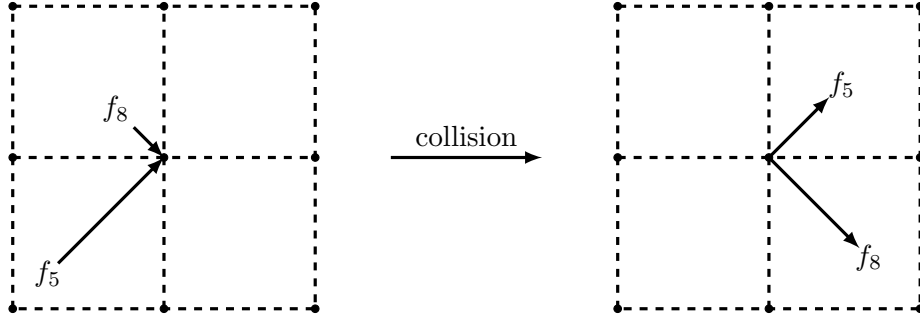


**Figure 4.1:** Illustration of the streaming process.

2. Collision: determination of the post-collision distribution functions - this step accounts for the majority of computational cost but can be parallelized, see Figure (4.2).

The process was captured mathematically by Ludwig Boltzmann in the renowned Boltzmann Equation (BE):

$$\left( \frac{\partial}{\partial t} + \mathbf{e} \cdot \nabla_{\mathbf{x}} + \mathbf{a} \cdot \nabla_{\mathbf{e}} \right) f(\mathbf{x}, \mathbf{e}, t) = C, \quad (4.1)$$



**Figure 4.2:** Illustration of the collision process of two distribution functions. Note that this is only one of many possible collision outcomes.

where  $f(\mathbf{x}, \mathbf{e}, t)$  is the particle distribution function (the probability to find a particle with a velocity  $\mathbf{e}$  at a location  $\mathbf{x}$  at time  $t$ ),  $\mathbf{e}$  the microscopic velocity,  $\mathbf{a}$  the microscopic acceleration due to the application of an external force and  $C$  the collision operator. The BE can be discretized as follows, assuming the absence of external forces [He and Luo \(1997\)](#):

$$f(\mathbf{x} + \mathbf{e}\delta t, \mathbf{e}, t + \delta t) - f(\mathbf{x}, \mathbf{e}, t) = C. \quad (4.2)$$

The collision operator  $C$  is assumed to contain all the parameters necessary to approximate the macroscopic behavior of a wide range of partial differential equations, including the Navier-Stokes Equations (NSE). This term is therefore nonlinear and LBMs currently available in literature differentiate themselves by adapting a different description of  $C$ . Given that all simulations will be performed in PowerFLOW, the only collision model that will be touched upon in the following subsection is the one that is implemented in this software package.

#### 4.1.2 Lattice Bhatnagar-Gross-Krook: PowerFLOW Collision Model

As mentioned previously, only one collision model will be addressed in detail here. Fortunately, it has been used extensively in previous simulations of respiratory airflow, see [Table \(4.1\)](#). Besides, it is well suited to deal with low Reynolds number ( $Re$ ) flows. A general overview of the LBM and its most common collision models can be found in the monographs by [Succi \(2001\)](#), [Aidun and Clausen \(2010\)](#) and [Mohamad \(2011\)](#).

The Lattice Bhatnagar-Gross-Krook (LBGK) method is the easiest to implement, albeit not the first to be proposed in 1992. It describes the collision operator in terms of a single-relaxation parameter  $\tau$ :

$$C \equiv -\frac{1}{\tau} (f(\mathbf{x}, \mathbf{e}, t) - f^{eq}(\mathbf{x}, \mathbf{e}, t)), \quad (4.3)$$

where  $f^{eq}(\mathbf{x}, \mathbf{e}, t)$  is the local equilibrium distribution function. Since  $\tau$  only manages the relaxation to a specified equilibrium state, the relation to the physical problem should be incorporated entirely in the definition of  $f^{eq}$ . Hence,  $f^{eq}$  is derived from the Boltzmann-Maxwellian distribution function under the requirements that the conservation laws for mass and momentum should be satisfied (which is achieved through the definition of the hydrodynamic moments of the distribution function), and that the symmetries of the NSE are

preserved. A rigorous derivation of  $f^{eq}$  is omitted here but can be found in [He and Luo \(1997\)](#). For the case of an athermal fluid it is defined as follows:

$$f_i^{eq} = \rho w_i \left\{ 1 + \frac{\mathbf{e}_i \cdot \mathbf{u}}{c_s^2} + \frac{(\mathbf{e}_i \cdot \mathbf{u})^2}{2c_s^4} - \frac{\mathbf{u}^2}{2c_s^2} \right\}, \quad (4.4)$$

where  $\rho$  is the macroscopic density,  $\mathbf{u}$  the macroscopic velocity,  $c_s$  the speed of sound of the system (in general dependent on the lattice), and  $w_i$  the weights corresponding to the lattice velocities  $\mathbf{e}_i$ . Since the macroscopic variables correspond to the hydrodynamic moments of the distribution functions they can be determined as such:

$$\rho = \sum_{i=0}^{n-1} f_i = \sum_{i=0}^{n-1} f_i^{eq} \quad \rho \mathbf{u} = \sum_{i=0}^{n-1} \mathbf{e}_i f_i = \sum_{i=0}^{n-1} \mathbf{e}_i f_i^{eq}. \quad (4.5)$$

The macroscopic pressure  $p$  can be determined from the equation of state of an ideal gas:

$$p = \rho c_s^2. \quad (4.6)$$

As mentioned before, the weights depend on the underlying lattice structure and are listed in Table (4.2) for the lattices most commonly used to simulate fluid flows in two and three dimensions: D2Q9, D3Q15, D3Q19 and D3Q27.<sup>1</sup> The definition of the velocities corresponding to the D2Q9 and D3Q15 lattice structures are depicted in Figures (4.3) and (4.4), respectively.

**Table 4.2:** The magnitude and the number of velocity directions for lattice models D2Q9, D3Q15, D3Q19 and D3Q27 and their corresponding weights  $w_i$  [Aidun and Clausen \(2010\)](#).

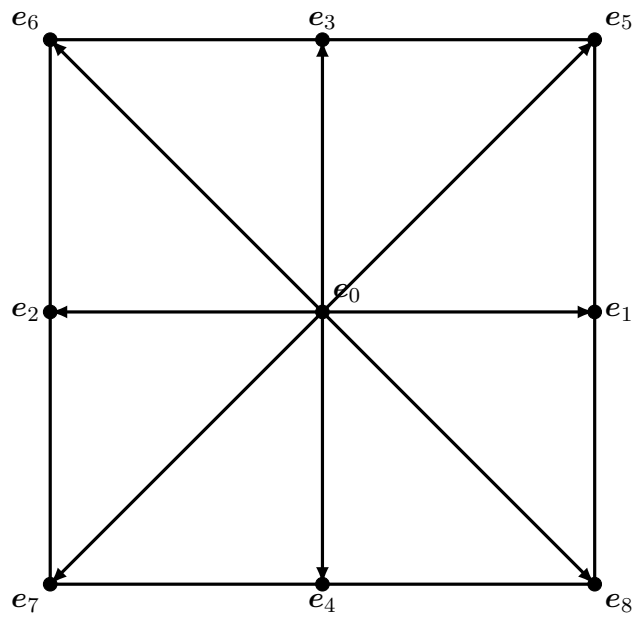
$w_i$	No. (2D)	$ \mathbf{e}_i $	D2Q9	D3Q15	D3Q19	D3Q27
$w_0$	1	0	4/9	2/9	1/3	8/27
$w_1$	6 (4)	1	1/9	1/9	1/18	2/27
$w_{\sqrt{2}}$	12 (4)	$\sqrt{2}$	1/36	0	1/36	1/54
$w_{\sqrt{3}}$	8 (0)	$\sqrt{3}$	0	1/72	0	1/216

Since all the physics are encapsulated within  $f^{eq}$ , both the advection and collision step can be performed in velocity space. This is not self-evident, given that there exist other collision models that perform the collision process in moment space (e.g., the Multiple-Relaxation-Time LBM) [Lallemand and Luo \(2000\)](#).

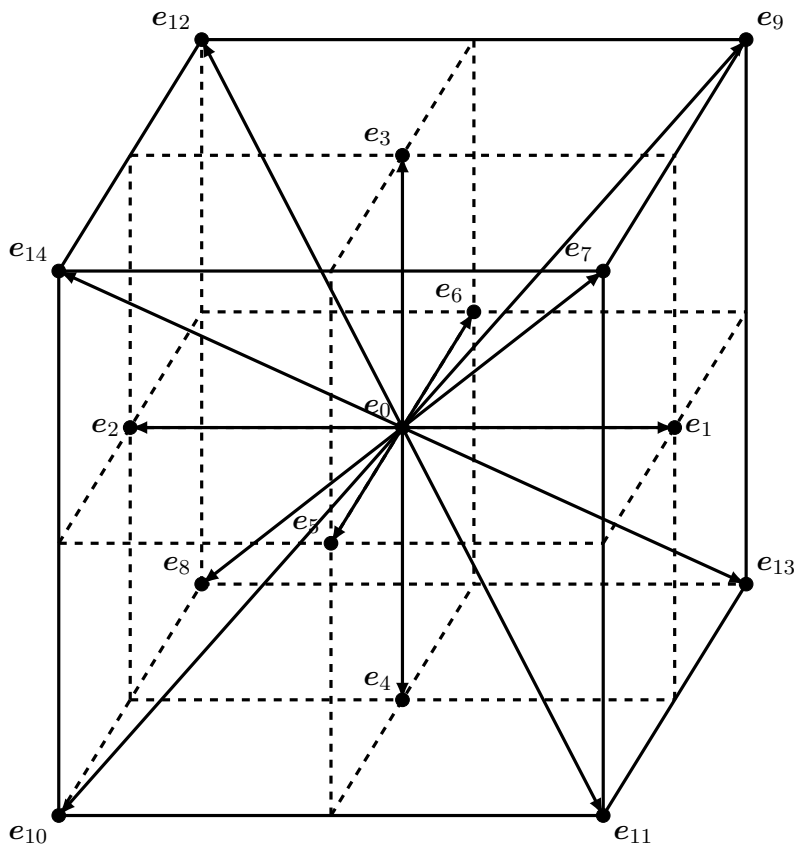
The only way to specify the kinematic viscosity  $\nu$  of the gas is through its relation with the relaxation parameter  $\tau$  [Mohamad \(2011\)](#):

$$\nu = \frac{\Delta x^2}{3\Delta t} \left( \tau - \frac{1}{2} \right). \quad (4.7)$$

<sup>1</sup>The notation DmQn was proposed by [Qian et al. \(1992\)](#) and indicates a lattice with  $n$  velocity directions in  $m$  dimensions. Not all lattice structures contain sufficient symmetries to approximate the NSE. [Chikatamarla and Karlin \(2009\)](#) gave a comprehensive overview of the allowable lattice structures and how they can be derived.



**Figure 4.3:** Definition of the microscopic velocities for the D2Q9 lattice.



**Figure 4.4:** Definition of the microscopic velocities for the D3Q15 lattice.



Note that  $\tau$  should be chosen larger than  $1/2$  for reasons of numerical stability, which limits the minimum viscosity that can be achieved using the LBGK approach [Chen et al. \(1992\)](#). Besides, the use of a single-relaxation parameter causes all transport parameters to decay at the same rate. This might compromise the numerical stability due to short-wave oscillations [Succi \(2001\)](#). An additional consequence is that thermal fluids are restricted to a fixed Prandtl number,  $Pr = 1$ . However, since the temperature properties of the flow are assumed constant throughout the simulation, the slight discrepancy in Prandtl number ( $Pr_{air} \approx 0.7 - 0.8$  over a large range of temperatures) should not be considered a drawback.

## 4.2 PowerFLOW Software

From a top-level perspective, PowerFLOW makes use of an adapted version of the LBGK collision model with a single-relaxation time scale. Assuming that some further insights into PowerFLOW's inner workings might prove useful in the analysis of future simulation data, this section includes a summary of all the available information regarding the turbulence and wall models incorporated in the program. Although the information is scarce (PowerFLOW remains a commercial program), it is expected to be sufficiently detailed for the purpose of this thesis.

### 4.2.1 Turbulence Model

As mentioned before, there is no in-depth theoretical description of the turbulence model available in the PowerFLOW manual. There are however several authors who briefly though unanimously discussed the issue [Habibi et al. \(2013\)](#); [Pérot et al. \(2010\)](#); [Noelting et al. \(2010\)](#); [Keating et al. \(2009\)](#); [Noelting et al. \(2008\)](#); [Li et al. \(2008\)](#); [Crouse et al. \(2006\)](#); [Belanger et al. \(2005\)](#).

Essentially, the single-relaxation time scale  $\tau$  is replaced by an effective turbulent relaxation time scale  $\tau_{turb}$ . This  $\tau_{turb}$  can be derived by applying a systematic renormalization group (RNG) procedure and is given by:

$$\tau_{turb} = \tau + C_\mu \frac{k^2/\epsilon}{T(1 + \tilde{\eta}^2)^{1/2}}, \quad (4.8)$$

where  $C_\mu = 0.085$ ,  $T$  the absolute temperature,  $k$  the turbulent kinetic energy,  $\epsilon$  the turbulent dissipation rate and  $\tilde{\eta}$  a combination of a local strain parameter  $\eta = k|S|/\epsilon$ , a local vorticity parameter  $\eta_w = k|\Omega|/\epsilon$  and local helicity parameters. The exact form of these parameters has not been publicly disclosed.  $k$  and  $\epsilon$  are determined according to the RNG  $k - \epsilon$  transport equations [Yakhot and Orszag \(1986\)](#):

$$\rho \frac{Dk}{Dt} = \rho \frac{\partial k}{\partial t} + \rho \mathbf{u} \cdot \nabla k = \frac{\partial}{\partial x_j} \left[ \left( \frac{\rho \nu_0}{\sigma_{ko}} + \frac{\rho \nu_T}{\sigma_{kT}} \right) \frac{\partial k}{\partial x_j} \right] + \tau_{ij} S_{ij} - \rho \epsilon, \quad (4.9)$$

$$\rho \frac{D\epsilon}{Dt} = \frac{\partial}{\partial x_j} \left[ \left( \frac{\rho \nu_0}{\sigma_{\epsilon o}} + \frac{\rho \nu_T}{\sigma_{\epsilon T}} \right) \frac{\partial \epsilon}{\partial x_j} \right] + C_{\epsilon 1} \frac{\epsilon}{k} \tau_{ij} S_{ij} - \left[ C_{\epsilon 2} + C_\mu \frac{\eta^3(1 - \eta/\eta_0)}{1 + \beta \eta^3} \right] \rho \frac{\epsilon^2}{k}, \quad (4.10)$$

where  $C_\mu = 0.085$ ,  $C_{\epsilon 1} = 1.42$ ,  $C_{\epsilon 2} = 1.68$ ,  $\sigma_{k_o} = \sigma_{k_T} = \sigma_{\epsilon_o} = \sigma_{\epsilon_T} = 0.719$ ,  $\eta_0 = 4.38$  and  $\beta = 0.012$ . The solution approach to these equations is detailed in [Teixeira \(1998\)](#). Note that the parameter  $\nu_T = C_\mu k^2 / \epsilon$  is defined here as the eddy viscosity, which immediately clarifies the relevance of the turbulent relaxation time scale, Equation 4.8. Indeed, the definition of  $\tau_{turb}$  includes the eddy viscosity, hence stipulating the link between the macroscopic Navier-Stokes equation and the microscopic kinetic theory from which the BE has been derived.

Interestingly, it has been shown that this two-equation LBM turbulence model is able to capture more physical aspects of the flow than its Navier-Stokes counterpart. According to [Li et al. \(2008\)](#), ‘*VLES carries flow history and upstream information and contains high order terms to account for the nonlinearity of the Reynolds stress. This is superior when compared with its Navier-Stokes counterpart, which uses the conventional linear eddy viscosity based Reynolds stress closure models and produces excessive dissipation when doing unsteady simulations*’.

It should finally be noted that the turbulence model also includes a swirl-based correction which enables the direct resolution of all turbulent scales wherever this is allowed by the grid size [de Jong et al. \(2013\)](#); [Noelting et al. \(2008\)](#).

## 4.2.2 Wall Model

PowerFLOW includes a wall-shear stress model that is based on an extended law-of-the-wall formulation. The extension introduces a means to account for the effects of local adverse pressure gradients. The model can be formulated as follows [Crouse et al. \(2006\)](#); [Belanger et al. \(2005\)](#); [Teixeira \(1998\)](#):

$$u^+ = f \left( \frac{y^+}{A} \right) = \frac{1}{\kappa} \ln \left( \frac{y^+}{A} \right) + B, \quad (4.11)$$

where  $u^+ = \bar{u} / u_\tau$  is a normalized velocity<sup>2</sup>,  $y^+ = y u_\tau / \nu$  the normalized normal distance from the wall,  $\kappa \approx 0.41$  the von Kármán constant and  $B \approx 5.2$  a constant [Pope \(2000\)](#).  $A$  represents the pressure gradient effects and is given by:

$$A = 1 + f \left( \frac{dp}{dx} \right). \quad (4.12)$$

This equation is iteratively solved to provide an estimated wall-shear stress for wall boundary conditions in the LBM calculation. A slip algorithm (a generalization of bounce-back and specular reflection process) is then used for the boundary process [Chen \(1998\)](#); [Chen et al. \(1998\)](#). The estimated friction forces from the wall shear stress model are supplied to alter the momentum of scattered near wall particles.

---

<sup>2</sup> $\bar{u}$  represents the mean velocity and  $u_\tau = \sqrt{\tau_w / \rho}$  the so-called friction velocity ( $\tau_w$  being the wall shear stress) [Pope \(2000\)](#).

According to [Crouse et al. \(2006\)](#), ‘The following empirical boundary condition for turbulent kinetic energy and dissipation is imposed at the near wall lattice positions’:

$$k^+ = \frac{k}{u_\tau^2} = \frac{1}{\sqrt{C_\mu}} - e^{-0.1y^+} \left( \frac{1}{\sqrt{C_\mu}} + 0.29y^+ \right), \quad (4.13)$$

$$\epsilon^+ = \frac{\epsilon \nu_0}{u_\tau^4} = 0.04y^+ - 0.0033y^{+2} + \frac{1.04}{10^4}y^{+3} - \frac{1.14}{10^6}y^{+4}. \quad (4.14)$$

### 4.2.3 PowerFLOW Actions

The majority of the aerodynamic results included in Part II and III of this thesis are presented in the format of either flow field images or fluid profiles. Nearly all this data is extracted directly from PowerFLOW without any post-processing actions, and most of the actions required to produce this data are neatly and unambiguously described in the software manuals. There are however two particular items that require some further explanation.

#### Extraction of Fluid Profiles

Essentially, fluid profiles can be extracted from the simulation fluid files in two ways. The first option, and undoubtedly the most convenient one, is to request the data straight from the command line with the following command:

```
exaritool fluid-profile.ri fluid_file variable -units units-rel -x x -y y -z
z > output_file
```

which requires the specification of the following parameters:

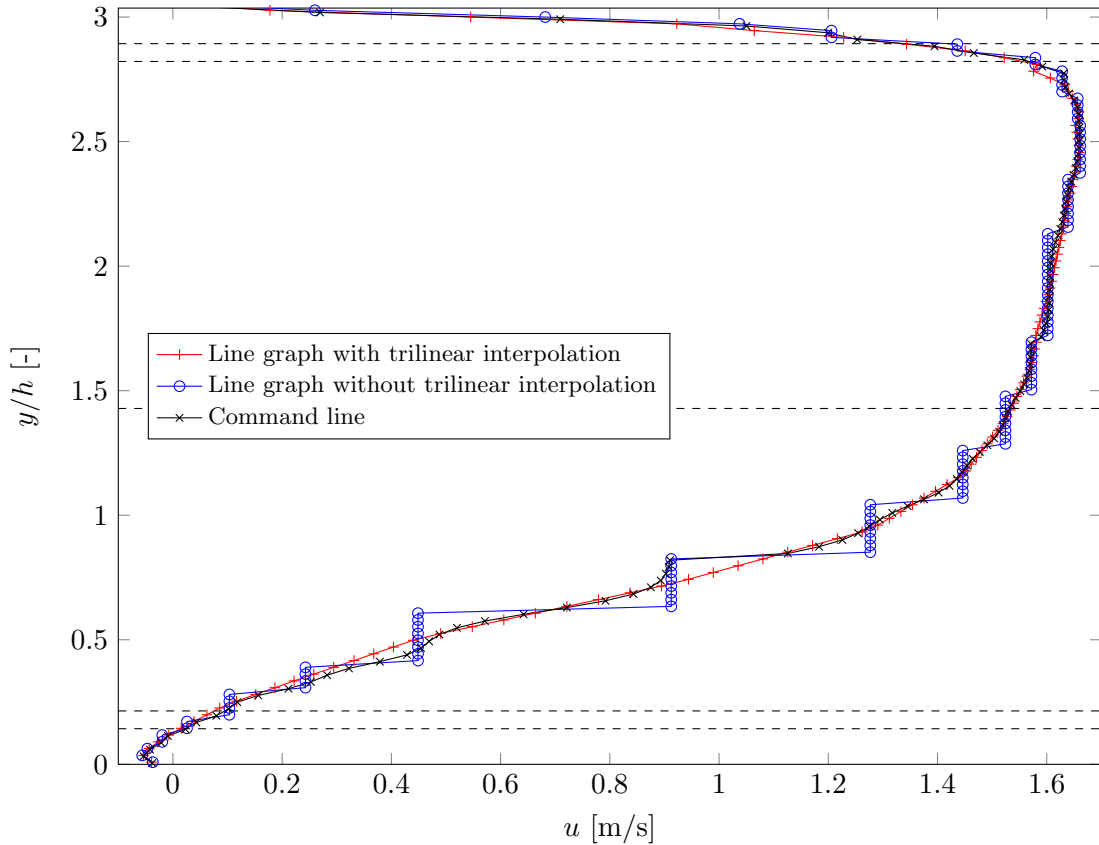
- *fluid\_file*: name of the file that contains the required data;
- *variable*: name of the desired variable;
- *units-rel*: specification of the coordinate units, default is `dimless` but `mks` (SI units) is often more convenient;
- *x y z*: coordinates of desired data point/line, only two variables need to be specified;
- *output\_file*: name of the desired output file with an extension of own choosing.

A second possibility is to obtain the data through the visual interface of PowerVIZ by going through the following list of actions:

1. Select `Fluid > Fluid Point`; the location of the fluid point coincides with the line graph.

2. Tick the **Trilinear Interpolation** box, which causes PowerFLOW to interpolate the data at each sample point from eight surrounding measurement cells.
3. Click **Activate Line** to create a line graph.
4. The **Sample Distance** along the line is set to twice the smallest voxel size but can be changed at will.
5. Downsample the data set based on the local voxel size.

It is also possible to obtain the raw results by unticking the **Trilinear Interpolation** box mentioned in step 2. Figure (4.5) compares the fluid profiles that result from these three possible extraction methods. Since the line graph with trilinear interpolation yields the smoothest and most accurate data, it was adopted as the chief method to extract fluid profiles from the PowerFLOW output files.



**Figure 4.5:** Comparison of three different means to extract fluid profiles from PowerFLOW: command line vs. PowerVIZ Line Graph with(out) tri-linear interpolation.

### Extraction of Turbulent Kinetic Energy Profiles

In PowerVIZ, the variable **Turb Kinetic Energy** only includes that part of the energy that is modeled by the turbulence model. In order to calculate the total turbulent kinetic energy

in the flow field, PowerACOUSTICS should be used. Three parameters are available that are all related to the turbulent kinetic energy:

- **Turb Kinetic Energy:** coincides with the PowerVIZ variable of the same name;
- **Fluctuation Kinetic Energy:** the turbulent kinetic energy that is actually resolved by the grid itself, and calculated from the Reynolds stresses;
- **Total Turb Kinetic Energy:** the sum of the aforementioned kinetic energy components.

Whenever these are calculated, the **Calculation Type** should be set to **Statistics > Mean**. In order to obtain a reasonable estimation of the values, instantaneous measurement frames should be used in the computation.



---

## Chapter 5

---

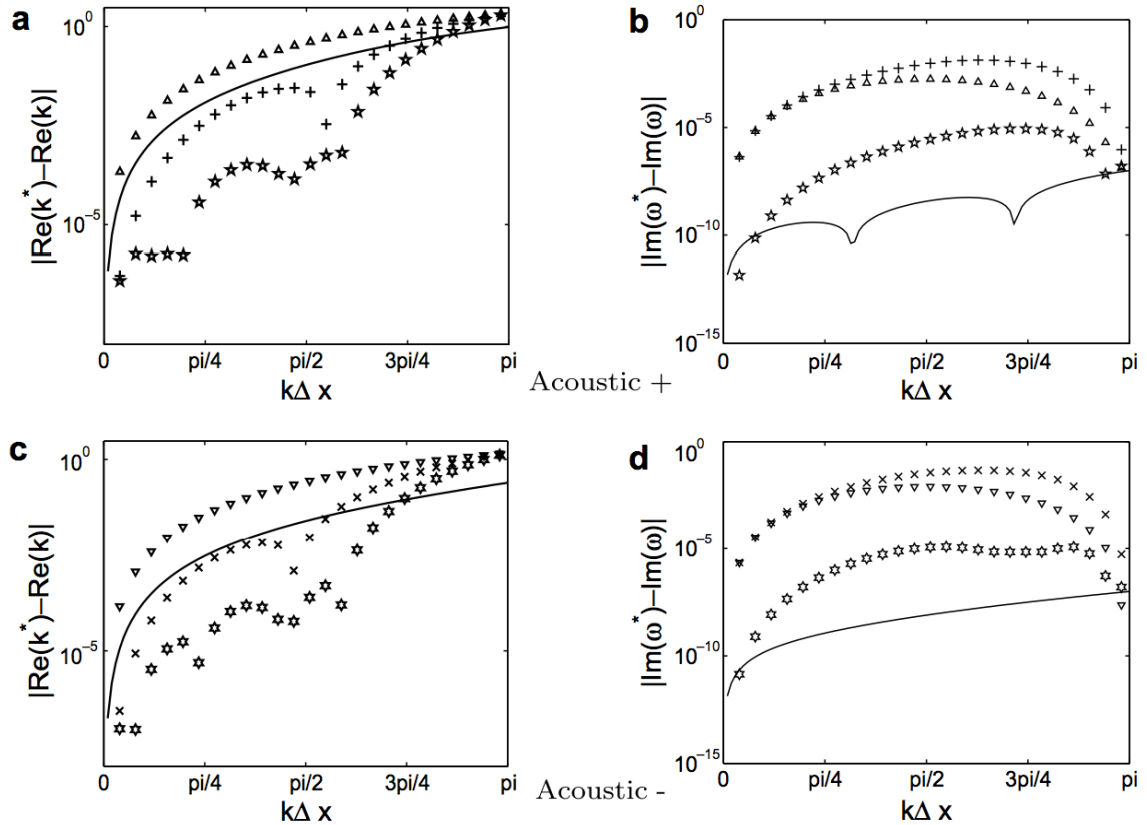
# Acoustics Modeling

There exist two solution approaches to aeroacoustic problems: hybrid and direct methods [Wagner et al. \(2007\)](#). In the direct approach the computational grid encapsulates both the source and the receiver. It requires the use of very accurate numerical schemes with low dispersion (change in wave propagation speed) and dissipation (change in wave amplitude) capabilities as to accurately propagate the low-energy acoustic perturbations. Since the disparity in energy content between the acoustic field and the flow field is of  $O(M^4)$ , the use of such numerical schemes becomes especially important in low Mach number ( $M$ ) flows [Gloerfelt and Lafon \(2008\)](#). In the hybrid approach the source field is first calculated with an appropriate numerical scheme, after which the information is coupled to an acoustic solver which propagates the acoustic field towards the far-field. In this way the computational requirements are lowered because the grids and schemes can be tailored to suit both problems individually. Nonetheless, if there is sufficient computational power available, it might be preferable to use the direct approach because this would avoid the storage of the large amount of data related to the aerodynamic calculations. Moreover, it is a convenient means to account for any fluid-acoustic interactions that might be present in the flow field. Since the receiver (microphone) will be positioned close to the region where the aerodynamic noise is generated, i.e., a couple of centimeters in front of the mouth, it is most likely feasible to adapt a direct approach at reasonable computational requirements in the simulation of stridor.

The chapter starts with a discussion of the aeroacoustic capabilities of the Lattice Boltzmann Method (LBM) in Section 5.1. Afterwards, Section 5.2 presents a concise description of the aerodynamic noise-generating mechanisms that are present in the upper airway. Since the latter topic is intricately related to the development of far-field propagation models, the text will also briefly elaborate on those. Finally, Section 5.3 contains an overview of those elements of the PowerACOUSTICS software that will be used extensively throughout this thesis.

## 5.1 Aeroacoustics and the Lattice Boltzmann Method

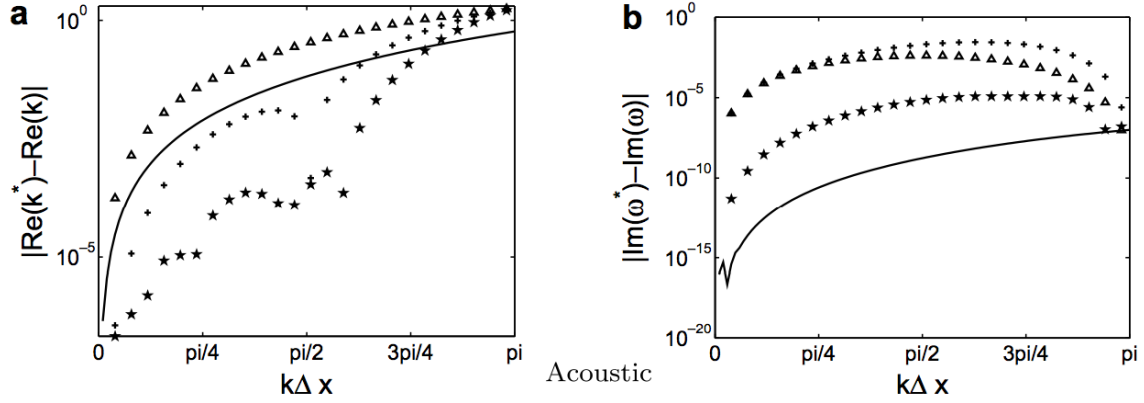
The purpose of this section is to investigate the aeroacoustic capabilities of the LBM as compared to high-order numerical schemes based on the Navier-Stokes Equations (NSE). [Marié et al. \(2009\)](#) performed an extensive analytic comparison of the dispersion and dissipation capabilities of LBGK and NSE high-order schemes, based on a von Neumann analysis of the linearized equations. The result of this comparison is displayed in Figures (5.1) and (5.2) for a non-zero and zero mean flow, respectively. It can be concluded that the LBGK has better dissipation capabilities overall, and better dispersion capabilities than a second-order in space, three-step Runge-Kutta in time classical finite-difference scheme.



**Figure 5.1:** (a)(c) Dispersion, and (b)(d) dissipation error with  $Ma = 0.2$ . (-) LBM, ( $\Delta$ ,  $\nabla$ ) 2nd order finite-difference, (+,  $\times$ ) 3rd order optimized finite-difference, ( $\star$ ,  $\star$ ) 6th order optimized finite-difference [Marié et al. \(2009\)](#).

[Brès et al. \(2009\)](#) additionally investigated the effect of turbulence modeling on the dispersion and dissipation capabilities of the LBGK using the commercial solver PowerFLOW 4.0d. The dispersion error remains practically invariant, but additional dissipation is introduced which tends to scale inversely with resolution. Based on these results, [Brès et al. \(2009\)](#) concluded that 12 - 16 points per wavelength ( $N_{ppw} = 2\pi/k\Delta x$ , where  $k$  represents the wavenumber) should be sufficient to minimize dissipation loss over distances within 1 m from the source





**Figure 5.2:** (a) Dispersion, and (b) dissipation error with  $Ma = 0.0$ . (–) LBM, ( $\Delta$ ) 2nd order finite-difference, (+) 3rd order optimized finite-difference, ( $\star$ ) 6th order optimized finite-difference [Marié et al. \(2009\)](#).

region. Indeed, many authors adopted the criterion put forward by [Brès et al. \(2009\)](#), which led to them to define the cut-off frequency according to:

$$f_{cut-off} = \frac{v}{N_{ppw} \Delta x_{mic}}, \quad (5.1)$$

where  $v$  is the wave propagation speed, and  $\Delta x_{mic}$  the largest voxel size in the intermediate domain that connects the acoustic source region with the microphone location.

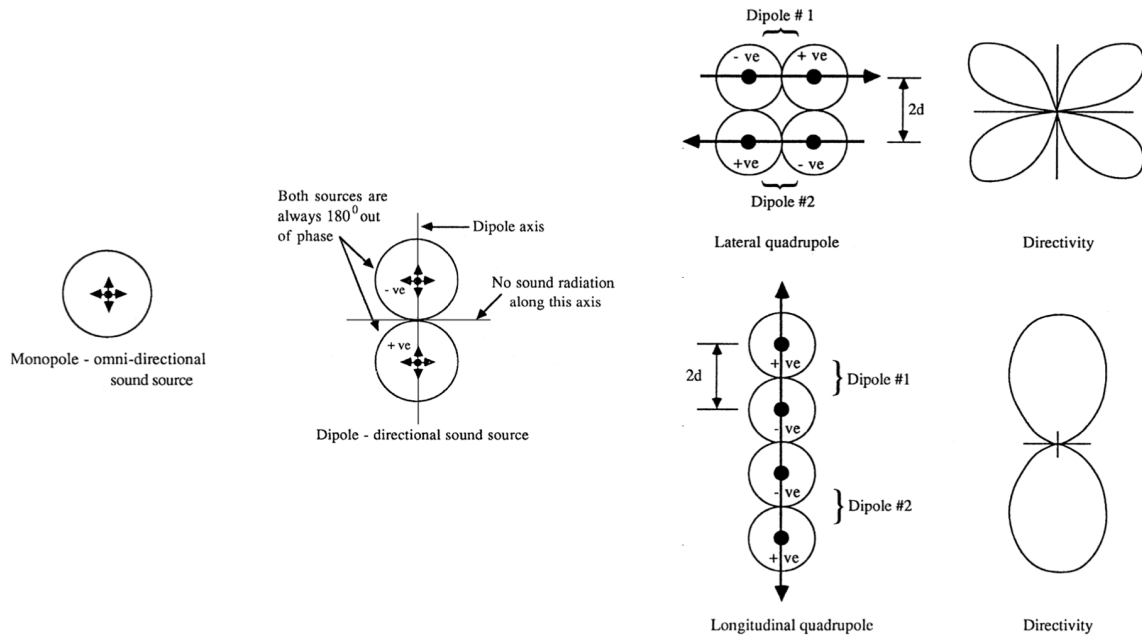
The range of aeroacoustic problems tackled using a LBM is extensive, and includes amongst others the simulation of cavity flows [de Jong et al. \(2013\)](#); [Premnath et al. \(2009\)](#), aircraft landing gear [Noelting et al. \(2010\)](#); [Keating et al. \(2009\)](#); [Li et al. \(2008\)](#); [Noelting et al. \(2008\)](#), ventilation ducts and vents [Pérot et al. \(2011, 2010\)](#) and high-lift trapezoidal wings [Satti et al. \(2008\)](#). Unfortunately, to this author's knowledge, the only researchers known to have assessed a fully internal flow field (a double diaphragm) using PowerFLOW are [Belanger et al. \(2005\)](#). This implies that there is almost no information available regarding best practices for such internal simulations.

## 5.2 Acoustic Sources and Propagation Models

This section will uncover the mechanisms that lie at the basis of aerodynamic noise generation in the upper airways. Although no use will be made of propagation models in the remainder of this thesis, the ways in which acoustic analogies are formulated clearly reveal the physical origin of noise-generating mechanisms in fluid flow. [Norton and Karczub \(2007\)](#) give a comprehensive overview of the matter, including some insightful derivations, and most of the material presented in this section is taken from their work.

## On Monopoles, Dipoles and Quadrupoles

There exist three fundamental types of noise sources. *Monopoles* are spherical sources that produce an omnidirectional sound radiation, and they can be seen as the building block of other sources. The noise is generated by the *net mass flow* that is created by the oscillation of a solid sphere. *Dipoles* consist of two monopoles that are in close proximity and oscillate  $180^\circ$  out-of-phase. While there is no net mass flow for this source type, the noise is created by a *net fluctuating force* or, in other words, a change of momentum. *Quadrupoles*, finally, are composed of two dipoles and appear in both longitudinal and lateral forms. As opposed to the other sources, quadrupole noise is caused by a *net fluctuating stress*. The radiation patterns of all sources are schematized in Figure (5.3).



**Figure 5.3:** Radiation patterns of monopoles, dipoles, and quadrupoles Norton and Karczub (2007).

## The Non-Homogeneous Wave Equation

At this point it should already be clear that the physical mechanisms that lie at the basis of the fundamental noise sources can also be found in the NSE (mass, momentum and stress), though a formal link still has to be established. To that end, it is insightful to study the mathematical appearance of these acoustic sources as solutions to the non-homogeneous wave equation:

$$\frac{1}{c^2} \frac{\partial^2 p}{\partial t^2} - \nabla^2 p = q'(\mathbf{y}, t). \quad (5.2)$$

Here, the source term  $q'$  reflects a non-zero rate of mass flux in the source region, i.e., the region where the noise is generated and which cannot be captured mathematically by the

homogenous wave equation. The solution to this equation can be derived heuristically and is given by Norton and Karczub (2007):

$$p(\mathbf{x}, t) = \int_V \frac{q'(\mathbf{y}, t - \frac{|\mathbf{x}-\mathbf{y}|}{c})}{4\pi|\mathbf{x}-\mathbf{y}|} d^3\mathbf{y} = \frac{1}{4\pi} \frac{\partial}{\partial t} \int_V \frac{q(\mathbf{y}, t - \frac{|\mathbf{x}-\mathbf{y}|}{c})}{|\mathbf{x}-\mathbf{y}|} d^3\mathbf{y}, \quad (5.3)$$

where  $\mathbf{x}$  is the distance between the origin and the observer (outside the source region), and  $\mathbf{y}$  the distance between the origin and the noise source. The solution clearly shows that the acoustic perturbations are due to the rate of change of mass flux per unit volume, which implies that it is the formal solution for a monopole noise source.

The next step is to derive a general solution to the non-homogenous wave equation with an arbitrary source function  $f$ . This can be achieved using free space Green's functions<sup>1</sup> and yields:

$$p(\mathbf{x}, t) = \int_V \frac{f(\mathbf{y}, t - \frac{|\mathbf{x}-\mathbf{y}|}{c})}{4\pi|\mathbf{x}-\mathbf{y}|} d^3\mathbf{y}, \quad (5.4)$$

which is valid in a stationary fluid without solid boundaries. Note the close resemblance of this solution with the one presented for a monopole sound source in Equation (5.3). A comprehensive explanation of the derivation can be found in Norton and Karczub (2007).

Now consider the solution to the non-homogeneous wave equation for a dipole noise source, for which the source function  $f$  can be written as the divergence of an externally applied force  $f_i(\mathbf{x}, t)$ :

$$f = -\frac{\partial f_i(\mathbf{x}, t)}{\partial x_i}. \quad (5.5)$$

In accordance with Equation (5.4) the solution can be written as:

$$p(\mathbf{x}, t) = -\int_V \frac{\text{div } f_i(\mathbf{y}, t - \frac{|\mathbf{x}-\mathbf{y}|}{c})}{4\pi|\mathbf{x}-\mathbf{y}|} d^3\mathbf{y} = -\frac{\partial}{\partial x_i} \int_V \frac{f_i(\mathbf{y}, t - \frac{|\mathbf{x}-\mathbf{y}|}{c})}{4\pi|\mathbf{x}-\mathbf{y}|} d^3\mathbf{y} \quad (5.6)$$

According to Norton and Karczub (2007), 'There is a subtle difference between these equations. In the former the source is represented as a series of monopoles of strength  $\partial f_i/\partial y_i$ . In the latter, it is represented as a dipole of strength  $f_i$  - the force exerted on the fluid volume is equal to the rate at which the momentum changes, since the mass flux in and out of the fluid volume is the same.'

## Turbulence and Lighthill's Acoustic Analogy

Although it has been difficult to associate the aforementioned sources with particular flow features, the advent of acoustic analogies gradually uncovered certain links. For the sake

<sup>1</sup>Green's functions are a quite abstract mathematical concept that are often applied in the solution of partial differential equations. For further information on this topic, the interested reader is referred to the monograph by Haberman (2004).

of completeness, it will first be addressed how these analogies fit into the overall field of aeroacoustics. Afterwards the two (historically) most disruptive analogies will be presented.

There are two possibilities to propagate the near acoustic disturbances to the far-field: computational and analytical transport. With the former method the propagation is described by a simplified model such as the linearized Euler equation or the wave equation. The method therefore requires discretization of the entire far-field domain and is preferable when the acoustic field is to be determined at multiple locations. The analytical methods are based on integral solutions of the (non)-homogenous wave equation, in which the use of Green's functions makes it possible to calculate the sound level at a single location. A distinction is made between volume and surface integral methods.

Within the set of analytical solutions, volume integrals make use of acoustic analogies which essentially constitute a rearrangement of the NSE in the form of a non-homogeneous wave equation. The source term of this wave equation is then composed of the non-linear terms appearing in the original equations. Sir Michael James Lighthill was the first to introduce such acoustic analogy, which can be written as follows [Lighthill \(1952\)](#):

$$\frac{1}{c^2} \frac{\partial^2 p}{\partial t^2} - \nabla^2 p = \frac{\partial^2 T_{ij}}{\partial x_i \partial x_j}, \quad (5.7)$$

In Equation (5.7),  $c$  is the speed of sound,  $p$  the acoustic pressure perturbation as compared to the pressure in a fluid at rest ( $p_0$ ), and  $T_{ij}$  the so-called Lighthill stress tensor. The latter can be written as:

$$T_{ij} = \rho u_i u_j + \delta_{ij} [(p - p_0) - c_0^2 (\rho - \rho_0)] - \tau_{ij}, \quad (5.8)$$

where  $\tau_{ij}$  is the viscous stress tensor. In case the fluid flow is isentropic and situated in the low- $M$  regime, and the sound levels are to be calculated at reasonably close distances (such that the influence of  $\tau_{ij}$  is negligible), the Lighthill stress tensor can be approximated as [Escobar \(2007\)](#); [Lighthill \(1952\)](#):

$$T_{ij} \approx \rho u_i u_j. \quad (5.9)$$

In other words, the acoustic signals are solely produced by fluctuating Reynolds stresses (momentum flux, turbulence) across surfaces fixed in space. It should be pointed out that this coincides with the definition of a quadrupole stated earlier in this section. Indeed, Lighthill himself stated that *'the sound field is that which would be produced by a static distribution of acoustic quadrupoles whose instantaneous strength per unit volume is  $T_{ij}$ '*. [Norton and Karczub \(2007\)](#) made an interesting comment concerning this result: *'Because of the double tendency for cancellation [the source term represents a double divergence] one would qualitatively expect quadrupole sound radiation to be less efficient than dipole sound radiation (...).'* It will later be shown that this is indeed the case for low- $M$  flows.

Finally, consider the solution to Equation (5.7):

$$p(\mathbf{x}, t) = \frac{\partial^2}{\partial x_i \partial x_j} \int_V \frac{T_{ij} \left( \mathbf{y}, t - \frac{|\mathbf{x} - \mathbf{y}|}{c} \right)}{4\pi |\mathbf{x} - \mathbf{y}|} d^3 \mathbf{y}, \quad (5.10)$$

and note its resemblance to the general solution given in Equation (5.4).

### Accounting for the Presence of a Surface: Ffowcs Williams-Hawkings Analogy

Lighthill's analogy only determines the aerodynamic noise generated by free turbulence. In most flows, including the ones that will be investigated in this thesis, the presence of solid boundaries should also be taken into account. With that purpose in mind, [Curle \(1955\)](#) extended Lighthill's acoustic analogy to account for the presence of a solid surface inside the flow, while [Ffowcs Williams and Hawkings \(1969\)](#) additionally accounted for the movement of this solid surface. Their acoustic analogy can be formulated as:

$$\frac{1}{c^2} \frac{\partial^2 p}{\partial t^2} - \nabla^2 p = \frac{\partial^2 T_{ij}}{\partial x_i \partial x_j} - \frac{\partial}{\partial x_i} \left( P_{ij} \delta(f) \frac{\partial f}{\partial x_j} \right) + \frac{\partial}{\partial t} \left( \rho_0 v_i \delta(f) \frac{\partial f}{\partial x_i} \right). \quad (5.11)$$

Because the terms that appear in Equation (5.11) can only be thoroughly explained by means of the full derivation, their definitions are omitted here. Additional information can be found in [Testa \(2008\)](#), [Escobar \(2007\)](#) and [Ffowcs Williams and Hawkings \(1969\)](#). For the purpose of this thesis, it suffices to examine the solution to this equation:

$$p(\mathbf{x}, t) = \underbrace{\frac{\partial^2}{\partial x_i \partial x_j} \int_V \frac{T_{ij} \left( \mathbf{y}, t - \frac{|\mathbf{x} - \mathbf{y}|}{c} \right)}{4\pi |\mathbf{x} - \mathbf{y}|} d^3 \mathbf{y}}_{\text{Quadrupole}} - \underbrace{\frac{\partial}{\partial x_i} \int_S \frac{P_{ij} n_j \left( \mathbf{y}, t - \frac{|\mathbf{x} - \mathbf{y}|}{c} \right)}{4\pi |\mathbf{x} - \mathbf{y}|} dS(\mathbf{y})}_{\text{Dipole}} \quad (5.12)$$

$$+ \underbrace{\frac{\partial}{\partial t} \int_S \frac{\rho_0 v_n \left( \mathbf{y}, t - \frac{|\mathbf{x} - \mathbf{y}|}{c} \right)}{4\pi |\mathbf{x} - \mathbf{y}|} dS(\mathbf{y})}_{\text{Monopole}}.$$

Upon comparison with the previous results from Equations (5.3) - (5.6) it becomes clear that the presence of a solid surface and its movement are directly linked to dipole and monopole sound sources, respectively.

In conclusion, it has been shown that aerodynamically generated sound stems from three sources: quadrupoles with strength density  $T_{ij}$  (linked to free turbulence), dipoles with strength density  $P_{ij} n_j$  (linked to fluctuating surface pressure), and monopoles with strength density  $\rho_0 v_n$  (linked to fluctuating volume displacement induced at moving surface).

### Dimensional Analysis of Source Terms: Relative Importance

It is interesting to look at the relative strength of these acoustic sources in order to identify which ones will be most critical in the following aeroacoustic simulations. Table (5.1) shows the pressure perturbations and sound intensity of each source as obtained from a dimensional analysis. From this table it can be derived that the ratio of sound intensity radiated by a dipole and that radiated by a quadrupole is given by

$$\frac{I(r)_D}{I(r)_Q} \sim \frac{1}{M^2}. \quad (5.13)$$

This relation shows that when  $M \ll 1$ , the fluctuating surface forces constitute the dominant acoustic sources. Given that the monopole sources will not be accounted for in this thesis (i.e., all model boundaries are considered stationary), this is an important consideration in the aeroacoustic analyses that follow.

**Table 5.1:** Results of a dimensional analysis performed separately on each of the source terms of the Ffowcs-Williams Hawkins acoustic analogy [Norton and Karczub \(2007\)](#).

Source Type	Pressure $p'$	Sound Intensity $I(r) = p^2/(\rho c)_0$
Monopole	$\frac{\rho D}{4\pi r} U^2$	$\frac{\rho^2 D^2}{16\pi^2 r^2 (\rho c)_0} U^4$
Dipole	$\frac{\rho D}{4\pi r} M U^2$	$\frac{\rho^2 D^2}{16\pi^2 r^2 (\rho c)_0} M^2 U^4$
Quadrupole	$\frac{\rho D}{4\pi r} M^2 U^2$	$\frac{\rho^2 D^2}{16\pi^2 r^2 (\rho c)_0} M^4 U^4$

### 5.3 PowerACOUSTICS Software

Since only direct aeroacoustic simulations will be carried out in this thesis, there is no need to elaborate on the type of acoustic analogies that are implemented in PowerACOUSTICS. The interested reader is referred to the accompanying literature study by [Foucart \(2014\)](#) for further information on this topic.

There are however two elements of the program that need to be clarified in order to ensure a proper understanding of the acoustic results that will be presented in the following chapters.

#### 5.3.1 From Pressure Signal to Sound Pressure Level

A wide range of instantaneous flow variables can be measured using acoustic probes, the locations of which have to be defined during the case set-up in PowerCASE (via the **Geometry** > **Points** tab). The diameter of the probe also has to be specified and is always set to `8LatticeLengths`. Once the simulation is finished, the probe data can be accessed and analyzed in PowerACOUSTICS. Most importantly, the Sound Pressure Level (SPL) can be calculated directly via **New Calculation** > **Power Spectrum**. Within this function a multitude of processing parameters have to be specified, and they are the same for all acoustic spectra presented in this thesis:

Spectrum Tab	
FFT Window Width Via	Smoothing optimal
Window Overlap	50 %
Window Type	Hanning ( $f(x) = 0.5(1 - \cos 2\pi x)$ )
Spectrum Type	Convert to dB
Bands Tab	
Frequency Banding Via	Every FFT band
Band Summation Via	Sum of power values
Spectral Density Via	Sum over bandwidth

Whenever the acoustic spectra of two or more different simulations are compared within the same figure, they are obtained over the same timespan, measured at the same sampling frequency  $f_s$ , and displayed with the same frequency bands  $\Delta f$  (unless specified otherwise). Note that the specifics of the Fourier transform are described in detail in the PowerACOUSTICS manual.

### 5.3.2 Extraction of Quadrupole Sources

Another interesting function of PowerACOUSTICS is that it allows to extract the divergence of the Lighthill tensor ( $\nabla T_{ij}$ ) directly. It can be computed and visualized by going through the following steps:

1. Select a new calculation with the following settings:
  - Calculation Function: Sample
  - Variables: add new variable (default is pressure), in this case Lighthill divergence tensor
  - Output: select entire field (yields an output file with .ncc extension)
2. Import this so-called companion file into PowerVIZ via **Import > Companion**. Note that the corresponding surface and fluid files should be imported first.
3. Visualization

Unfortunately, it is not possible to extract the dipole sources in a similar way. They have to be calculated by defining a new variable in PowerVIZ via **Project > Equations**.





## **Part II**

# **PowerFLOW Validation**



---

## Chapter 6

---

# Validation of PowerFLOW Turbulence and Wall Models

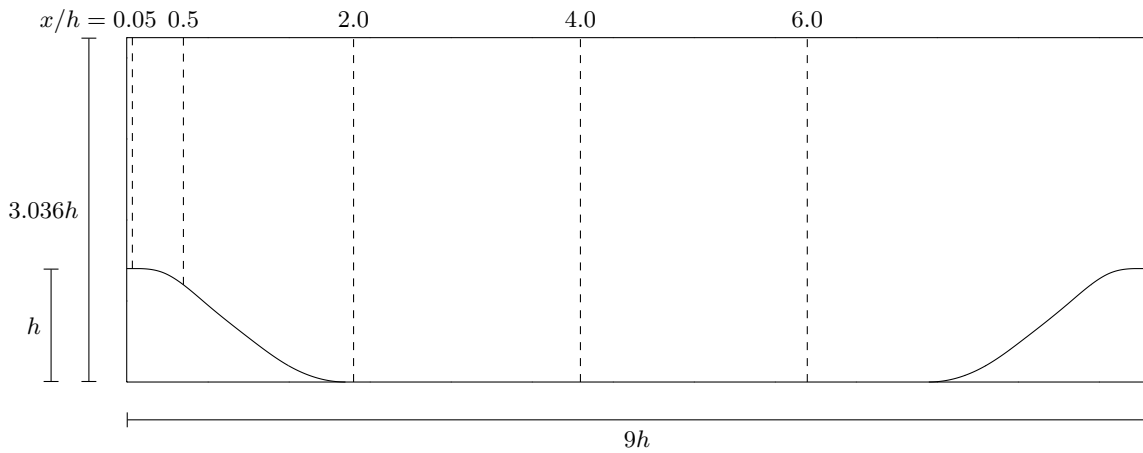
PowerFLOW is most often applied to tackle external flow problems in the automotive and aerospace industries. Typical attributes of such problems are the relatively high speeds (with correspondingly high Mach and Reynolds numbers), and the fact that most separation processes occur at sharp edges. Naturally, these flow types differ from those that are present in the upper airway. The distinction between both flow problems can be made with respect to geometry (the upper airway only includes smooth curvatures with the exception of the epiglottis, see Chapter 2), but also in terms of flow speeds.

To this author's knowledge, there have been no thorough validation studies dealing with this particular flow regime. Therefore, this chapter investigates whether the turbulence and wall models implemented in PowerFLOW (and discussed in Chapter 4) are also able to accurately reproduce the separation process from a surface with smooth curvature. The fluid flow over periodic hills was chosen for this purpose because there exists a wide range of benchmark data for this specific flow problem [Breuer et al. \(2009\)](#); [Fröhlich et al. \(2005\)](#); [Mellen et al. \(2000\)](#). Moreover, the proposed hill geometry resembles structural features that are also present in the upper respiratory system, e.g., stenosis and duct curvature.

Section 6.1 discusses the details of the case geometry. Next, Section 6.2 elaborates on the choice of boundary conditions, which are necessarily different from those used in the reference papers. A brief description of the reference data that was used as a benchmark for the PowerFLOW simulations is provided in Section 6.3. Section 6.4 then investigates the properties of the turbulence model through a grid convergence study, while Section 6.5 analyzes the wall model accuracy. In order to approximate the boundary conditions that were used in the benchmark simulations more closely, a geometry of five consecutive hills has also been simulated, the findings of which are elaborated upon in Section 6.6. Finally, Section 6.7 investigates the performance of an alternative turbulence model.

## 6.1 Case Geometry

A two-dimensional view of the case geometry is shown in Figure (6.1). The exact case geometry as it is printed here was first presented by Mellen et al. (2000) as a computationally feasible and physically relevant test case to validate turbulence models, in particular Large Eddy Simulations (LES). Given the robustness of the model, it has since been used by many other researchers as an appropriate basis for their validation studies. The model also acted as the main test case at two ERCOFTAC workshops on refined turbulence modeling Manceau et al. (2002); Jakirlić et al. (2001).



**Figure 6.1:** Two-dimensional view of the periodic hill geometry. The dashed lines indicate the measurement locations.

Based on the geometry of a three-dimensional bump first proposed by Almeida et al. (1993), the hill shape is fully described by a collection of third-order polynomials, see Appendix A. Hill height was set to  $h = 28$  mm, while the spacing between successive hill crests equals  $L_x = 9h$ . The increased spacing with respect to earlier models allows the flow to naturally reattach between the hills, after which it can recover before accelerating over the next hill. This flow feature poses increased requirements on the turbulence model since natural reattachment is more difficult to simulate than either forced reattachment or acceleration due to interference of the second hill. Model height and width were set to  $L_y = 3.036h$  and  $L_z = 4.5h$ , respectively. This particular height avoids interference of the upper boundary layer with the flow in the region of interest around the hills, whilst economizing the computational cost. The model width, on the other hand, has been the subject of several studies that tried to determine its optimal value by studying the possible correlation of the flow structures in the spanwise direction Breuer et al. (2009); Fröhlich et al. (2005). This research showed that a model width of at least  $L_z = 7h$  would be necessary to achieve spanwise decorrelation, but for reasons of computational cost the reduced width is still adhered to. This does not necessarily lead to a flawed model, because it was shown by Fröhlich et al. (2005) that, ‘if (...) LES or DNS computations are undertaken with the same spanwise periodicity imposed, the comparison of the associated results is not affected’.

## 6.2 Boundary Conditions

The original case has both streamwise and spanwise periodic boundary conditions, while the lower and upper walls are modeled with no-slip boundary conditions. The required Reynolds number ( $Re$ ) is then achieved by superimposing a fictional pressure gradient on the momentum equations that leads to the desired mass flux. A detailed explanation of the iterative procedure can be found in Xu et al. (2005). Unfortunately, PowerFLOW does not accommodate the means to add such a fictional pressure gradient to the underlying equations, hence requiring a different set of boundary conditions.

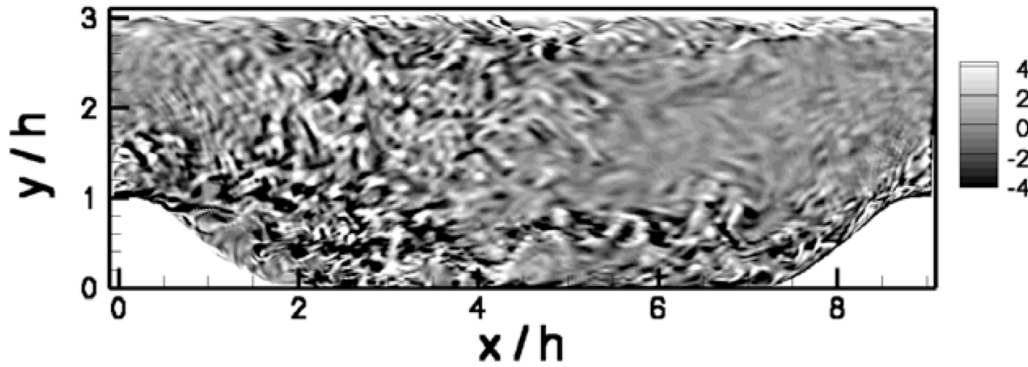
Since PowerFLOW allows the specification of a three-dimensional gravitational field, one possibility is to substitute the aforementioned pressure gradient for a gravitational body force. Given that acceleration ( $\mathbf{a}$ ) and pressure gradient ( $\nabla\mathbf{p}$ ) can be linked according to

$$\mathbf{a} = -\frac{1}{\rho}\nabla\mathbf{p}, \quad (6.1)$$

PowerFLOW would indeed be able to mimic the periodic boundary conditions, albeit from a different perspective. Because the update equation for the pressure gradient requires knowledge of the mass flux after each temporal iteration, the mass flux should be measured, stored and subsequently loaded back into PowerFLOW prior to the next time step. Measurement and storage of the mass flux can be achieved by implementing a **Composite Sampled Face Measurement** (.csnc-file) in the case definition, a measurement type that automatically integrates parameters over a specified domain. This data should then be stored in a separate text file according to specified PowerFLOW-table formatting rules, such that it can be reloaded into PowerFLOW through the **Calculations > Tables** tab. Finally, the use of time-dependent boundary conditions through the **Calculations > Equations** tab allows to meet the reference boundary conditions. It should be noted that the body force can only be determined iteratively because the converged fictional pressure force is not explicitly mentioned in reference papers.

Evidently, this is a rather cumbersome procedure that implies extensive computational time. It was therefore decided to eliminate the streamwise periodicity in favor of a mass flux boundary condition that yields the desired  $Re = 10,595$ . The inlet flow condition - which should essentially mimic the outlet flow condition - then had to be modeled in best possible accordance with the inlet conditions found in the reference papers. It is important to realize here that, apart from the velocity profile at the inlet, the inlet vorticity also influences the flow field downstream. Figure (6.2) exemplifies the need to account for these fluctuations in vorticity.

Simulation of the single hill configuration with kinematic viscosity  $\nu = 1.49 \times 10^{-5} \text{ m}^2/\text{s}$  and corresponding characteristic velocity  $u_{char} = 2.769 \text{ m/s}$  showed no sign of flow reattachment, hence emphasizing the need to relate the inlet parameters to those present in the reference solution. Given that specification of a three-dimensional velocity surface is not possible within the PowerFLOW environment, the only two velocity parameters that can be altered are its averaged magnitude and direction. Because the flow was assumed to enter normal to the inlet, the only parameter that was effectively varied was the average inlet flow speed (2.769 - 33.452 m/s), necessarily accompanied by an increase in viscosity due to the require-



**Figure 6.2:** Instantaneous vorticity component  $\omega_z$  normal to the cross-section at an arbitrarily chosen instant in time Breuer et al. (2009).

ments on  $Re$ . Even though this velocity increase does not reduce the discrepancy with respect to the shape of the reference velocity profile, it was hypothesized that it would positively influence the reattachment process because PowerFLOW may not behave optimally at low flow speeds. Nevertheless, none of these  $u_{char} - \nu$  combinations were able to attain the required reattachment of the flow between successive hills. It was therefore decided to fix the inlet velocity at  $u_{char} = 5.538 \text{ m/s}$  ( $\nu = 3.0 \times 10^{-5} \text{ m}^2/\text{s}$ ), whilst focusing on the inlet turbulence settings.

A possible way to influence the inlet vorticity is to trip the boundary layer that develops along a flat plate positioned upstream of the first hill crest, such that relevant turbulence settings are created at the inlet position. However, this would require a rather cumbersome trial-and-error procedure during which the correct turbulence settings are obtained by changing the flat-plate length and/or the trip height/shape. Moreover, it would not be possible to achieve turbulent fluctuations in the entire inlet region with a boundary layer trip (instead, they would be limited to the region close to the hill crest). Therefore a different approach has been chosen here. It was decided to adapt both the turbulence intensity (TI) and the turbulent length scale (LS) of the inlet flow until a reattachment point became visible that was comparable to the one presented in the reference paper. Although the inlet velocity profile is not matched exactly, tuning these inlet turbulence settings did allow the required flow reattachment to take place. Also, adapting the turbulence settings is an acceptable option because it allows for a homogeneous vorticity distribution to be produced at the inlet. The actual choice of turbulence settings is discussed in Section 6.4.

It is acknowledged that the line of reasoning does not correspond to the original test case in a one-to-one fashion. Nevertheless, the aim of the simulations presented in this chapter was not to obtain the closest possible match with the reference data, but rather to investigate the relative convergence to this data when applying different grid settings. In that respect, the test case was anticipated to provide insightful information regarding the accuracy of both wall and turbulence models. In order to strengthen the conclusions drawn from the single hill simulations, an additional test case was included that models the flow field over multiple hills, which more closely resembles periodic boundary conditions.

## 6.3 Description of the Reference Data

All benchmark data presented in this chapter was taken from a study by Breuer et al. (2009) and is freely available at [http://uriah.dedi.melbourne.co.uk/w/index.php/UFR\\_3-30\\_Test\\_Case](http://uriah.dedi.melbourne.co.uk/w/index.php/UFR_3-30_Test_Case). The aim of this study was to investigate the effect of  $Re$  on the physical flow phenomena. Therefore, flow data was acquired for a large range of  $700 \leq Re \leq 10,595$  using two independent numerical methodologies as well as experimental Particle Image Velocimetry (PIV) techniques. Because  $Re$  was fixed at 10,595 in the current study, only the numerical methodology related to this particular value will be discussed further.

The simulations are based on the so-called LESOCC code, a finite-volume method for arbitrary non-orthogonal and non-staggered block-structured grids. It is a second-order in space, three-step second-order Runge-Kutta in time scheme, where the time advancement is further refined by applying a corrector step in which the Poisson equation for the pressure correction is solved implicitly by the incomplete LU decomposition method of Stone (1968). Subgrid scale eddies are modeled according to the dynamic Smagorinsky model proposed by Lilly (1992).

The computational mesh consists of 13.1 million grid points. Special consideration was given to the resolution in the wall region in order to comply with the requirements for a wall-resolved LES prediction for both the lower and the upper wall. As discussed in the previous section, streamwise and spanwise periodicity is assumed, while the required mass flow is achieved by adding a source term to the underlying momentum equations.

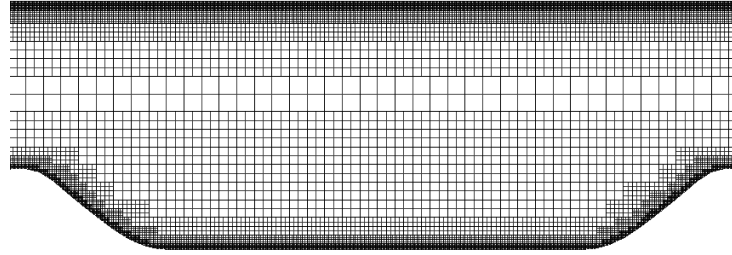
The accuracy of the flow data was positively verified by comparing the results with those from earlier numerical simulations with lower grid resolution Fröhlich et al. (2005) as well as data obtained from experimental PIV measurements performed during the course of the same study. The experimental geometry consisted of 10 successive hills in order to achieve periodicity in the streamwise direction, whereas the measurement section was positioned between hills seven and eight.

## 6.4 Turbulence Model

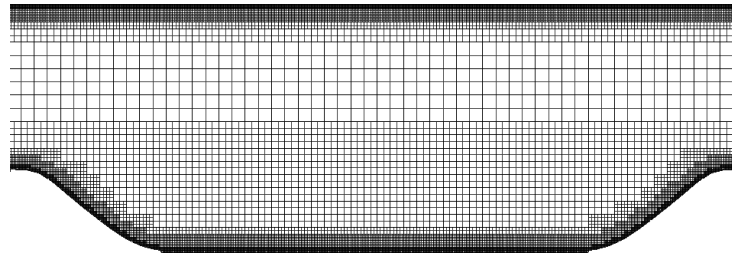
In this section the accuracy of the turbulence model will be investigated. In order to minimize the influence of the wall model on the simulation results, only wall-resolved LES computations were carried out. The wall model is then discussed separately in Section 6.5.

The first step is to construct an appropriate computational grid. Regarding this topic, Breuer et al. (2009) mentioned that *‘the grid points are clustered in the vicinity of the lower wall, the upper wall, and the region where the free shear layer appears’*. Most important in this list is the resolution around the hill crest because this will influence the location of the separation point and, consequently, also the location of the reattachment point. According to Temmerman et al. (2003), *‘there is a fairly strong correlation between the separation and*

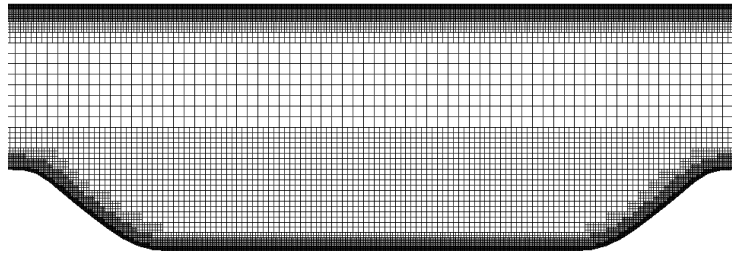
reattachment locations: typically, a forward shift of the separation point by 0.15 hill heights results in a shortening of the recirculation zone by 1 hill height'. Therefore, the basic lay-out of the grid includes refinements in exactly those regions as stipulated by Breuer et al. (2009), see Figure (6.3).



(a) Medium mesh,  $3.927 \times 10^6$  voxels,  $\Delta/h = 0.0136$



(b) Fine mesh,  $6.664 \times 10^6$  voxels,  $\Delta/h = 0.0104$



(c) Finest mesh,  $12.376 \times 10^6$  voxels,  $\Delta/h = 0.0082$

**Figure 6.3:** Selection of grids used in the periodic hill grid convergence study.

The four meshes considered in this grid convergence study distinguish themselves solely through their resolution levels (specified between brackets in the next sentence), i.e., the number of voxels along a characteristic length, which is  $2.036h$  in this case. These resolution levels lead to mesh sizes of  $1.105 \times 10^6$  (100),  $3.927 \times 10^6$  (150),  $6.664 \times 10^6$  (200), and  $12.376 \times 10^6$  (250) cells for the coarse, medium, fine, and finest mesh, respectively. The associated Variable Resolution (VR) levels, as well as the actual voxel sizes, are listed in Table (6.1) for all meshes. Note that the voxel size is doubled between each VR level to allow a correct transition of the flow variables (i.e., distribution functions) Chen et al. (2006).

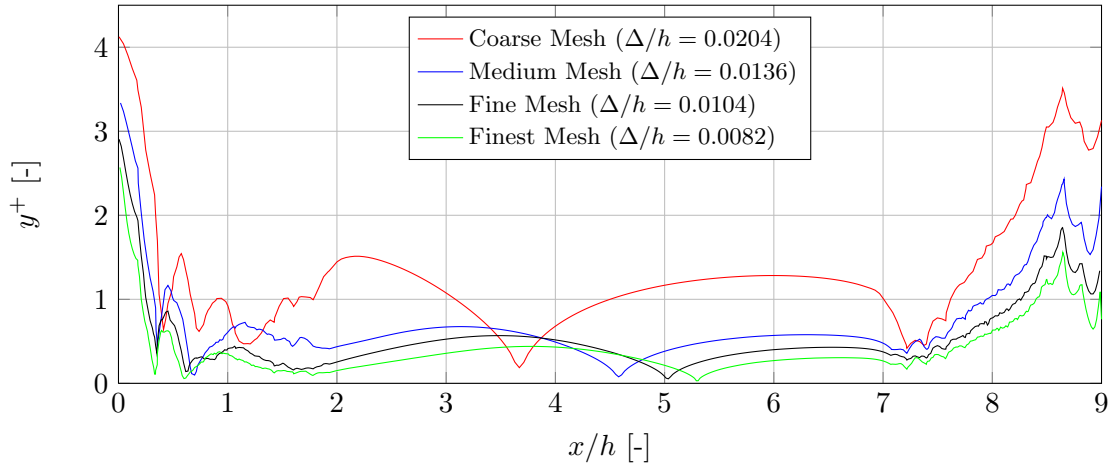


**Table 6.1:** Voxel sizes (in mm) associated with the VR regions used in the periodic hill meshes.

VR	Coarse	Medium	Fine	Finest
4	0.57	0.38	0.29	0.23
3	1.14	0.76	0.57	0.46
2	2.28	1.52	1.14	0.91
1	4.56	3.04	2.28	1.82
0	9.12	6.08	4.56	3.65

### Grid Resolution in the Boundary Layer

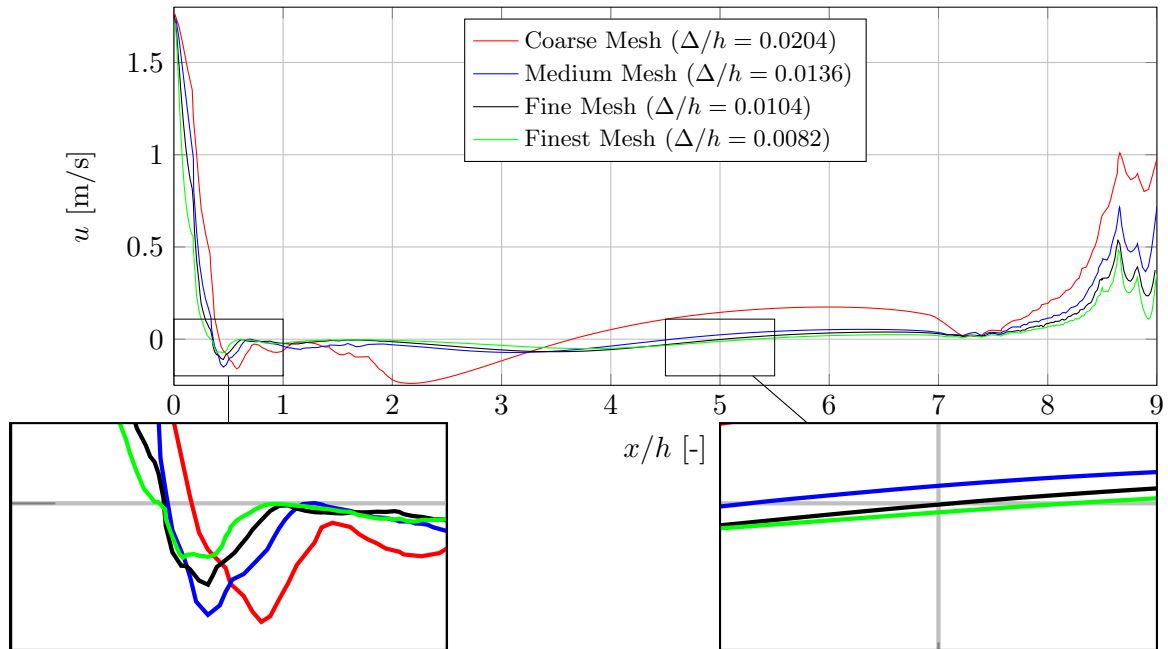
It is possible to reduce the influence of the wall model by adapting a sufficiently fine grid resolution in the boundary-layer region. Figure (6.4) compares values of  $y^+$ , a measure for the position of the first off-wall voxel, for all meshes. This parameter basically acts as an indicator for the degree by which the boundary layer is resolved. Increased refinements in the grid resolution clearly result in lower values of  $y^+$ , which implies that the results of the finest mesh rely less on the accuracy of the wall model than do the results of the coarser grids.

**Figure 6.4:** Instantaneous values of  $y^+$ , a measure of the position of the first off-wall voxel position, at the lower boundary, mid-span. The bracketed values represent the non-dimensional smallest voxel size.

However, not only the inversely proportional relationship between resolution and  $y^+$  is important. The actual values should also lie within certain limits. It is generally accepted that the boundary layer is well-resolved when  $y^+ < 5$ , i.e., the first voxel lies within the linear sublayer [Piomelli \(2008\)](#); [Wagner et al. \(2007\)](#); [Mellen et al. \(2000\)](#). Figure (6.4) shows that this limit is indeed met by all meshes, such that the effects of the wall model on the flow behavior are kept to a minimum. Nonetheless, it should be mentioned that the  $y^+$ -values show distinguished spikes in the vicinity of the hill crests. Due to the strong sensitivity of the separation process on the grid resolution, it is expected that the gradual increase in  $y^+$ -values when going from the finest to the coarse mesh will induce marked differences in the flow results.

## Separation and Reattachment

The average separation and reattachment locations are normally determined based on the values of the skin friction coefficient or, equivalently, the wall shear stress. Since PowerFLOW only returns the absolute values of these parameters, they cannot be used to reliably estimate these locations. Alternatively, either  $y^+$  or the streamwise velocity  $u$  can be used to estimate them. Figure (6.5) displays the values of the streamwise velocity along the lower wall. A quantitative overview of the derived separation and reattachment locations is given in Table (6.2), along with reference data from Breuer et al. (2009). It can be argued that there exists a fairly good correspondence between the values determined using  $y^+$  and  $u$ . There is however no perfect match because it is difficult to pinpoint the exact separation/reattachment point in the  $y^+$ -data. One can only consider local minima in this data set, while the minima corresponding to the separation and reattachment locations do not necessarily coincide with the measurement points (if they would, the  $y^+$ -values would be zero at some point according to its definition). In other words, due to the finite mesh resolution the separation and reattachment locations can only be determined with an accuracy equal to the smallest voxel size. On the other hand, the velocity data set is interpolated in better accordance with the underlying flow behavior because it also contains negative values (backflow). As a result, the estimation accuracy is not limited to the local voxel size but is rather dependent on the accuracy of the linear interpolation. Hence, it is considered more accurate to work with the velocity data.



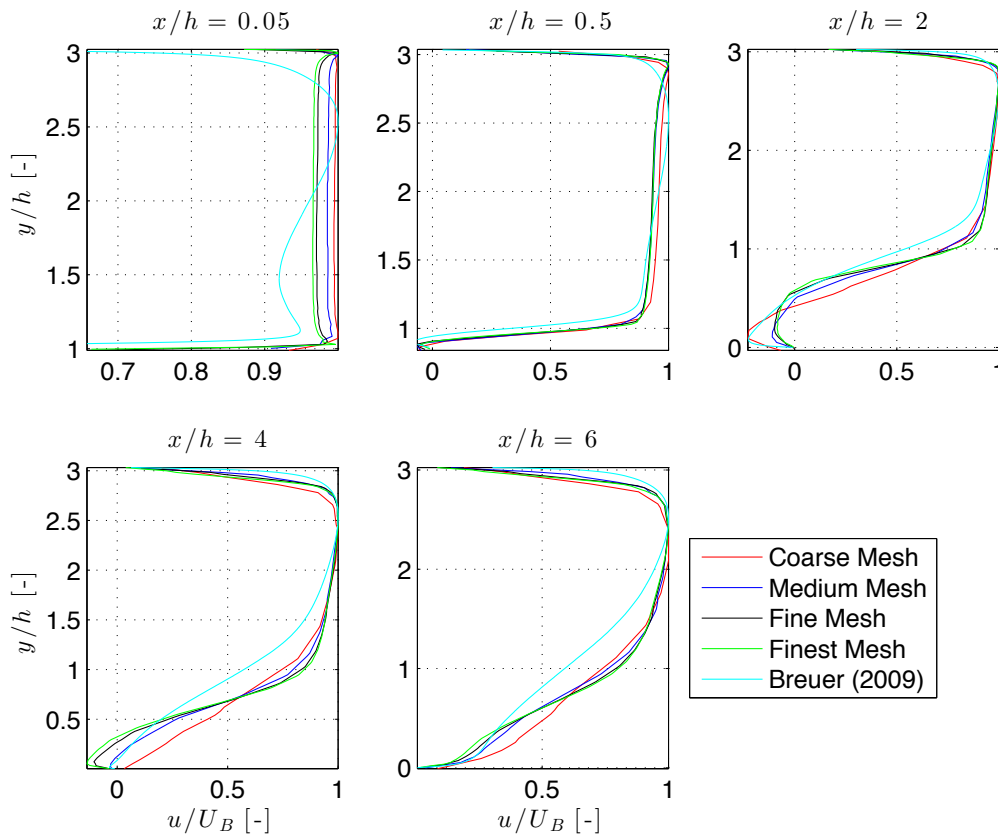
**Figure 6.5:** Averaged values of  $u$  at the first off-wall voxel position, lower boundary, mid-span. The zero-crossings (transition to/from backflow) yield an indication to the separation and reattachment locations. The bracketed values represent the non-dimensional smallest voxel size.

Comparison with the reference data (see Table (6.2)) does not provide a decisive conclusion regarding the influence of the mesh size on the flow results. While the reattachment point

lies closest to the reference location for the medium mesh, the finest mesh outperforms the other meshes with regard to separation. An explanation for the general separation delay is to be found in the discrepancy of the inlet velocity profiles with respect to the benchmark data, see Figure (6.6) at  $x/h = 0.05$ .

**Table 6.2:** Comparison of approximated separation and reattachment locations with those obtained by Breuer et al. (2009).

Case	Separation Point [ $x/h$ ]		Reattachment Point [ $x/h$ ]	
	$u$	$y^+$	$u$	$y^+$
Breuer et al. (2009)	0.19	0.19	4.69	4.69
Coarse Mesh	0.416	0.412	3.646	3.629
Medium Mesh	0.361	0.356	4.566	4.579
Fine Mesh	0.352	0.351	5.032	5.034
Finest Mesh	0.343	0.339	5.305	5.307



**Figure 6.6:** Comparison of the averaged streamwise-velocity profiles with those obtained by Breuer et al. (2009) at six streamwise positions, mid-span.

Even though the separation and reattachment locations do not match exactly with their corresponding reference locations, an important conclusion can be drawn from the results: an

upstream shift of the separation point causes the flow to reattach further downstream. This confirms the hypothesis mentioned in general literature [Temmerman et al. \(2003\)](#). Moreover, the quantitative data presented in Table (6.2) clearly demonstrates that a small shift in separation location can lead to strong variations in the reattachment location.

Further insights can be drawn from the fluid profiles presented in Figure (6.6). Firstly, despite the fact that their inlet velocity profiles are dissimilar, the velocity field shows behavior that is similar to the benchmark data further downstream. Secondly, the fluid profiles are increasingly similar with increased mesh refinement: the results of the fine and finest mesh almost coincide, while the coarse mesh clearly performs worse. This evolution hints at a convergence to DNS-type results, and strengthens the belief that the turbulence model is able to handle separation from a curved surface within an internal geometry. Based on these two observations, the following hypothesis was put forward:

*The fluid profiles converge to the benchmark data if the boundary conditions of both simulations are matched.*

If the hypothesis were to be confirmed, this would lead to a decisive conclusion regarding the accuracy of the turbulence model. A further analysis is presented in Section 6.6.

### Setting the Correct Boundary Condition: Effect of Inlet Turbulence Settings

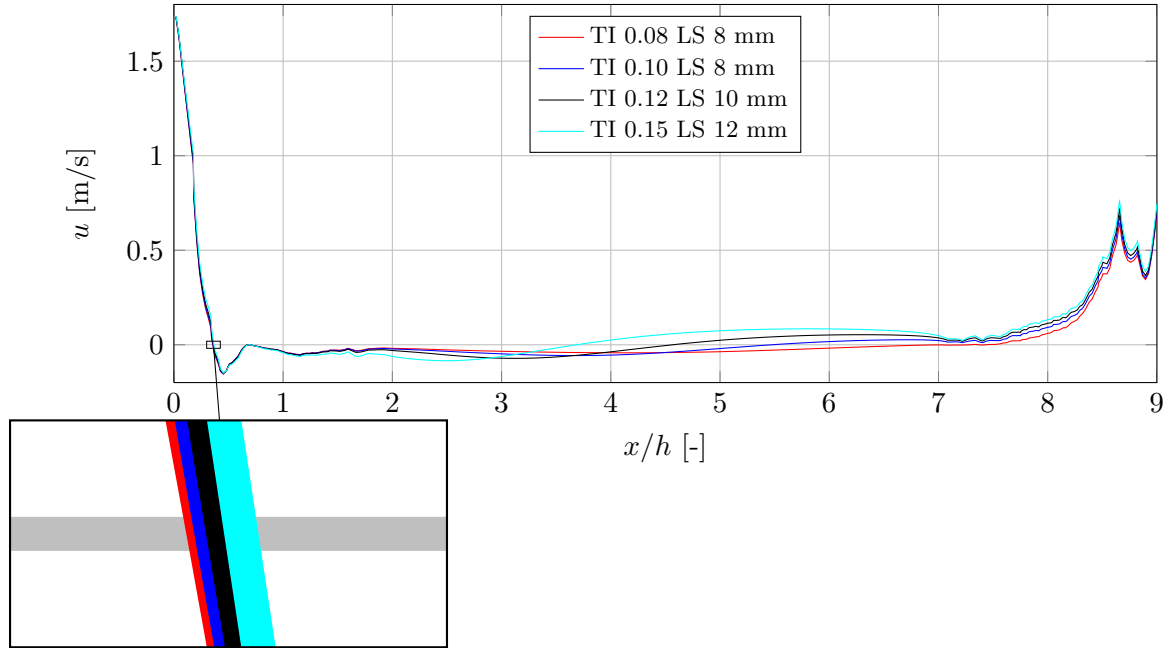
In Section 6.2 it has been discussed that PowerFLOW offers the possibility to change the turbulence intensity (TI) and the length scale of the turbulent eddies (LS) at the inlet. The impact of these inlet turbulence settings on the flow field was assessed by cross-comparing the separation/reattachment locations obtained from four different parameter sets. All simulations were carried out on the medium mesh to reduce computational cost.

**Table 6.3:** Comparison of approximated separation and reattachment locations for different inlet turbulence settings with those obtained by [Breuer et al. \(2009\)](#).

Case	Separation Point [ $x/h$ ]	Reattachment Point [ $x/h$ ]
<a href="#">Breuer et al. (2009)</a>	0.19	4.69
TI 0.08 LS 8 mm	0.355	7.429
TI 0.10 LS 8 mm	0.358	5.475
TI 0.12 LS 10 mm	0.361	4.566
TI 0.15 LS 12 mm	0.366	3.691

The data is summarized in Table (6.3) and Figure (6.7). In general, the turbulence settings only have a minor influence on the separation location, while the reattachment location varies markedly under the influence of these vorticity variations. Consequently, the decision regarding the (sub-)optimal<sup>1</sup> turbulence settings was based solely on the reattachment location.

<sup>1</sup>The word sub-optimal is preferred here because there has been no optimization study in order to determine the parameter set that attains the optimal correspondence with the reference reattachment location.



**Figure 6.7:** Averaged values of  $u$  at the first off-wall voxel position, lower boundary, mid-span, for different inlet turbulence settings. The zero-crossings (transition to/from backflow) yield an indication to the separation and reattachment locations. Medium mesh ( $\Delta/h = 0.0136$ ).

Because the ‘TI 0.12 LS 10 mm’ settings led to the best correspondence with the reference reattachment location, these turbulence settings were used for all simulations presented in this chapter.

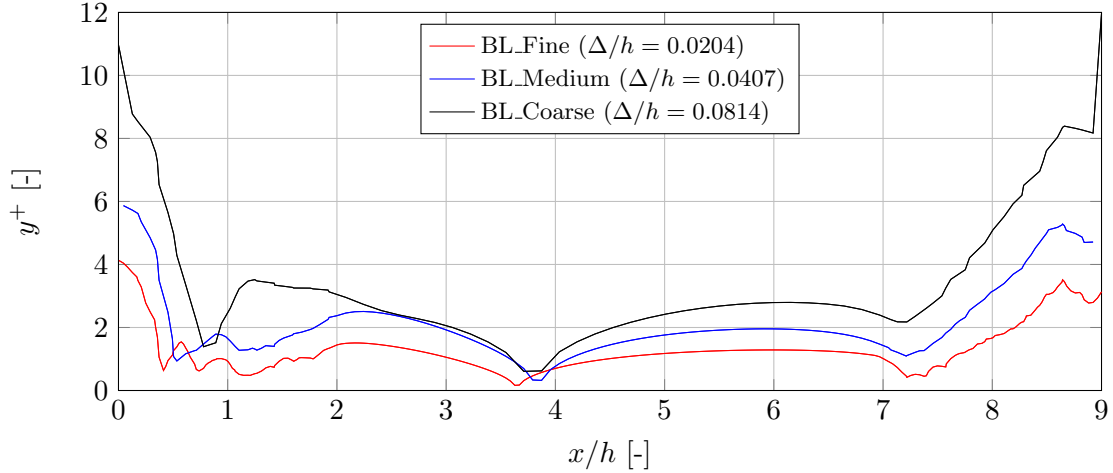
Note that the findings are again in line with the hypothesis put forward by [Temmerman et al. \(2003\)](#): increased turbulence at the inlet causes the separation point to lie further downstream, which in turn causes the reattachment location to shift upstream.

## 6.5 Wall Model

In order to assess the accuracy of the wall model the coarse mesh was used as a baseline set-up (BL\_Fine) from which two other configurations have been derived (BL\_Medium and BL\_Coarse). The size of the wall-nearest voxel is doubled between each configuration, whilst retaining the same resolution in the remainder of the computational domain. This can be achieved by eliminating the finest VR level from the mesh definition while simultaneously halving the resolution, a procedure which resulted in  $4.56 \times 10^5$  (50) and  $8.83 \times 10^4$  (25) voxels for the BL\_Medium and BL\_Coarse configurations, respectively. The values between brackets again represent the case resolution.

The wall-nearest voxel size is increased so that  $y^+$  would be shifted outside the linear sublayer ( $y^+ > 5$ ). In that case, the simulation can no longer be regarded as wall-resolved and the effect

of the wall model on the flow field becomes much more pronounced. Figure (6.8) indicates that the increase in voxel size is indeed translated into the required increase in  $y^+$ , albeit only in the hill regions. Because those are the regions where the most intricate flow phenomenon takes place (the separation process impacts the entire flow field), the proposed coarsening of the grid is considered sufficient as a means to investigate the wall model accuracy.



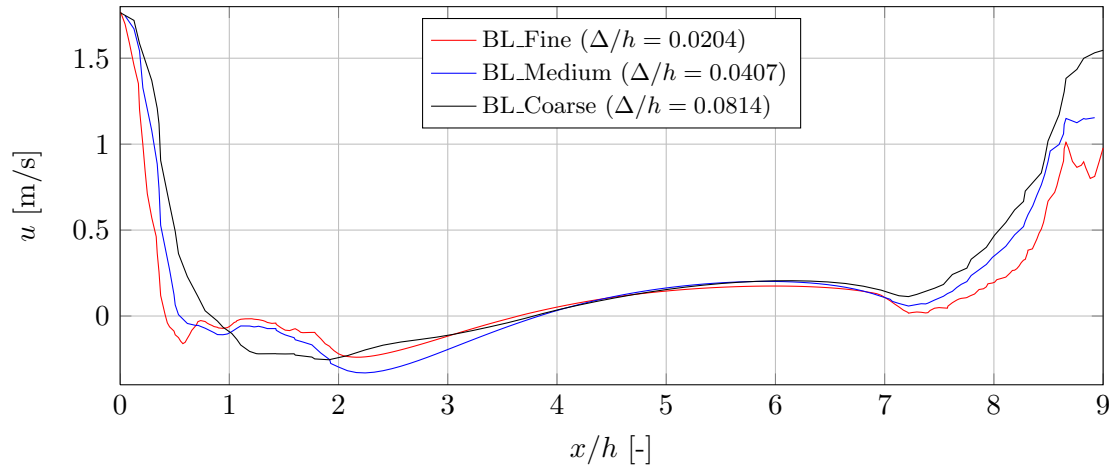
**Figure 6.8:** Instantaneous values of  $y^+$  at the lower boundary, mid-span, for different boundary-layer resolutions. The bracketed values represent the non-dimensional smallest voxel size.

The separation/reattachment locations for all configurations can be derived from Figure (6.9) and are summarized in Table (6.4). Corresponding fluid profiles are compared in Figure (6.10). Clearly, a decrease in resolution causes a considerable downstream shift in the separation location while the reattachment locations remain very similar. Also, the results are no longer compliant with the hypothesis proposed by [Temmerman et al. \(2003\)](#). Based on these findings it can be concluded that the wall model introduces strong discrepancies in the boundary-layer behavior, even at relatively low values of  $y^+$  (normally the wall-nearest voxel can be shifted outside the viscous sublayer ( $y^+ > 50$ ) when use is made of wall models).

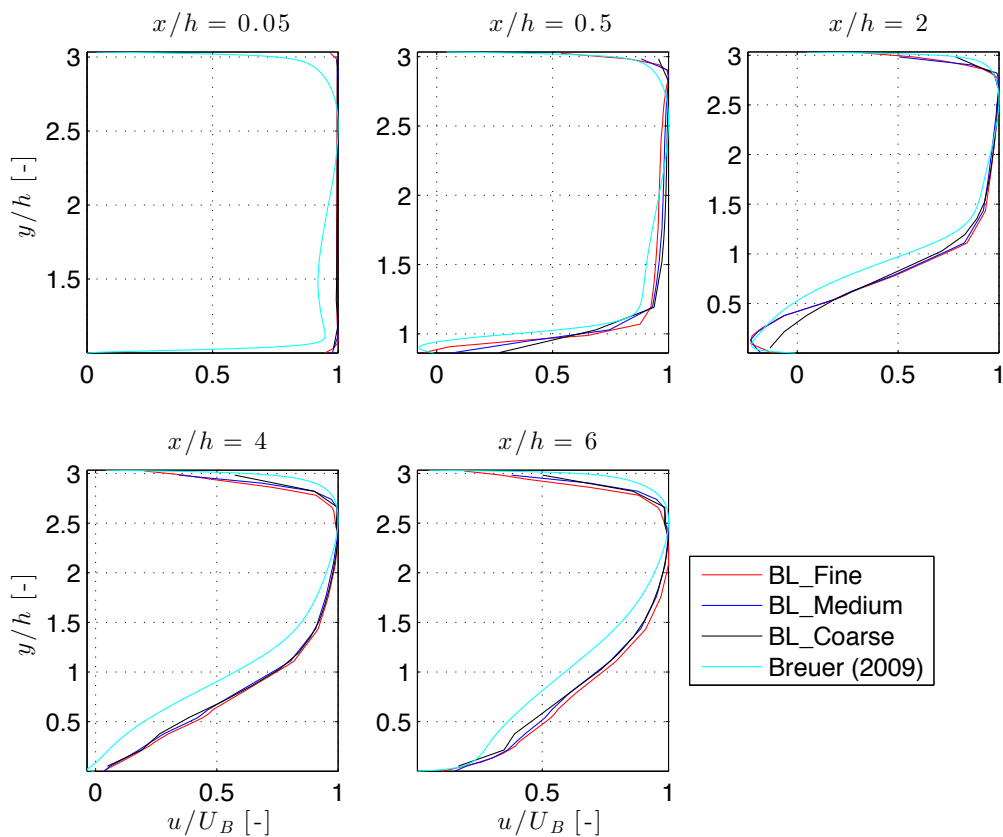
A possible way to minimize the number of voxels required, based on the  $y^+$ -values presented in Figure (6.8), might be to refine the boundary in the vicinity of the hills (and especially in the region around the separation line) while using a coarser boundary-layer resolution in the region between the hills. Nevertheless, it was decided not to pursue this matter any further.

**Table 6.4:** Comparison of approximated separation and reattachment locations for different boundary-layer resolutions with those obtained by [Breuer et al. \(2009\)](#).

Case	Separation Point $[x/h]$	Reattachment Point $[x/h]$
<a href="#">Breuer et al. (2009)</a>	0.19	4.69
BL_Fine	0.416	3.646
BL_Medium	0.547	3.836
BL_Coarse	0.836	3.787



**Figure 6.9:** Averaged values of  $u$  at the first off-wall voxel position, lower boundary, mid-span, for different boundary-layer resolutions. The zero-crossings (transition to/from backflow) yield an indication to the separation and reattachment locations.



**Figure 6.10:** Comparison of the averaged streamwise-velocity profiles for the different boundary-layer resolutions with those obtained by Breuer et al. (2009) at six streamwise positions, mid-span.

## 6.6 Quintuple Hill Geometry

In order to reach a decisive conclusion regarding the accuracy of the PowerFLOW turbulence model, the fluid data presented in Section 6.4 should be compared with that retrieved from a Direct Numerical Simulation (DNS). If the results can be shown to converge to the DNS data for increasing grid resolutions, this would prove the ability of the turbulence model to resolve the intricate flow separation from a curved surface. However, PowerFLOW does not allow the specification of the previously determined inlet turbulence conditions when performing a DNS. Consequently, the flow conditions imposed on the DNS computation would not correspond to those that have been applied in the turbulent simulations, which implies that the DNS simulation would effectively solve a different flow problem. Any conclusions drawn from the comparison of both data sets would then be considered unsatisfactory proof of the turbulence model accuracy.

In accordance with the hypothesis presented in Section 6.4, it is alternatively attempted here to achieve a better match with the boundary conditions used in Breuer et al. (2009) by simulating the flow field over five consecutive hills. It is expected that the effects of the inlet condition will be damped further downstream<sup>2</sup>, hence leading to an increasingly better representation of streamwise periodicity for each consecutive hill. Although experiments mostly include ten consecutive hills as a means to reproduce the periodic boundary conditions Rapp et al. (2010); Breuer et al. (2009), this number was reduced to five following a trade-off between two opposing requirements: (1) limit computational time and (2) allow the inlet conditions to be sufficiently damped. The second requirement showed to be the critical one for the following reasons:

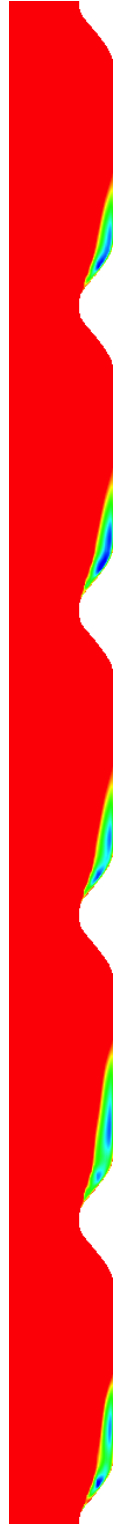
- The results of the first hill cannot be taken into consideration because the influence of the inlet boundary conditions is still very apparent in this region - for similar reasons the second hill is also excluded from the discussion;
- Because the outlet boundary conditions might interfere with the flow field over the fifth hill, the data from that region should also be omitted from the discussion;
- A quintuple hill geometry allows an investigation into the relative convergence of the flow fields over the third and fourth hill to the reference solution.

The configuration is fitted with both the medium mesh ( $19.59 \times 10^6$  voxels) as well as the fine mesh ( $33.26 \times 10^6$  voxels). Even though the finest mesh was shown to provide the most accurate results, these coarser meshes are preferred here as a means to limit simulation time. Moreover, it is expected that the periodicity effects will already be apparent for these lower resolutions.

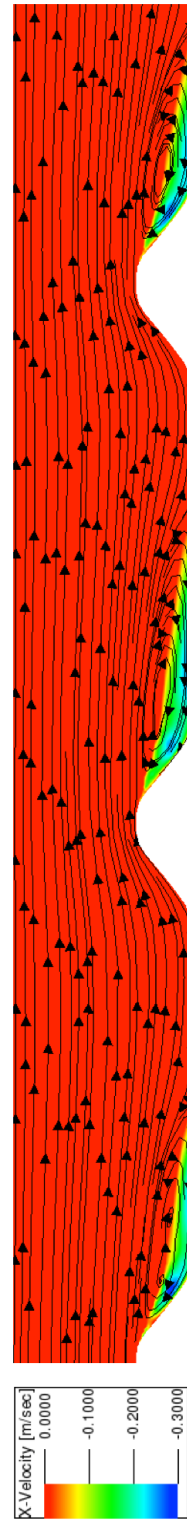
---

<sup>2</sup>Note that the turbulence settings remained unchanged with respect to the single hill configuration. Although it is acknowledged that these settings might no longer be (sub-)optimal for the current configuration (lower values would most likely lead to better results because the turbulence can now develop within the flow itself), it was decided not to investigate this issue due to time limitations.





**Figure 6.11:** Snapshot of the average streamwise velocity  $u$  (levels between  $-0.3$  and  $0$  m/s), quintuple hill geometry, medium mesh, mid-span.

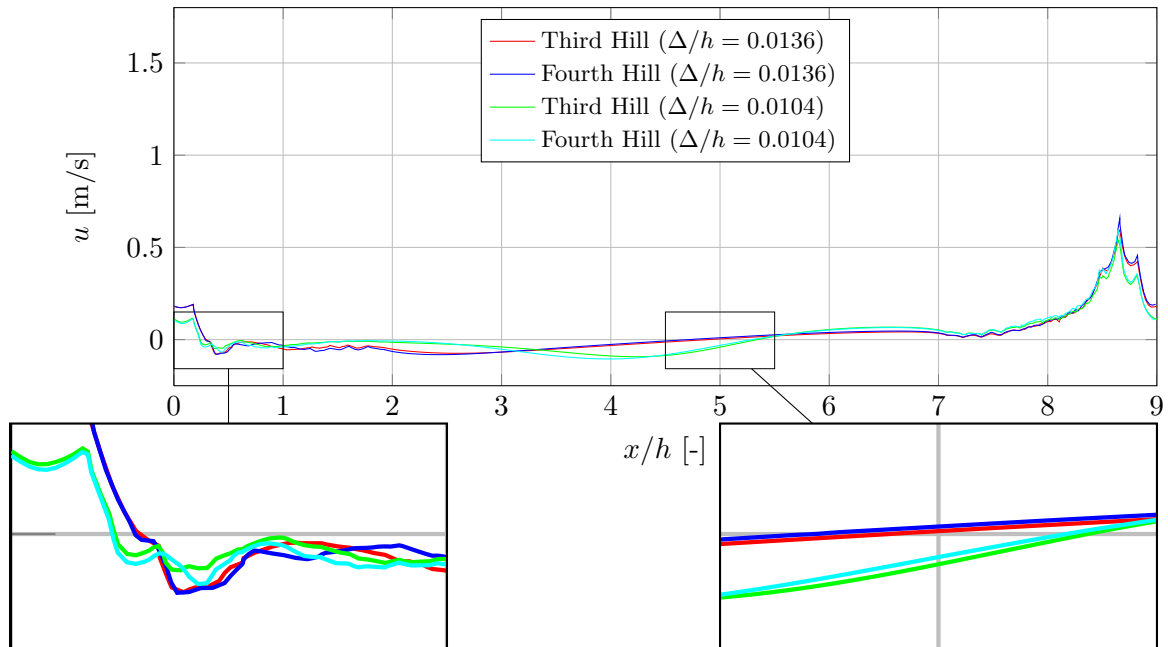


**Figure 6.12:** Snapshot of the average streamwise velocity  $u$  (levels between  $-0.3$  and  $0$  m/s) superimposed with a selection of streamlines, quintuple hill geometry, medium mesh, mid-span.

Figure (6.11) shows the average streamwise velocity field over the quintuple hill geometry, while Figure (6.12) shows the same velocity field over the first three hills, superimposed with a selection of streamlines. These qualitative results already indicate that there exist marked differences between the flow fields over the consecutive hills. As an example, the flow separation over the second hill already appears smoother, an observation which is confirmed by the smoothness of the streamlines in that region. Also, this smooth separation causes an enlarged separation region downstream of the second hill.

Figure (6.13) and Table (6.5) compare the separation and reattachment locations of the third and fourth hill. It is obvious that the separation point on these hills lies much closer to the reference point than any of the finer grids was able to achieve. Moreover, the accompanying downstream shift in the reattachment location is less severe as compared to the finer grid results. Once again, the fine grid provides a better match with the benchmark separation location.

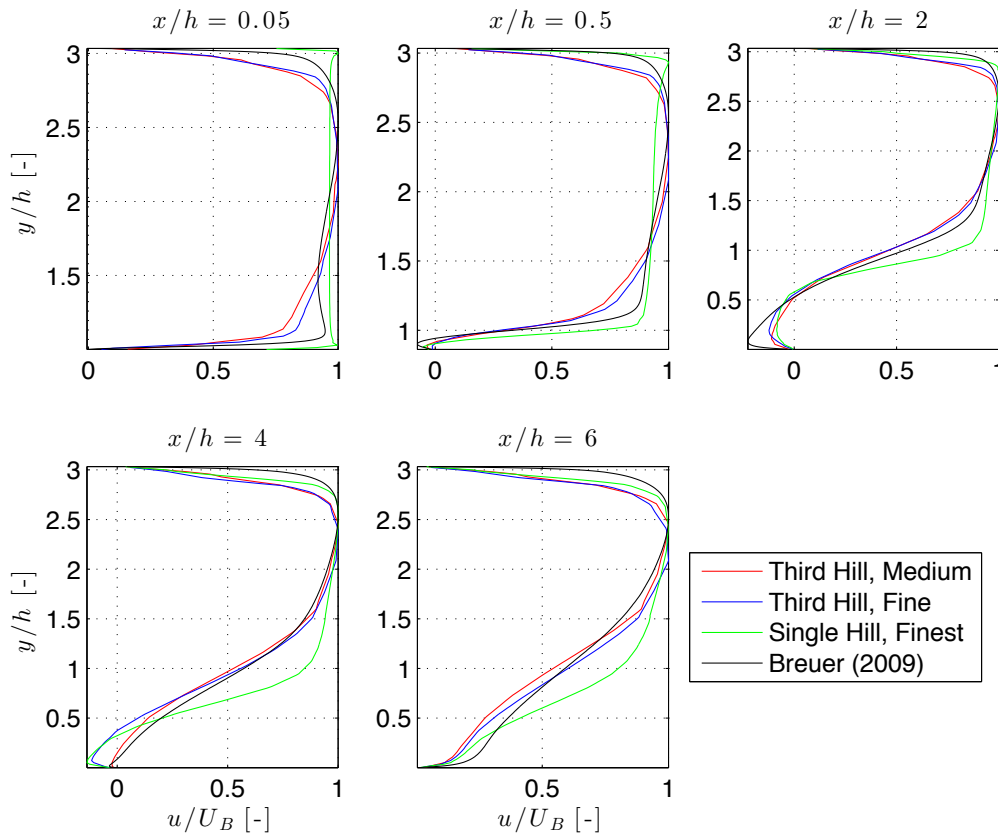
Another insight that can be derived from this data is that the flow over the fourth hill deviates from the aforementioned inverse relationship between separation and reattachment location [Temmerman et al. \(2003\)](#), and does so consistently for both grid resolutions. This is indeed a very promising result: it shows that both the separation as well as the reattachment locations converge to the benchmark data with each consecutive hill. While this trend might lead to a reattachment location that is too far upstream in case of the medium mesh, it is clear that this will be less so for the fine mesh, and will eventually lead to matching results for increasing grid resolutions.



**Figure 6.13:** Averaged values of  $u$  at the first off-wall voxel position, lower boundary, mid-span, quintuple hill geometry. The zero-crossings (transition to/from backflow) yield an indication to the separation and reattachment locations.

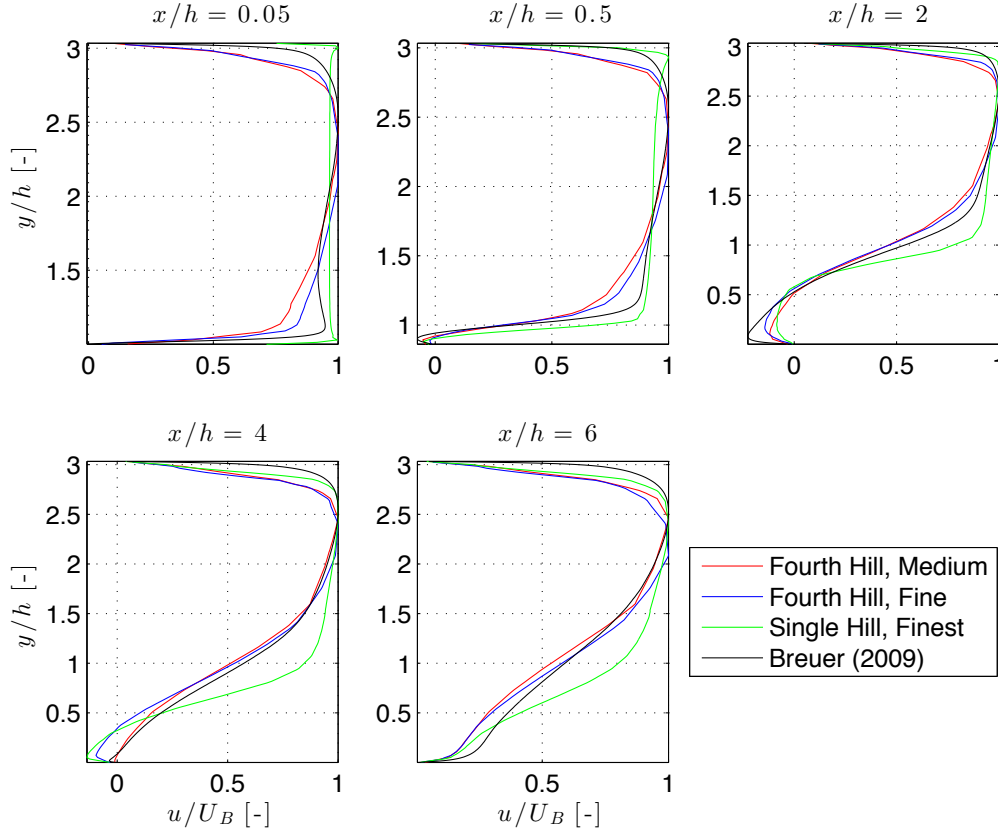
**Table 6.5:** Comparison of approximated separation and reattachment locations for the quintuple hill geometry with those obtained by Breuer et al. (2009). The single hill data is repeated from Table (6.2) for the reader's convenience.

Case	Separation Point [ $x/h$ ]	Reattachment Point [ $x/h$ ]
Breuer et al. (2009)	0.19	4.69
Single Hill, Medium	0.361	4.566
Third Hill, Medium	0.298	4.887
Fourth Hill, Medium	0.286	4.715
Single Hill, Fine	0.352	5.032
Third Hill, Fine	0.240	5.340
Fourth Hill, Fine	0.234	5.293



**Figure 6.14:** Comparison of the streamwise-velocity profiles downstream of the third hill in the quintuple hill geometry with those obtained by Breuer et al. (2009) at six streamwise positions, mid-span.

The streamwise velocity profiles over, and downstream of, the third and fourth hill are displayed in Figures (6.14) and (6.15), along with the reference data from Breuer et al. (2009) as well as the data from the single hill configuration. Clearly, the flow over the downstream



**Figure 6.15:** Comparison of the streamwise-velocity profiles downstream of the fourth hill in the quintuple hill geometry with those obtained by Breuer et al. (2009) at six streamwise positions, mid-span.

hills has a much smaller discrepancy with respect to the results from Breuer et al. (2009) than does the flow of the single hill configuration. One exception to this behavior is noted at the upper wall, where the flow field of the single hill configuration is in closest accordance with the reference data. This deviation from the general trend could be explained by the fact that the presence of the hills does not influence the flow field at the upper wall. In other words, the evolution of the boundary layer at the upper wall is strongly influenced by the inlet conditions, such that there is no evident reason for the flow field to converge to the reference solution further downstream.

## 6.7 Alternative Turbulence Model

All results discussed in the previous sections were obtained using a  $k - \epsilon$  turbulence model, since this is the only one that can be readily accessed in the PowerFLOW simulation software. Nonetheless, it is possible to force PowerFLOW to adapt an Implicit LES (ILES).

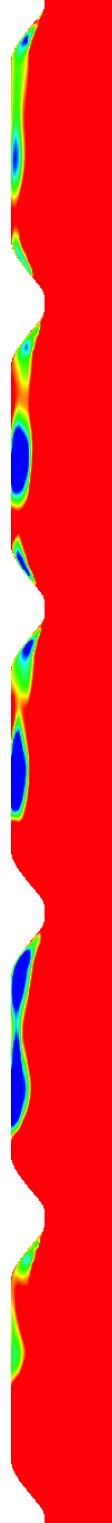
This section very briefly evaluates whether the use of this ILES model can improve the accurateness of the simulation. Figures (6.16) - (6.17) map the average streamwise velocity field and the corresponding streamlines for the central three hills. Clearly the ILES model introduces very different flow behavior, which is by no means in better correspondence with the benchmark data.

## 6.8 Conclusions

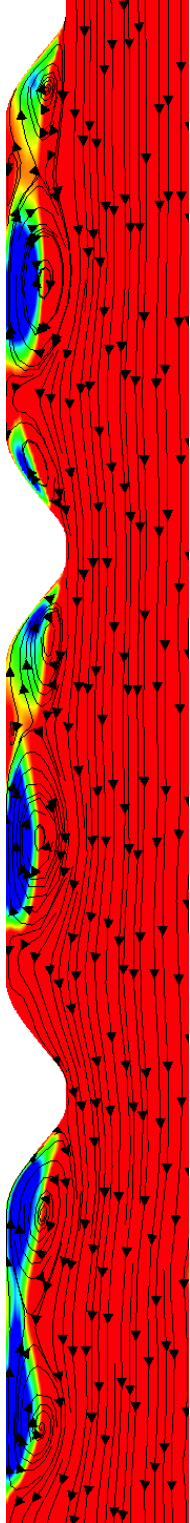
The results obtained from the quintuple hill geometry indicate that, should PowerFLOW offer the possibility to model the exact boundary conditions, the resulting flow field would be likely to approach the reference data. These findings positively confirm the hypothesis that was put forward in Section 6.4.

Once the boundary conditions are modeled correctly, the results are mainly influenced by the grid size. In that respect, it was shown that the results for the medium to finest grids are already in good agreement with the reference data, taking into account the discrepancies introduced by the inlet conditions. Given that the number of voxels used in these grids is still much smaller than that required for a DNS, it can be concluded that the turbulence model incorporated in PowerFLOW is able to simulate the fluid flow over geometries with smooth curvatures with good accuracy. An additional investigation into the performance of an implicit turbulence model showed that it is not advisable to switch to such ILES model for this type of simulations.

The results for the wall model are less conclusive. While it was shown that the boundary-layer behavior along the curved surface is already strongly altered for low values of  $10 < y^+ < 15$ , there has been no fundamental investigation into the effect of the wall model on the boundary-layer development along a flat plate. Given the preliminary results presented in this chapter, it is advised to keep  $y^+ < 5$ , especially for geometries with strong concave curvatures.



**Figure 6.16:** Snapshot of the average streamwise velocity  $u$  (levels between  $-0.3$  and  $0$  m/s), quintuple hill geometry, medium mesh, ILES turbulence model, mid-span.



**Figure 6.17:** Snapshot of the average streamwise velocity  $u$  (levels between  $-0.3$  and  $0$  m/s) superimposed with a selection of streamlines, quintuple hill geometry, medium mesh, ILES turbulence model, mid-span.

---

## Chapter 7

---

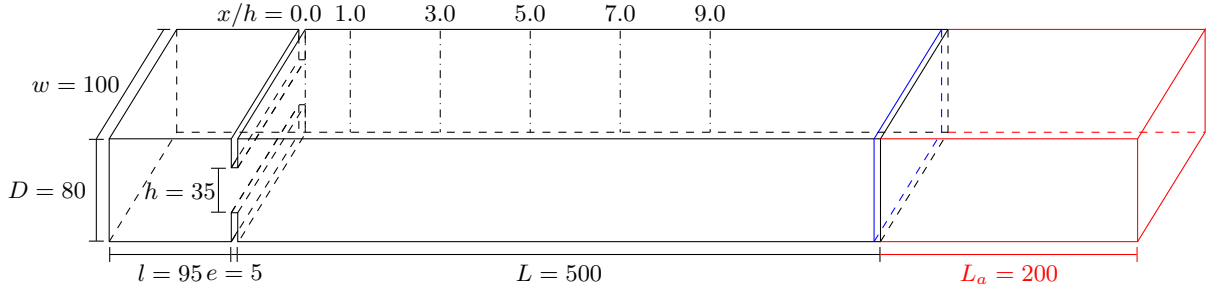
# Validation of PowerFLOW Acoustic Model

The Lattice Boltzmann Method (LBM) is widely acknowledged for its capability to accurately model unsteady fluid flows, an essential prerequisite for aeroacoustic simulations. Extensive research by [Marié et al. \(2009\)](#) also showed that the Lattice Bhatnagar-Gross-Krook collision model (LBGK) has better dissipation capabilities overall, and better dispersion capabilities than a second-order in space, three-step Runge-Kutta in time classical finite-difference scheme (see Chapter 5). This chapter investigates whether PowerFLOW is able to accurately capture the aeroacoustic characteristics of an internal flow field by performing a case study on a single diaphragm flow. Given the sudden expansion/contraction associated with the diaphragm geometry, it is directly related to the flow field through the upper airway; consider, amongst other geometrical features, the expansion at the inlet of the oral cavity and the expansion/contraction in the vicinity of the laryngeal ventricle.

First, Section 7.1 includes a concise description of the case geometry. Next, Sections 7.2 - 7.3 elaborate on the boundary conditions and the benchmark data, respectively. Section 7.4 then presents an extensive discussion concerning the results of a grid convergence study. Finally, Section 7.5 thoroughly evaluates the aeroacoustic characteristics of the flow field, including a further examination of the workings of the turbulence model, a consideration of nonreflecting boundary conditions, and a directivity analysis.

### 7.1 Case Geometry

The diaphragm geometry is shown in Figure (7.1). Following an inlet section of  $l \times D \times w = 95 \times 80 \times 100 \text{ mm}^3$ , a single diaphragm is positioned. This diaphragm has an aperture of  $h = 35 \text{ mm}$  and extends for  $e = 5 \text{ mm}$ . With a length of  $L = 500 \text{ mm}$ , the outlet section is long enough to allow an unobstructed evolution of the disturbed flow field coming from the diaphragm aperture. This particular geometry was chosen to allow verification of the results with those obtained by [Piellard and Bailly \(2010\)](#) and [Gloerfelt and Lafon \(2008\)](#).



**Figure 7.1:** Three-dimensional view of the simulated diaphragm model. The additional outlet is designated in **red**, while the acoustic measurement plane is shown in **blue**. The  $(-\cdot-)$  lines indicate the streamwise position of the measurement locations.

## 7.2 Boundary Conditions

A uniform velocity field with  $u = 6$  m/s is specified at the inlet, while the outlet is modeled with a zero static pressure boundary condition. All walls are considered to have a no-slip boundary condition.

The acoustic simulations require the additional specification of a Nonreflecting Boundary Condition (NRBC), which will be further explained in Section 7.5.

## 7.3 Description of the Reference Data

The acoustic spectra discussed in Section 7.5 are compared with those obtained from a Direct Noise Computation (DNC) performed by [Gloerfelt and Lafon \(2008\)](#). In order to accurately capture and propagate the low-energy acoustic perturbations, numerical schemes were applied that minimize numerical dispersion and dissipation (see Chapter 5). A new explicit 10-point-stencil finite-difference scheme was applied in combination with a staggered arrangement of the conservative variables to increase its robustness. Temporal discretization was achieved using an explicit six-step fourth-order Runge-Kutta method. The Large Eddy Simulation (LES) model uses explicit selective filtering without an additional eddy-viscosity model as a means to prevent grid-to-grid oscillations.

Computations were performed on a non-uniform Cartesian grid (stretching occurs towards the walls and the open sections) with  $345 \times 115 \times 101$  cells, while the chosen time step corresponded to a maximum CFL number of 0.9. With regard to the boundary treatment, reflection of acoustic waves at the outlet was minimized through the combined use of a 1D characteristic boundary condition and sponge zones. The inlet velocity was set to  $u = 6$  m/s, while atmospheric pressure conditions were imposed at the outlet using a corrective term of the form  $\alpha(p - p_\infty)$  as to minimize reflection. All walls were modeled with no-slip conditions.



The pressure perturbations were measured at 12 streamwise locations positioned both upstream and downstream of the diaphragm, which allowed a further investigation of the flow development and its impact on the measured acoustic spectra. The benchmark spectrum presented in Section 7.5 was obtained by averaging the measurements from 10 sensors (spaced evenly along the span) positioned at the lower wall, 1.5 m downstream of the diaphragm.

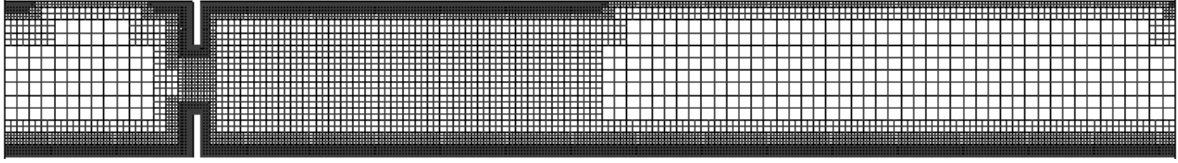
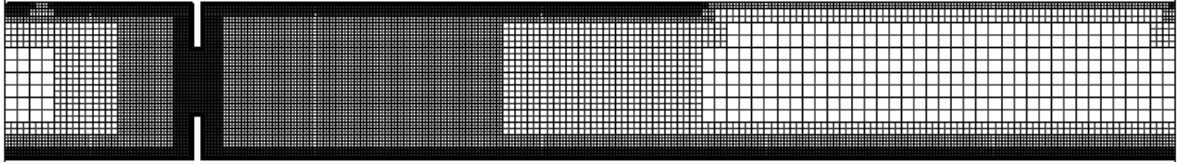
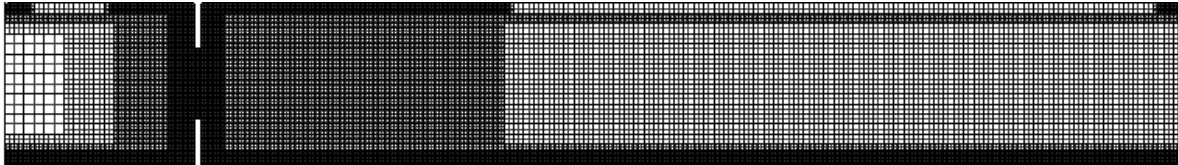
Instantaneous velocity and vorticity fields presented in Section 7.4 are also compared with data from [Gloerfelt and Lafon \(2008\)](#). Because these snapshots are not accompanied with corresponding fluid profiles, however, those were taken from a different paper by [Piellard and Bailly \(2010\)](#). Here, four different flow solutions (including 2D and 3D incompressible Fluent computations, a 3D incompressible OpenFOAM calculation, and a 3D compressible simulation using Argo) were compared with the aforementioned DNC performed by [Gloerfelt and Lafon \(2008\)](#). Out of these four cases, the 3D incompressible Fluent 6.3 code was shown to provide the best correspondence with the DNC data, hence the reason for adopting it as the benchmark solution in this chapter. The simulation was carried out on a mesh with 8 million cells, structured with finest cells downstream of the diaphragm of the order  $h/70$ . Central differencing was used for the discretization of the momentum equation, PRESTO! for the pressure question, and the pressure-velocity coupling was taken into account via a PISO scheme. The chosen time step corresponded to a maximum CFL number of 0.78.

## 7.4 Fluid Simulations

A first important issue that needs to be addressed is the choice of grid. To this end, a grid convergence study has been performed using the three grids shown in Figure (7.2). With a total of  $7.157 \times 10^6$  (200),  $7.789 \times 10^6$  (200) and  $13.630 \times 10^6$  (250) cells these grids are henceforth referred to as coarse, medium, and fine mesh, respectively. Similar to the grid presentation in Chapter 6, the values between brackets represent the number of voxels along a characteristic length, the latter which is equal to  $D = 80$  mm. The main difference between the coarse and medium mesh is the increase of resolution in the region around the diaphragm aperture, including part of the inlet and a considerable length of the outlet. In the fine mesh, the resolution of the entire diaphragm has been increased with 25 %, with the resolution of the outlet being additionally doubled to investigate the evolution of the flow structures towards the outlet and their interaction with the diaphragm jet. All meshes include five Variable Resolution (VR) regions, see Table (7.1).

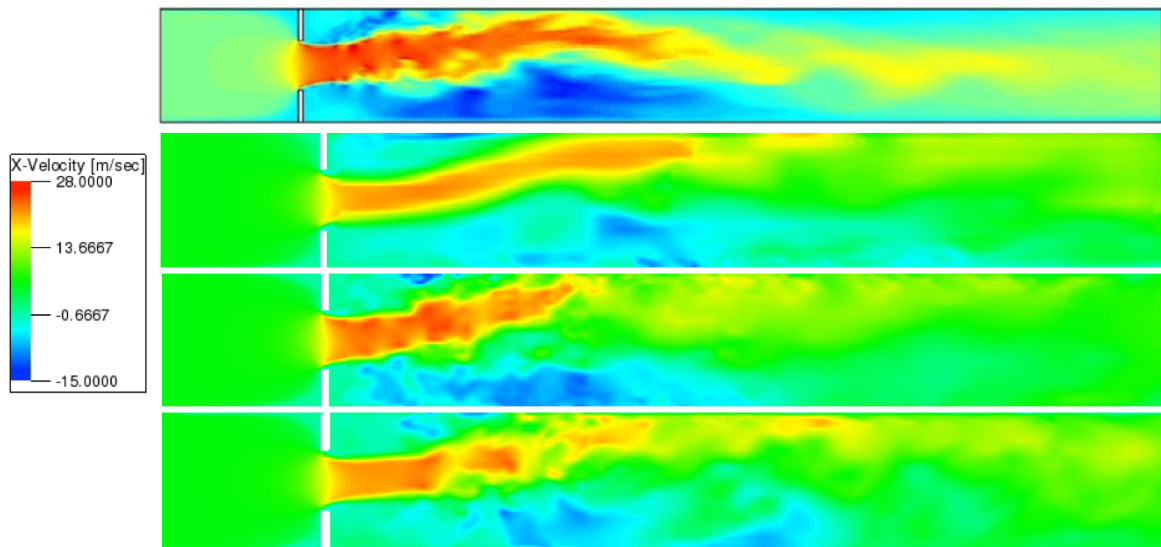
**Table 7.1:** Voxel sizes (in mm) associated with the VR regions used in the diaphragm meshes.

VR	Coarse	Medium	Fine
4	0.4	0.4	0.32
3	0.8	0.8	0.64
2	1.6	1.6	1.28
1	3.2	3.2	2.56
0	6.4	6.4	5.12

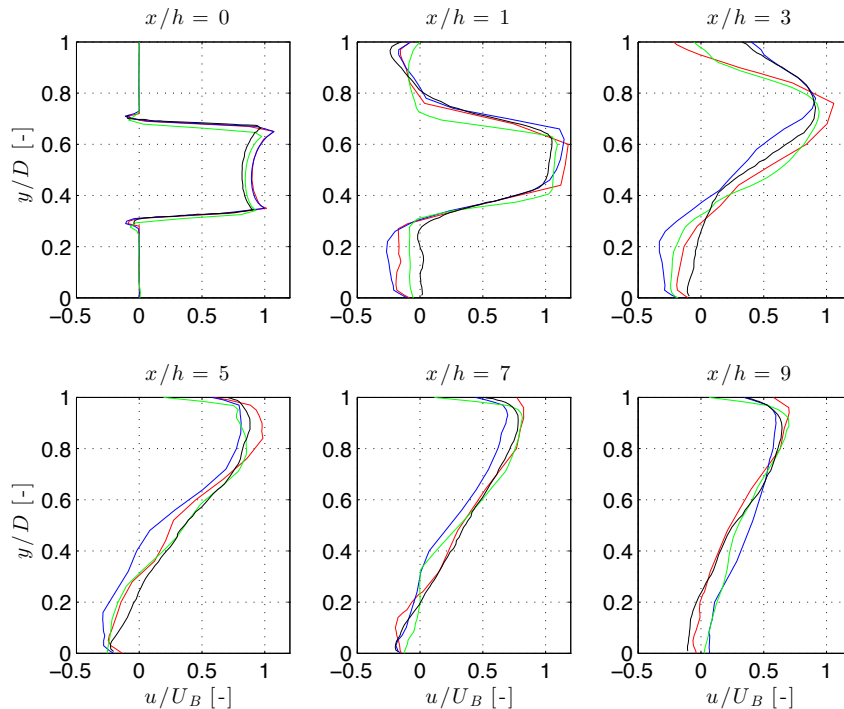
(a) Coarse mesh,  $7.157 \times 10^6$  voxels,  $\Delta/D = 0.005$ (b) Medium mesh,  $7.789 \times 10^6$  voxels,  $\Delta/D = 0.005$ (c) Fine mesh,  $13.630 \times 10^6$  voxels,  $\Delta/D = 0.004$ **Figure 7.2:** Grids used in the diaphragm grid convergence study.

The instantaneous streamwise, crossflow, and spanwise velocity fields at mid-span are compared with those obtained by [Gloerfelt and Lafon \(2008\)](#) in Figures (7.3), (7.5) and (7.7), respectively. Prior to drawing any conclusions it should be mentioned that these figures represent instantaneous results which can differ significantly between time steps, given the inherent unsteadiness of the flow field. Also, the results for the medium and fine mesh have been mirrored about the  $y$ -axis to allow a better comparison with the reference data. Note that this causes them to have a reversed color scaling in the comparison of crossflow velocities.

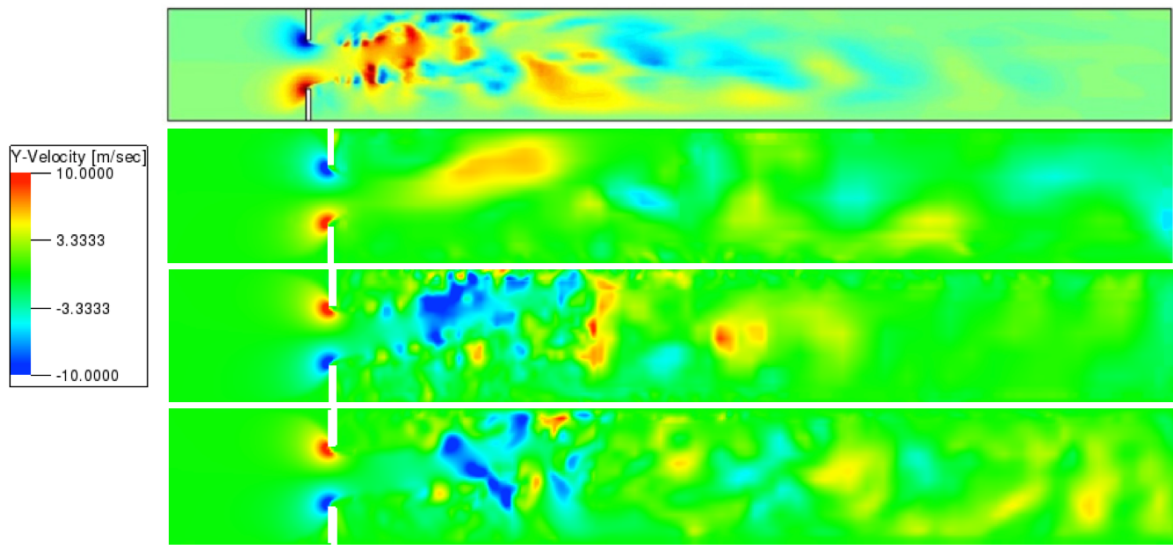
The streamwise velocity fields clearly show similar patterns. Asymmetry of the jet, a feature which can be attributed to the Coanda effect, causes it to impinge on the upper or lower wall of the outlet, with both solutions being equally valid [Piellard and Bailly \(2010\)](#). With regard to the actual attachment location of the jet it can be observed that the medium and fine meshes perform significantly better than the coarse mesh. None of the computational grids was however able to resolve the detachment of the jet further downstream. Given the high values of  $5 \leq y^+ \leq 45$  at the upper wall, even for the fine mesh, one reason for this discrepancy might be the inability of the PowerFLOW wall model to correctly resolve the breakdown of the jet structures that takes place near the wall [Gloerfelt and Lafon \(2008\)](#). A Direct Numerical Simulation (DNS) of the diaphragm case could provide the data required to validate this hypothesis but was not performed due to time constraints and limited access to processing power.



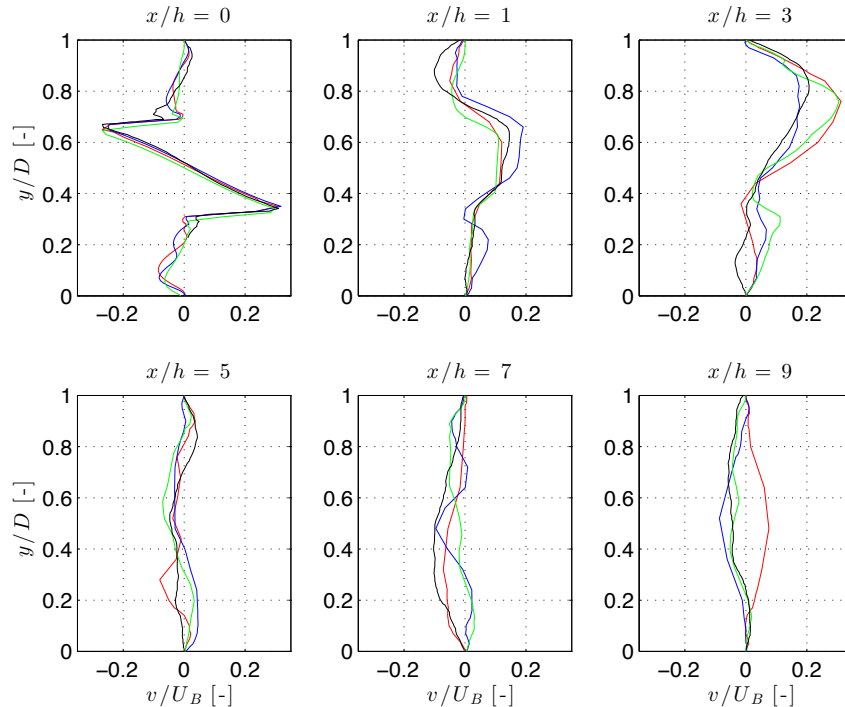
**Figure 7.3:** Comparison of the instantaneous longitudinal velocity  $u$  (levels between -15 and 28 m/s), mid-span. From top to bottom: Gloerfelt and Lafon (2008), coarse mesh, medium mesh, fine mesh.



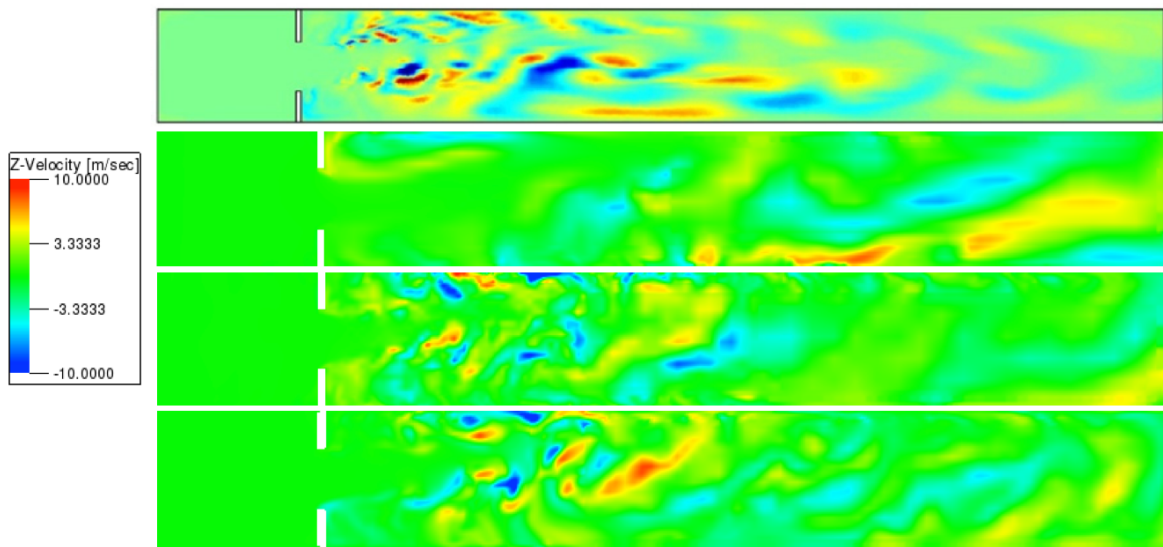
**Figure 7.4:** Comparison of the averaged streamwise-velocity profiles at six streamwise positions, mid-span. Red: coarse mesh, blue: medium mesh, green: fine mesh, black: reference data Piellard and Bailly (2010).



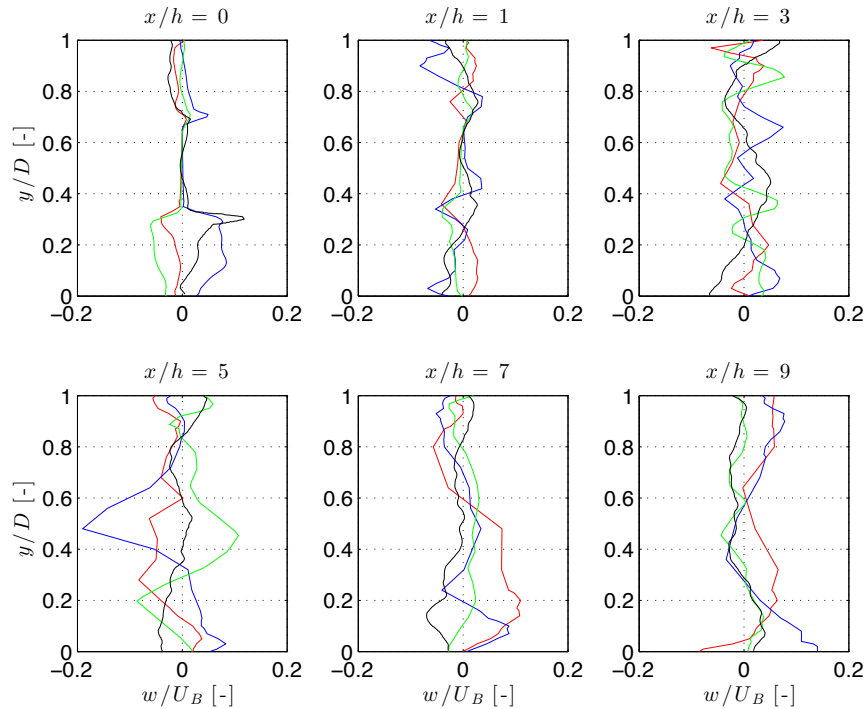
**Figure 7.5:** Comparison of the instantaneous crossflow velocity  $v$  (levels between -10 and 10 m/s), mid-span. From top to bottom: Gloerfelt and Lafon (2008), coarse mesh, medium mesh, fine mesh.



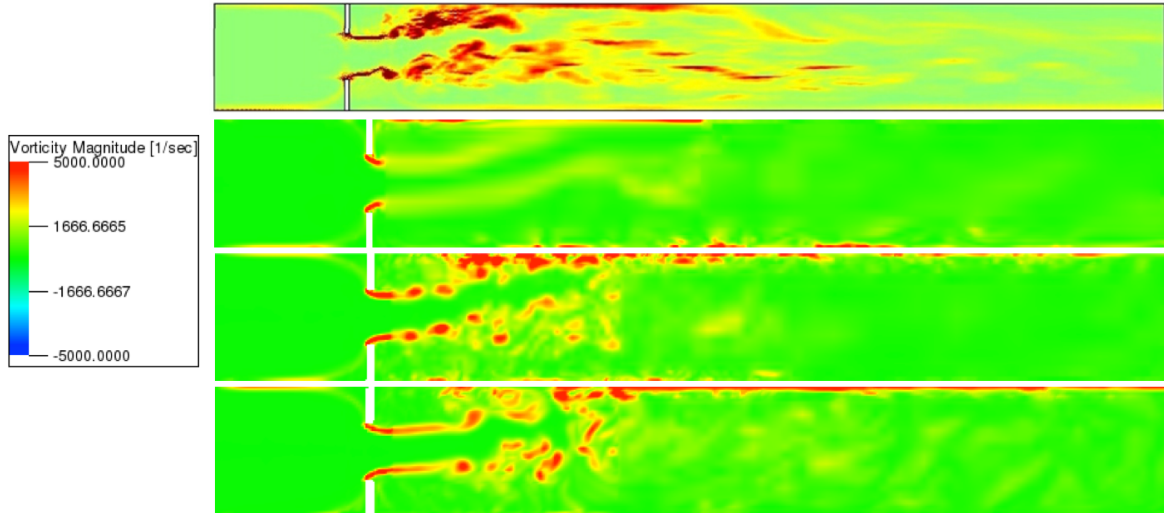
**Figure 7.6:** Comparison of the averaged crossflow-velocity profiles at six streamwise positions, mid-span. Red: coarse mesh, blue: medium mesh, green: fine mesh, black: reference data Piellard and Bailly (2010).



**Figure 7.7:** Comparison of the instantaneous spanwise velocity  $w$  (levels between -10 and 10 m/s), mid-span. From top to bottom: Gloerfelt and Lafon (2008), coarse mesh, medium mesh, fine mesh.



**Figure 7.8:** Comparison of the averaged spanwise-velocity profiles at six streamwise positions, mid-span. Red: coarse mesh, blue: medium mesh, green: fine mesh, black: reference data Piellard and Bailly (2010).



**Figure 7.9:** Comparison of the instantaneous vorticity magnitude  $\|\omega\|$  (levels between  $-5,000$  and  $5,000 \text{ s}^{-1}$ ), mid-span. From top to bottom: [Gloerfelt and Lafon \(2008\)](#), coarse mesh, medium mesh, fine mesh.

Two other dissimilarities between the flow fields are worth noticing. Firstly, the extension of the jet towards the outlet is limited, which is most likely due to an insufficient grid refinement in that region. Secondly, although the recirculation region appears to be less pronounced this is solely due to a slight difference in color scaling: the averaged streamwise velocity profiles in Figure (7.4) indicate that the backflow levels are comparable to the benchmark data presented by [Piellard and Bailly \(2010\)](#).

Both the crossflow and spanwise velocity fields produced by the medium and fine meshes can be argued to show a sufficient amount of detail, except in that region directly behind the diaphragm aperture. Moreover, the data compares well in terms of maximum and minimum velocity strengths reached. Most importantly, the results clearly indicate that the flow field is underresolved for the coarse mesh, while the results for the medium and fine meshes are comparable.

A final property that can be used to verify the correctness of the simulation data is the instantaneous vorticity magnitude  $\|\omega\|$ , see Figure (7.9). The coarse mesh only attained low vorticity levels in the diaphragm wake, which is most likely due to the enhanced numerical dissipation levels associated with coarse voxel sizes. On the other hand, the medium and fine meshes show vorticity levels that are comparable to those obtained by [Gloerfelt and Lafon \(2008\)](#). Nevertheless, even these finer meshes were not able to accurately resolve the mixing process in the shear layer (which is initialized by Kelvin-Helmholtz instabilities). Moreover, the regions of increased vorticity are shown to have a larger downstream extent in case of the benchmark data.

As an additional means to study the effect of grid resolution on the fluid flow, Figures (7.4), (7.6), and (7.8) compare averaged fluid profiles for the streamwise, crossflow, and spanwise

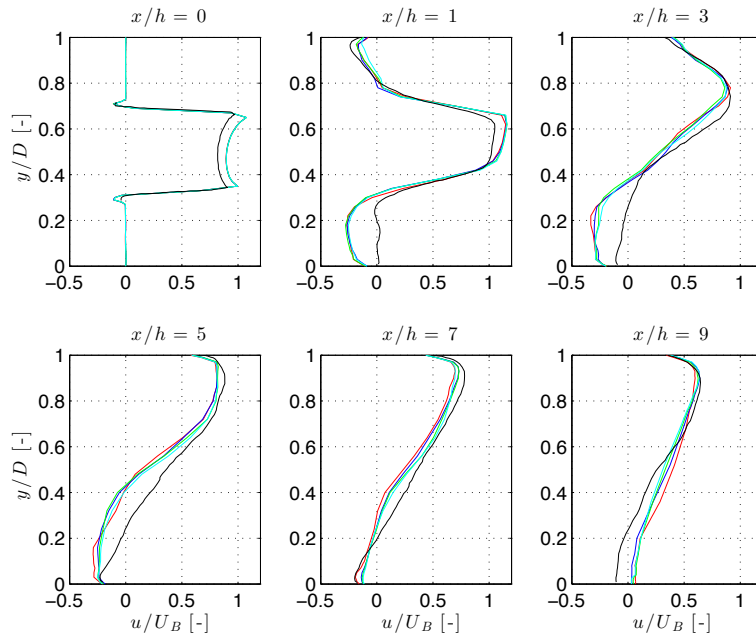


velocities, respectively, with those obtained by Piellard and Bailly (2010). Although the streamwise and crossflow velocity profiles show similar behavior compared to the benchmark data, there appears to be no clear convergence with increasing grid resolution.<sup>1</sup> This observation is not in accordance with the trends derived from the instantaneous data, and the discrepancies might be attributed to a number of different aspects (listed by decreasing importance):

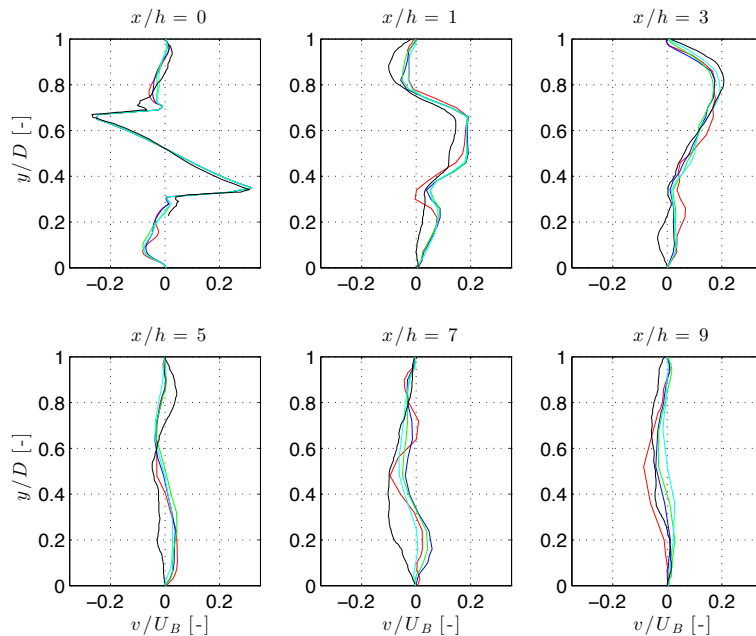
- Although the computational grids have been constructed in a symmetrical fashion it can be seen in Figure (7.2) that they are not symmetrical about the  $y$ -axis. Since this has a negative impact on the overall grid quality (especially at the upper wall), it reduces the effectiveness of an increased grid resolution, hence resulting in a slower-than-expected convergence rate.
- Given the strong unsteadiness of the flow field, averages should be taken over a sufficiently long time span in order to smoothen the results. The average results presented here have been acquired in two steps:
  1. The results are averaged in PowerFLOW itself in order to limit the required storage space. In general, PowerFLOW advises to match the averaging interval  $\Delta$  with the measurement period  $P$ . In the current simulations however,  $\Delta = 1000$  and  $P = 5000$ , thereby forgoing the opportunity to include an additional 4000 timesteps in each averaged timeframe.
  2. The averaged results output by PowerFLOW are further averaged over a number of consecutive timeframes (TF). As shown in Figures (7.10) - (7.11), the amount of timeframes included in this average impacts the resulting fluid profiles, especially for the crossflow velocities. Because the fluid profiles display a convergent behavior with increasing number of TFs, it is advisable to include as many timeframes as possible. However, the fluid profiles presented here have been averaged for a similar amount of physical time across the different simulations, and given the limited data available for the finest mesh, the results were only averaged over 0.083 s.
- The grid convergence study presented here did not only comprise of an overall increase in grid resolution, but also included the introduction of local refinement regions. It is possible that shifting the relative position of the VR regions impacted the overall flow field in such a way that the expected convergence towards the (average) benchmark data is obscured.

From the previous analysis it can be concluded that the medium mesh is the most appropriate one to use in further analyses. It clearly performs better than the coarse mesh in terms of resemblance with the results of Gloerfelt and Lafon (2008), while the small differences with respect to the fine mesh do not justify the doubled computational cost associated with the latter.

<sup>1</sup>According to Piellard and Bailly (2010): ‘Spanwise velocity profiles show very different behaviors from one simulation to the other, in terms of shape as well as in terms of levels (...) nothing has been published regarding the spanwise velocity evolution’. Consequently, the spanwise velocity profiles were merely included for the sake of completeness, since they offer no further insight into the accuracy of the simulation.



**Figure 7.10:** Comparison of the averaged streamwise-velocity profiles at six streamwise positions, medium mesh, mid-span. **Red:** TF 9 - 12 (0.083 s), **blue:** TF 9 - 16 (0.193 s), **green:** TF 9 - 20 (0.303 s), **cyan:** TF 9 - 27 (0.495 s), **black:** reference data [Piellard and Bailly \(2010\)](#).

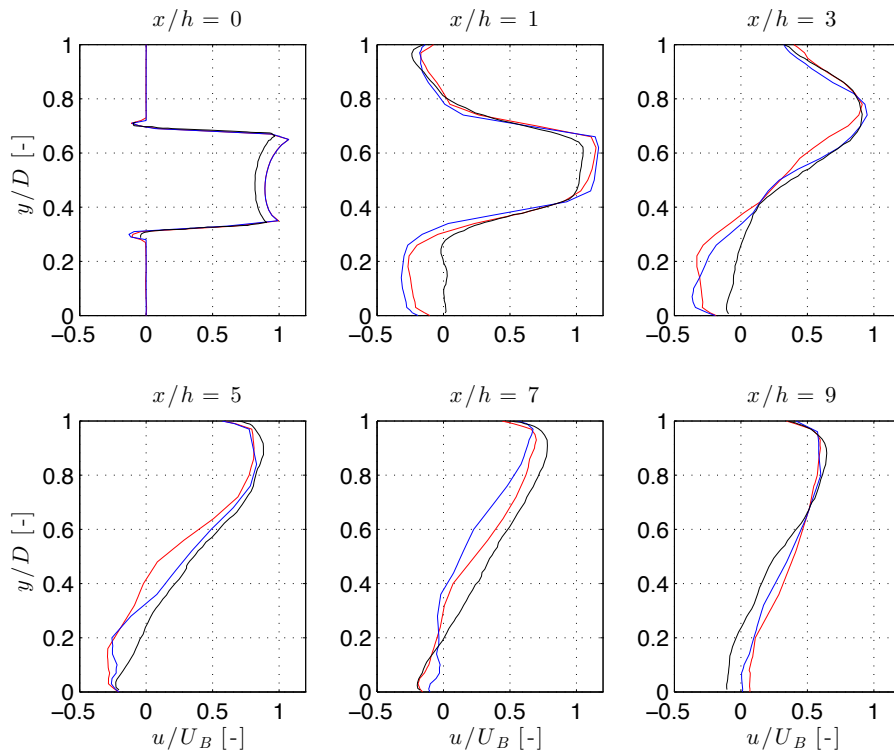


**Figure 7.11:** Comparison of the averaged crossflow-velocity profiles at six streamwise positions, medium mesh, mid-span. **Red:** TF 9 - 12 (0.083 s), **blue:** TF 9 - 16 (0.193 s), **green:** TF 9 - 20 (0.303 s), **cyan:** TF 9 - 27 (0.495 s), **black:** reference data [Piellard and Bailly \(2010\)](#).



### Alternative Turbulence Model

Similar to Section 6.7, this subsection investigates whether the use of an Implicit LES (ILES) turbulence model can improve the accurateness of the simulation. Since the flow unsteadiness and the difference in jet direction between both cases make it difficult to compare spanwise and crossflow velocities, only the streamwise velocity fields and the vorticity levels are considered as indicators for the simulation accurateness. Figure (7.12) shows that the evolution of the streamwise velocity is very similar for both turbulence models. Moreover, the actual magnitude of the streamwise velocity reaches similar levels, as indicated in Table (7.2).

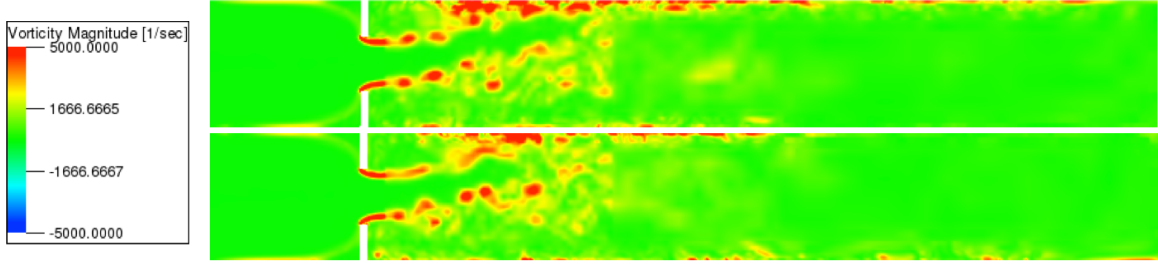


**Figure 7.12:** Comparison of the averaged streamwise-velocity profiles at six streamwise positions, medium mesh, mid-span. Red:  $k-\epsilon$ , blue: ILES, black: reference data Piellard and Bailly (2010).

**Table 7.2:** Streamwise velocity magnitudes in m/s at six streamwise positions as simulated by the  $k-\epsilon$  and ILES turbulence models.

$x/h$	0.0	1.0	3.0	5.0	7.0	9.0
$k-\epsilon$	12.84	22.64	18.91	15.55	12.02	10.89
ILES	12.82	22.93	18.71	15.89	12.05	10.98

Upon comparison of the vorticity levels, see Figure (7.13), it may be concluded that the  $k-\epsilon$  turbulence model is able to generate more vorticity around the point of jet impingement than the ILES turbulence model. Although this might seem contradictory, it can be argued that the influence of the ILES model is only minor in this particular case due to the acuteness of the separation process - i.e., sudden expansion.



**Figure 7.13:** Comparison of the instantaneous vorticity magnitude  $\|\omega\|$  (levels between -5,000 and  $5,000 \text{ s}^{-1}$ ) as simulated by the  $k - \epsilon$  (top) and ILES (bottom) turbulence model, mid-span.

Based on these results it can be concluded that there exist no clear advantages in switching turbulence models. Hence, all further simulations in this chapter incorporate the standard PowerFLOW  $k - \epsilon$  turbulence model.

## 7.5 Aeroacoustic Simulations

Now that decisions have been made regarding the most efficient grid as well as the most appropriate turbulence model, focus can be shifted towards the acoustic aspects of the diaphragm test case. An important realization is that the previous simulation data cannot be used directly for the purpose of acoustic analysis since it was acquired at an accelerated Mach number<sup>2</sup> ( $M$ ). Therefore, the first step was to investigate the influence of different Mach number settings on the flow field, and by extension their influence on the acoustic spectra. This matter is closely examined in Subsection 7.5.1. Subsection 7.5.2 then elaborates on the acoustic test case geometries as well as the location of the acoustic probes. Finally, Subsection 7.5.3 compares the Sound Pressure Levels (SPL) measured by the microphones with reference data from [Gloerfelt and Lafon \(2008\)](#).

### 7.5.1 Mach Number: Chosen by PowerFLOW versus Same as Experiment

The grid convergence study described in Section 7.4 was carried out with the **Mach number Chosen by PowerFLOW** (CbP) setting. This specific setting allows the user to accelerate simulations, i.e., reduce computational cost, through an increase in  $M$ . To this author's knowledge, PowerFLOW achieves this higher  $M$  by increasing the timestep  $\Delta t$ , which in turn causes a reduction in the speed of sound because these parameters are related according to:

$$c_{0,ph} = c_{0,la} \frac{\Delta x}{\Delta t}, \quad (7.1)$$

<sup>2</sup>In PowerFLOW this setting corresponds to a Mach number **Chosen by PowerFLOW**, which speeds up the simulation. For aeroacoustic simulations PowerFLOW advises to set  $M$  to **Same as Experiment**.

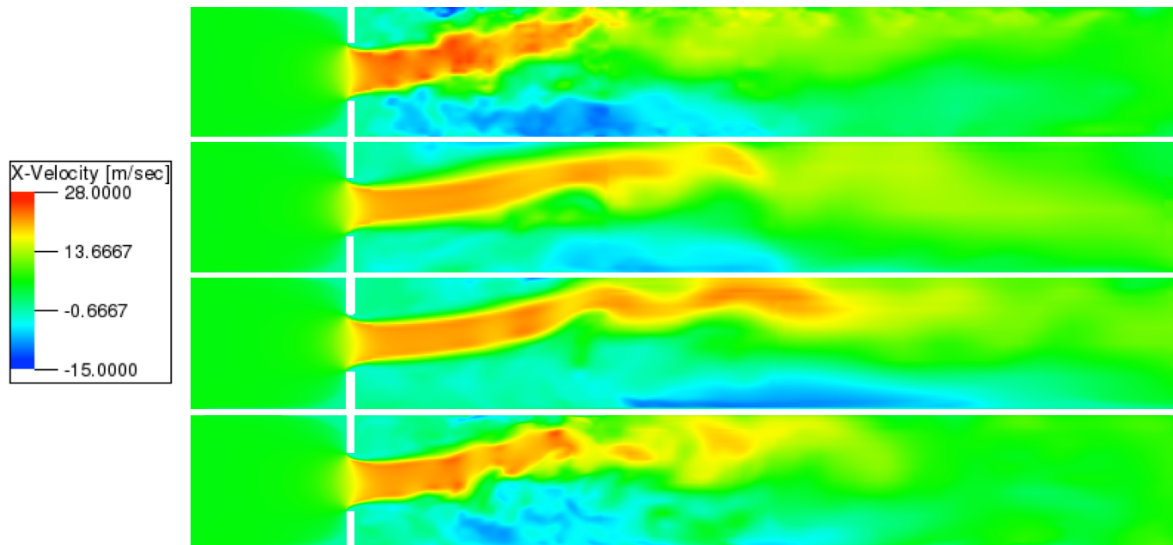
where the subscripts  $ph$  and  $la$  denote the physical and lattice speed of sound, respectively [Viggen \(2014\)](#). Naturally, the change in the lattice speed of sound alters the propagation speed of acoustic waves ( $v = u \pm c_0$ ) as they travel through the computational domain. Since this change in simulation conditions will impact the resulting acoustic spectra (see Chapter 5), it is preferable to match the simulated  $M$  with that which would be encountered during experiment. This can be achieved in PowerFLOW by changing the Mach number setting to `Mach number Same as Experiment (SaE)`. It is noted here that, to this author's knowledge, only [Van Herpe et al. \(2012\)](#) conducted a numerical investigation into the effect PowerFLOW's Mach number settings, the results of which confirmed that the speed of sound is indeed decreased when adopting the CbP setting.

The issue that will be addressed here is whether the change in Mach number settings also influences the actual flow field, i.e., whether a reduction in  $M$  (CbP  $\rightarrow$  SaE,  $\downarrow \Delta t$ ,  $\uparrow c_0$ ) impacts the amount of acoustic sources that are resolved by a given grid. Should this be the case, the question rises whether the reasoning behind the grid choice in Section 7.4 remains valid.

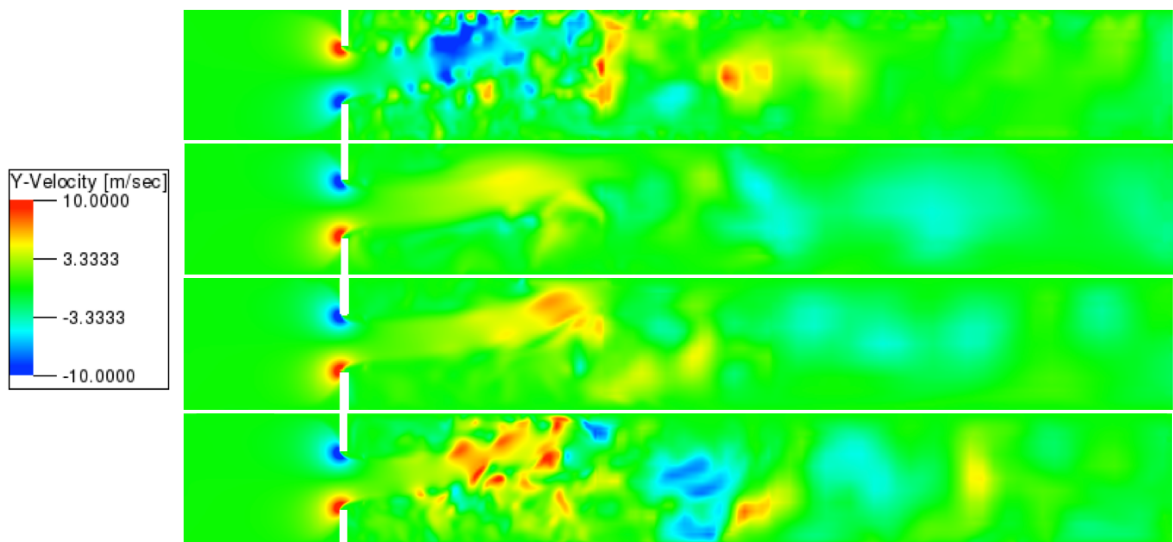
Figures (7.14) - (7.17) quantitatively compare the flow fields obtained using the medium grid (CbP) with those acquired from aeroacoustic simulations on both the medium, fine, and newly created finest grid<sup>3</sup> ( $26 \times 10^6$  voxels, roughly twice the amount of voxels used in the fine mesh). It can be clearly observed that equal grids do not produce similar levels of detail in the CbP and SaE flow fields. Even the fine grid (SaE) is unable to approach the amount of flow structures that are resolved by the medium grid (CbP). With regard to the medium/fine mesh (SaE), Figure (7.14) reveals that the location where the jet attaches to the upper wall is shifted downstream. The crossflow and spanwise velocity fields presented in Figures (7.15) - (7.16) further indicate that the resolved flow structures are larger compared to the CbP case, while the vorticity levels displayed in Figure (7.17) confirm that the mixing process that is expected to occur in the shear layer remains largely underresolved.

From these observations it can be concluded that the Mach number settings strongly influence the amount of flow details that can be resolved on a given grid. Based on the results of the finest grid (SaE), it could be argued that there has to be a three- to fourfold increase in the number of voxels when going from CbP to SaE settings in order to resolve similar levels of flow structures. Because it is expected that this voxel ratio will be dependent on the underlying flow type, it is considered more relevant to perform grid convergence studies with the SaE setting when dealing with aeroacoustic simulations. Unfortunately, it was not possible to perform such additional study (beyond the finest mesh) due to time restrictions. Because this process will be equally (or more) time-consuming when dealing with the upper airway geometry, Subsection 7.5.3 contains a discussion on whether the acoustic spectra obtained with the CbP setting can be rescaled in accordance with the physical Mach number. If this would be possible, it would allow for all further simulations to be run with CbP settings, thereby significantly reducing the computational cost.

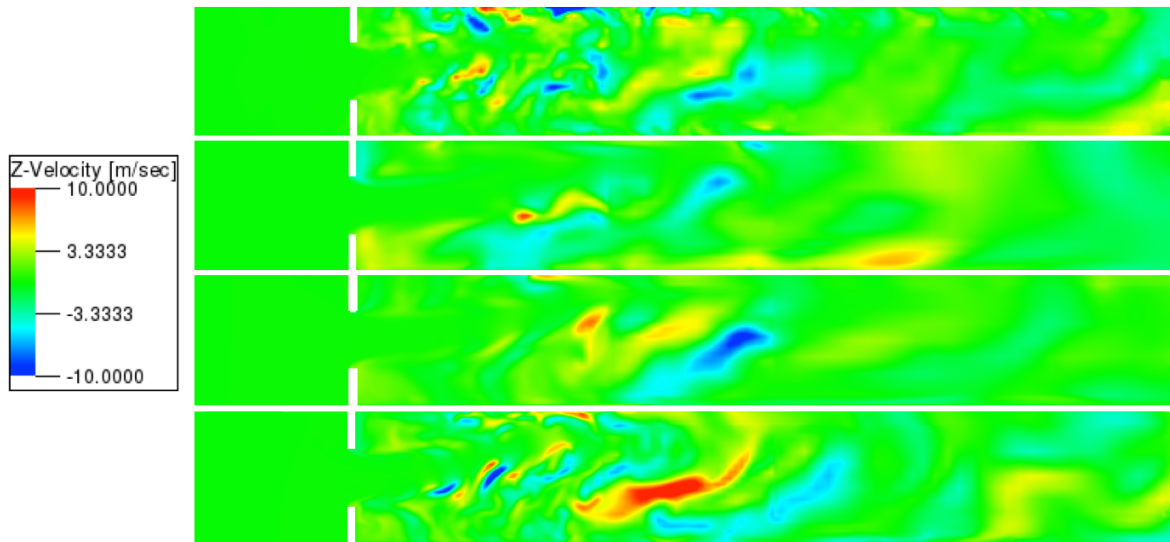
<sup>3</sup>Although unanticipated at the start of the test case (hence the reason for not mentioning the grid in the earlier sections), the results provided by the finest grid proved to be of great relevance in the discussion of the aeroacoustic results. This will become increasingly obvious towards the end of this chapter. Also note that the finest mesh has the same lay-out as the fine mesh, but with an increased resolution of 350 (voxels/characteristic length).



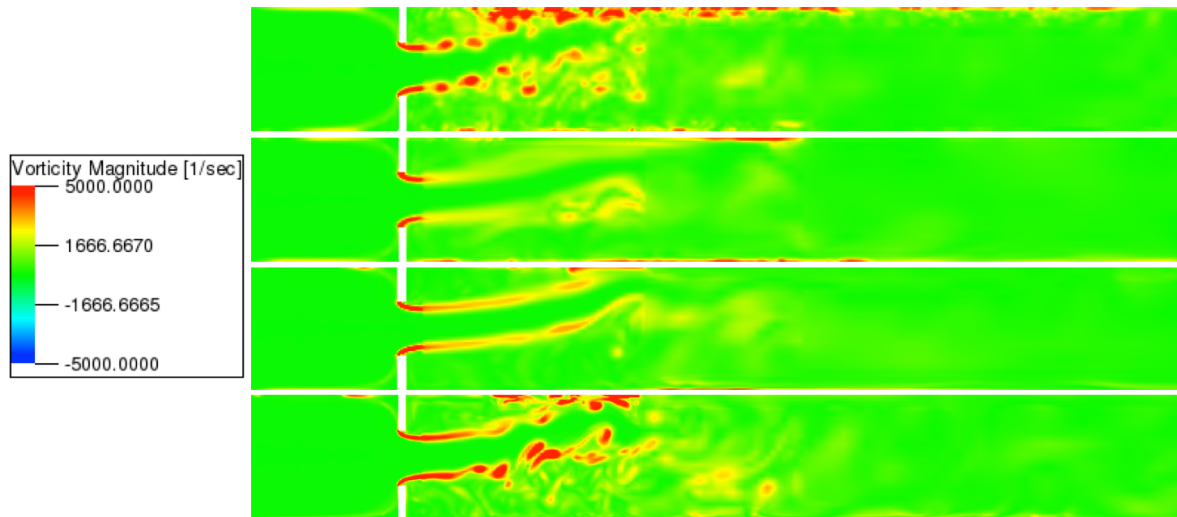
**Figure 7.14:** Comparison of the instantaneous longitudinal velocity  $u$  (levels between -15 and 28 m/s), mid-span. From top to bottom: medium mesh (CbP), medium mesh (SaE), fine mesh (SaE), finest mesh (SaE).



**Figure 7.15:** Comparison of the instantaneous crossflow velocity  $v$  (levels between -10 and 10 m/s), mid-span. From top to bottom: medium mesh (CbP), medium mesh (SaE), fine mesh (SaE), finest mesh (SaE).



**Figure 7.16:** Comparison of the instantaneous spanwise velocity  $w$  (levels between -10 and 10 m/s), mid-span. From top to bottom: medium mesh (CbP), medium mesh (SaE), fine mesh (SaE), finest mesh (SaE).

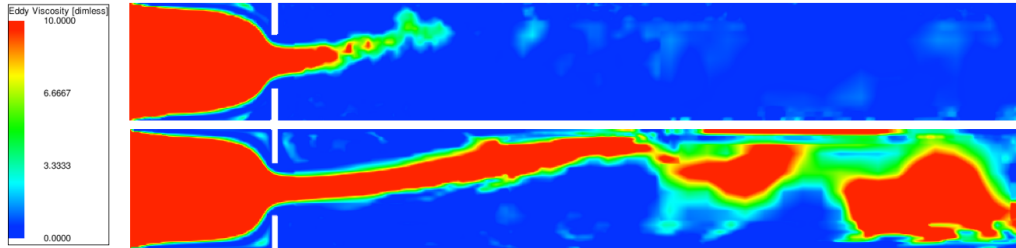


**Figure 7.17:** Comparison of the instantaneous vorticity magnitude  $\|\omega\|$  (levels between -5,000 and  $5,000\text{ s}^{-1}$ ), mid-span. From top to bottom: medium mesh (CbP), medium mesh (SaE), fine mesh (SaE), finest mesh (SaE).

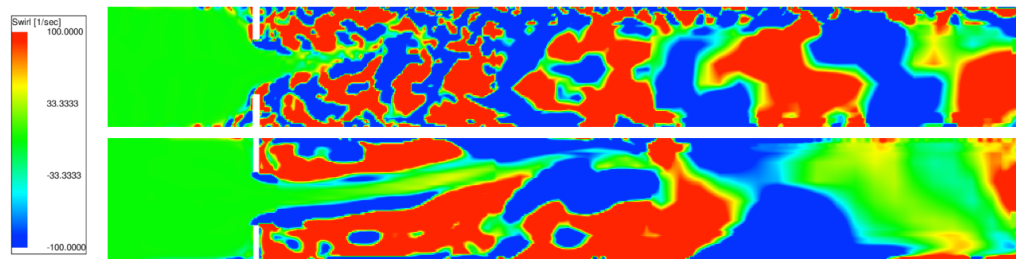
### Impact of Turbulence Model: Swirl and Eddy Viscosity

Prior to the actual analysis of the acoustic spectra, it is deemed appropriate to investigate why the underlying model causes the SaE flow fields to be less accurate than their CbP counterparts for a given grid. Indeed, the results are somewhat counterintuitive: under normal circumstances it is expected that a smaller time step  $\Delta t$ , all other things equal<sup>4</sup>, would allow for more turbulent timescales to be resolved, hence resulting in a more detailed flow field.

According to Duda et al. (2015), ‘*this [other-than-expected] behavior can be attributed to the underlying turbulence model and the insufficient spatial resolution [for the given  $\Delta t$ ]: no mechanism to trigger the resolution of turbulent fluctuations is possible and the shear layer is treated in a standard RANS fashion [with high eddy viscosity ratios]*’. In other words, Duda et al. (2015) states that the turbulence model is more active in the SaE computations, which implies higher numerical dissipation levels to account for the unresolved eddies. Figure (7.18) qualitatively compares instantaneous snapshots of the dimensionless eddy viscosity ratios for both Mach settings. Since higher values indicate a stronger influence of the turbulence model (see Chapter 4), it can be concluded from this figure that the turbulence model is indeed more active in the SaE simulation, especially for  $x/h > 3$ . This behavior is confirmed quantitatively by Figures (7.20) - (7.21), which compare eddy viscosity profiles along the central longitudinal axis and at six streamwise positions, respectively.



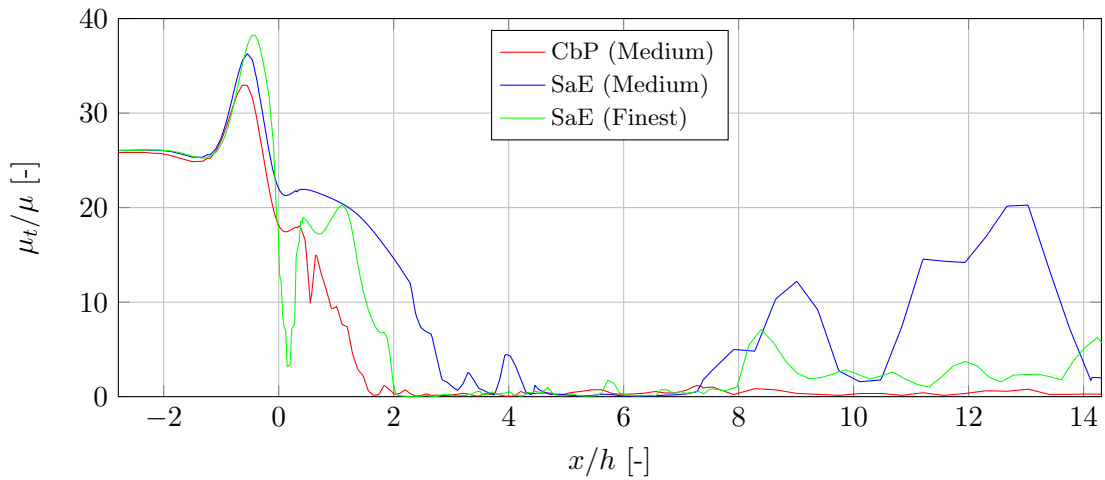
**Figure 7.18:** Comparison of the instantaneous dimensionless eddy viscosity  $\mu_t/\mu$  (levels between 0 and 10), mid-span, medium mesh. From top to bottom: Chosen by PowerFLOW, Same as Experiment.



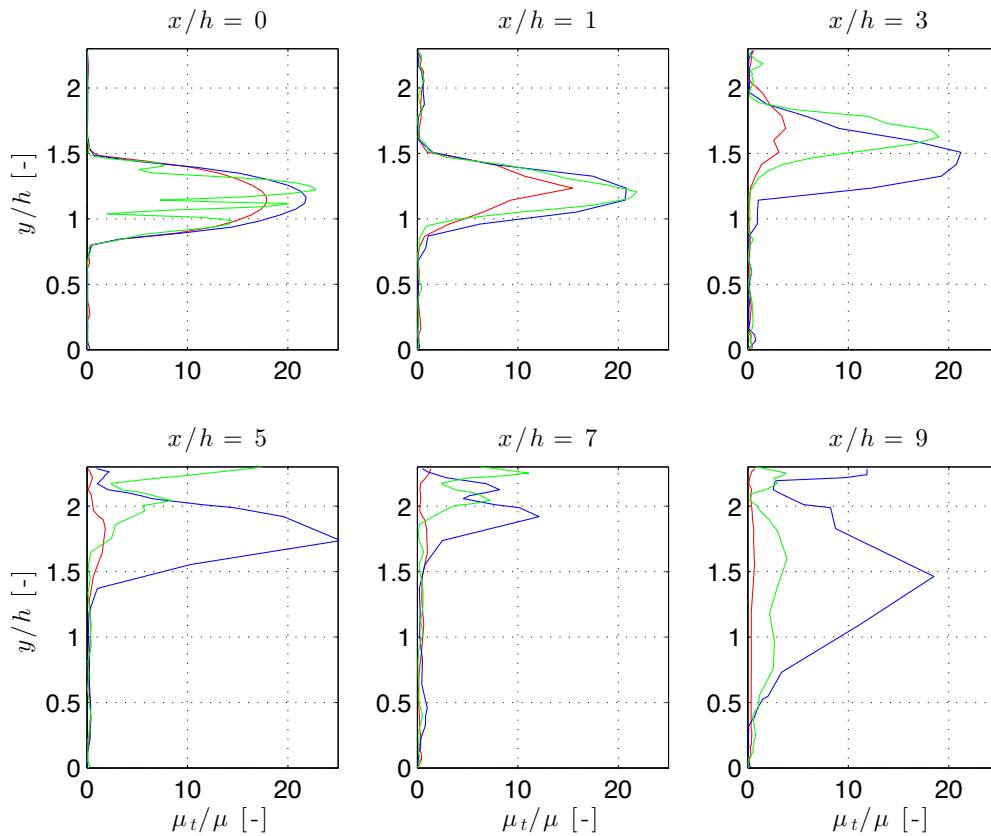
**Figure 7.19:** Comparison of the instantaneous swirl  $S = \mathbf{u} \cdot (\nabla \times \mathbf{u})$  (levels between -100 and 100), mid-span, medium mesh. From top to bottom: Chosen by PowerFLOW, Same as Experiment.

<sup>4</sup>It is noted here that the speed of sound only has a minor impact on the flow field (through aeroacoustic interactions).





**Figure 7.20:** Comparison of instantaneous dimensionless eddy viscosity  $\mu_t/\mu$  profiles for different Mach number settings along the central longitudinal axis, medium mesh.



**Figure 7.21:** Comparison of instantaneous dimensionless eddy viscosity  $\mu_t/\mu$  profiles for different Mach number settings at six streamwise positions, mid-span, medium mesh. **Red:** medium mesh (CbP), **blue:** medium mesh (SaE), **green:** finest mesh (SaE).

The statement of Duda et al. (2015) also implies that the influence of the turbulence model should gradually decrease with increasing resolution. In order to verify this statement, an additional simulation was ran on the finest mesh. As shown in Figures (7.20) - (7.21) the finest mesh yields lower eddy viscosity values than the medium mesh (SaE) at nearly all locations, hence confirming the aforementioned statement. The deviant behavior at  $x/h = 5, 7$  is caused by the difference in jet direction between both simulations, as evidenced by the relative shift of the peak values at  $x/h = 3$  (where the finest mesh is in closer accordance with the CbP results). The figures also reveal that the finest mesh (SaE) is not yet sufficiently resolved given its strong discrepancies with respect to the medium mesh (CbP).

To conclude the assessment of the turbulence model impact, Figure (7.19) shows snapshots of the instantaneous swirl  $S = \mathbf{u} \cdot (\nabla \times \mathbf{u})$  for both Mach settings. The parameter is directly related to the amount of turbulent fluctuations that are resolved by the underlying grid. From the figure it can be observed that CbP settings give rise to more intricate swirl regions in a larger portion of the diaphragm, again showing that SaE settings cause less of the turbulent fluctuations to be resolved on a particular grid. Given that regions with high swirl levels have correspondingly low eddy viscosities, these results further clarify the importance of the swirl-based correction incorporated in the turbulence model and mentioned in Chapter 4.

### 7.5.2 Description of Aeroacoustic Test Cases

The results presented in Subsection 7.5.3 are split in four different parts, each of which will touch upon a particular feature of aeroacoustic simulations. With the exception of the results presented in the fourth and final part, all simulations have been performed with the **Mach Number Same as Experiment** setting.

In the first part, the impact of grid resolution on the acoustic spectrum is assessed. To that end three acoustic spectra were acquired using the medium, fine and finest mesh. The second part is dedicated to Nonreflecting Boundary Conditions (NRBCs), since these are generally considered a prerequisite for the acquisition of accurate acoustic spectra. Such NRBC can be implemented in PowerFLOW through the **Activate Reflection Damping** feature, which is available at any static pressure outlet boundary condition. Whenever the option is activated, all pressure waves will be gradually damped towards the outlet, thereby avoiding their unphysical reflection back into the computational domain. The extent of the region in which this damping process occurs can be regulated through the **Distance to Reflecting Surface** option. In practical terms, the following two cases were simulated in order to assess the influence of a NRBC on the acoustic spectrum:

- Original diaphragm model with fine mesh in which the outlet has been extended by  $L_a = 200$  mm (black + red box in Figure (7.1)) - the **Reflection Damping** boundary condition is activated in this extended outlet region.
- Original diaphragm model with medium mesh in which the outlet has been extended by  $L_a = 200$  mm (black + red box in Figure (7.1)) - the **Reflection Damping** boundary

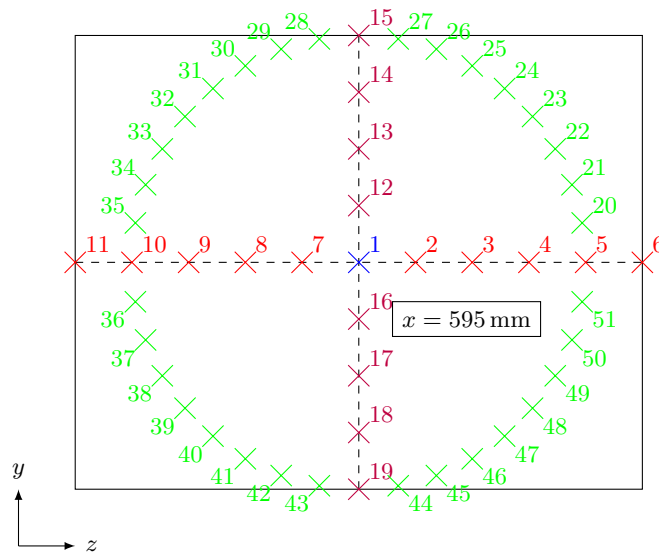


condition is activated in this extended outlet region - this case was included to provide further insight in the grid convergence results of part I.

The third part then briefly discusses the results of a directivity analysis. Three separate simulations were ran for this purpose, all of which used the fine mesh:

- Original diaphragm model with fine mesh, 51 probes positioned in  $yz$ -plane at a distance  $x = 595$  mm from the inlet;
- Original diaphragm model with fine mesh, 51 probes positioned in  $yz$ -plane at a distance  $x = 300$  mm from the inlet;
- Original diaphragm model with fine mesh in which the outlet has been extended by  $L_a = 200$  mm (**Reflection Damping** boundary condition), 51 probes positioned in  $yz$ -plane at a distance  $x = 595$  mm from the inlet.

Each acoustic probe measures the pressure at every time step (note that the number of pressure data points decreases with increasing voxel size, since larger voxels are not updated during every time step). The location of these probes is shown in Figure (7.22). It should be mentioned here that only those simulations that are used in the directivity analysis were fitted with 51 probes. All other simulations only included the first 19 probes.



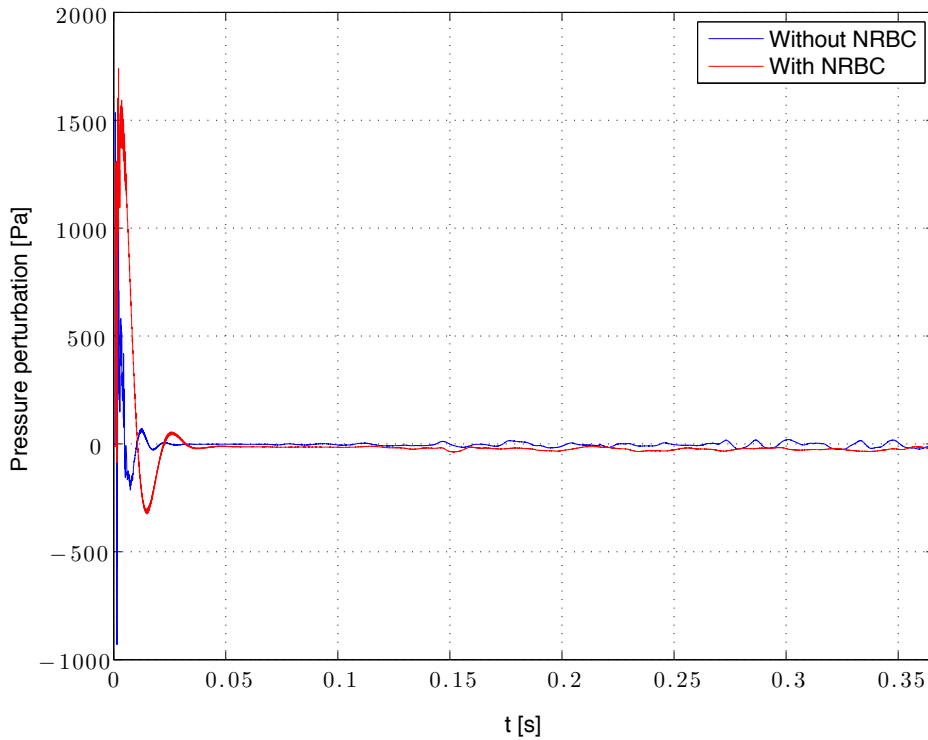
**Figure 7.22:** Location of acoustic probes relative to the diaphragm model,  $x = 595$  mm (with the exception of one simulation used in the directivity analysis).

The final part, though perhaps the most interesting with regard to future simulations, investigates whether the acoustic spectra acquired with the CbP setting can be rescaled according to the physical Mach number. In order to do so, three additional pressure measurements were performed on a fine, medium, and coarsest mesh ( $3.9 \times 10^6$  voxels, lay-out of medium mesh with reduced resolution of 150) with the **Mach Number Chosen by PowerFLOW** setting.

### 7.5.3 Aeroacoustic Results

Because the acoustic probes are positioned within the computational domain, the simulations can be classified as direct aeroacoustic simulations (see Chapter 5). Therefore, the pressure signals do not have to be propagated to the far field and can be processed directly in PowerACOUSTICS.

Figure (7.23) shows the pressure perturbation measured at Probe # 8 (fine mesh, the signal is very similar for the other probes). The transient start-up period that can be discerned prior to  $t \approx 0.05$  s was excluded from the spectral analysis because it is not representative for the acoustic spectrum. Other processing parameters include a 50% window overlap and the use of a Hanning window function<sup>5</sup> ( $f(x) = 1/2(1 - \cos(2\pi x))$ ), both incorporated to smoothen the frequency spectrum. A complete overview of the PowerACOUSTICS settings can be found in Chapter 5.

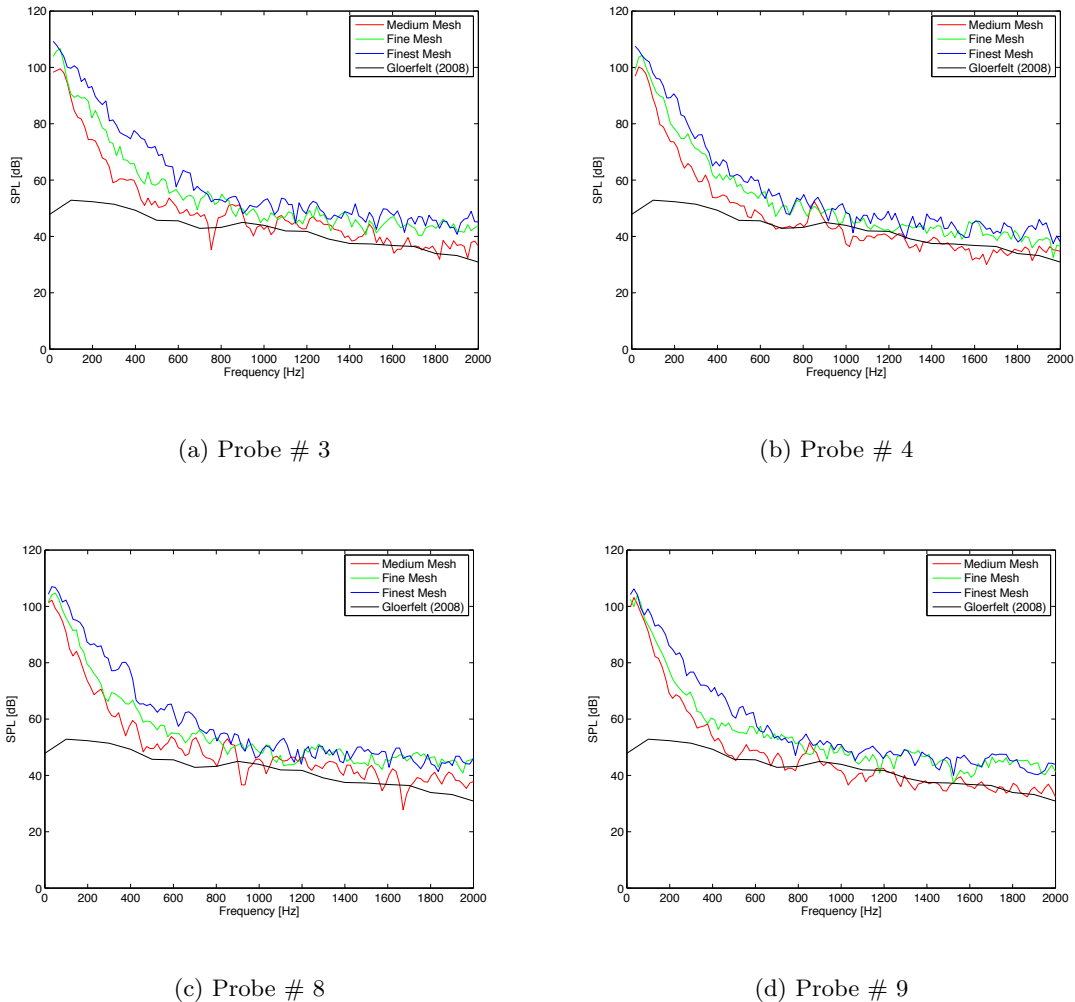


**Figure 7.23:** Pressure perturbation determined from the pressure signal at Probe # 8, fine mesh, Mach Number Same as Experiment. Note the transient start-up prior to  $t \approx 0.05$  s.

<sup>5</sup>PowerACOUSTICS allows the choice between four window functions: Bartlett (saw-tooth), Welch (parabola), Hanning (cosine) and trapezoidal end taper. Analysis showed that the first three window functions retain the same trends in the frequency spectrum, with minimal discrepancies in the absolute sound pressure levels. A comparison is included in Appendix B.

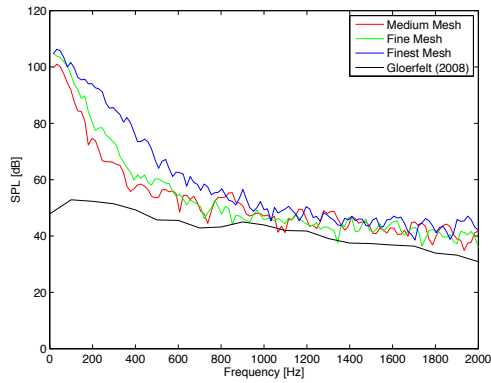
### I: Impact of Grid Resolution

The SPLs from three different meshes are compared with those from [Gloerfelt and Lafon \(2008\)](#), who also performed a direct aeroacoustic simulation (see Section 7.3). Since the acoustic spectrum presented in the reference paper is derived from the pressure signals measured by probes positioned 1.5 m downstream of the diaphragm, no exact comparison is possible (recall that the current geometry only extends for 0.5 m behind the diaphragm, the probes being positioned 5 mm prior to the outlet). Therefore, the acoustic spectra measured at multiple horizontal and vertical probes are compared with the reference data, see Figures (7.24) and (7.25).

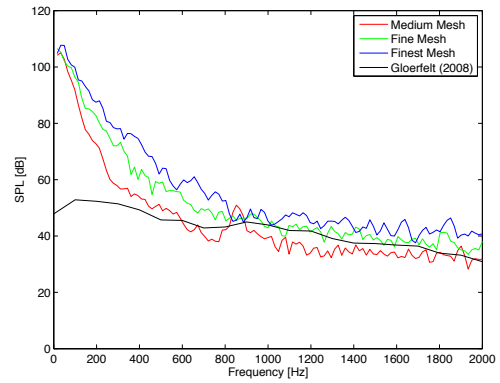


**Figure 7.24:** Sound Pressure Levels at selected horizontal probe locations for different grid resolutions,  $f_s \approx 24$  kHz,  $\Delta f \approx 16.4$  Hz. Comparison with results from [Gloerfelt and Lafon \(2008\)](#).

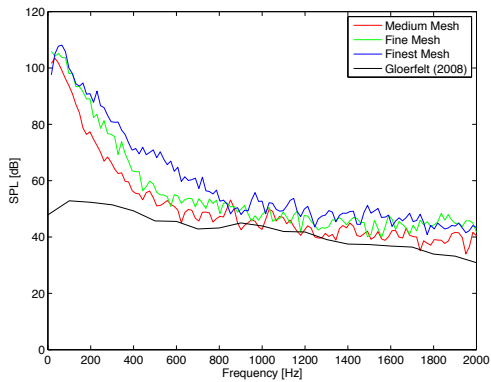
Overall, the acoustic spectra show a good correspondence with the reference data, especially in the  $f > 500$  Hz-regime. The relative peak in the SPL at lower frequencies has been discussed by [Piellard and Bailly \(2010\)](#): based on an analysis of experimental measurement



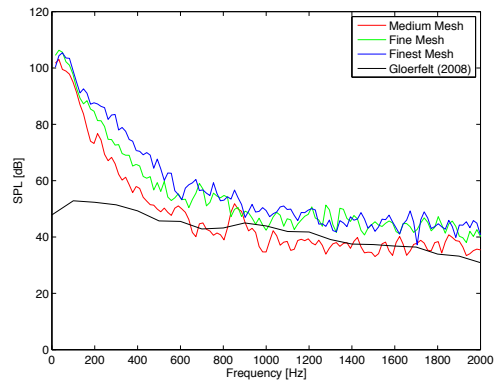
(a) Probe # 12



(b) Probe # 13



(c) Probe # 16



(d) Probe # 17

**Figure 7.25:** Sound Pressure Levels at selected vertical probe locations for different grid resolutions,  $f_s \approx 24$  kHz,  $\Delta f \approx 16.4$  Hz. Comparison with results from [Gloerfelt and Lafon \(2008\)](#).

data acquired by [Van Herpe \(1994\)](#), they concluded that the peak has a (further unexplained) physical origin.

With regard to the effects of grid resolution on the acoustic spectrum, it can be inferred from the figures that coarser resolutions lead to an overall better correspondence with the reference line (two notable exceptions being probes # 12/13, though this might be attributed to the difference in streamwise probe location with respect to the benchmark data). This observation is definitely at odds with the instantaneous flow field results presented in Subsection 7.5.1, and a possible explanation may be found in the fact that all simulations were ran without a NRBC. During the previous analysis of the impact of the turbulence model on the fluid flow results, it was shown that finer grids lead to lower levels of numerical dissipation. Consequently, the acoustic waves reaching the outlet of the finest mesh have higher amplitudes than those reaching the outlet of coarser grids. Because there is no NRBC at the outlet that reduces

the reflection of these waves back into the computational domain, the artificial increase of the SPLs caused by these reflections will be highest for the finest mesh, hence leading to the coarser grid's acoustic spectra being in closer accordance with the reference data. If this statement were to be true, the following should hold:

*NRBCs reduce the reflection of acoustic waves at the outlet, thereby lowering the SPLs below those obtained from a simulation without NRBC, provided that both simulations are ran on the same grid. As a result, the acoustic spectra obtained from the medium grid will shift below the benchmark line, while those obtained from finer grids will shift to a level that is in closer correspondence with the reference line.*

In the next part it will be shown that this statement is indeed correct. As a final remark on the results presented in this part, it is pointed out that the acoustic spectra from the medium grid show a clear peak at  $f \approx 850$  Hz for multiple probes. This is no coincidence, and it is useful in this respect to cite the paper by [Gloerfelt and Lafon \(2008\)](#):

*'The presence of the flow can induce either attenuation or amplification of the transmitted and reflected waves. For low Helmholtz number, low Mach number, unsteady flows [all of which is true for the current simulations], the diaphragm dissipates acoustic energy. This behavior is coherent with the Bechert-Howe theory of dissipation of acoustics by an edge at low Helmholtz numbers. The imposition of an unsteady Kutta condition at the edges of the slit-shaped diaphragm, or equivalently the rate of vorticity shedding (in the form of Kelvin-Helmholtz vortices in the present study) converts a part of the acoustic energy into kinetic energy. This phenomenon also explains why the intense Kelvin-Helmholtz peak near 425 Hz in the first velocity spectra induces no peak in the acoustic spectra.'*

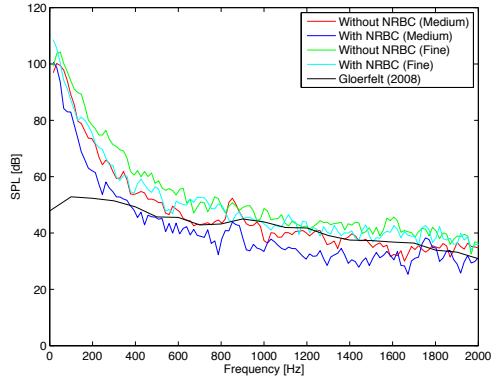
Because the medium mesh is not able to correctly model the breakdown of vortices in the diaphragm wake (see Figure (7.17)), the peak in the velocity spectra as mentioned by [Gloerfelt and Lafon \(2008\)](#) remains visible in the acoustic spectra, albeit most pronounced at the second harmonic frequency.

## II: Impact of Nonreflecting Boundary Condition

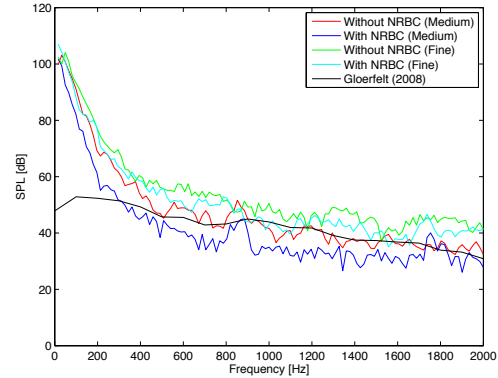
Figure (7.26) displays the effect of a NRBC on the acoustic spectra by comparing the acoustic spectra from simulations with and without such a NRBC. In accordance with the discussion of part I, the comparison includes both medium and fine grid data. It can be clearly perceived from the results that the SPLs obtained from the simulations that included a sponge zone near the outlet are consistently lower than those obtained from the original simulations. This observation holds true at nearly all of the probe locations, with the measurements at probe # 13 once more deviating from the general behavior (see part I). The shift in SPLs as a result of the NRBC are frequency-dependent and may be as large as 10 dB, especially for the medium grid.

More importantly, the overall reduction in SPLs confirms the statement of part I: when NRBCs are included in the case definition, the acoustic spectra of the fine mesh show a

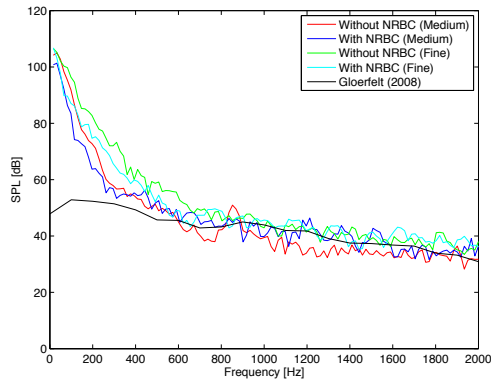
better correspondence with the reference data than the acoustic spectra from the medium mesh. Hence, it may be concluded that the **Reflection Damping** option is most effective in decreasing the reflection of acoustic waves at the outlet. Nevertheless, in order to obtain a full understanding of these NRBCs, it is advisable to perform an additional investigation on their influence when dealing with the upper airway geometry.



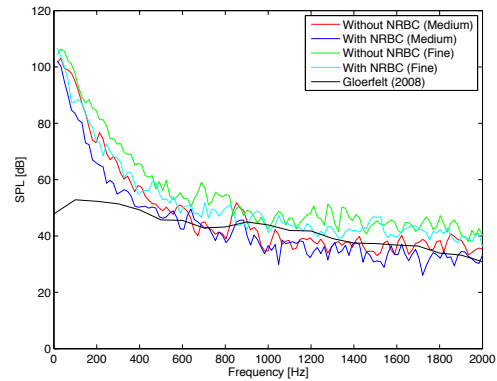
(a) Probe # 4



(b) Probe # 9



(c) Probe # 13



(d) Probe # 17

**Figure 7.26:** Sound Pressure Levels at selected horizontal and vertical probe locations for test cases with(out) NRBC,  $f_s \approx 24$  kHz,  $\Delta f \approx 16.4$  Hz. Comparison with results from **Gloerfelt and Lafon (2008)**.

### III: Directivity Analysis

It is impossible to determine the jet direction at the outlet based on the instantaneous flow field data presented in Subsection 7.5.1. Although not discussed in reference papers, it is interesting to investigate whether this jet direction can be discerned from the acoustic data at the diaphragm outlet. To that end, the pressure signals measured at the 36 acoustic

probes positioned circumferentially about the diaphragm midpoint (# 5, 10, 15 and 19 - 51 in Figure (7.22)) should first be transformed into the frequency spectrum with one-third octave frequency bands, after which they are averaged into the so-called Overall Sound Pressure Level (OASPL). This can be achieved using the following equations:

$$\text{SPL} = 20 \log \left( \frac{p}{p_{ref}} \right) \iff p = 10^{\frac{\text{SPL}}{20}} p_{ref}, \quad (7.2)$$

$$\text{RSS} = \sqrt{\sum p_i^2}, \quad (7.3)$$

$$\text{OASPL} = 20 \log \left( \frac{\text{RSS}}{p_{ref}} \right), \quad (7.4)$$

where RSS stands for the Root Square Sum of the pressure data, and where the pressure data should be obtained by selecting the **Frequency Banding Via: One-Third Octave** in the **Bands** tab.

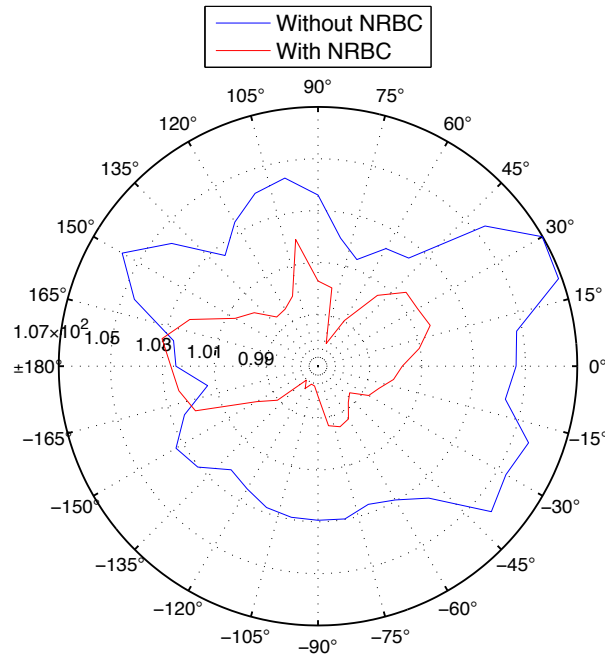
The directivity patterns that resulted from simulations performed on the fine mesh, both with and without a NRBC, are displayed in Figure (7.27), while the corresponding averaged OASPLs are summarized in Table (7.3). Although the averaged OASPL in the upper half of the domain is about 1 dB higher compared to the lower half for both cases, the jet direction is not particularly discernible. Note that the frequency levels obtained with a NRBC are again lower than those obtained without a NRBC, which is consistent with the findings presented in part II.

In order to verify whether the jet direction can indeed be determined from the acoustic measurements, a similar analysis has been carried out based on the pressure measurements of probes located in a  $yz$ -plane at a distance  $x = 300$  mm from the inlet. In order to allow a consistent comparison of the results, the fine mesh has also been applied for these purposes. The data is compared with that obtained from the probes at  $x = 595$  mm in Figure (7.28). Two observations can be made from this figure. Firstly, the averaged OASPL is approximately 5 dB higher in the upper half of the diaphragm (see Table (7.3)), which clearly indicates that the jet is directed into that region. Secondly, the OASPLs are much higher compared to those measured at  $x = 595$  mm, independent of the direction.

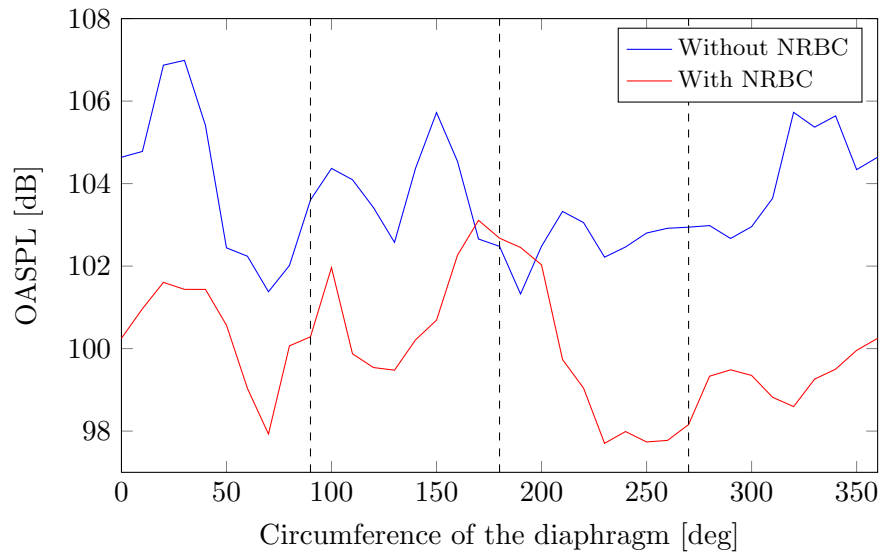
**Table 7.3:** Average OASPL-values in the upper (10 - 170°) and lower (190 - 350°) diaphragm.

Case	Upper Diaphragm	Lower Diaphragm
Without NRBC, $x = 595$ mm	104.05	103.34
With NRBC, $x = 595$ mm	100.46	99.23
With NRBC, $x = 300$ mm	115.97	110.75

Finally, closer examination of the OASPLs measured at  $x = 300$  mm further reveals that they have two distinct but similar peaks at 20° and 160°. These might be attributed to the reflection of acoustic waves off the model walls.



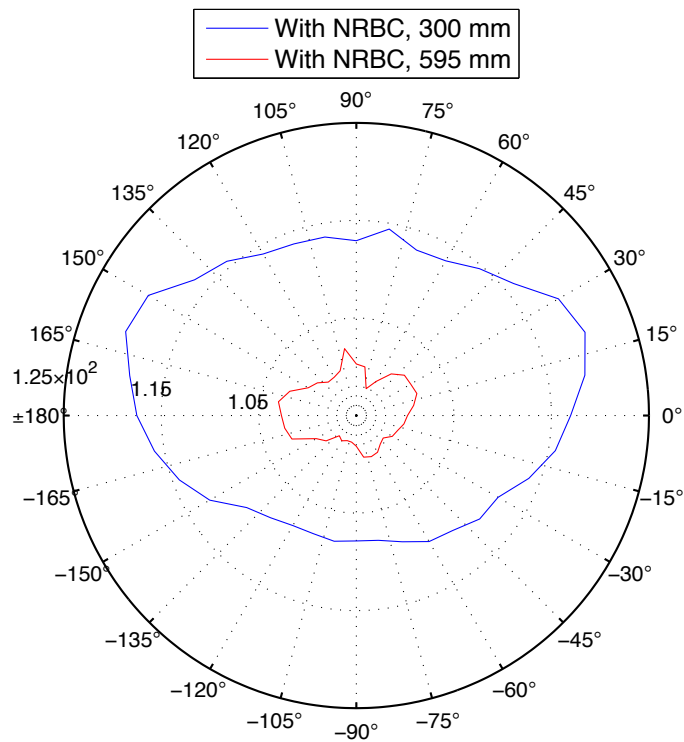
(a) Polar



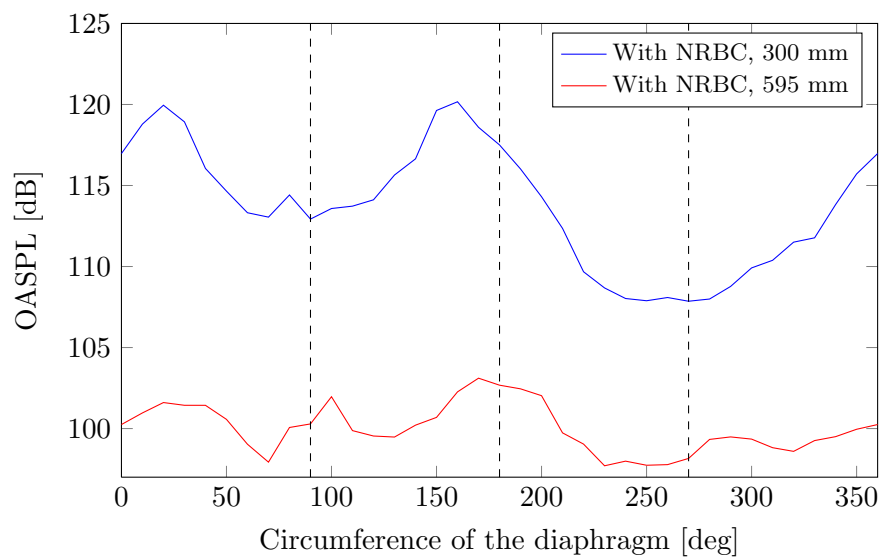
(b) Linear

**Figure 7.27:** Directivity analysis at the diaphragm outlet ( $x = 595$  mm), fine mesh.





(a) Polar



(b) Linear

**Figure 7.28:** Directivity analysis at the inner diaphragm ( $x = 300$  mm), fine mesh.

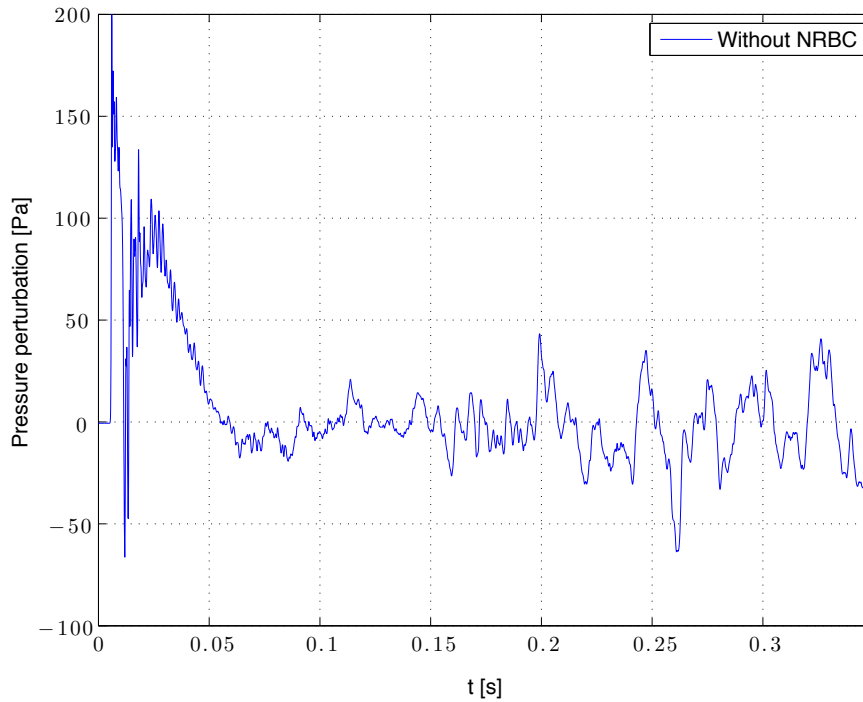
#### IV: Scaling of Results Obtained with Mach Number Chosen by PowerFLOW Setting

According to the theoretical relation between the pressure perturbation  $p'$  and the Mach number, presented in Chapter 5, it should be possible to downscale the acoustic results obtained at an upscaled Mach number (CbP) to the actual experimental Mach number. Given that acoustic dipoles are the dominant noise sources in low-Mach number simulations (in the absence of monopoles), the scaling relation can be expressed as

$$p'_{SaE} \sim p'_{CbP} \frac{M_{SaE}}{M_{CbP}}, \quad (7.5)$$

where  $M_{SaE} = 0.01734$  and  $M_{CbP} = 0.14537$  for the current test case. In other words, PowerFLOW increased  $M$  by a factor 8.4 upon switching between SaE and CbP settings.

Before delving into the analysis of the acoustic spectra, two items should be mentioned about the general behavior of the pressure signals and how they were acquired. Figure (7.23) shows the temporal evolution of the pressure signal at Probe #8 (fine mesh, the signal is again very similar for the other probes). As opposed to the SaE signals, the transient start-up period is prolonged until  $t \approx 0.1$  s. Therefore, all pressure data prior to  $t = 0.1$  s was discarded from the spectral analyses. Note that this observation is in accordance with the discussion presented in the beginning of this section: given that an upscaled  $M$  causes a reduction in the wave propagation speed it takes longer for the pressure information to travel to the probe location, which ultimately leads to a prolonged start-up period.



**Figure 7.29:** Pressure perturbation determined from the pressure signal at Probe # 8, fine mesh. Mach Number Chosen by PowerFLOW. Note the transient start-up prior to  $t \approx 0.1$  s.

The second item is related to the sampling frequencies. Because all probes are positioned within the lowest VR of the mesh, the pressure is only measured at every 16th timestep. Combined with the fact that the timesteps in the CbP simulations are about 8 times longer than those in the SaE simulations, matching the sampling frequencies of the CbP simulations would result in unacceptable values for the maximum frequencies that can be resolved by the grid  $f_{max} < 2$  kHz. It was therefore decided not to alter the sampling frequencies, and an overview is given in Table (7.4). However, it is expected that this discrepancy will not influence the conclusions drawn from the comparison between acoustic spectra, because the flow is almost entirely converged during the measurement interval.

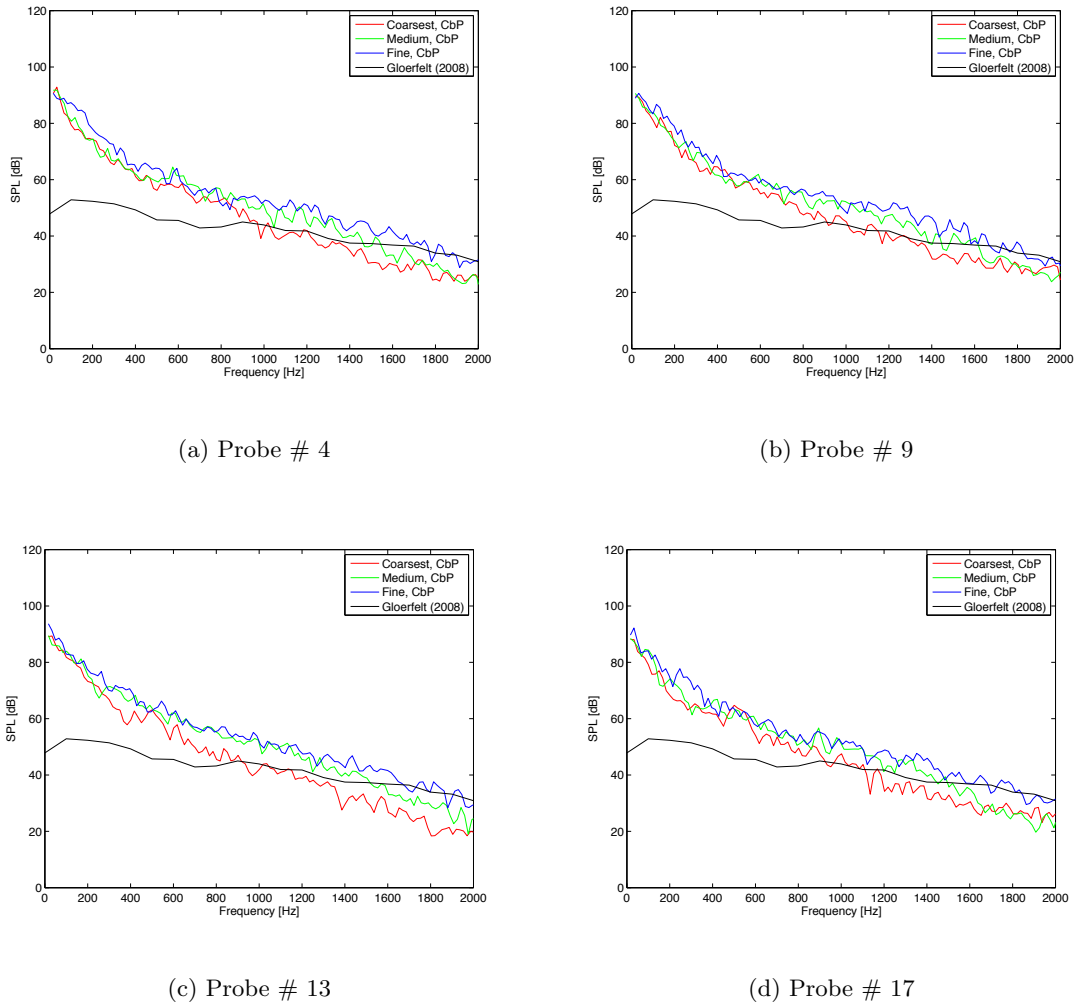
**Table 7.4:** Overview of the timesteps, sampling frequencies and maximum frequencies of the CbP simulations.

	$\Delta t$ [ $\mu$ s]	$f_s$ [kHz]	$f_{max}$ [kHz]
Coarsest Mesh	7.311	8.552	4.265
Medium Mesh	5.483	11.404	5.682
Fine Mesh	4.387	14.252	7.115

The scaled acoustic spectra from three different grids are compared with the benchmark data of [Gloerfelt and Lafon \(2008\)](#) in Figure (7.30). In general, it can be perceived that none of the grids show a particularly good correspondence with the reference line, with SPLs varying almost linearly with frequency. Moreover, finer grids do not perform better than coarser grids, especially because their spectra almost coincide at lower frequencies. There is a nuance to this observation, however, and it is to be found in the discrepancy between the acoustic spectra at higher frequencies: there appears to be a certain threshold frequency above which the spectra diverge. This divergence is in favor of the finer grids, since it causes the slope of their spectra to match closer with that of the reference line. Upon the introduction of a NRBC (which causes a general downward shift of the acoustic spectra), this similarity in slope will most likely cause the finer grids to be in closer accordance with the benchmark data.

Now that the general behavior of the CbP acoustic spectra has been discussed, it becomes possible to focus on the most interesting part of this section, i.e., investigating whether the scaled CbP spectra match with their SaE counterparts. If this is shown to be true, it would allow that all SUAM/RUAM simulations be ran at accelerated Mach numbers (CbP), after which the measured acoustic spectra are scaled according to the theoretical dipole scaling factor given by Equation (7.5). Of greater interest, it would simultaneously allow a significant reduction of the processing power required to simulate these geometries.

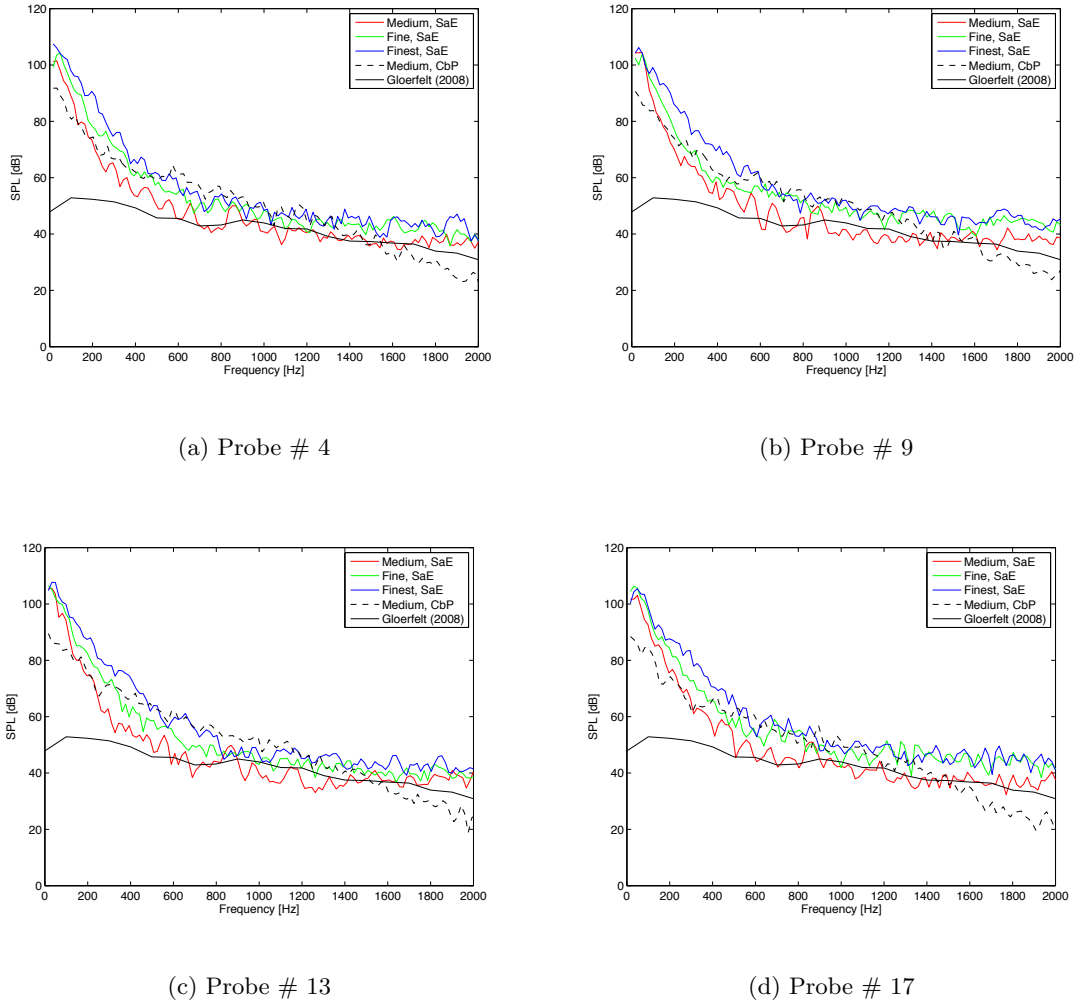
First and foremost, it should be recalled from the discussion in Subsection 7.5.1 that the Mach number settings strongly influence the amount of flow details that can be resolved on a given grid. It would therefore not be reasonable to expect a match between the acoustic spectra of CbP/SaE simulations (on the same grid), precisely due to the fact that they contain a different amount of acoustic sources. Because the CbP spectrum was shown to be in closer accordance with the underlying physics than its SaE counterpart, and assuming that it is indeed possible to scale the acoustic spectra, the following should hold:



**Figure 7.30:** Sound Pressure Levels at selected horizontal and vertical probe locations for different grid resolutions, Mach Number Chosen by PowerFLOW, sampling frequencies given in Table (7.4),  $\Delta f \approx 16.4$  Hz. Comparison with results from [Gloerfelt and Lafon \(2008\)](#).

*The SaE spectrum matches (converges to) the CbP spectrum when both simulations model the flow field with a same level of accuracy.*

In order to verify this hypothesis, Figure (7.31) compares the acoustic spectrum of the medium CbP simulation with the spectra of SaE simulations ran on increasingly refined grids (up until the finest grid, which was mainly introduced for this purpose). According to the aforementioned hypothesis, and taking into account the results presented in Subsection (7.5.1), the finest mesh (SaE) should have the closest match with the CbP spectrum. From the figure it can be observed that this statement is valid in the frequency range  $600 \text{ Hz} < f < 1,400 \text{ Hz}$  (depending on the location). Outside this range, the CbP spectrum essentially bears no resemblance with any of the SaE spectra, and the main dissimilarities can be described as follows:



**Figure 7.31:** Comparison between CbP and SaE Sound Pressure Levels at selected horizontal and vertical probe locations,  $f_{s,CbP} \approx 11.4$  kHz,  $f_{s,SaE} \approx 11.9$  kHz,  $\Delta f_{CbP,SaE} \approx 16.4$  Hz. Comparison with results from [Gloerfelt and Lafon \(2008\)](#).

1. the low-frequency peak is about 10 - 15 dB lower, depending on the probe location;
2. there is a more gradual decline from the low-frequency peak towards the reference data;
3. there is no discernible plateau at higher frequencies.

Due to the limited availability of information concerning the ways in which PowerFLOW achieves the higher  $M$ , it was impossible to trace the causes of these discrepancies. Even though it might seem a good way to start, taking into account the effect of quadrupole sources would induce a further downward shift in the CbP spectrum ( $p' \sim M^2$ ), which is most certainly not the desired direction.

An explanation that is worth considering is related to the fact that the influence of the Mach number might extend further than the elements that were already touched upon in Subsection 7.5.1. In view of this it should be mentioned that the author is not entirely reassured that the increase in  $M$  is achieved only by changing the lattice speed of sound. According to the results of Van Herpe et al. (2012) this was a logical conclusion, but Sanjosé et al. (2014) also mentions an increase in the characteristic lattice speed. As a result, it is possible that changing  $M$  affects the Reynolds number at which the flow is simulated. It is expected that this is not an issue when dealing with automotive or aeronautical problems where the experimental  $M$  is already high, and where the increase in  $M$  is limited to a factor 2 - 3. However, the combination of a relatively low Reynolds numbers for the current diaphragm case with the large increase in  $M$  ( $\times 8.4$ ) might significantly alter the Reynolds number upon changing from SaE to CbP simulations (or the other way around). In other words, it is possible that CbP and SaE simulations are solving a different flow problem with respect to the Reynolds number. While this would not be truly problematic when simulating flows at relatively high  $M$  that can be classified as being Reynolds-independent, the impact for the current test case might be severe. If this were to be true, it once more emphasizes the need to run the low Reynolds number test cases at the experimental  $M$ .

The hypothesis should ideally be discussed with the engineers at Exa Corporation, but it is also possible to perform a basic investigation by manually and gradually increasing  $M$  via the **Mach Number Chosen by User** setting. Upon comparison of the outcomes of these different simulations it could then be verified whether the CbP (scaled) and SaE acoustic spectra converge when going from  $M_{CbP}$  to  $M_{SaE}$ . Note that the CbP simulations should be carried out on the same grid in order to make a reasonable comparison. Due to time constraints, this topic will not be pursued further in the course of this thesis.

## 7.6 Conclusions

Given the large amount of information presented in this chapter, a brief summary is presented here that touches upon the most important conclusions.

In the first part of the chapter it was shown that PowerFLOW can accurately model the flow through a diaphragm. This is an important conclusion given that the upper airway contains geometrical features that pose a similar obstruction to the incoming flow, e.g., the epiglottis in the Simplified Upper Airway Model (see Chapter 3). Although they were not obtained deliberately, the flow field results of the coarsest mesh (Appendix C) once more exemplified the fruitfulness of a well-defined mesh. While the grid contains only half the amount of voxels included in the coarse mesh, its ability to resolve flow details in the diaphragm wake is considerably higher. This shows that both the region where the vorticity is created (in this case the diaphragm lips) as well as the wake portion of this region should have a sufficiently high grid resolution in order to ensure a correct transition from modeled to resolved turbulence.

The second part of the chapter showed the profound influence of the turbulence model on the flow field: high eddy viscosity levels in regions where the grid is insufficiently refined (in order

to resolve a certain level of turbulent eddies) cause the rapid dissipation of flow structures. It is partly due to this intervention that SaE simulations (experimental Mach number) fail to resolve the same amount of flow details compared to CbP simulations (accelerated Mach number) on the same grid. It is expected that this statement will no longer be valid once the grid becomes sufficiently resolved, but given the time restrictions it was not possible to further investigate this issue.

Next came a thorough analysis of the acoustic spectra associated with the diaphragm flow. In this regard it was shown that finer grids yield an increasingly better resemblance to the benchmark data, provided that a Nonreflecting Boundary Condition is incorporated in the case definition. In fact, the fine grid (with NRBC) exhibits a very good correspondence with the benchmark data above a certain threshold frequency.

Finally, an attempt to rescale the acoustic spectra obtained at an accelerated Mach number back to the experimental Mach number led to a reasonable correspondence with the SaE spectrum, albeit only in the frequency range  $600 \text{ Hz} < f < 1,400 \text{ Hz}$ . The discrepancies between the sound pressure levels outside this frequency range are similar at every probe location, and it is therefore expected that they can be altered by changing some of the simulation parameters. However, due to the fact that only limited information is available about the workings of the PowerFLOW software (especially with regard to Mach number settings), it was not possible to identify the cause(s) of these discrepancies, nor any solutions. It is therefore advised to perform the aeroacoustic SUAM/RUAM simulations with the **Mach Number Same as Experiment** setting.





## **Part III**

# **Upper Airway Simulations**



---

## Chapter 8

---

# Simplified Upper Airway Model

The preceding case studies provided numerous insights into the capabilities of PowerFLOW, whilst simultaneously setting out best practices. This accumulated knowledge base will now be employed in the aeroacoustic study of stridor.

A first issue that presents itself is the absence of a comprehensive set of benchmark data for flow studies that include a realistic model of the upper airway<sup>1</sup>. Therefore, it is necessary to introduce an intermediate step in the research process, wherein it is validated that the PowerFLOW software can accurately capture the flow phenomena in the human upper airway. To that end, this chapter describes the results of several (aeroacoustic) simulations of the fluid flow within a Simplified Upper Airway Model (SUAM), a geometry for which benchmark data is readily accessible. Apart from its validation purpose, this intermediate phase is considered to be a meaningful step towards obtaining a thorough understanding of the wide variety of flow patterns that are present in the upper airway, and how they can be reliably simulated. Perhaps most importantly, this step offers an opportunity to develop an optimal set of simulation parameters that can later be used as baseline parameters when studying more complicated geometries. Given the extensive computational requirements pertaining to this type of simulations, the most effective example of such overarching parameter specification is the development of a well-defined computational grid that can be applied to similar geometries without the need to perform an additional grid convergence study.

Another item that requires explicit attention is the specification of the type of Upper Airway Obstruction (UAO) that will be studied. Indeed, the description of stridor causes in Chapter 2 already indicated the existence of numerous UAOs that may lead to stridor and hence many different ways to simulate this symptom. However, the simplified problem statement adopted in this thesis quickly narrowed down the list of possible choices. Most notable within this set of simplifications is the decision to exclude all fluid-structure interactions, which limits the choice of UAO to the subset of static obstructions. Besides, it should be possible to

---

<sup>1</sup>Often realistic geometries are applied in case studies with direct practical applications (e.g., analyses of particle deposition patterns) that lack thorough and fundamental descriptions of the flow field.

make a sensible comparison between flow results of the PowerFLOW simulations and those obtained by conventional Computational Fluid Dynamics (CFD) methods (e.g., finite-volume or finite-element methods). Given this set of restrictions it was decided to simulate a patient suffering from cartilaginous subglottic stenosis, such that results can be compared with those obtained by Lynch (2012) and van der Velden (2012). Moreover, subglottic stenosis is an UAO that can be easily integrated in a physical version of the SUAM. This is considered advantageous because a comparison between numerical and experimental aeroacoustic data might prove to be an important next step in the development of a non-intrusive diagnostic technique for UAOs.

The chapter is purposely divided in sections bearing the same names as those in the preceding chapter as the general problem approach remained unchanged. First, Sections 8.1 - 8.3 outline the details of the case geometry, the boundary conditions, and the benchmark data, respectively. Next, Section 8.4 elaborates on the grid choice and the difference in flow characteristics between healthy and constricted models. Finally, Section 8.5 is dedicated to the acoustic aspects of this case.

## 8.1 Case Geometry

Figure (8.1) shows the Simplified Upper Airway Model (SUAM) that was used as a basis for the current validation study. Brouns et al. (2006) created this idealized geometry and subsequently moulded it into a transparent physical model. This allowed them to conduct an investigation into the flow patterns in the upper airway using Particle Image Velocimetry (PIV). The model was constructed by taking a physiologically relevant<sup>2</sup> average of Computed Tomography (CT)-images of five male adults, all of which were acquired during the inhalation phase of the respiration cycle Brouns et al. (2007). All relevant dimensions of the model can be consulted in Chapter 3.

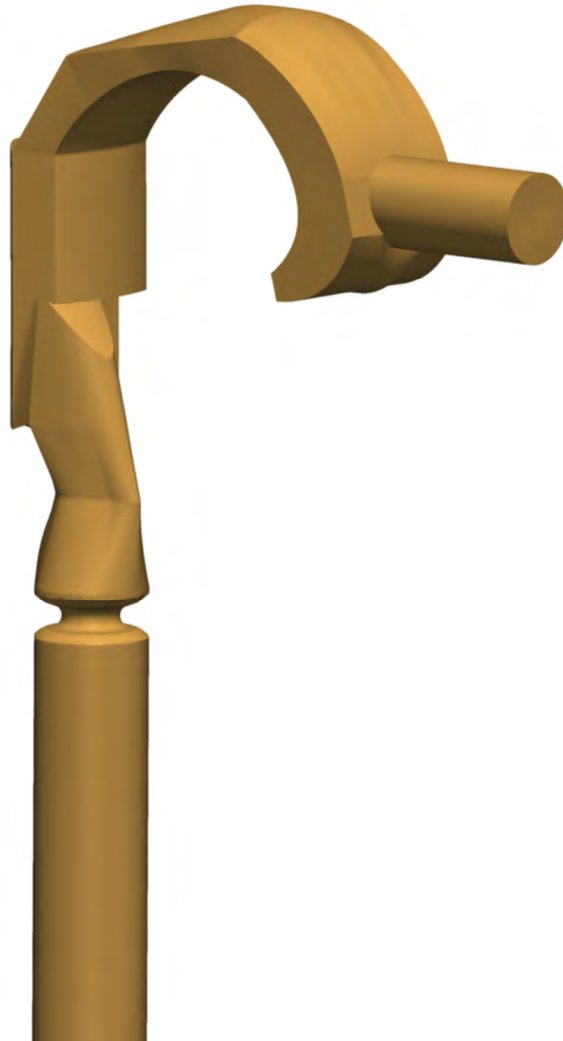
Lynch (2012) later inserted symmetric constrictions as a means to investigate the aeroacoustic characteristic of stridor as part of his MSc thesis. This procedure produced two additional models that reflect a symmetrical reduction of the tracheal lumen by 50 and 75 %, respectively.

High-quality versions of both the healthy and the constricted models were provided by W. van der Velden, a researcher at the Delft University of Technology. Regardless of the quality, a few adaptations were required to ensure a simplified and fully accurate treatment of the models during the case set-up in PowerCASE. All alterations were performed in PowerDELTA, according to the following sequence of steps:

- The `Fill Mesh Holes` feature was used to close the inlet and outlet of the model, which is necessary for two reasons.
  - It allows a simplified and more accurate implementation of boundary conditions.

---

<sup>2</sup>With ‘physiologically relevant’ it is meant here that the CT-images were averaged as such that the major flow patterns were retained.



**Figure 8.1:** Three-dimensional view of the simulated SUAM (developed by [Brouns et al. \(2006\)](#)), including a 75 % constriction in the tracheal lumen at the level of the vocal cords, which has been introduced by [Lynch \(2012\)](#) as a means to investigate the acoustic characteristics of stridor.

By ticking the **Create a Mesh Face for Each Cap** box, the newly introduced boundaries can be recognized by PowerCASE as separate faces, which implies they can be selected directly in the **Boundary Conditions** tab.

- The model can be inverted upon import in PowerCASE, such that offset regions can be specified in the interior domain only (as opposed to a symmetrical two-way offset otherwise).
- The quality of the mesh was assessed using the **Mesh Diagnostics** feature. Whenever the model turned out to contain flaws (disabling its correct use in PowerFLOW), these errors were rectified with the **Edit Mesh** feature. Common flaws were overlapping facets, mostly remnants of the previous step. Note that especially the realistic models were prone to these type of errors due to the non-circular extent of their inlet and outlets.

With regard to the actual geometrical features of the model, the following can be perceived in Figure (8.1). The air enters the oral cavity through the mouth (the cylinder is included to achieve a more realistic velocity profile at the mouth inlet), where it almost immediately impinges on the tongue. After covering the 180° bend along the curvature of the tongue, it reaches the oropharynx with its backward-facing step geometry. Shortly thereafter the epiglottis, which is somewhat more pronounced here than it would be in a realistic model, poses another distinct obstruction to the flow field. Just downstream from the epiglottis, the glottic aperture significantly reduces the cross-sectional area, though the lumen rapidly enlarges again upon reaching the level of the trachea.

## 8.2 Boundary Conditions

Considering the validation purpose of this chapter, the simulated conditions should be in accordance with those applied in the benchmark studies. Therefore, the model was necessarily fitted with boundary conditions that produce steady inspiratory conditions at a flow rate of 30 L/min. Although such flow rate is seldom encountered under normal breathing conditions (see Chapter 2), it was applied by [Jayaraju et al. \(2008\)](#) in their study of the particle deposition efficiency of dry powder inhalers, devices that require the user to inhale rapidly and deeply. In order to realistically model the inhalation process (i.e., the expanding thoracic cavity creating a negative intrathoracic pressure) the inlet is set to a fixed static pressure equal to the atmospheric pressure, while a constant mass flow rate of 30 L/min is specified at the outlet. All walls are fitted with no-slip boundary conditions.

In Chapter 7 it was shown that NRBCs have to be incorporated in the case definition in order to arrive at a truthful acoustic spectrum. Unfortunately, the **Reflection Damping** option is not available in combination with either of the aforementioned boundary conditions, hence excluding the use of this built-in means to arrive at a NRBC. An alternative option is to enhance the dissipation levels near the inlet/outlet by gradually<sup>3</sup> increasing the voxel size towards those extremities. However, there exists no guide that sets out best practices regarding the implementation of such grid-related damping, e.g., discussing the optimal spacing between the different dissipation regions. Moreover, the model inlet/outlet cannot readily be extended because the geometry was made available in a .stl-format that cannot be altered directly by CAD software such as Catia. A potential workaround is to extend the fluid domain at the inlet using spheres while using voxel damping at the outlet (see Appendix D), although this will introduce discrepancies in the inlet velocity profile with respect to the benchmark simulations. In addition, increasing the voxel size at the outlet would require a shift in the microphone location outside this coarsened domain, which leads to a different location compared to the microphone of [van der Velden \(2012\)](#).

This discussion shows that there is no easy way to implement NRBCs in this configuration, and it was therefore decided to omit them from the case definition. Although it is acknowledged that the absence of NRBCs will impact the broadband SPL levels, it should be recalled that

---

<sup>3</sup>If the voxel size is increased acutely, pressure waves might still be reflected due to the large difference in dispersion properties between the adjacent voxels [Wagner et al. \(2007\)](#).

the aim of this project is not to provide the most accurate acoustic spectrum of stridor. Instead, its primary goal is to investigate whether the Lattice Boltzmann Method can discern the level of obstruction based on the acoustic spectrum. Hence, of dominant interest here is the relative difference between the acoustic spectra produced by healthy and stridorous patients, disregarding the absolute pressure levels. With regard to further investigations on this topic, it is expected that there exists an elegant implementation method for NRBCs that might be worked out in collaboration with the researchers at Exa.

### 8.3 Description of the Reference Data

The benchmark data that can be found throughout this chapter is mainly drawn from two sources. All fluid profiles presented in the grid convergence study of Subsection 8.4.1 were taken from the comprehensive particle deposition study of [Jayaraju et al. \(2008\)](#). It was decided to include both the Reynolds-Averaged Navier-Stokes (RANS) and Large Eddy Simulation (LES) results of this paper as to provide the reader with an idea on the relative accuracy of different turbulence models. Given that [Jayaraju et al. \(2008\)](#) validated the numerical methodologies by comparing them with PIV data, their results can be considered sufficiently accurate to be used as a benchmark here. Nonetheless, for the sake of completeness, the experimental results are also included in the velocity profile comparison. Three-dimensional turbulent kinetic energy profiles, on the other hand, will only be shown for the RANS and LES turbulence models ([Jayaraju et al. \(2008\)](#) did not include the experimental values in their report). Although the experimental profiles are available for the 2D kinetic energy, 3D profiles were favored because they can be extracted directly with PowerACOUSTICS, without the need for any post-processing (see Chapter 5).

The RANS was based on a low Reynolds number variant of the SST  $k-\omega$  model that requires a fine grid resolution in the near-wall region. Indeed,  $y^+$ -values were shown to approach unity for a grid with 800,000 hexahedral cells (stretching ratio 1.2). The momentum equation was discretized in space using a second-order upwind scheme, while the third-order MUSCL scheme was employed in the discretization of the  $k-\omega$  equation. The SIMPLE algorithm was used for pressure-velocity coupling. With regard to the LES two constant sub-grid scale models were tested, but only one is considered here, namely the Smagorinsky-Lilly model. A second-order implicit formulation is used for temporal discretization and central differencing for spatial discretization of the momentum equation. The computational mesh consisted of  $1.9 \times 10^6$  hexahedral cells with increased refinement towards the wall (stretching ratio 1.05,  $y^+ \sim 0.2$ ).

Finally, it should be pointed out that [Jayaraju et al. \(2008\)](#) applied different boundary conditions to arrive at a steady mass flow of 30 L/min. They fixed the static pressure at the outlet whilst applying a steady top-hat velocity profile along with 5% turbulence intensity at the inlet. Although this will induce a different flow behavior near the inlet, it is reasonable to assume that the influence of the boundary conditions is sufficiently reduced at the locations of comparison.

All instantaneous flow field images, as well as the acoustic spectra and kinetic energy profiles pertaining to the constricted airway models are compared against the results of [van der Velden \(2012\)](#). This MSc thesis is virtually the only available work in literature that provides a detailed discussion of the flow field in constricted airway models, and it is unique in the sense that it also relates these differences in flow patterns to the aeroacoustic characteristics of stridor. The interested reader is referred to a recent paper by [van der Velden et al. \(2015\)](#) that provides a comprehensive summary of both his thesis and the valuable work that preceded it, i.e., the MSc thesis of [Lynch \(2012\)](#).

## 8.4 Fluid Simulations

This section includes a twofold discussion on the simulation of fluid flow through the upper airway. First, Subsection 8.4.1 relates the findings of a grid convergence study that was performed on the unconstricted model. Once a proper grid has been established, it is then applied in conjunction with the constricted models. The resulting flow patterns are discussed in Subsection 8.4.2.

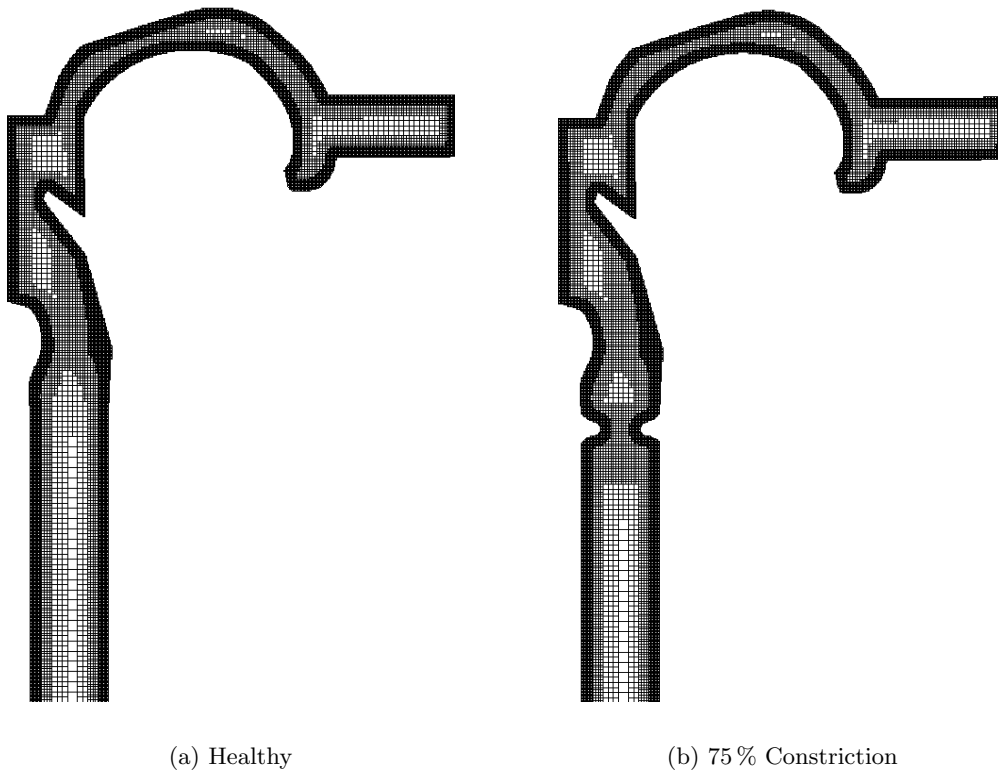
Adopting the same grid across different geometries is considered an adequate solution approach since the geometries are identical except for the region surrounding the constriction. Also, it would be difficult to perform a thorough grid convergence study on the constricted models because there is insufficient benchmark data available for these geometries. Regardless of these arguments it was still decided to insert an additional refinement region in the vicinity of the constriction, see Figure (8.2). This is deemed necessary as it is expected that a lot of vorticity will be created in this region. Failing to resolve this vorticity would have a profound impact on the resulting acoustic spectra due to its direct connection with quadrupole sound sources (see Chapter 5).

### 8.4.1 Grid Convergence Study: Healthy Model

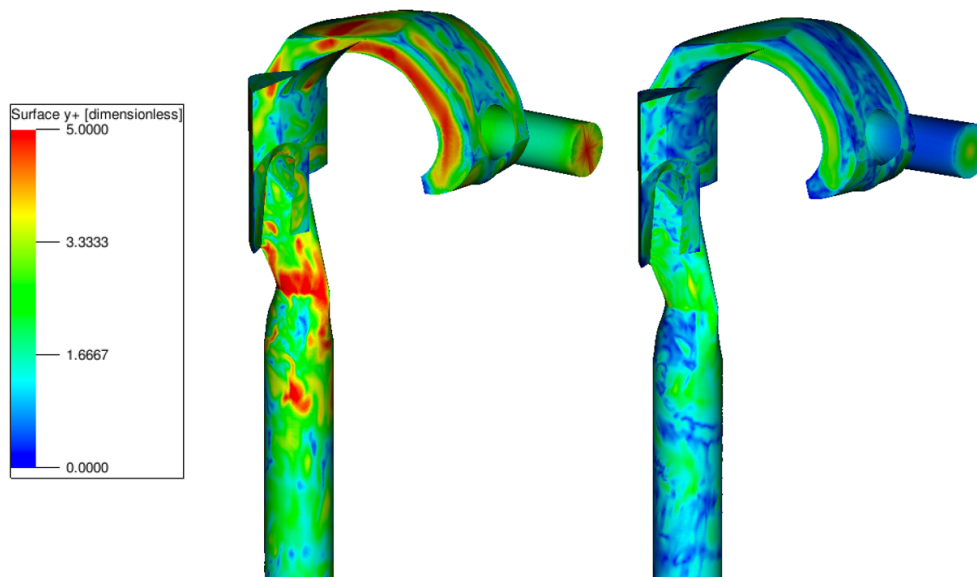
Prior to obtaining any acoustic data, it should be determined what grid resolution is required in order to model the fluid flow accurately whilst economizing computational cost. To that end, three different grids have been assessed: a coarse mesh with  $1.17 \times 10^6$  voxels (2 cells/mm), a medium mesh with  $5.81 \times 10^6$  voxels (4 cells/mm), and a fine mesh with  $39.65 \times 10^6$  voxels (8 cells/mm). The grids have exactly the same lay-out, see Figure (8.2), but the voxel size has been halved for each consecutive grid. Considering the near-wall resolution, the fine grid has  $y^+$ -values that are smaller than five throughout almost the entire airway. This upper limit increases to about 15 in case of the medium mesh, see Figure (8.3).

In order to extend the current database of benchmark results a Direct Numerical Simulation (DNS) was also carried out. This was achieved by changing the `Simulation Options` in `PowerCASE` from `Turbulence Model` to `Direct`. In other words, the turbulence model nor the wall model are active during this simulation. The grid that was adopted for this computation has the same lay-out as the other grids but consisted of  $286.14 \times 10^6$  voxels (16 cells/mm).





**Figure 8.2:** Computational grid of the SUAM geometry in the central sagittal plane, every second grid line is shown, fine mesh ( $39.65 \times 10^6$  voxels).



**Figure 8.3:** Instantaneous snapshot of  $y^+$  (levels between 0 and 5), a measure for the near-wall resolution, healthy model. From left to right: medium mesh, fine mesh.

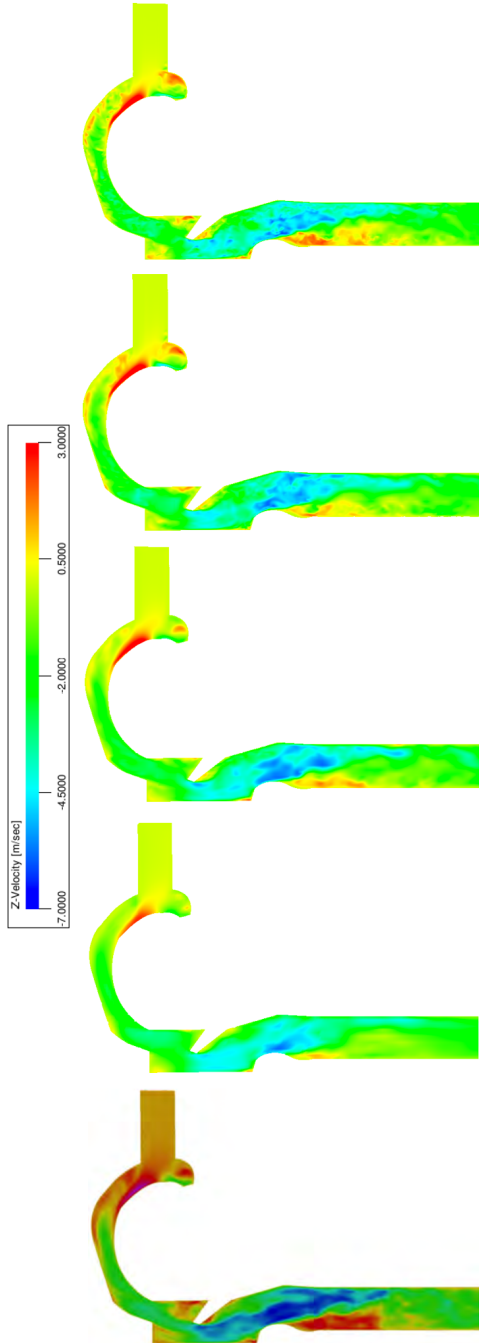
## Qualitative Analysis

The fluid flow results that have been obtained using the different meshes are first compared qualitatively with the benchmark results from [van der Velden \(2012\)](#). From Figures (8.4) and (8.5) it can be observed that all but the coarse grids are able to resolve the major flow patterns. Evidently, the fine mesh yields the best comparison with the reference results, but the differences with respect to the medium grid are minimal. In terms of the amount of vorticity that is resolved, on the other hand, the fine mesh clearly performs better. This is evidenced by Figure (8.6), where it can be seen that vorticity levels are considerably higher in case of the fine mesh for both the near-wall as well as the central jet regions. Initial analysis of the  $y^+$ -values in Figure (8.3) already indicated that the near-wall regions were somewhat underresolved for the medium mesh, especially at the height of the glottis. The corresponding increase in numerical dissipation most likely prevents the transition from modeled to resolved turbulence further downstream in the jet shear layer (see Chapter 7). Given that resolving these vortex structures is a crucial aspect of the aeroacoustic simulations, it can be argued that the medium mesh is too coarse for this purpose.

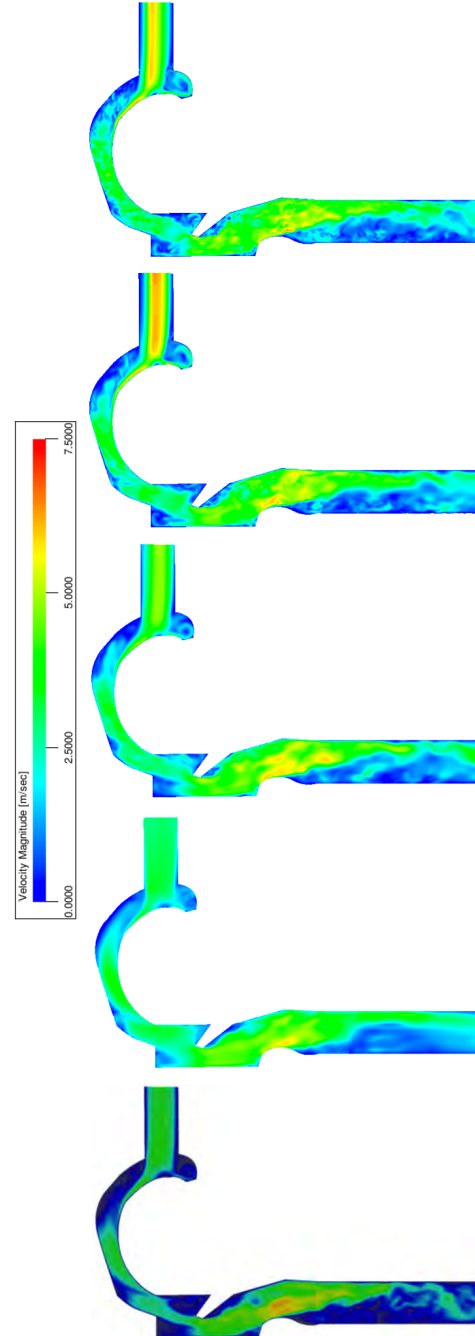
Note that the comparison between the pressure perturbation fields in Figure (8.7) is included here not only for completeness, but also due to the relevance of the pressure deficit as a parameter to assess the severeness of an airway obstruction. This will become clear when the constricted models are discussed in Subsection (8.4.2).

At this point it is interesting to provide a general overview of the flow patterns that are present in the upper airway. Throughout the discussion the remarks between square brackets point out how the presence of certain flow features can be discerned from the figures.

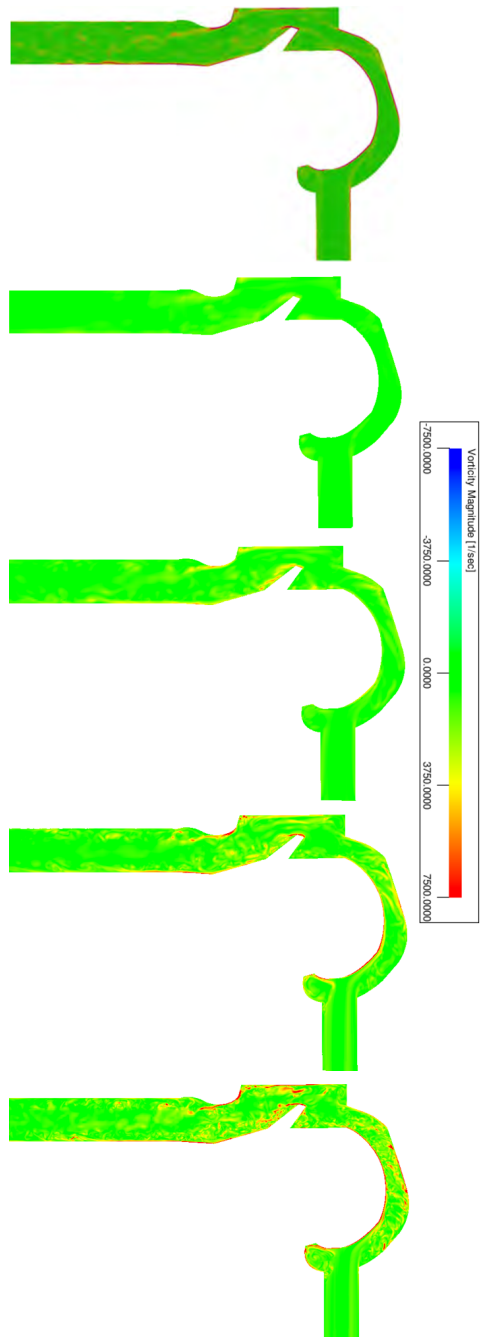
At the junction between the cylindrical inlet and the start of the oral cavity, the sudden expansion in cross-sectional area causes the flow to recirculate in the inferior region [increased vorticity levels, circulatory appearance of velocity magnitude]. There is also recirculation in the upper region though it is much less apparent [positive horizontal velocity, see Figure (8.8)]. After completing the  $180^\circ$  bend around the tongue the air reaches the oropharynx, where the presence of a so-called backward-facing step and a distinct epiglottis creates additional flow features. In particular, the sudden expansion causes the formation of a free jet and a corresponding recirculation region at the posterior pharynx wall [positive vertical velocity]. Due to the presence of the epiglottis, however, the jet is forced to the posterior side of the airway, which causes the bubble to reattach much faster than is typical for a backward-facing step (about five to seven times the height of the step, [Heenan et al. \(2003\)](#)). Anteriorly, the epiglottis itself blocks the flow which induces another region of flow separation [again, positive vertical velocity]. Besides, there exists a separation bubble that propagates from its leading edge [increased vorticity levels]. Just downstream from the epiglottis, the glottis reduces the cross-sectional area, thereby creating a laryngeal jet that impinges anteriorly in the tracheal region [evolution of velocity magnitude]. Simultaneously, a large recirculation region is formed at the posterior wall [positive vertical velocity].



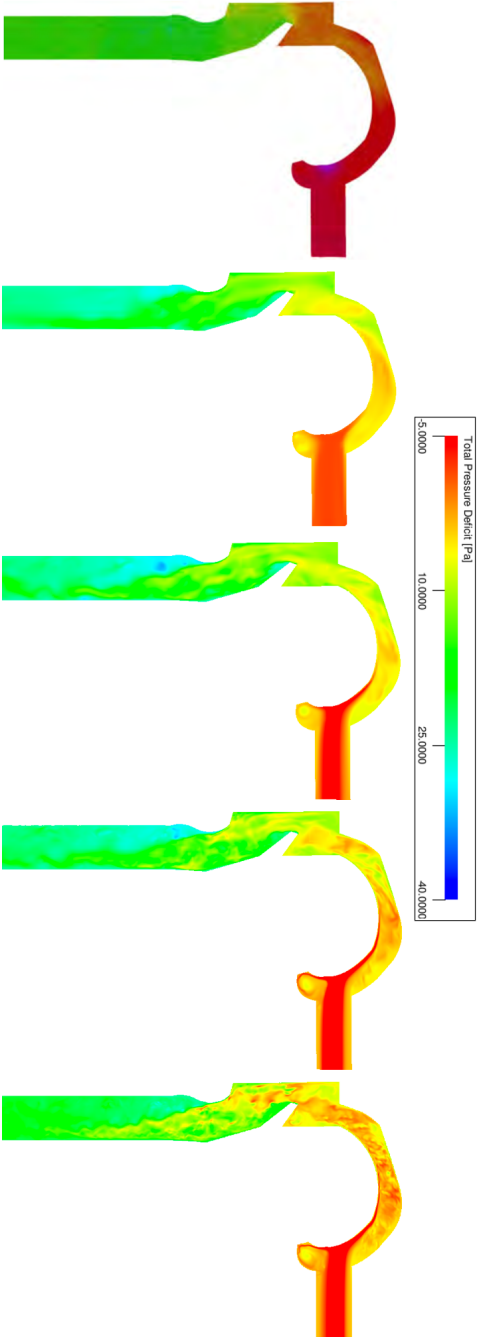
**Figure 8.4:** Comparison of the instantaneous vertical velocity  $u_z$  (levels between -7 and 3 m/s) in the central sagittal plane, healthy model. From left to right: van der Velden (2012), coarse mesh, medium mesh, fine mesh, DNS.



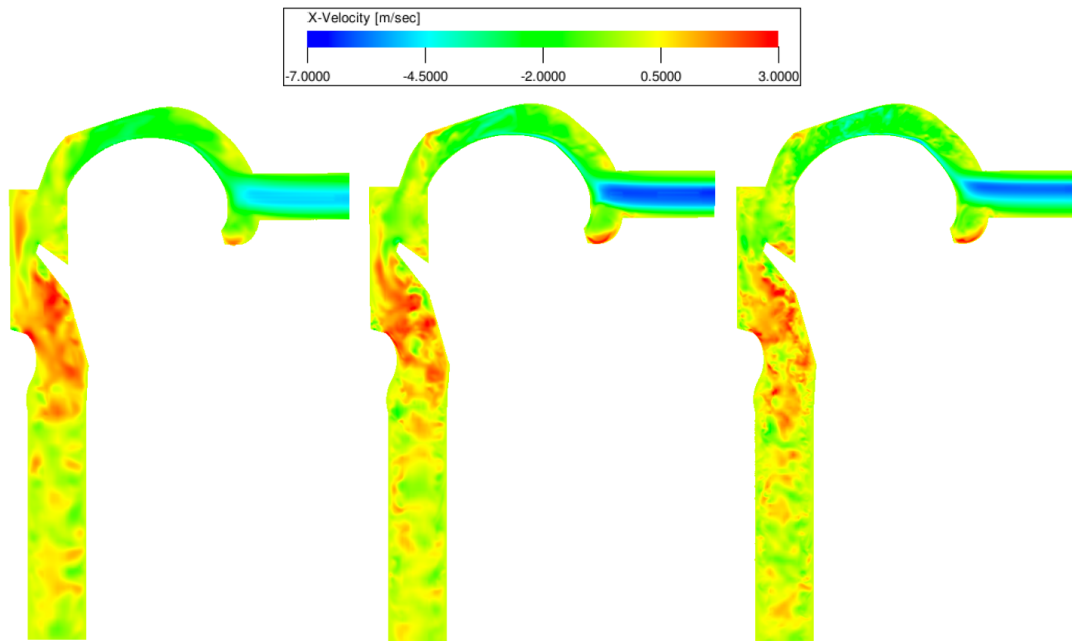
**Figure 8.5:** Comparison of the instantaneous velocity magnitude  $\|\mathbf{u}\|$  (levels between 0 and 7.5 m/s) in the central sagittal plane, healthy model. From left to right: van der Velden (2012), coarse mesh, medium mesh, fine mesh, DNS.



**Figure 8.6:** Comparison of the instantaneous vorticity magnitude  $\|\omega\|$  (levels between  $-7,500$  and  $7,500 \text{ s}^{-1}$ ) in the central sagittal plane, healthy model. From left to right: van der Velden (2012), coarse mesh, medium mesh, fine mesh, DNS.



**Figure 8.7:** Comparison of the instantaneous pressure deficit  $p'$  (levels between  $-5$  and  $40 \text{ Pa}$ ) in the central sagittal plane, healthy model. From left to right: van der Velden (2012), coarse mesh, medium mesh, fine mesh, DNS.



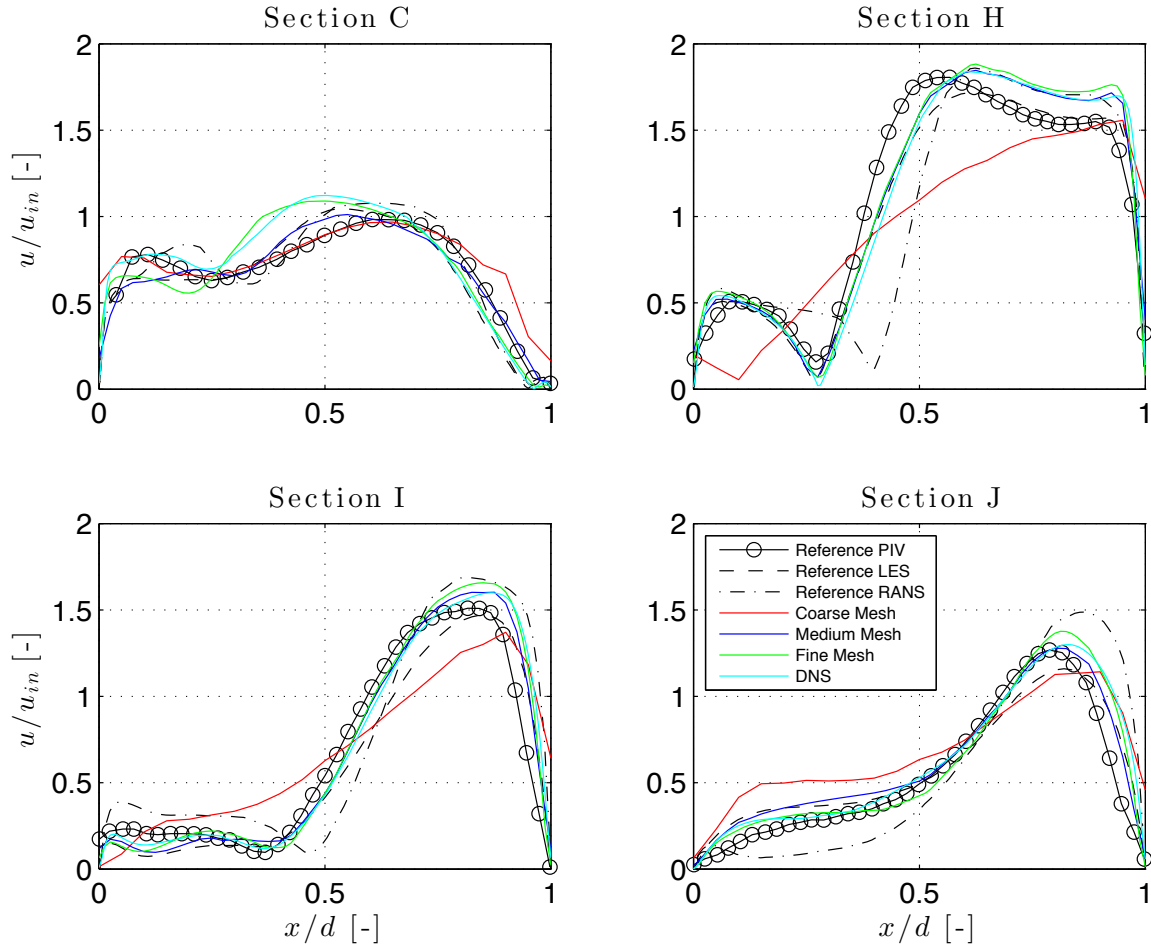
**Figure 8.8:** Snapshot of the instantaneous horizontal velocity  $u_x$  (levels between -7 and 3 m/s) in the central sagittal plane, healthy model. From left to right: medium mesh, fine mesh, DNS.

### Quantitative Analysis

Now that it has been shown, based on an analysis of instantaneous flow images, that only the fine mesh is able to resolve flow structures up to an acceptable level of detail, it will be verified whether this statement also holds true quantitatively.

With that goal Figure (8.9) compares the averaged velocity magnitude in the central sagittal plane with the reference results from [Jayaraju et al. \(2008\)](#). The first thing that can be observed is that even the DNS profiles do not match entirely with the PIV data. As a result of the flow complexity in the pharyngeal region, Section C is where the largest discrepancies occur. More specifically, the DNS simulation systematically overestimates the velocity near the anterior wall in the tracheal region, while slightly underestimating it in the same part of the pharyngeal region. Similar trends can be discerned for the medium and fine grids, while the coarse mesh is clearly insufficiently resolved to capture all the flow patterns with a reasonable accuracy. The discrepancies with respect to the reference results might be attributed to three issues: (i) slightly different measurement locations, due to the fact that [Jayaraju et al. \(2008\)](#) does not provide exact coordinates; (ii) the aforementioned difference in boundary conditions and (iii) a different turbulence intensity at the inlet (1% in the current simulations versus 5% in the set-up of [Jayaraju et al. \(2008\)](#)).

Figure (8.10) compares the averaged turbulent kinetic energy profiles. For each grid two different lines are displayed: the dashed line corresponds to the turbulent kinetic energy that is actually resolved by the grid, while the solid line represents the total turbulent kinetic energy, i.e., including the portion that is created by the turbulence model. Apart from

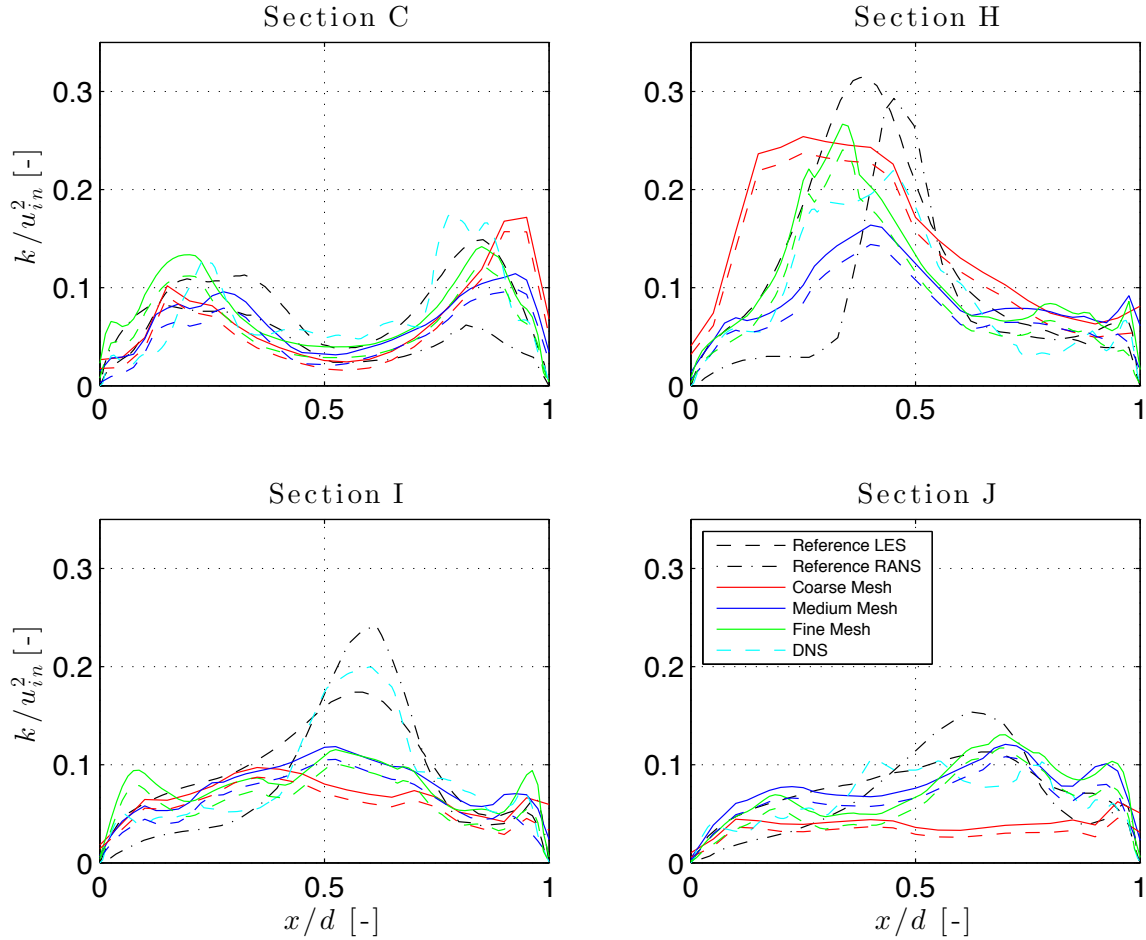


**Figure 8.9:** Comparison of normalized 2-component ( $u_x$  and  $u_z$ ) velocity magnitude in the central sagittal plane with reference data from [Jayaraju et al. \(2008\)](#), healthy model. The specified locations (C, H - J) coincide with those of Figure (3.2). The fluid profiles are measured from the posterior to the anterior wall of the airway.

the general structure of the profiles, there is no particularly good correspondence with the reference results. Both the fine and the medium mesh almost consistently underestimate the levels in the central region, while overestimating them near the walls. It is unclear what causes these differences but one explanation might be the limited amount of timeframes that were included in the calculation<sup>4</sup>.

Despite these differences the current results clearly exhibit flow patterns that are similar to the benchmark results. The fact that even the DNS results do not match entirely with the reference data indicates that a further grid refinement will not significantly improve the accuracy of the results. Finally, it should be mentioned that it is not possible to distinguish a convergence pattern towards the DNS results. Therefore, it can be argued from a quantitative viewpoint that the medium and fine grids perform equally well.

<sup>4</sup>Only a limited amount of instantaneous data was stored for each simulation in order to limit the required storage capacity.



**Figure 8.10:** Comparison of normalized 3-component turbulent kinetic energy  $k$  in the central sagittal plane with reference data from Jayaraju et al. (2008), healthy model. The specified locations (C, H - J) coincide with those of Figure (3.2). The fluid profiles are measured from the posterior to the anterior wall of the airway.

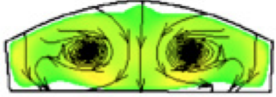
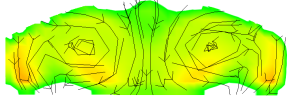
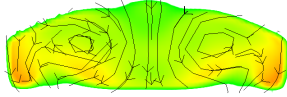
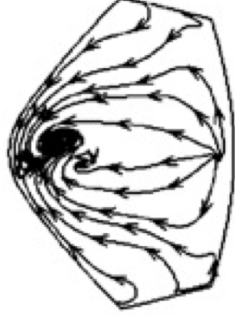
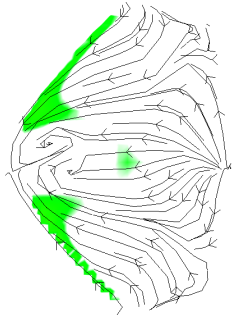
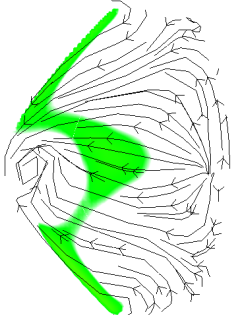

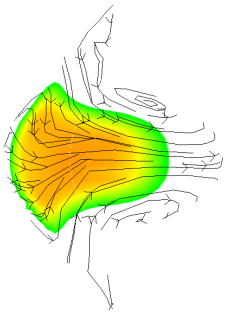
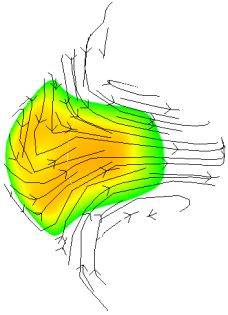
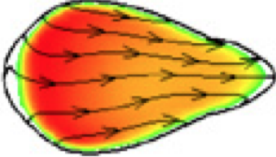
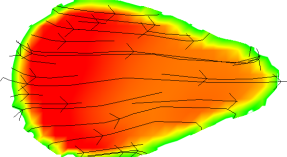
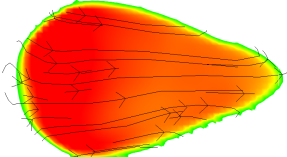
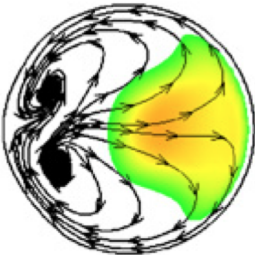
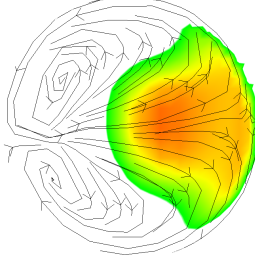
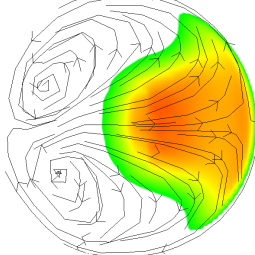
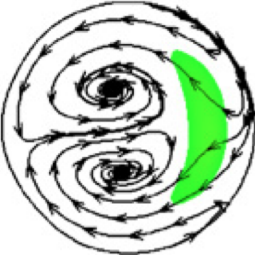
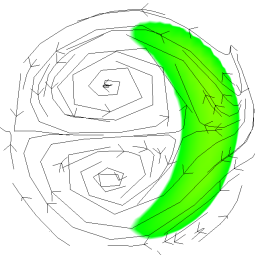
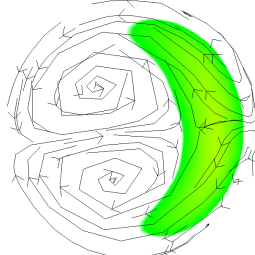
### Secondary Flow Structures

The previous discussions were exclusively related to two-dimensional flow structures. Given that the flow through the upper airway is highly three-dimensional it is also important to investigate the extent to which the proposed grids are able to resolve secondary flow structures.

Table (8.1) gives an overview of averaged secondary velocity streamlines at selected cross-sections. The figures included in this table also show the velocity magnitude, which has been filtered as to show only those values that are higher than 2.6 m/s ( $\sim 50\%$  of maximum velocity). Comparison with the reference results from Jayaraju et al. (2008) reveals a remarkable correspondence. Moreover, the differences between the medium and fine mesh results are almost negligible.



**Table 8.1:** Overview of averaged velocity magnitude  $\|u\|$  (levels between 0 and 5.2 m/s) with superimposed secondary velocity streamlines, healthy model. The specified locations (A, C - D, G - H, J) coincide with those of Figure (3.2).

Sec.	Jayaraju et al. (2008)	Medium Mesh	Fine Mesh
A			
C			
D			
G			
H			
J			



For a detailed discussion about the behavior of these secondary flow structures the interested reader is referred to the accompanying text by Foucart (2014). It suffices to mention that the results are very comparable to those presented in literature.

### Grid Choice

In conclusion, both the medium and the fine grid results show a satisfying correspondence with the reference data. However, the higher vorticity levels predicted by the fine mesh show the relevance of the increased grid resolution, an argument that is especially valid when switching to aeroacoustic simulations. It was therefore decided to adopt the fine mesh as the standard mesh for the simulations on the constricted geometries.

#### 8.4.2 Healthy versus Stridorous Flow Patterns

As mentioned before two ‘stridorous’ models have been considered. These models have a 50 and 75 % reduction in cross-sectional area at the level of the subglottic region, respectively. In order to simplify the terminology throughout the paragraphs that follow these constricted geometries will henceforth be referred to as the 50 %- and 75 %-model.

Instantaneous snapshots of the vertical velocity fields are displayed in Figure (8.11). The fact that the geometries are identical down to the level of the constriction causes the flow fields to be nearly the same up until the level of the glottis. Subtle differences between the models are apparent, but they can mainly be attributed to the instantaneous nature of the flow fields, i.e., they may vary slightly from one timestep to the next given the unsteadiness of the flow. A clear description of the flow patterns in the pharyngeal region has already been provided in Subsection 8.4.1 and will not be repeated here.

Downstream of the glottis the flow fields can be seen to vary markedly, mainly in terms of the position and strength of the laryngeal jet. In order to confirm that this flow pattern is not an instantaneous phenomenon, Figure (8.12) displays averaged vertical velocity fields that are superimposed with a selection of streamlines. Note that the regions in which the vertical velocity is positive are colored in pink. The figure shows that the constricted models exhibit a recirculation region at the anterior tracheal wall which is not present in the healthy model. Moreover, the behavior of the laryngeal jet is clearly dependent on the degree of tracheal constriction: while it is still directed anteriorly in the 50 %-model, it can be seen to divert towards the posterior wall in the 75 %-model. It is primarily this directional change that influences the relative size of the recirculation regions.

Next it can be derived from Figure (8.13) that not only the direction of the jet is dependent on the degree of the constriction, but also its corresponding velocity magnitude. As a means to quantify the increase in jet velocity with increasing constriction severity, Figure (8.14) displays averaged velocity magnitude profiles at the height of the constriction. Although somewhat unexpected, the 50 %-model only saw an increase in its jet velocity of about 10 % with respect to the healthy model. The 75 %-model, on the other hand, achieved a 75 % increase in jet velocity.

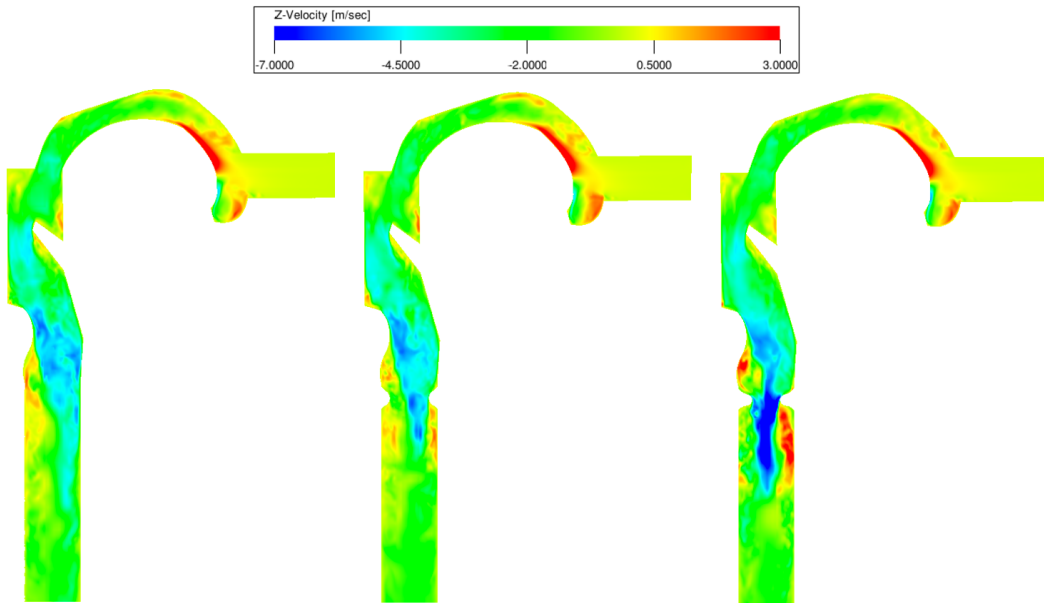
A final insight that can be drawn from the instantaneous velocity magnitude fields relates to the extension of the jet towards the tracheal outlet. The constricted models experience a faster decline in jet velocity as compared to the healthy model, which causes a faster transition from skewed velocity profiles at the start of the laryngeal jet to more uniform ones further downstream. This is due to a more efficient mixing process in the tracheal region as a result of the central jet location.

Instantaneous vorticity fields are displayed in Figure (8.15). There it can be perceived that the vorticity levels in the tracheal region become higher with increasing constriction size. Especially in case of the 75 %-model, the vorticity extends further downstream as a result of the increased mixing in the tracheal region. Given that vorticity can be identified as the cause of acoustic quadrupole sources (see Chapter 5), these findings are in line with medical observations: a patient who suffers from (critical) subglottic stenosis will exhibit stridor upon inspiration. Whether this stridor derives directly from the presence of quadrupole sources remains yet to be determined.

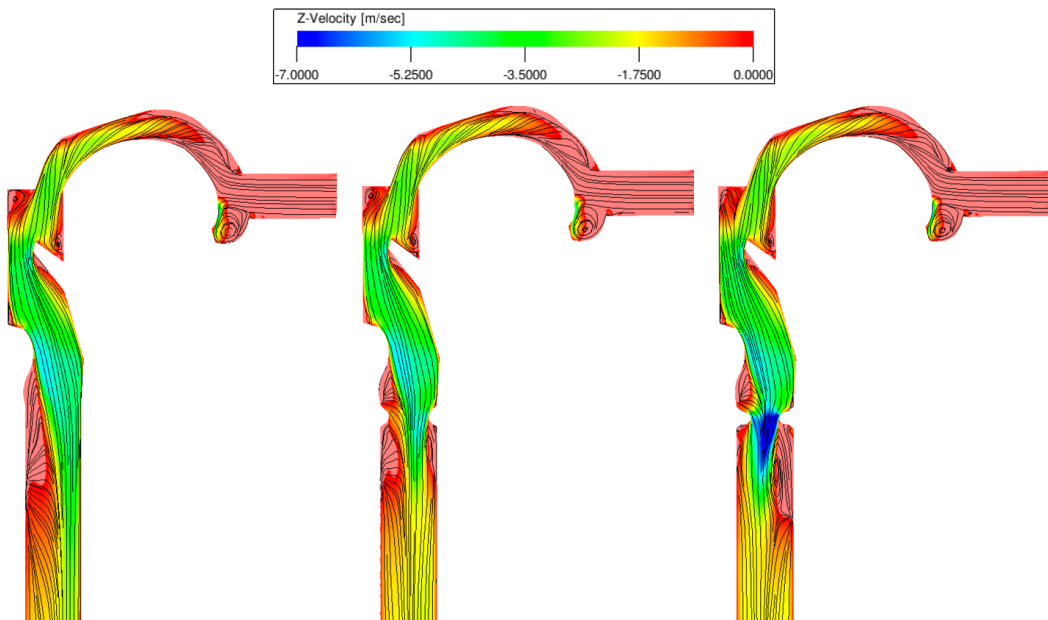
Finally, Figure (8.16) compares the pressure perturbation fields of all models. While these are very similar for the healthy and the 50 %-model, there is a significant pressure drop over the constriction ( $\Delta P$ ) in the 75 %-model. Further investigation into the evolution of the averaged<sup>5</sup> pressure deficit along the upper airway in Figure (8.17) yielded a  $\Delta P \sim 4.5$  Pa for the 50 %-model and a  $\Delta P \sim 25.5$  Pa for the 75 %-model. These results are similar to those obtained by [Brouns et al. \(2007\)](#), who conducted an investigation on the pressure drop over multiple stenoses varying in type (type I weblike versus type II elongated) and severity (50 - 90 % reduction of the tracheal lumen). As was already mentioned by [Brouns et al. \(2007\)](#), this is an important observation, because it is exactly this pressure drop that causes breathing difficulties in patients suffering from an Upper Airway Obstruction (UAO). Given that respiration is controlled by the intrathoracic pressure, a strong pressure drop upstream of this region implies that a lower intrathoracic pressure is needed compared to a healthy person in order to draw a similar amount of air into the lungs.

---

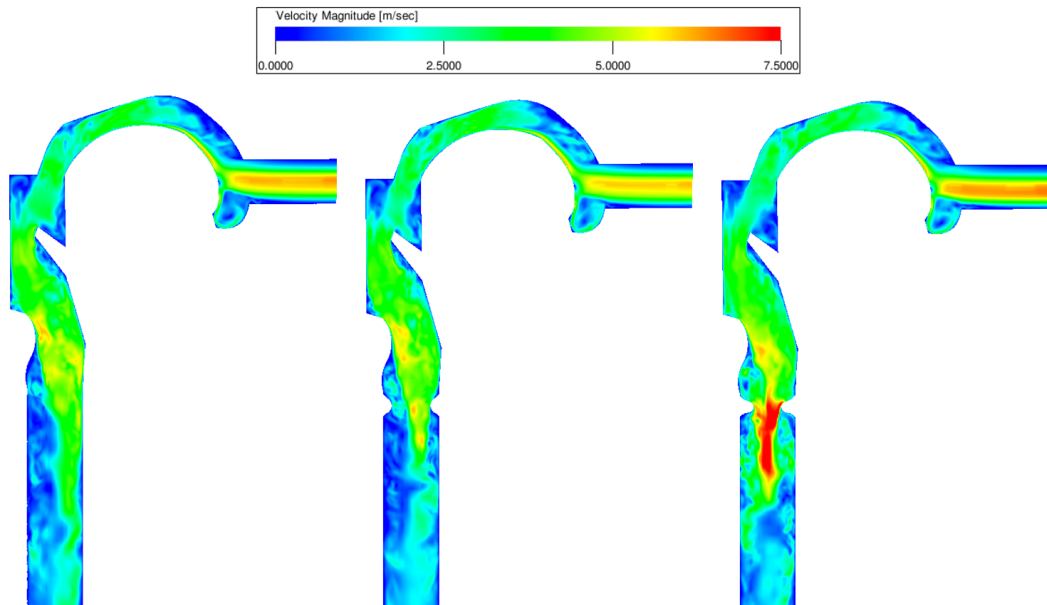
<sup>5</sup>The pressure levels shown in Figure (8.17) are obtained by averaging the pressure over the entire cross-section.



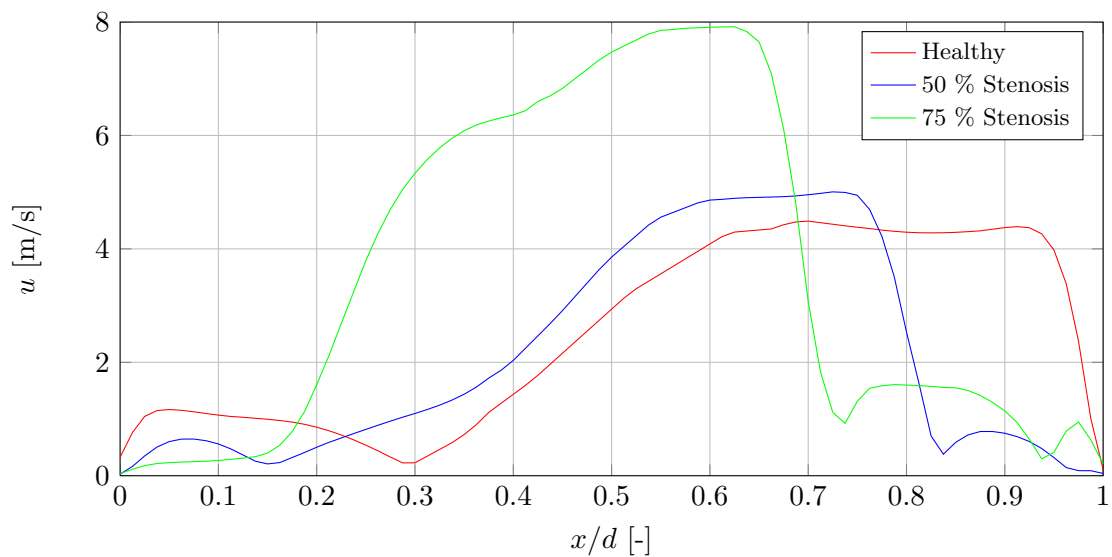
**Figure 8.11:** Snapshot of the instantaneous vertical velocity  $u_z$  (levels between -7 and 3 m/s) in the central sagittal plane, fine mesh. From left to right: healthy model, 50 % constriction, 75 % constriction.



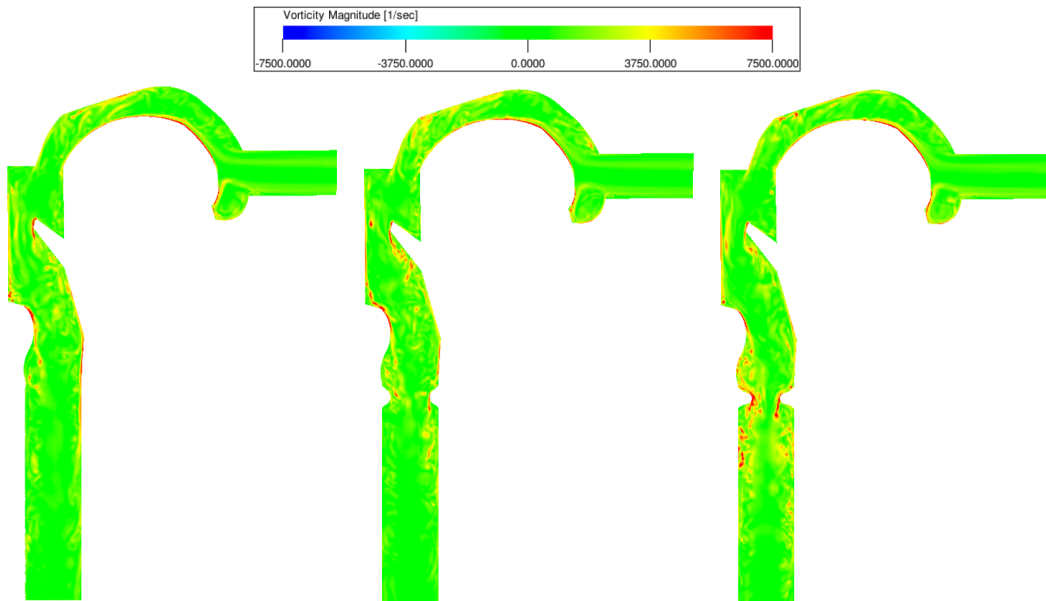
**Figure 8.12:** Snapshot of the average vertical velocity  $u_z$  (levels between -7 and 0 m/s) in the central sagittal plane, superimposed with a selection of streamlines, fine mesh. Areas in pink correspond to regions with positive vertical velocity. From left to right: healthy model, 50 % constriction, 75 % constriction.



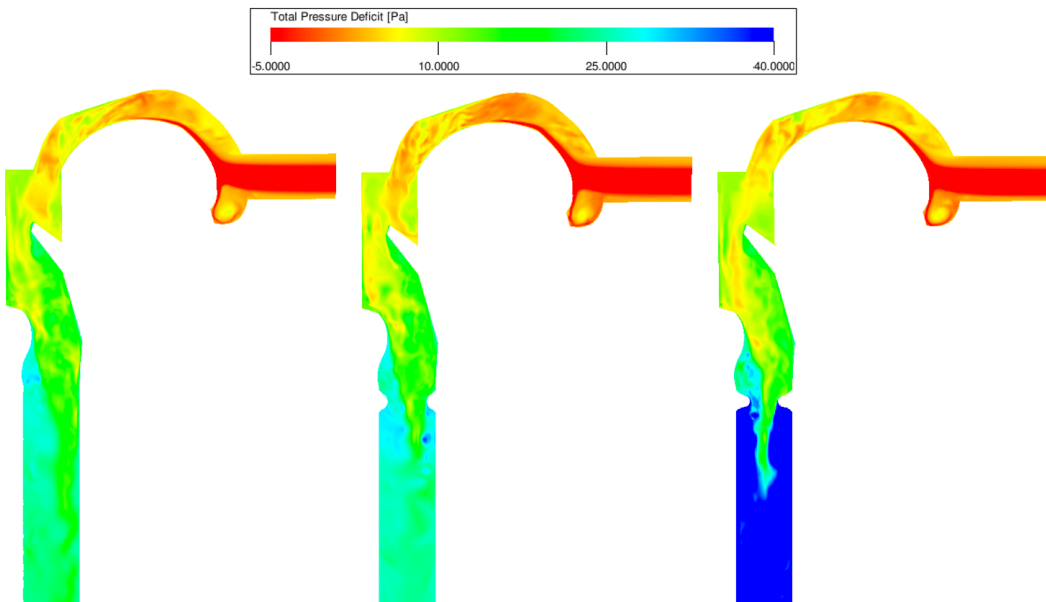
**Figure 8.13:** Snapshot of the instantaneous velocity magnitude  $\|\mathbf{u}\|$  (levels between 0 and 7.5 m/s) in the central sagittal plane, fine mesh. From left to right: healthy model, 50 % constriction, 75 % constriction.



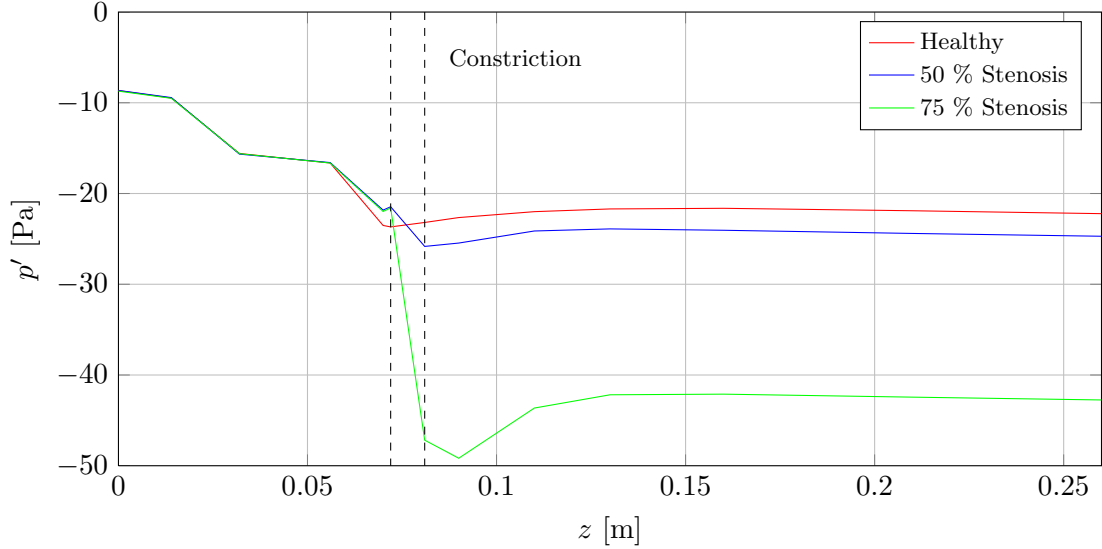
**Figure 8.14:** Comparison of the averaged velocity magnitude  $\|\mathbf{u}\|$  at the end of the constriction in the central sagittal plane, fine mesh.



**Figure 8.15:** Snapshot of the instantaneous vorticity magnitude  $\|\omega\|$  (levels between  $-7,500$  and  $7,500 \text{ s}^{-1}$ ) in the central sagittal plane, fine mesh. From left to right: healthy model, 50 % constriction, 75 % constriction.



**Figure 8.16:** Snapshot of the instantaneous pressure deficit  $p'$  (levels between  $-5$  and  $40 \text{ Pa}$ ) in the central sagittal plane, fine mesh. From left to right: healthy model, 50 % constriction, 75 % constriction.



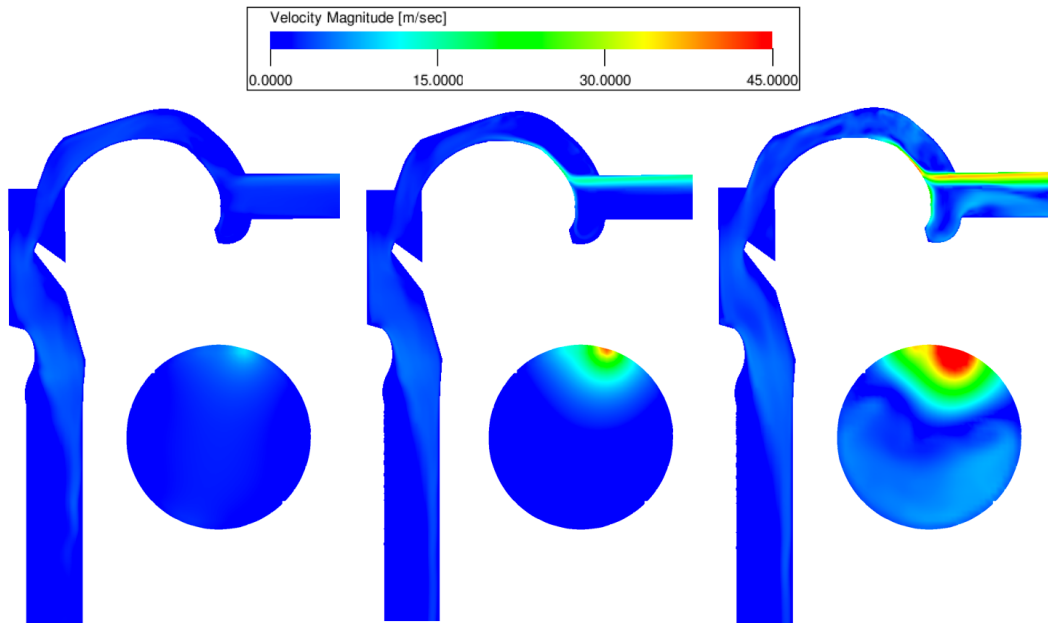
**Figure 8.17:** Comparison of the averaged pressure deficit  $p'$  in the pharyngeal-laryngeal-tracheal region, fine mesh. Positions are measured from the start of the oropharynx (Section B'-B in Figure (3.2)).

## 8.5 Aeroacoustic Simulations

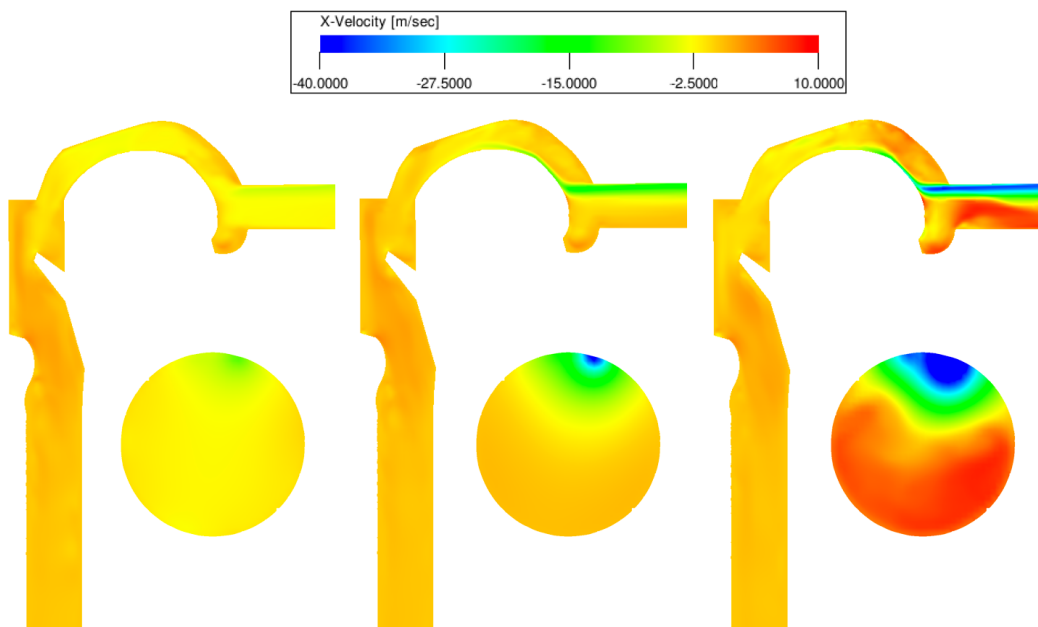
In the previous section it has been established unambiguously that the fine grid yields the most accurate flow results amongst all grids considered, especially in terms of resolved vorticity. Upon changing the Mach number ( $M$ ) setting from **Chosen by PowerFLOW** (CbP) to **Same as Experiment** (SaE) the reduction in timestep was approximately thirteen-fold ( $M_{CbP} = 0.09449 \rightarrow M_{SaE} = 0.00722$ ). This implies that the SaE computation has to run 13 times longer to simulate the same amount of physical time. Since this yielded an unacceptable computational cost of approximately 22,000 CPU hours it was decided to adopt a coarser mesh with  $17.84 \times 10^6$  voxels (6 cells/mm). This is reasonable because the fine mesh did not resolve a significantly larger amount of flow structures than the medium mesh. Nonetheless, this choice has been validated by running additional CbP simulations on all models, the flow results of which are included in Appendix E.1. For the sake of convenience, the newly introduced mesh will henceforth be addressed as ‘acoustic mesh’.

### 8.5.1 Mach Number: Chosen by PowerFLOW versus Same as Experiment

Upon analysis of the SaE results it became clear that PowerFLOW is not able to correctly model the flow field at the experimental Mach number. Note that this statement holds for all models, see Appendix E.2. After approximately 0.05s of simulation time a strong jet came into existence at the upper boundary of the inlet, which increased in strength and size until  $\sim 0.2$ s and then remained constant, see Figure (8.18). Due to the mass flow condition specified at the outlet this strong inlet velocity was countered by an outflow of fluid across the boundary in the lower portion of the inlet. This can be clearly deduced from the presence



**Figure 8.18:** Temporal evolution of the averaged velocity magnitude  $\|u\|$  (levels between 0 and 45 m/s), Mach Number Same as Experiment, healthy model, acoustic mesh. The front views are taken within 1 mm from the inlet boundary. Note the development of the erroneous jet at the inlet. From left to right: 0.05 s, 0.1 s, 0.29 s.



**Figure 8.19:** Temporal evolution of the averaged horizontal velocity  $u_x$  (levels between -40 and 10 m/s), Mach Number Same as Experiment, healthy model, acoustic mesh. The front views are taken within 1 mm from the inlet boundary. Note the strong backflow in the cylindrical inlet region. From left to right: 0.05 s, 0.1 s, 0.29 s.

of a region with positive horizontal velocity in Figure (8.19). While this flow solution does not violate the boundary conditions that were specified at the inlet and outlet, it does violate the no-slip condition. Moreover, it is an unphysical solution. While the exact reason(s) for this behavior is (are) unknown, it is very likely that it is due to the combined effects of the very low Mach number ( $M_{SaE} = 0.00722$ ) and the way in which the boundary conditions are implemented. Two attempts have been made to arrive at a correct flow field whilst adhering to the experimental Mach number. They are described in the following paragraphs.

### I: Fine Mesh

The first approach was to run the aeroacoustic simulation on the fine grid. It was expected that the increase in grid resolution (especially in the near-wall region) would yield a better response at the inlet boundary because there is a similar increase in the amount of flow details that can be resolved.

Although the simulation was not run for the same amount of physical time as the original SaE simulations (in order to limit the use of processing power), the occurrence of a jet at the inlet boundary was still very apparent, see Appendix E.3. It was therefore concluded that increasing the grid resolution (within reasonable bounds of computational cost) does not lead to more accurate flow results.

### II: Different Initial Conditions

In the second approach the initial conditions of the SaE simulation were changed. Instead of starting the simulation with uniform velocity and pressure settings it was initiated with the end result (checkpoint file) of the corresponding CbP simulation on the same grid. This could be achieved by adding the following command to the run file (note that this does not work for full checkpoint files):

```
exaqsu -seed checkpoint_file_name
```

Given the close resemblance between the CbP results and the benchmark data (see Section 8.4), the CbP solution should be roughly similar to the one that is modeled by an SaE simulation. More importantly, the SaE simulation does not have to cover the entire transient start-up period during which the inlet jet is initiated, and it was expected that this would avoid the initiation of the jet in the first place.

Unfortunately, the difference in initial conditions only delayed the convergence to the erroneous flow solution. This behavior indicates that PowerFLOW sees this as the only 'correct' solution to the flow problem. Moreover, it implies that the SaE simulation will never be able to model the correct flow field with the current boundary conditions. It should be noted that in order to limit the computational cost this seeding was only tested for the healthy and the 75 %-model, but there is no apparent reason to believe that the results would be different for the 50 %-model. The corresponding flow fields are included in Appendix E.4.



In order to validate the aforementioned statement concerning the unique solution, an additional case was considered in which the erroneous SaE checkpoint file was seeded to a CbP simulation on the same grid. As expected, the jet gradually disappears in favor of the original CbP solution (see Appendix E.5).

### III: Solution?

It can be concluded from the previous results that the SaE simulation will consistently converge to a solution that includes a jet at the inlet, independent of initial conditions or grid resolution. Consequently, the only means to arrive at the correct flow solution would be a change in the boundary conditions. This change is not limited to an adaptation in the type of boundary condition (e.g., velocity at the inlet, pressure at the outlet), but can also focus on an extension of the computational domain at the inlet. In fact, the latter option is preferred because the current boundary conditions closely resemble the actual breathing process.

Combining the uncertainty on how to specify a new boundary condition with the extensive computational time that is required to obtain a single result evidently makes the search for a new boundary condition a lengthy process. It was therefore decided not to perform such elaborate investigation but rather to include the acoustic results of the CbP simulation in Subsection 8.5.2.

#### 8.5.2 Aeroacoustic Results

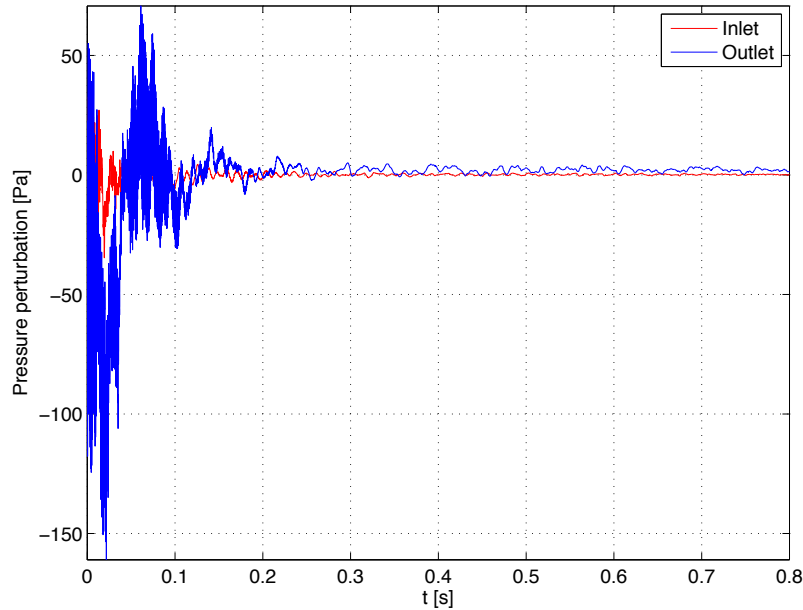
Due to the unavailability of accurate SaE flow data, this subsection discusses the acoustic spectra that are obtained from the CbP simulations. Because the higher Mach number impacts both the levels and the shape of the acoustic spectrum (see Chapter 7), the results that will be presented hereafter are not in accordance with reality. It remains important to discuss them because they will provide information on whether it is possible to distinguish the different models based on their acoustic spectra. If this holds true for CbP results, it will most likely also be possible to distinguish the models based on the eventual SaE spectra.

First and foremost, Figure (8.20) shows the pressure behavior over time as measured by the inlet and outlet probes. These probes are positioned at a normal distance of 3.78 and 3.35 mm as measured from the midpoint of the inlet and outlet boundary, respectively<sup>6</sup>. Since it is evident that the transient start-up effects extend until approximately 0.25 s, this timeframe was excluded from the spectral analysis. All other processing parameters can be found in Chapter 5.

Secondly, it is important to mention that the healthy and 50%-models were ran at a different Mach number ( $M = 0.09449$ ) than the 75%-model ( $M = 0.06299$ ). This difference is caused by the dissimilarity in **Maximum Expected Velocity** between the two simulations

---

<sup>6</sup>In the current model these positions have the following coordinates (in mm): inlet (80, -26, 112.3), outlet (-17.02, -25.98, -221).



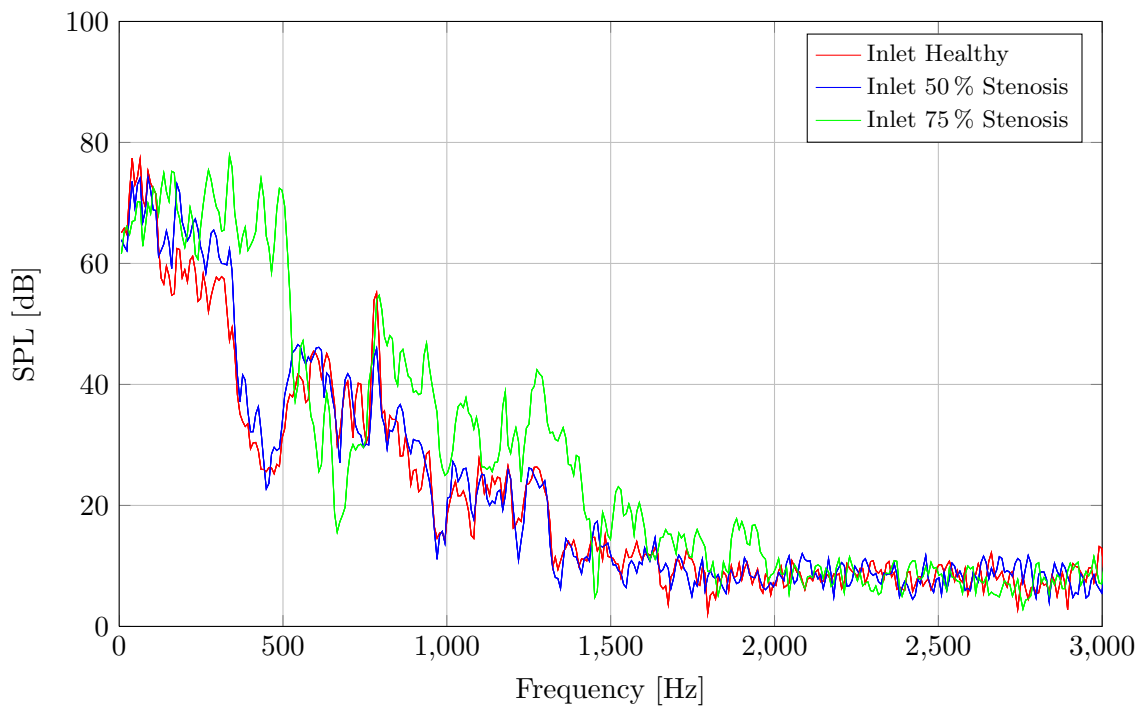
**Figure 8.20:** Pressure perturbation as measured by the acoustic probes, healthy model, Mach Number Chosen by PowerFLOW. Note the transient start-up prior to  $t = 0.25$  s.

(5 m/s for the healthy and 50 %-models versus 7.5 m/s for the 75 %-model)<sup>7</sup>. Although the exact influence of the Mach number is yet unknown, it is clear that this difference might complicate the comparison.

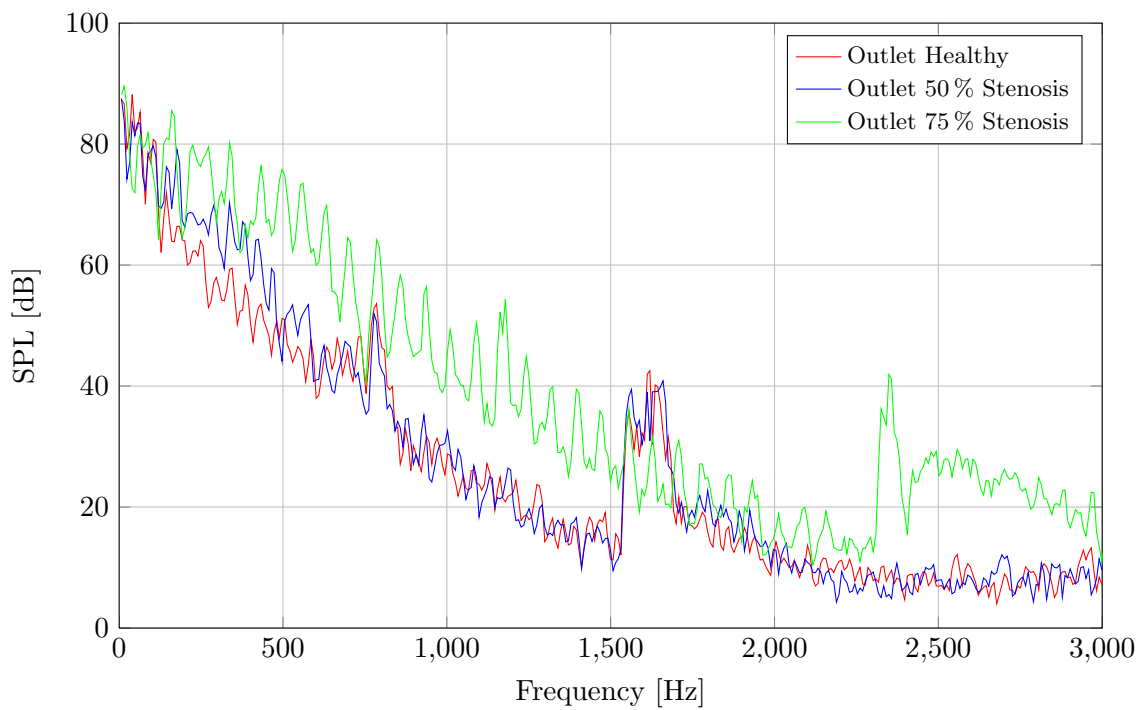
Figures (8.21) and (8.22) display the acoustic spectra at the inlet and outlet of all three models, respectively. In general the Sound Pressure Levels (SPLs) are very similar for the healthy model and the 50 %-model, while the 75 %-model leads to stronger pressure perturbations. This difference is more pronounced at the outlet probe, where the pressure levels of the 75 %-model are 5 to 10 dB higher. It should be mentioned that the general increase in SPL with increasing luminal obstruction is compliant with the flow results of Section 8.4. There it was already anticipated that the increased vorticity levels would lead to higher noise levels.

At this point it is interesting to study the differences between the inlet and outlet spectra into more detail. The discussion is split in two parts. The first part will elaborate on the overall difference in pressure levels between the inlet and outlet probes, while the second part will focus on the shape of the acoustic spectra.

<sup>7</sup>The **Maximum Expected Velocity** has to be specified in PowerCASE and is used by the program to calculate the upscaled Mach number in case the CbP setting is chosen. There exists an inversely proportional relation between the two parameters. Although it was not investigated how a change in the **Maximum Expected Velocity** would influence the flow field, it is known that PowerFLOW issues a non-critical warning whenever this velocity is exceeded somewhere in the flow field. Subject to the requirement of not triggering this warning, the **Maximum Expected Velocity** is generally kept as low as possible because this allows for higher Mach numbers and hence faster simulations. For the healthy and 50 %-models a value of about 5 m/s was found to be most suitable, while the stronger jet in the 75 %-model necessitated an increase to 7.5 m/s in order to avoid the PowerFLOW-warning.



**Figure 8.21:** Sound Pressure Levels at inlet probes for the healthy and constricted models,  $f_s \approx 35.1$  kHz,  $\Delta f \approx 8$  Hz.



**Figure 8.22:** Sound Pressure Levels at outlet probes for the healthy and constricted models,  $f_s \approx 35.1$  kHz,  $\Delta f \approx 8$  Hz.

## I: Difference in SPL between Inlet and Outlet Probes

The overall increase in pressure levels at the outlet can be assessed by investigating the location of acoustic source regions. First it should be recalled that the noise in this test case stems only from quadrupole and dipole sources, because monopole sources were not yet accounted for. Ideally, the magnitude of these two sources should be plotted in the same units such that their relative importance can be estimated. Because PowerFLOW does not include an easy means to extract those source terms in a form that is equal to the one by which they appear in Curle's acoustic analogy (see Chapter 5), it was decided to estimate their magnitude by comparable measures. Although this is not the best solution, it still offers the opportunity to localize those regions that inhibit an increased amount of noise sources.

For the quadrupole sources the measure is the divergence of the Lighthill tensor ( $\nabla T_{ij}$ ), while the surface force magnitude ( $\|\mathbf{F}\|$ ) acts as a measure for the dipole source strength. It should be stressed once more that the absence of direct quadrupole and dipole measures prevents a comparison between the strength of these separate signals. Nevertheless, an in-depth investigation into these signals is only required in the process of determining an accurate scaling factor between CbP and SaE results. Note that the potential of such scaling method has already been discussed extensively in Chapter 7.

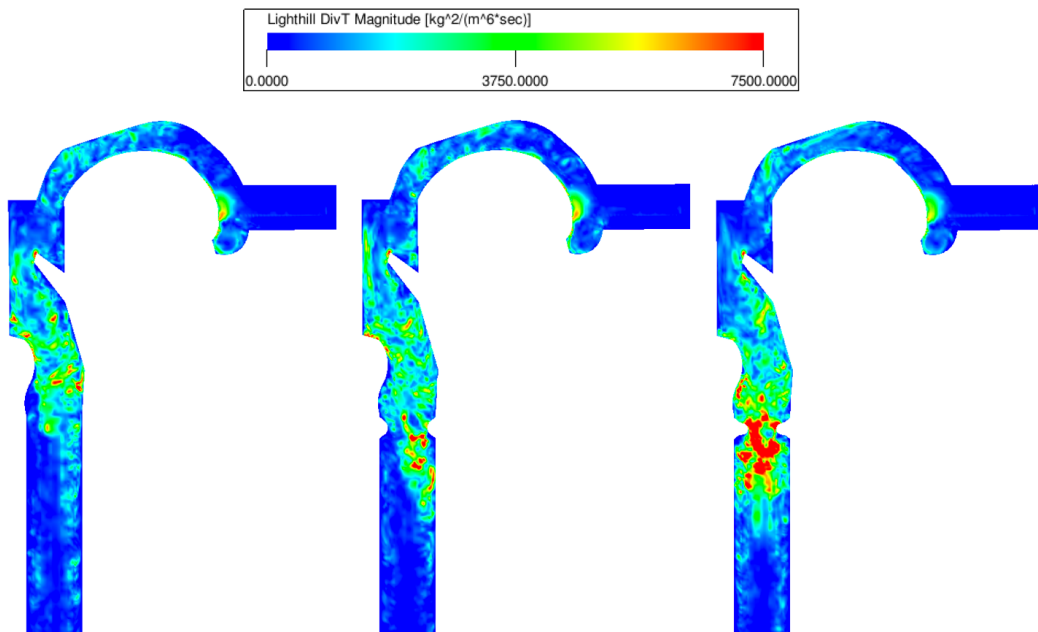
The measures for the quadrupole and dipole sources are shown in Figures (8.23) and (8.24), respectively. With regard to the quadrupole sources it can be observed that they are similar for all models in the region above the constriction.<sup>8</sup> Downstream of the constriction, a stronger mixing in the models with a higher percent of luminal obstruction (due to the combined effect of increasing velocity and different jet direction) causes an increase in vorticity and consequently also an increase in quadrupole noise sources. The presence of this enhanced mixing is further exemplified by the increased levels of turbulent kinetic energy for the constricted models, displayed in Figure (8.25). From this figure it can also be discerned that the levels are similar to the ones predicted by [van der Velden et al. \(2015\)](#).

The measure for the dipole sources follows a similar pattern. Although it can be argued that the difference between the healthy and 50 %-model is smaller compared to the quadrupole sources, this is mainly due to the color scaling. Upon closer examination it can be seen that the 50 %-model displays slightly larger force magnitudes.

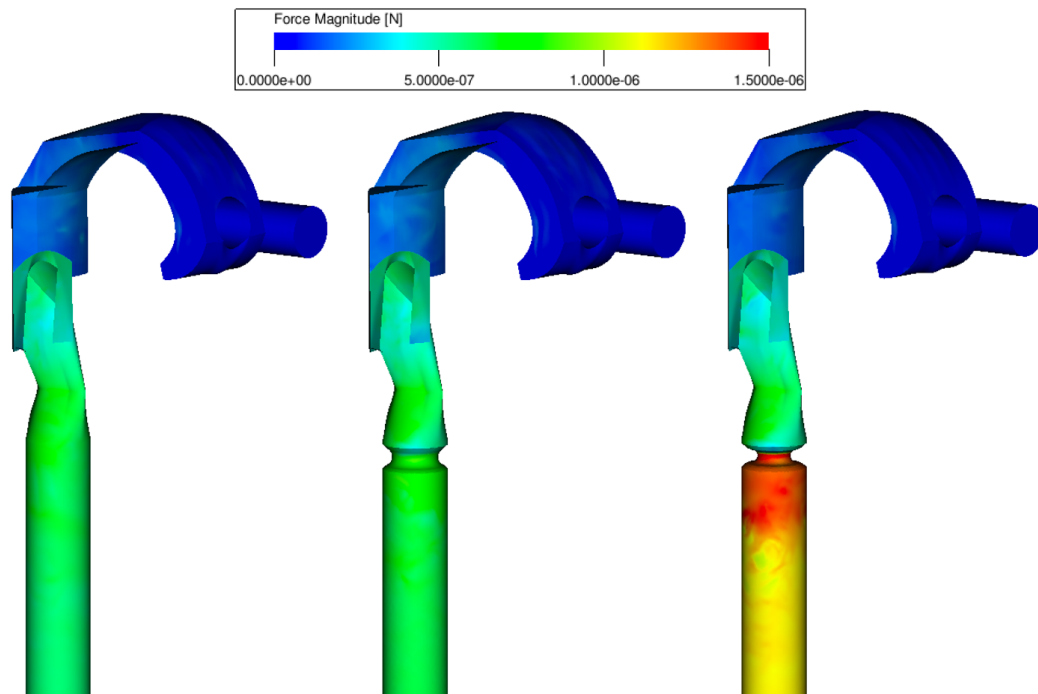
The observation that the majority of the noise sources is created downstream of the constriction is an important element in the explanation of the lower pressure levels at the inlet. Essentially, the decrease in luminal cross-sectional area at the level of the constriction (as well as the glottis) prevents part of the pressure signals to propagate upstream, which leads to an immediate reduction in SPLs at the inlet. This phenomenon also explains why the discrepancy between inlet and outlet spectra is largest for the 75 %-model, which has the largest degree of luminal obstruction. It should be noted here that similar results were obtained by [van der Velden \(2012\)](#).

---

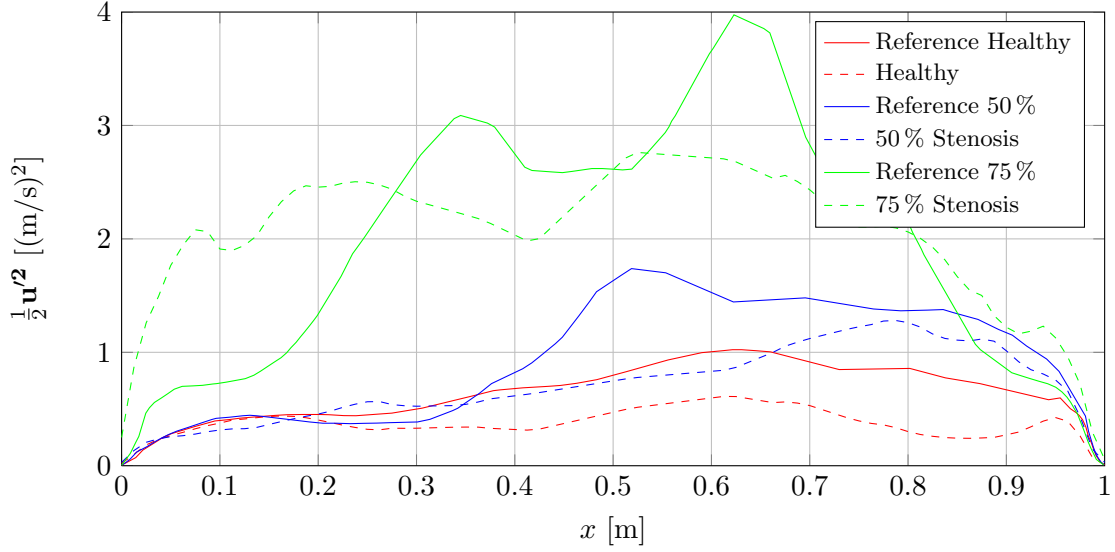
<sup>8</sup>Note that the small differences can be attributed to the fact that these are instantaneous figures which may vary from one timestep to the next, especially for unsteady flow.



**Figure 8.23:** Snapshot of the instantaneous divergence of the Lighthill tensor  $\nabla T_{ij}$  (levels between 0 and  $7,500 \text{ kg}^2/(\text{m}^6\text{s})$ ), a measure for the strength of quadrupole sound sources, in the central sagittal plane, acoustic mesh. From left to right: healthy model, 50 % constriction, 75 % constriction.



**Figure 8.24:** Snapshot of the instantaneous force magnitude  $\|\mathbf{F}\|$  (levels between 0 and  $1.5 \times 10^{-6} \text{ N}$ ), a measure for the strength of dipole sound sources, acoustic mesh. From left to right: healthy model, 50 % constriction, 75 % constriction.



**Figure 8.25:** Comparison of turbulent kinetic energy ( $k$ ) profiles in the central sagittal plane, 20 mm downstream of constriction, with reference data from [van der Velden et al. \(2015\)](#).

A final distinction between the inlet and outlet probes is related to the steady-level background noise, which is reached at  $f \approx 1,800$  Hz for the inlet probe and  $f \approx 2,300$  Hz for the outlet probe (with the exception of the 75%-model). The fact that this level is reached at a different frequency for the inlet and outlet probes can once more be related to the difficult propagation of acoustic waves through the constriction/glottis. The source of this background noise is the mesoscopic character of the Lattice Boltzmann Method (LBM). Besides resolving the macroscopic flow behavior, the LBM also models the continuous collision between individual (collection of) particles at the mesoscopic level (see Chapter 4). It is this collision process that is mainly responsible for the background noise (and which is not modeled by the Navier-Stokes equations). It would be interesting to perform an additional simulation with zero mean-flow in order to obtain more information regarding this subject.

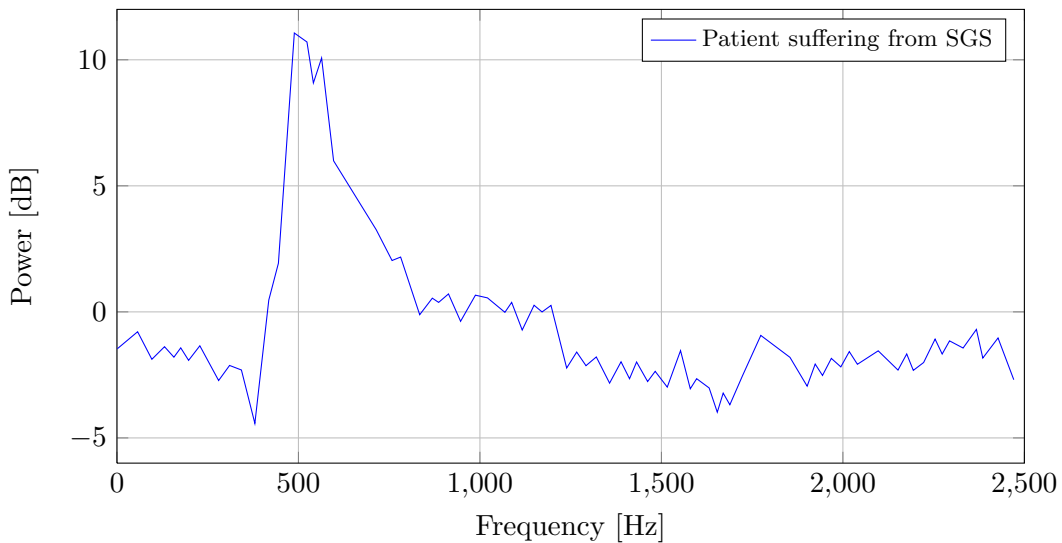
## II: Shape of the Acoustic Spectra

Next to the discrepancy in overall pressure levels, the probes also measured a different shape of the acoustic spectrum. Regardless of the probe position, a first observation is that the 75%-model appears to have experienced a frequency shift with regard to the healthy and 50%-models. This might be related to the aforementioned difference in Mach number.

At the inlet probe all spectra experience a sharp decrease in pressure levels at  $f \approx 500$  Hz. A tonal peak can be discerned for all models at  $f \approx 780$  Hz, while the 75%-model has another tonal peak at  $f \approx 1,275$  Hz. The plateau at frequencies below 500 Hz might be attributed to an unphysical standing wave between the inlet and the outlet, which is centered at a frequency of  $f = v/\lambda \approx 173$  Hz (where  $\lambda$  is the wavelength and  $v$  the wave propagation speed). It is expected that these high SPLs would diminish, if not disappear, upon the implementation of a suitable NRBC.

At the outlet probe two tonal peaks can be discerned for each model. In case of the healthy and 50%-models, the first peak coincides with the one measured at the inlet probe ( $f \approx 780$  Hz), while a second and broader peak is visible around  $f \approx 1,600$  Hz. The 75%-model shows a first sharp tonal peak at  $f \approx 1,170$  Hz, which is about 100 Hz lower than the one measured at the inlet. Similar to the other models, a second broader peak can be seen at  $f \approx 2,350$  Hz. At higher frequencies the behavior of the spectrum is somewhat different compared to the healthy and 50%-models.

As mentioned before, the limitations of the results prohibit a comprehensive discussion regarding the link between the simulated spectra and stridor signals produced by actual patients suffering from Subglottic Stenosis (SGS). Nonetheless, it is instructive to investigate how a typical SGS-signal would look like. Surprisingly, there is not a lot of (publicly available) research that presents an acoustic analysis of stridor signals from real patients, see Chapter 2. [Gray et al. \(1985\)](#) and [Zwartenkot \(2010\)](#) are two notable exceptions, and both indicate that a typical SGS-spectrum consists of broadband noise with one or multiple sharp tonal peaks. An example of such signal (acquired from a one-year-old boy) is shown in Figure (8.26). Although it can be argued that the acoustic spectra presented here also inhibit such sharp tonal peaks, they are equally visible for the healthy model. Therefore, there is no particular reason to believe that these spectra actually represent an SGS-signal, except for the increase in broadband pressure levels with increasing percent of luminal obstruction.



**Figure 8.26:** Power spectrum of infantile stridor, acquired from a one-year-old boy who suffers from subglottic stenosis (SGS). Figure taken from [Gray et al. \(1985\)](#). Note that [Gray et al. \(1985\)](#) refer to the power scale as ‘arbitrary’.

Next to the fact that the Mach number is not matched, there are two other reasons that might explain this discrepancy. Firstly, the model under consideration does not cover the intricate geometry of a real upper airway. Secondly, monopole sources have not been accounted for. The latter issue might be especially important as was already indicated by [van der Velden et al. \(2015\)](#), and it will be discussed further when dealing with a realistic upper airway model in Chapter 9.

## 8.6 Conclusions

The acoustic results presented in this chapter remain subject to two major uncertainties. Firstly, the simulations were ran at an accelerated Mach number because PowerFLOW is unable to deal with the experimental Mach number. Due to time restrictions the reason(s) behind this anomaly were not further investigated, but it is strongly recommended to resolve this problem prior to any future attempts at simulating the aeroacoustic flow field through the upper airway. Secondly, monopole sources were not taken into account, mostly because the coupling between the fluid and the airway walls cannot be integrated within the PowerFLOW software. External coupling is certainly possible but this topic requires further research.

Regardless of the ‘roughness’ of the results, some important conclusions can be drawn regarding the aspects of the flow field through both healthy and stridorous upper airways. Firstly, the results indicate that there exists a certain threshold constriction below which the flow field is nearly independent of the constriction diameter. Also, a luminal obstruction of 50% is expected to introduce minimal breathing difficulties in the patient due to a very limited pressure drop over the constriction. Moreover, it is expected that such patient would not present with stridor. The validness of this statement is provisional as it remains subject to the aforementioned restrictions.

The most important outcome of the efforts presented in this chapter is that they proved that PowerFLOW can reliably simulate the fluid flow through an upper airway, albeit at an upscaled Mach number. This provided the certainty that was required before switching to a realistic upper airway model in Chapter 9.



---

## Chapter 9

---

# Realistic Upper Airway Model

The final stage of this thesis will focus on an investigation of the aeroacoustic flow field within a Realistic Upper Airway Model (RUAM). Although it is acknowledged that the development process is not yet sufficiently advanced as to start the assessment of RUAMs<sup>1</sup>, the timeframe of this research project is limited and the author wants to provide future researchers with a broad knowledge base. Besides, it is always tempting to peek one step ahead, and this was another important driver in the decision to include this chapter. It will provide additional insights into the fluid flow through actual airway systems, as well as the ways in which the acoustic spectra differ from their simplified counterparts.

It is advised that the reader approaches this chapter as a sort of preliminary insight into what might be achieved with this method. The proper sequence of research steps will be further discussed in Chapter 11, which contains a comprehensive road map that sets out the milestones in the development process of the non-intrusive diagnostic tool for Upper Airway Obstructions (UAOs).

Lynch (2012) and van der Velden (2012) were the first ones to simulate the aeroacoustic flow field through a realistic airway model. Although their results are insufficiently validated to be used as benchmarks, it was decided to adopt the same geometry. The reasoning behind this model choice will be explained in Section 9.1, which also contains a short description of the peculiarities of the geometry. Next, Section 9.2 discusses the choice of boundary conditions. Section 9.3 will then elaborate on the flow patterns that are present within the RUAM, thereby exposing the main differences with respect to the SUAM flow fields. Finally, Section 9.4 presents the acoustic characteristics of the case, including a summary of the pioneering work of van der Velden et al. (2015) and the outcomes of the experimental Mach number ( $M$ ) simulations.

---

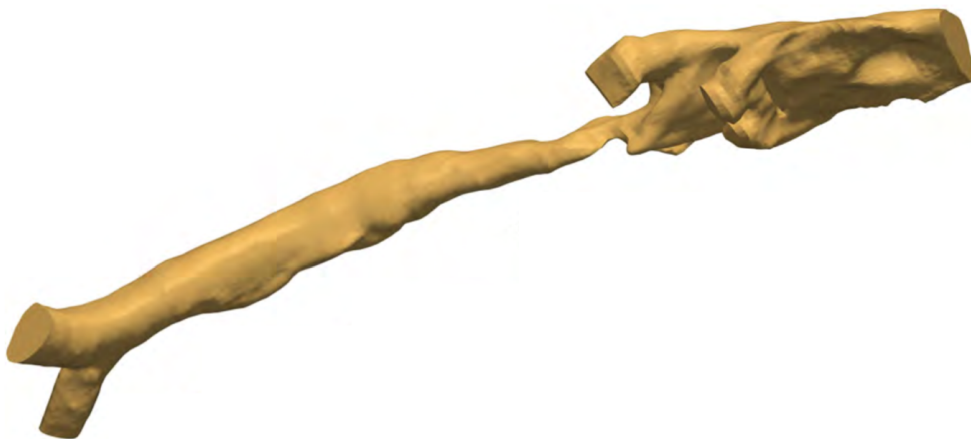
<sup>1</sup> Note that this is especially true when considering the fact that PowerFLOW was not able to model the flow field through the Simplified Upper Airway Model at the experimental Mach number, see Chapter 8.

## 9.1 Model Geometry

Figure (9.1) shows a three-dimensional picture of the RUAM, taken from an angle that enables a clear view of all its features. Although Chapter 3 contains a general description of the model, there are some peculiar geometrical attributes that require further explanation.

First and foremost, it can be perceived that the model starts at the nasopharynx instead of the oral cavity. It also covers the entire length of the trachea and a small portion of the primary bronchi, which causes it to have a double outlet. These changes with respect to the simplified model will impact the way in which the boundary conditions are specified. For instance, the flow might become turbulent and/or separate prior to the start of either the nasopharynx or the oropharynx (depending on the breathing route). Also, the acoustic signal needs to be measured at the start of the nasopharynx, which implies that it is not representative for the signal that would be acquired directly from the patient. While this prevents a thorough comparison with benchmark data, it should (unfortunately) not be considered an issue due to the unavailability of any reliable patient measurements. Moreover, similar to the discussion on the acoustic signal for the Simplified Upper Airway Model (SUAM), the major goal here is to investigate whether it is possible to distinguish between the healthy and stridorous breathing sounds.

The two extensions that can be discerned at the anterior side of the model are in fact air pockets caused by tissue that is connected to the epiglottis. Similar appendages at the posterior side resemble connections to the esophagus. Another feature that was not present in the SUAM is the v-shaped protrusion at the level of the glottis. It is caused by the connection points of the vocal cords.



**Figure 9.1:** Three-dimensional view of the Realistic Upper Airway Model, which has been built from Computed Tomography images. Picture taken from [van der Velden \(2012\)](#).

As was already mentioned in Chapter 3, the original model was acquired from a patient who suffered from Subglottic Stenosis (SGS). Figure 9.1 shows that the constriction is positioned just below the vocal cords. [Lynch \(2012\)](#) later performed ‘virtual surgery’ on the model in order to obtain the healthy counterpart of this in vivo model. These adaptations were

performed in consultation with dr. H.L.J. Hoeve, a pediatric otorhinolaryngology specialist at the Erasmus Medical Center.

In order to omit ambiguities in the remainder of the discussion, the models will consistently be referred to as the healthy and stridorous model. W. van der Velden, a researcher at the Delft University of Technology, provided .stl-versions of both models, which were slightly adapted in order to ensure their correct (and simplified) use in PowerFLOW. The steps that were taken to incorporate these changes are clearly described in Chapter 8.

## 9.2 Boundary Conditions

Since the human airway is built from compliant material it assumes a different form throughout the respiration cycle. This implies that the boundary conditions should correspond to the ones that act on the upper airway when the Computed Tomography (CT)-images are acquired. Given that the CT-scan was taken during inspiration, the model was fitted with boundary conditions that mimic steady inspiratory conditions.

It is assumed that the patient was breathing slowly during the CT-scan. According to Hooper (2001), this respiratory condition corresponds to a mass flow between 5 and 12 L/min (see Chapter 2). It was decided to adopt a mass flow at the high end of this range (12 L/min) for two reasons. Firstly, the patient was known to be suffering from non-critical SGS at the time of image acquisition, which most likely induced a slightly different breathing pattern with a tendency towards larger air intakes. Secondly, this mass flow was also adopted by Lynch (2012) and van der Velden (2012) in their studies, and it might be interesting for future researchers to have a broader database of simulations that were ran at similar conditions.

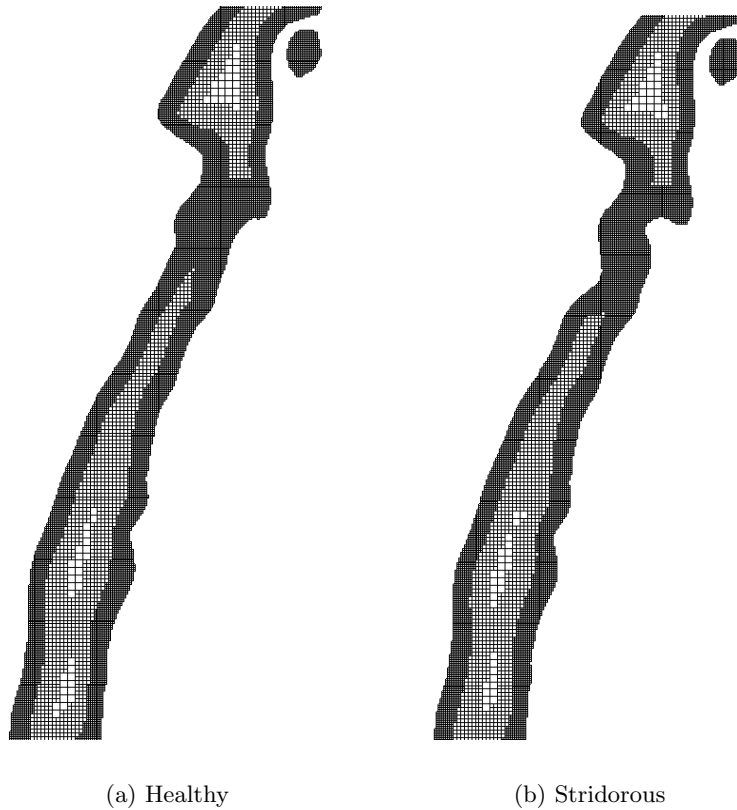
Although the flow conditions at the level of the nasopharynx differ from those at the entrance to the oral cavity, it was decided to adopt a constant static pressure boundary condition at the inlet (equal to the atmospheric pressure). The situation at the outlet is more complicated because there are two outlets with a slightly different cross-sectional area. De Backer et al. (2008a) showed that the outflow at the bronchi is not only related to the cross-sectional area. It would therefore be physiologically incorrect to divide the mass flow between the bronchi based only on their respective outlet areas. Ideally, the mass flow at each outlet should be determined directly from the patient, e.g., by means of gamma scintigraphy De Backer et al. (2008a). Once the patient-specific outlet conditions are known, the best way to implement them would be through an iteratively changing outlet pressure. Evidently, such boundary condition cannot be easily implemented within PowerFLOW, nor is there any information available regarding the mass flow division between the two bronchi. For the sake of simplicity, it was decided to divide the mass flow of 12 L/min equally over both bronchi, i.e., 6 L/min for both the left and the right bronchus. These simplifications are justified given the preliminary nature of this study. All airway walls are fitted with no-slip boundary conditions.

For reasons similar to the ones presented with regard to the SUAM in Chapter 8, no use has been made of Nonreflecting Boundary Conditions (NRBCs). In fact, it would be even more

difficult to elongate the RUAM at the inlet and outlets due to the strongly irregular shape of its cross-section at these positions.

### 9.3 Fluid Flow Results

Given that this is a preliminary investigation into the aeroacoustic flow characteristics of a RUAM, it was decided not to execute a grid convergence study. Instead, all models were fitted with a slightly adapted version of the acoustic mesh (6 cells/mm) presented in Chapter 8, including additional refinements around the vocal cords and the constriction, see Figure (9.2). This yielded a total of  $7.51 \times 10^6$  voxels for the healthy model and  $7.46 \times 10^6$  voxels for the stridorous model. With regard to the boundary-layer resolution it should be mentioned that both grids achieved  $y^+$ -values that were smaller than 5, except at the level of the glottis and the constriction, see Appendix F.1.



**Figure 9.2:** Computational grids of the RUAM geometry in the central sagittal plane, every second grid line is shown, acoustic mesh ( $\sim 7.5 \times 10^6$  voxels).

Figure (9.3) compares the vertical velocity fields (as measured in the central sagittal plane) of the healthy and stridorous models. This figure indicates that the flow fields are very similar throughout the entire airway. In fact, they are nearly identical up until the level of the

glottis, which was expected due to the fact that there exist no dissimilarities between both geometries in this particular region. It is interesting to see that the flow features in this region are similar to the ones that were present in the SUAM. For example, a small recirculation region appears at the posterior wall of the oropharynx as a result of the changing flow direction towards the larynx. This is further exemplified by Figure (9.4), which displays the average vertical velocity fields superimposed with a selection of streamlines (areas in pink correspond to recirculation regions). The figure additionally identifies a smaller recirculation region in the v-shaped protrusion of the vocal cords for the stridorous model.

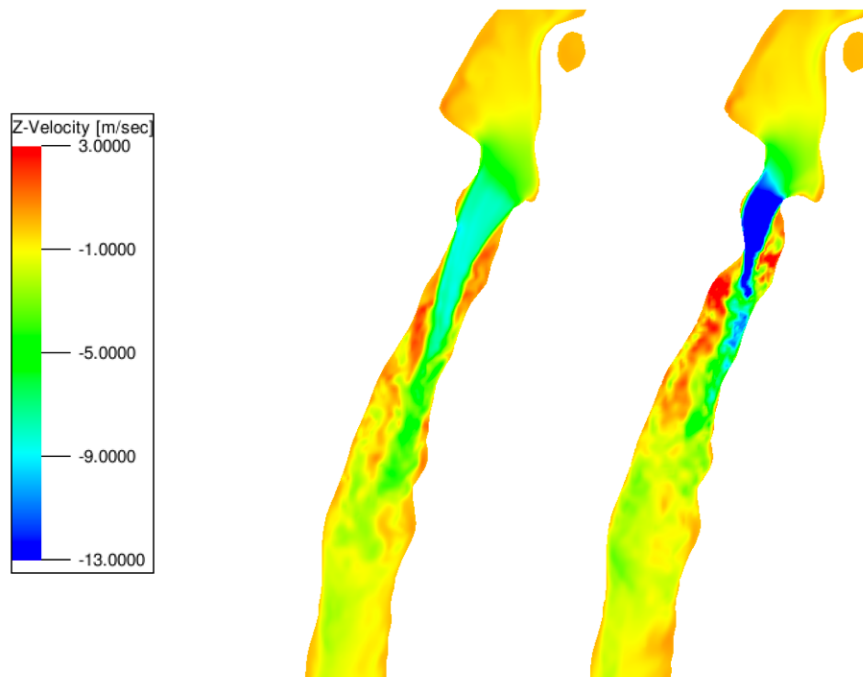
Further downstream, a strong jet comes into existence and attaches to the anterior wall of the trachea for both models. It should however be mentioned that it is initially deflected posteriorly. Figure (9.4) also shows that the jet is accompanied by two elongated recirculation regions.

The effects of the SGS on the flow field are twofold. The strong reduction in cross-sectional area causes the recirculation regions to have a different shape and location compared to the healthy model. Anteriorly, the sudden contraction and expansion causes the flow to separate faster than is the case for the healthy model, additionally leading to a broader recirculation region. Posteriorly, the strong deflection of the jet causes the recirculation region to be much wider. This induces a more efficient mixing process which partially explains why the region is shorter than its healthy counterpart.

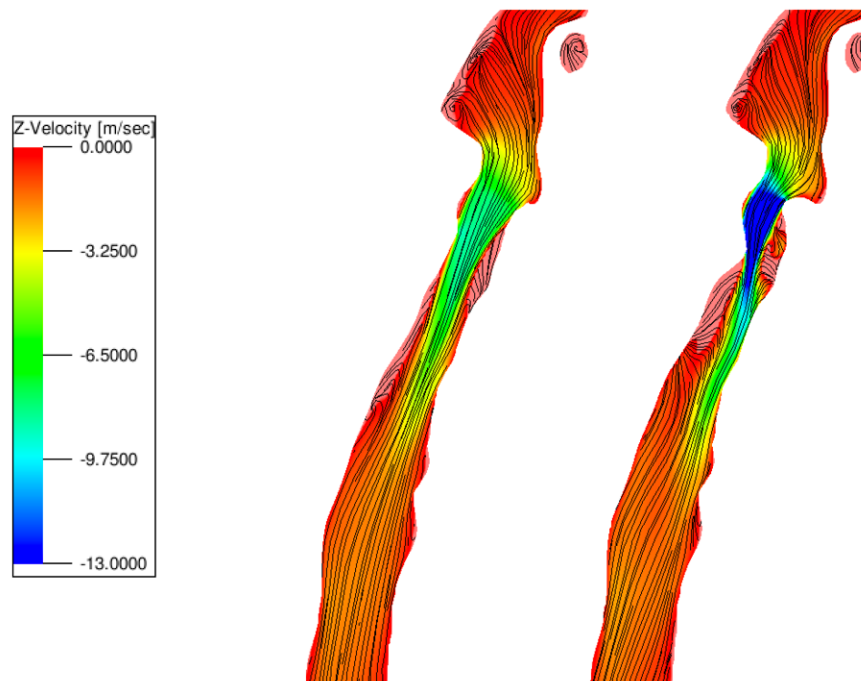
The constriction also induces a stronger jet velocity. This is confirmed by the velocity magnitude fields presented in Figure (9.5). While the healthy model achieved a maximum (averaged) jet velocity of 8.91 m/s at the end of the constriction, the stridorous model reached a velocity of 18.75 m/s, which is approximately 110% higher. Compared to the constricted SUAM results, it can be argued that the realistic SGS has a much stronger impact on the flow field (recall that the 75%-model had a maximum jet velocity that was 75% higher than the healthy model). The shape of the velocity profiles can be seen in Figure (9.6).

Another interesting parameter is the vorticity magnitude due to its connection to the strength of quadrupole sound sources (see Chapter 5). It is compared for both models in Figure (9.7), where it can be seen that the vorticity levels are clearly higher for the stridorous model. Besides, the vorticity within this model has a much larger spread, especially near the anterior wall. This might be explained by the presence of stronger mixing in the shear layer as a result of the increased jet velocity. More importantly, the increased vorticity levels point to a more intense sound radiation for the stridorous model.

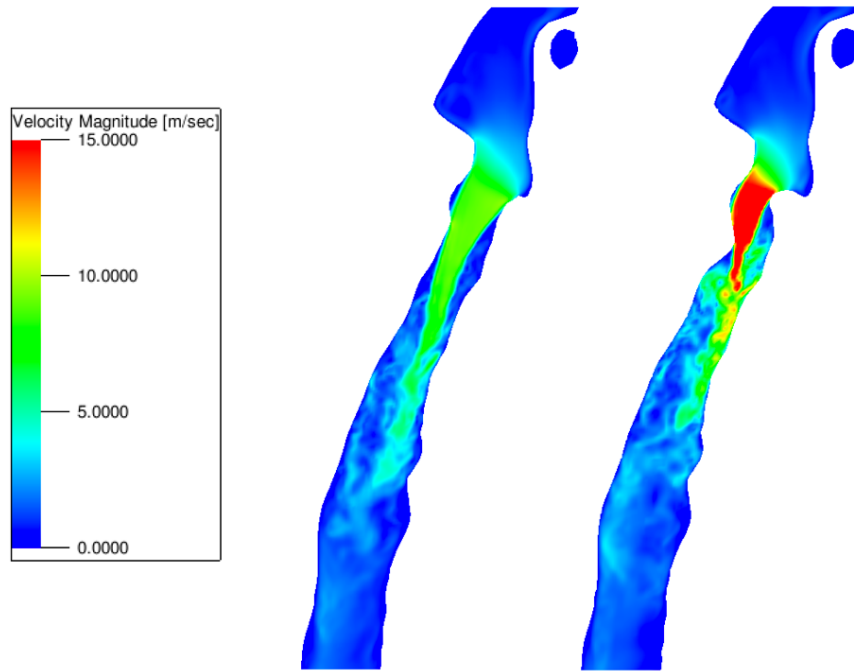
Finally, Figure (9.8) compares the evolution of the pressure deficit. Clearly, the stridorous model demonstrates a much stronger pressure drop over the constriction. Quantitative analysis indeed showed that the averaged pressure drop over the constriction equals  $\Delta P = 24.12$  Pa for the healthy model and  $\Delta P = 149.96$  Pa for the stridorous model. Further comparison with the SUAM pressure data from Chapter 8 revealed that the pressure drop is much larger when dealing with realistic models. Based on these results it can be concluded that the stridorous patient most likely experiences serious breathing difficulties as a result of the SGS.



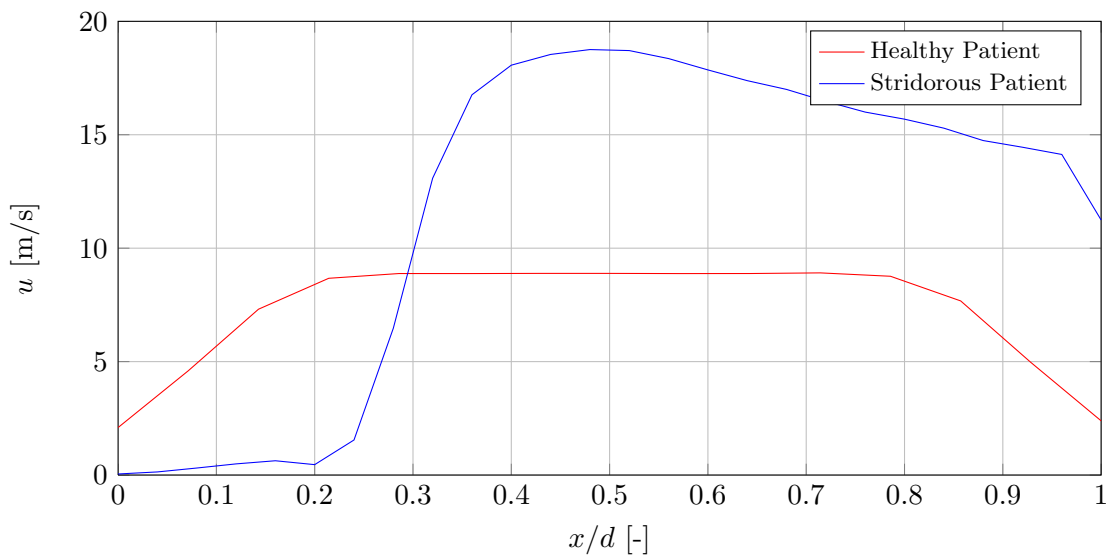
**Figure 9.3:** Snapshot of the instantaneous vertical velocity  $u_z$  (levels between -13 and 3 m/s) in the central sagittal plane, acoustic mesh. From left to right: healthy model, stridorous model.



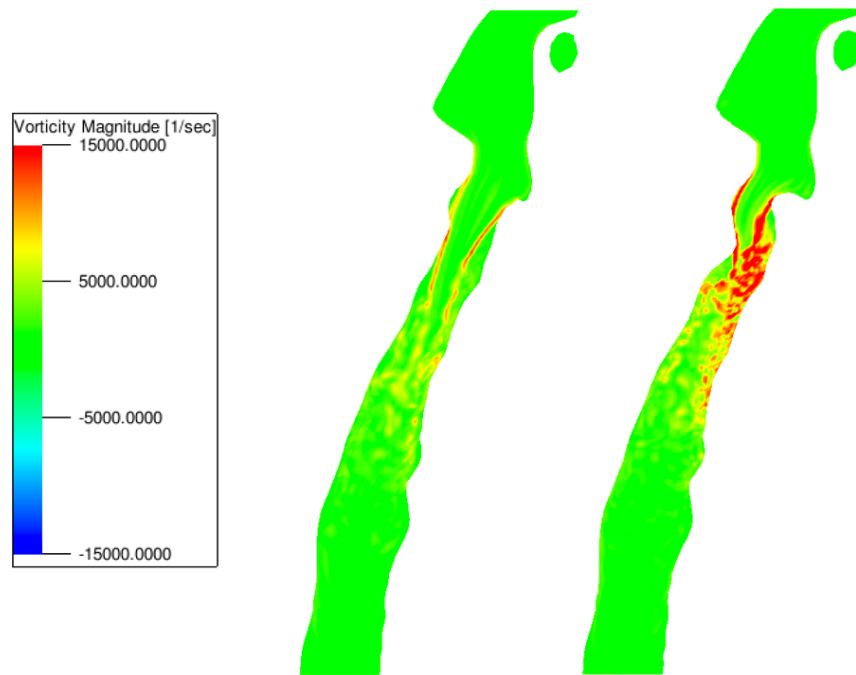
**Figure 9.4:** Snapshot of the average vertical velocity  $u_z$  (levels between -13 and 0 m/s) in the central sagittal plane, superimposed with a selection of streamlines, acoustic mesh. Areas in pink correspond to regions with positive vertical velocity. From left to right: healthy model, stridorous model.



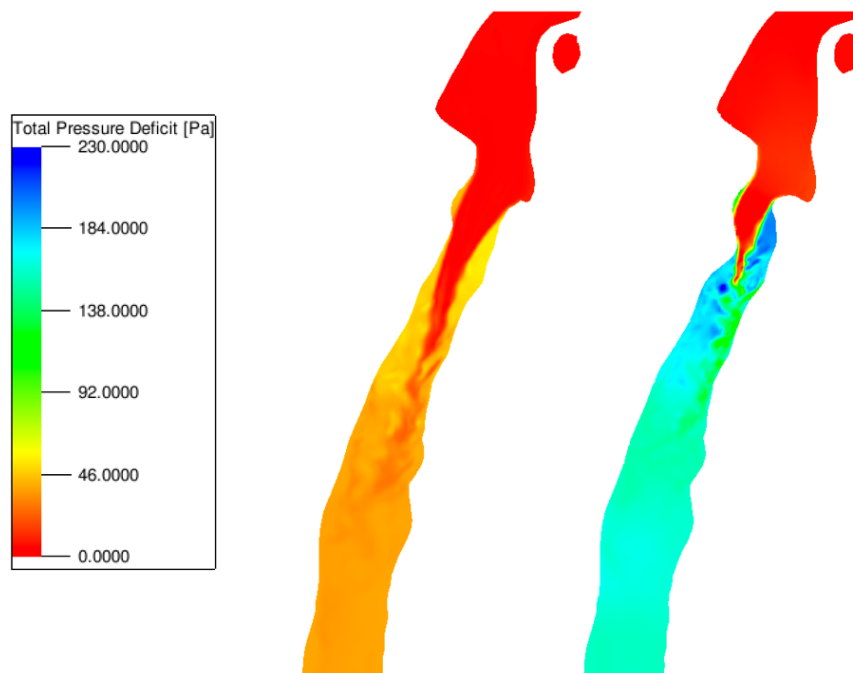
**Figure 9.5:** Snapshot of the instantaneous velocity magnitude  $\|\mathbf{u}\|$  (levels between 0 and 15 m/s) in the central sagittal plane, acoustic mesh. From left to right: healthy model, stridorous model.



**Figure 9.6:** Comparison of the averaged velocity magnitude  $\|\mathbf{u}\|$  at the end of the constriction in the central sagittal plane, acoustic mesh.



**Figure 9.7:** Snapshot of the instantaneous vorticity magnitude  $\|\omega\|$  (levels between -15,000 and 15,000  $\text{s}^{-1}$ ) in the central sagittal plane, acoustic mesh. From left to right: healthy model, stridorous model.



**Figure 9.8:** Snapshot of the instantaneous pressure deficit  $p'$  (levels between 0 and 230 Pa) in the central sagittal plane, acoustic mesh. From left to right: healthy model, stridorous model.



## 9.4 Aeroacoustic Simulations

This section is dedicated to a description of the aeroacoustic characteristics of the airflow through the RUAM. In order to provide the reader with an idea of the previous research that has been carried out in this field, Subsection 9.4.1 presents a summary of the pioneering work. Subsection 9.4.2 then discusses the impact of changing the Mach number setting in PowerFLOW from Chosen by PowerFLOW (CbP) to Same as Experiment (SaE). Finally, Subsection 9.4.3 investigates the acoustic spectra of the CbP simulations, after which it briefly addresses the differences with respect to the SaE spectra.

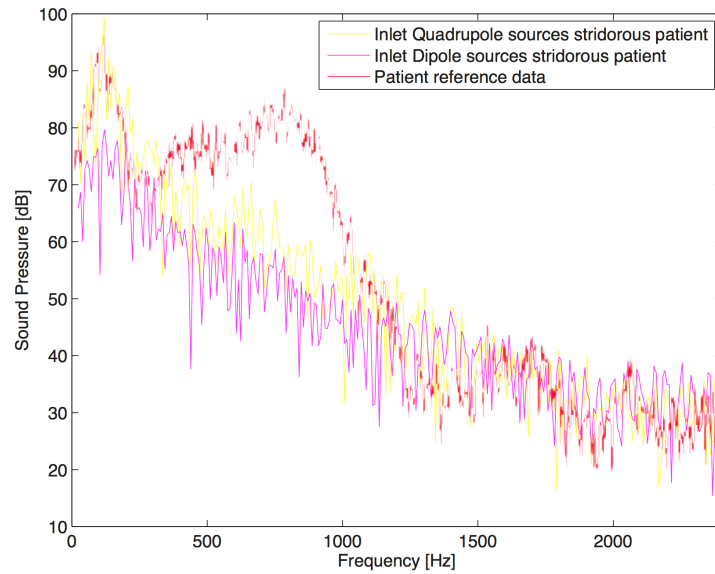
### 9.4.1 Pioneering Work

There have been two previous attempts to determine the acoustical spectrum of stridor based on Computational Fluid Dynamics (CFD) analysis of the fluid flow through the upper respiratory system. Lighthill's acoustic analogy was used by Lynch (2012) to calculate the Sound Pressure Level (SPL) near the mouth and in the bronchial region of a patient suffering from subglottic stenosis. One of the most important observations in this study was that the SPL at the inlet was similar for both the healthy and stridorous patient. On the other hand, the signals at the outlet probe showed marked differences. Lynch (2012) attributed this result to the constriction blocking the sound propagation towards the inlet and validated the hypothesis by investigating the propagation of a tracheal sound perturbation.

A more elaborate analysis of the stridor spectrum was performed by van der Velden (2012). Next to the quadrupole sources he also investigated the contribution of the dipole sources (and to some extent the monopole sources) by applying the Ffowcs Williams-Hawkings acoustic analogy to the CFD data. In contrast to the results from Lynch (2012), van der Velden (2012) does note a clear difference between the inlet signals. The difference is attributed to the dipole sources already being active at the constriction itself, making it more likely for the acoustic signals to propagate towards the inlet. This was confirmed by an analysis of the individual contributions, which showed that the dipole signal of the stridorous patient is in general 10 dB higher compared to that of the healthy patient, while the stridorous quadrupole signal is only 5 dB higher than its healthy counterpart.

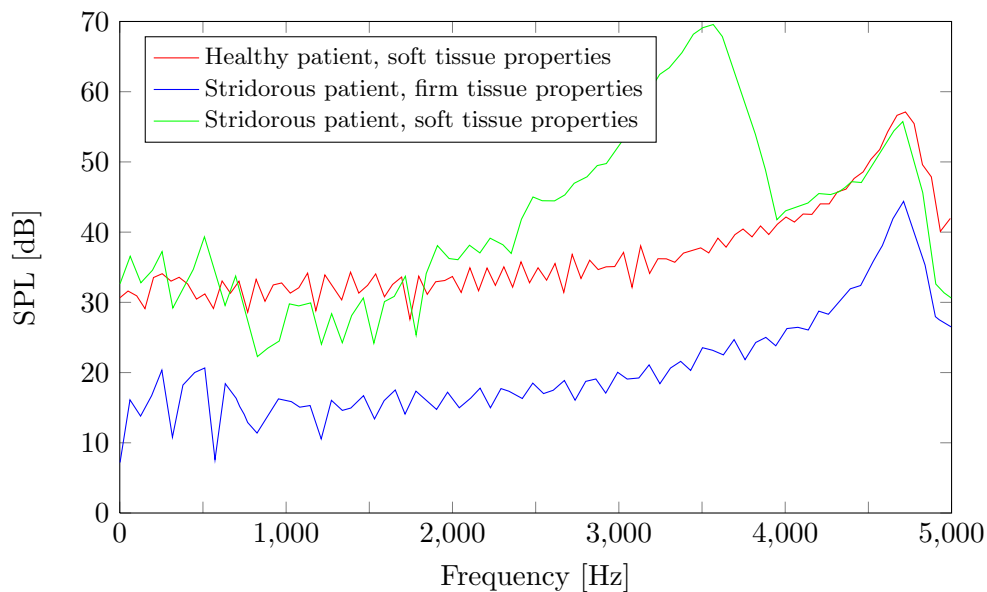
van der Velden (2012) also compared his results with actual patient reference data, see Figure (9.9). The patient was a 1-month-old male suffering from combined laryngomalacia and subglottic stenosis. Overall, the simulated signal matches the patient reference data except for a large peak in the 500 - 1,000 Hz frequency range. van der Velden (2012) anticipated that the discrepancy might be due to multiple causes: the simulation model does not correspond to that of the neonate nor does it include laryngomalacia, and the monopole sources are yet to be accounted for. Nonetheless, these type of promising results are certainly an incentive for further research.

Building on the combined knowledge of the aforementioned works, van der Velden et al. (2015) further investigated the effect of monopole sources on the acoustic spectrum. The results of



**Figure 9.9:** Sound pressure results versus frequency from the inlet probe of the RUAM compared with actual patient data from Zwartenkot (2010). Graph taken from van der Velden (2012).

their efforts are displayed in Figure (9.10), and they are indeed very promising. The stridorous patient for which the upper airway has been modeled with soft tissue properties has a broad peak in the frequency range  $f = 2,000 - 4,000$  Hz which is not visible in case of the healthy patient. Given that this peak occurs in the range at which stridor signals are commonly expected, this result once more emphasizes the need to model monopole sound sources in order to arrive at an accurate noise prediction.



**Figure 9.10:** Monopole source sound pressure measured at the outlet probe. Figure taken from van der Velden et al. (2015).

### 9.4.2 Mach Number: Chosen by PowerFLOW versus Same as Experiment

In Chapter 8 it was shown that the SaE simulations of the SUAM modeled an erroneous flow field at the cylindrical inlet. Because the source of this error has not yet been identified it was decided to perform a similar simulation in combination with a RUAM as a means to acquire additional insight into the matter.

The difference between the Mach numbers of the CbP and the SaE simulations is approximately 13-fold ( $M_{SaE} = 0.00722$  and  $M_{CbP} = 0.09449$ ). According to the hypothesis presented in Chapter 7 the combined effect of this high multiplication factor and the low Reynolds number ( $Re \approx 2,600$ , based on the hydraulic diameter of the inlet) might have a significant impact on the flow field. It should also be noted that both models had to be simulated with a different **Maximum Expected Velocity**: 7.5 m/s for the stridorous model ( $M = 0.06299$ ) and 5 m/s for the healthy model ( $M = 0.09449$ ). The reasoning behind these different values is thoroughly explained in Chapter 8.

As opposed to the SUAM, the SaE simulations yielded reasonable flow results. Although this omits a further investigation into the aforementioned low Mach number discrepancy, it allows a comparison between the acoustic data from the SaE and CbP simulations. The most important fluid flow results are included in Appendix F.2. Upon comparison of these figures with those attained from the CbP simulation it can be clearly observed that the SaE setting resolves less flow details than the CbP setting, most notably in terms of vorticity. This is likely due to an increased level of numerical dissipation, a phenomenon which is described in detail in Chapter 7. Of greater interest to this particular discussion is the fact that two important changes can be identified with respect to the CbP flow field.

- Following a weak deflection towards the anterior tracheal wall, the jet is redirected posteriorly in the healthy model. In case of the stridorous model the effect of the SGS is so strong that the jet remains attached to the anterior wall. The core jet velocities also remained similar since they are mainly impacted by the degree of luminal obstruction.
- The average pressure drop over the constriction is larger:  $\Delta P = 24.63$  Pa for the healthy model and  $\Delta P = 161.86$  Pa for the stridorous model.

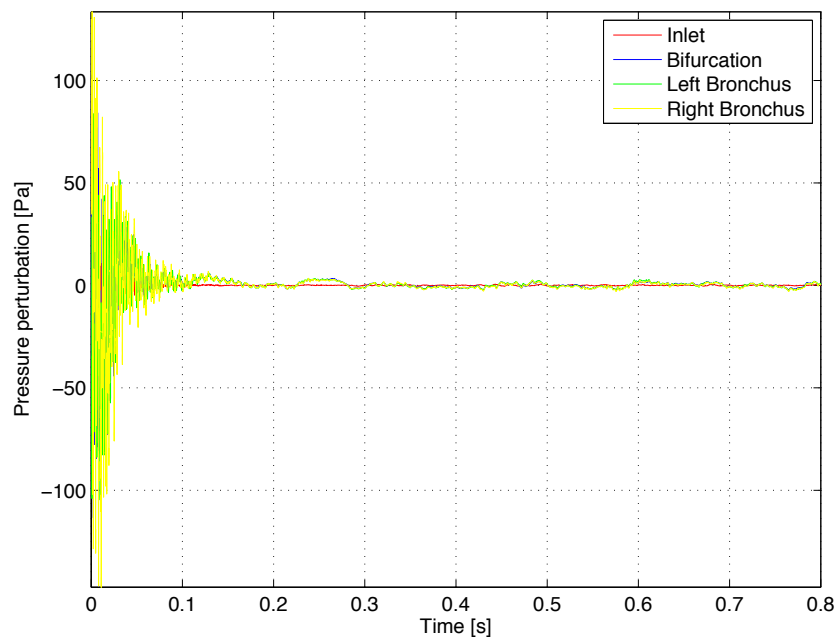
Regardless of these differences, it can be argued that the flow fields of both simulations bear a close resemblance. The following section will analyze the impact of these flow changes on the acoustic spectra.

### 9.4.3 Aeroacoustic Results

This subsection discusses the acoustic spectra of the CbP and SaE simulations. First it should be mentioned that all RUAM models were fitted with four measurement probes at the following locations (the values between brackets denote the coordinates (in mm) of the probes as measured in the current model):

- Inlet (171, 127, -490) - normal distance of approximately 1 mm as measured from the midpoint of the inlet;
- Bifurcation to the primary bronchi (166.61, 189.04, -690.5) - normal distance of 1.08 mm as measured from the actual split between the primary bronchi;
- Left bronchial outlet (152.5, 188.5, -695) - normal distance of approximately 2 mm as measured from the midpoint of the left outlet;
- Right bronchial outlet (181, 189.5, -697) - normal distance of approximately 2 mm as measured from the midpoint of the right outlet.

Note that due to the irregular shape of the end surfaces it is only possible to provide approximate values for the normal distance. Figure (9.11) shows the pressure signals that were measured by all probes of the healthy model. In order to minimize the influence of the transient start-up effects all pressure data prior to  $t = 0.25$  s was discarded from the analysis. Closer examination of the signals also reveals that the pressures that were measured at the bifurcation and the bronchi are very similar. Therefore, it was decided to include only the bifurcation data in the spectral analysis.



**Figure 9.11:** Pressure perturbation as measured by the acoustic probes, healthy model, Mach Number Chosen by PowerFLOW. Note the transient start-up prior to  $t = 0.25$  s.

A similar analysis for the SaE results indicated that the transient start-up period is reduced to  $t \approx 0.05$  s for this case, see Appendix F.3. This trend is in accordance with the data from Chapter 7, where a full account is given of the reasons behind this shortened start-up interval.

### Size and Shape of CbP Spectra

Figures (9.12) and (9.13) present the CbP acoustic spectra as measured by the probes at the inlet and at the bifurcation towards the bronchi, respectively. In general, these spectra display trends that are very similar to the ones that were determined for the SUAM case, albeit that these trends are much more pronounced for this case.

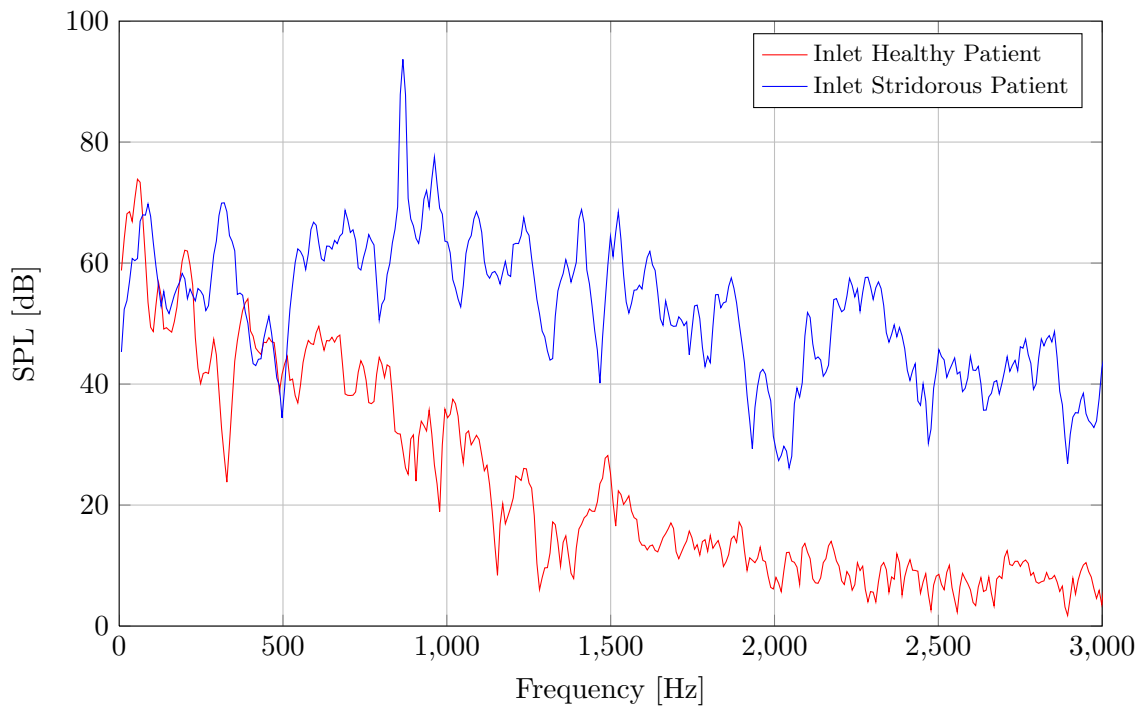
Most importantly, there exists a larger difference between the healthy and stridorous spectra. At the bifurcation the relative increase in the broadband pressure levels amounts to 30 - 40 dB (especially for  $f > 800$  Hz), while the inlet probe experienced a slightly lower increase of 20 - 35 dB. Nevertheless, this is still considerably higher compared to the SUAM signals, for which the difference between the healthy and stridorous models was close to indiscernible at the inlet probe. However, it should be taken into account that the SUAM pressure signals also had to cover the 180° bend around the tongue before arriving at the inlet probe, which makes a direct comparison with the RUAM results difficult.

An explanation for the elevated broadband pressure levels can be formulated from an analysis of the comparable measures for quadrupole and dipole sound sources, which are included in Figures (9.14) and (9.15), respectively. An explanation of these measures is provided in Chapter 8. From the figures it can be perceived that part of the quadrupole and dipole sources are already active above the level of the glottis. Moreover, there are not many obstructions between the subglottic region and the inlet probe that could impede the wave propagation between both regions (with the exception of the constriction and the glottis, naturally). The combination of these observations most likely explains the distinctive difference between the healthy and stridorous spectra at the inlet probe.

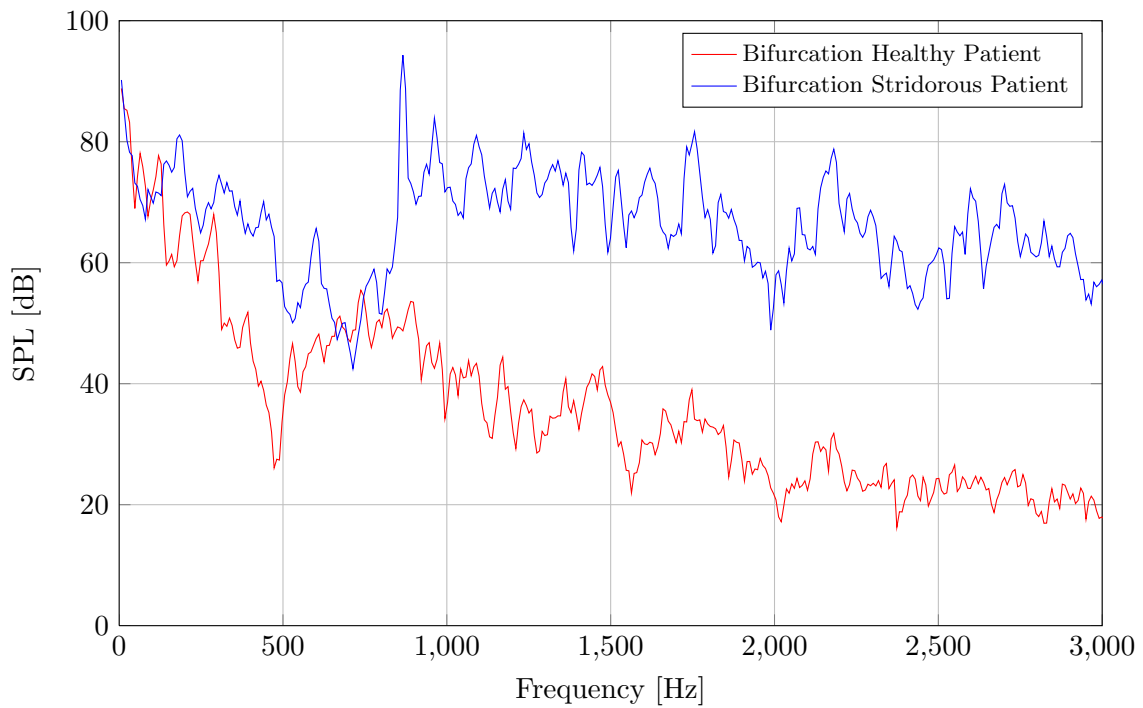
A final comment should be made with regard to shape of the acoustic spectra and its relation to the presence of Subglottic Stenosis (SGS). It was already mentioned in Chapter 8 that the acoustic spectrum of stridor that is heard from patients who suffer from SGS usually exhibits elevated broadband pressure levels with one or more distinct tonal peaks. Combining the results from the previous discussion with the tonal peak at  $f \approx 865$  Hz shows that the current results are in accordance with the data presented by [Zwartenkot \(2010\)](#) and [Gray et al. \(1985\)](#).

### Difference Between CbP and SaE Acoustic Spectra

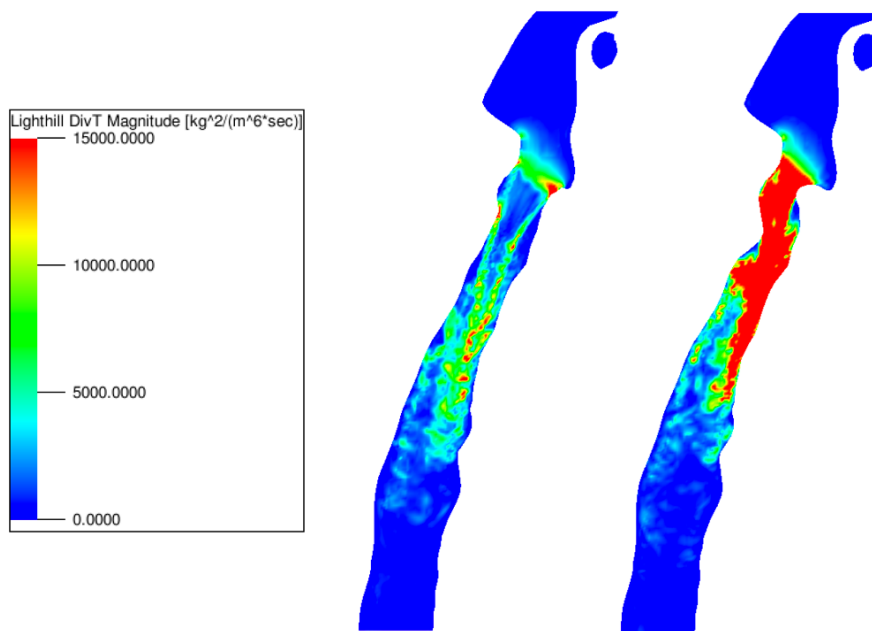
The acoustic spectra and corresponding quadrupole and dipole measures for the SaE simulations are shown in Figures (9.16) - (9.19). A first observation is that the acoustic spectra have shapes that are markedly different from their CbP counterparts. Also, the reduced level of flow details causes the SPLs to be lower in general. This can be observed directly from Figure (9.18): lower vorticity levels lead to weaker quadrupole sources, which in turn impact the acoustic spectra. Also, there is no longer a distinct peak at  $f \approx 865$  Hz. It is replaced by multiple broader peaks at higher frequencies. Note that the low-frequency peak around  $f \approx 283$  Hz might be attributed to a non-physical standing wave between the inlet and outlet of the model (which could be resolved by introducing a nonreflecting boundary condition).



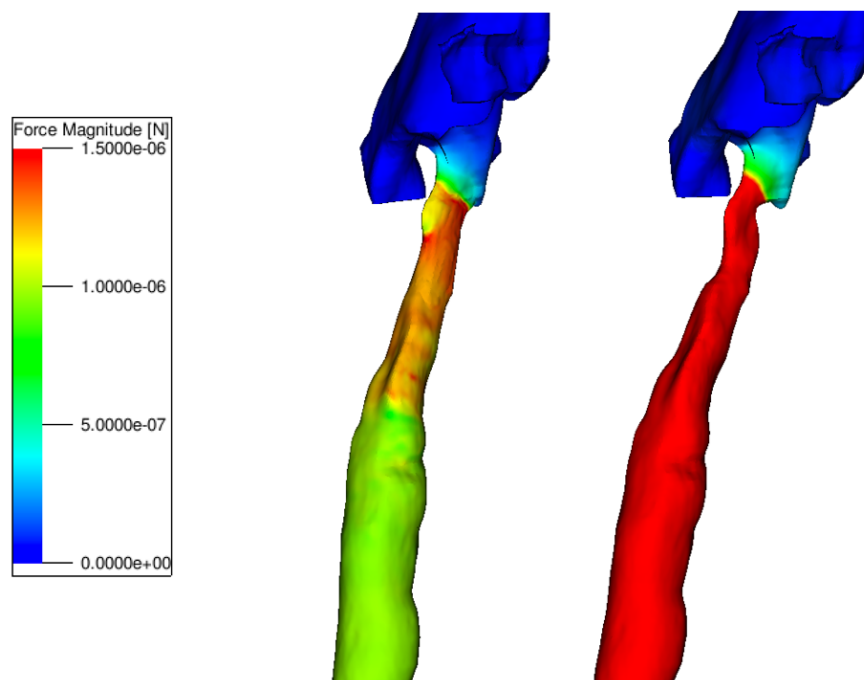
**Figure 9.12:** Sound Pressure Levels at inlet probes for the healthy and stridorous patient, Mach Number Chosen by PowerFLOW,  $f_s \approx 70.1$  kHz,  $\Delta f \approx 8$  Hz.



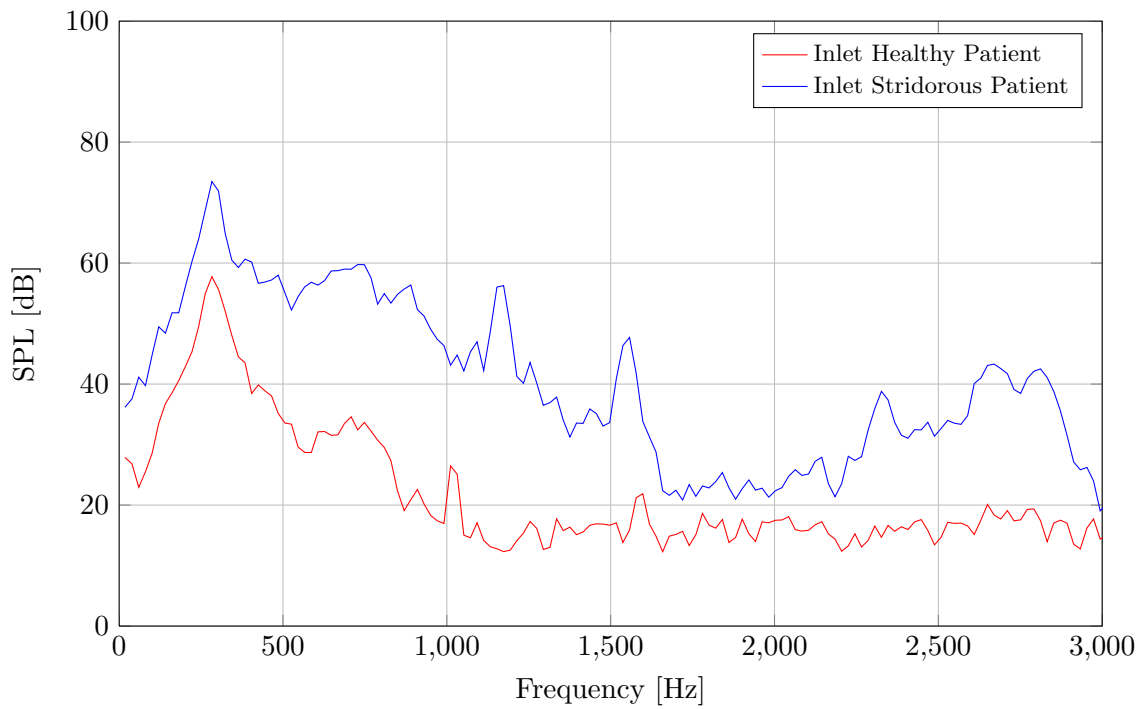
**Figure 9.13:** Sound Pressure Levels at bifurcation probes for the healthy and stridorous patient, Mach Number Chosen by PowerFLOW,  $f_s \approx 70.1$  kHz,  $\Delta f \approx 8$  Hz.



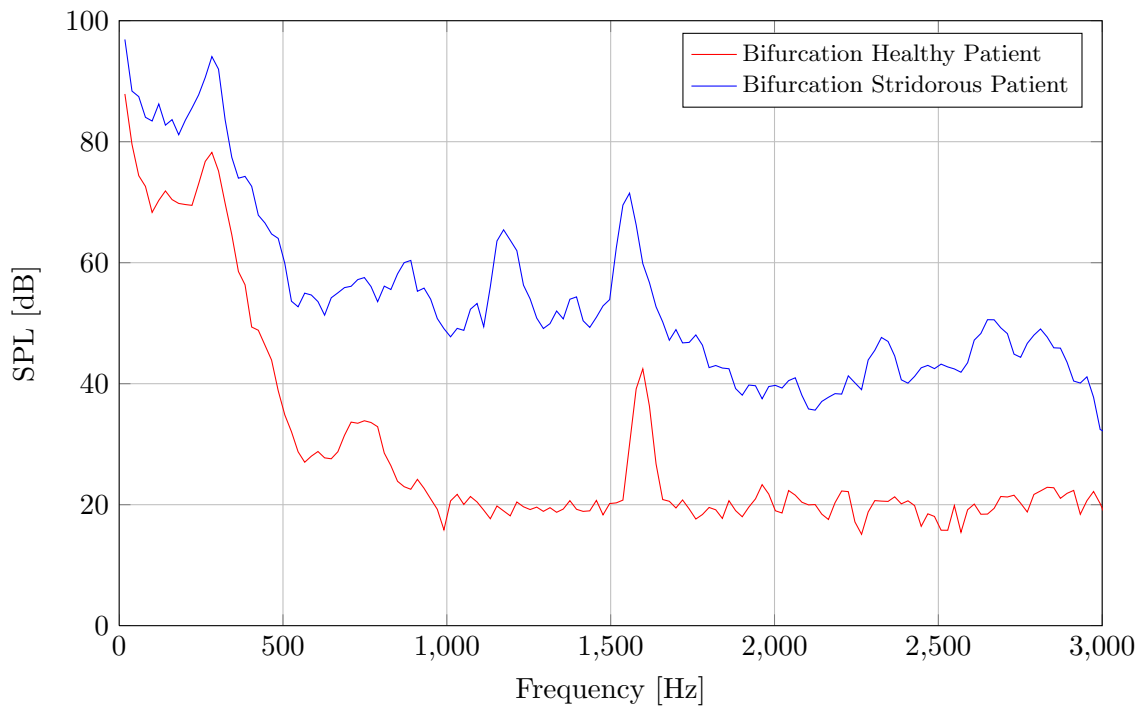
**Figure 9.14:** Snapshot of the instantaneous divergence of the Lighthill tensor  $\nabla T_{ij}$  (levels between 0 and  $15,000 \text{ kg}^2/(\text{m}^6\text{s})$ ), a measure for the strength of quadrupole sound sources, in the central sagittal plane, Mach Number Chosen by PowerFLOW, acoustic mesh. From left to right: healthy patient, stridorous patient.



**Figure 9.15:** Snapshot of the instantaneous force magnitude  $\|F\|$  (levels between 0 and  $1.5 \times 10^{-6} \text{ N}$ ), a measure for the strength of dipole sound sources, Mach Number Chosen by PowerFLOW, acoustic mesh. From left to right: healthy patient, stridorous patient.

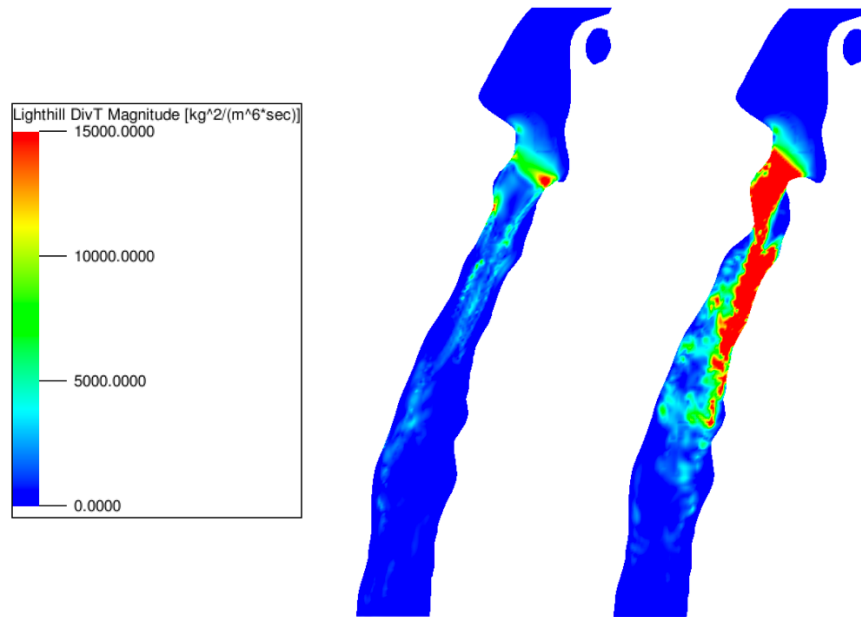


**Figure 9.16:** Sound Pressure Levels at inlet probes for the healthy and stridorous patient, Mach Number Same as Experiment,  $f_s \approx 69.9$  kHz,  $\Delta f \approx 20.2$  Hz.

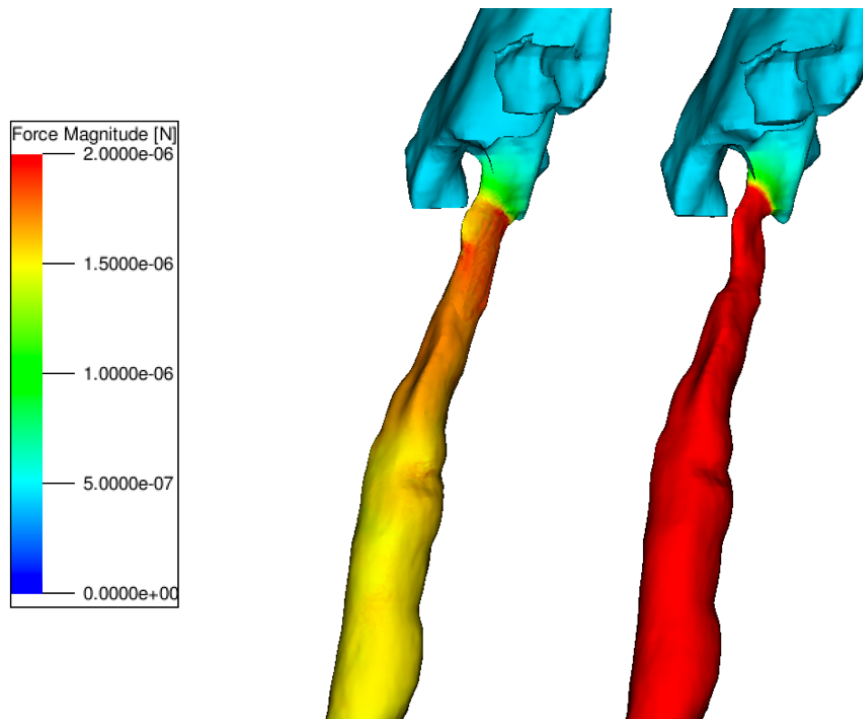


**Figure 9.17:** Sound Pressure Levels at bifurcation probes for the healthy and stridorous patient, Mach Number Same as Experiment,  $f_s \approx 69.9$  kHz,  $\Delta f \approx 20.2$  Hz.





**Figure 9.18:** Snapshot of the instantaneous divergence of the Lighthill tensor  $\nabla T_{ij}$  (levels between 0 and 15,000  $\text{kg}^2/(\text{m}^6\text{s})$ ), a measure for the strength of quadrupole sound sources, in the central sagittal plane, Mach Number Same as Experiment, acoustic mesh. From left to right: healthy patient, stridorous patient.



**Figure 9.19:** Snapshot of the instantaneous force magnitude  $\|\mathbf{F}\|$  (levels between 0 and  $2 \times 10^{-6}$  N), a measure for the strength of dipole sound sources, Mach Number Same as Experiment, acoustic mesh. From left to right: healthy patient, stridorous patient.

## 9.5 Conclusions

Even though the Realistic Upper Airway Model should not yet have been considered at this stage of the overall research project, this chapter yielded some very interesting insights.

Most importantly, it was shown that PowerFLOW is able to simulate the fluid flow through a RUAM at both the experimental and the accelerated Mach number. This indicates that the erroneous flow field that was encountered during the simulation of the simplified model might be a standalone case. Due to the lack of reliable benchmark data it was not possible to provide an analysis of the level of accuracy to which the flow field was simulated. Given the preliminary nature of this research, especially with regard to the RUAM, it was considered sufficient to show that PowerFLOW outputs a sensible flow field, i.e., according to expectations. Further refinement of the model can then be carried out during a follow-up study.

Yet another crucial insight is the lack of resemblance between the acoustic spectra of the simulations with experimental and accelerated Mach numbers. Although there has been no quantitative comparison between both spectra, it is now considered increasingly likely that it is impossible to rescale acoustic spectra that have been acquired at accelerated Mach numbers. This statement only holds true for the current simulation parameters ( $M_{CbP} \sim 10 \times M_{SaE}$ ,  $Re = 2,000 - 3,000$ ), and further investigation is required into whether a sensible user-defined increase in Mach number might provide better results.

Finally, it has been shown that the patient from which the simulation model has been acquired is very likely to have experienced breathing difficulties as a result of his/her medical condition. This statement is supported by the strong pressure drop over the constriction ( $\Delta P \approx 150$  Pa), and the considerable increase in broadband sound pressure levels.

## **Part IV**

# **Project Close-Out**



---

# Chapter 10

---

## Conclusion

This thesis investigated the reliability of the Lattice Boltzmann Method (LBM) for use in the aeroacoustic simulation of fluid flow through the human upper airways. The research fits into a larger project that aims at the development of a non-intrusive diagnostic tool for Upper Airway Obstructions (UAOs). Such a tool is desired because the currently applied endoscopy might cause additional injuries to the patient under examination.

Instead of developing a new numerical model, all simulations were carried out in PowerFLOW. This commercial software package has been developed by Exa Corporation, primarily for use in automotive and aeronautical engineering. The fluid flows that are encountered in this branch of the industry are very different from the low Reynolds number, low Mach number flows within the upper airway. Therefore, it was necessary to validate PowerFLOW prior to tackling the main research question.

### **PowerFLOW Validation**

An analysis of the fluid flow over a periodic hill configuration revealed that the PowerFLOW turbulence model is able to accurately model the flow separation from a smoothly curved surface within the confines of an internal geometry. With regard to the wall model, more fundamental investigations are required in order to determine its capabilities, especially in the presence of transitional and reversed boundary-layer flow. In order to avoid any uncertainty regarding the influence of this wall model on further simulations, it was decided to minimize its impact by applying a sufficiently high grid resolution in the boundary layer ( $y^+ < 5$ ).

A second validation study on a single diaphragm mainly focused on clarifying the aeroacoustic capabilities of PowerFLOW. In general it was established that the simulated spectra and, by extension, the flow fields show a good correspondence with the benchmark once a number of conditions are fulfilled. One necessary condition is the usage of a Nonreflective Boundary Condition (NRBC) in order to reduce the unphysical reflection of pressure waves at the model boundaries. Another condition is that the simulated Mach number is matched with

the experimental Mach number. This issue was considered because the user has the possibility to choose between the experimental Mach number and an upscaled Mach number, the latter which is determined by PowerFLOW. These options yielded different acoustic spectra, both in terms of shape as well as broadband pressure levels, with the experimental Mach number simulation offering the best match with the reference data. Unfortunately the underlying causes of these differences could not be readily identified, but it was postulated that they might be related to a change in the Reynolds number at which the flow is simulated.

### **LBM as an Alternative Means to Simulate Respiratory Airflow**

The main goal of this thesis was to perform an aeroacoustic simulation of the airflow through a human upper airway. This was done in two stages. First the numerical methodology was validated on both healthy and ‘stridorous’ Simplified Upper Airway Models (SUAM). Subglottic Stenosis (SGS) was chosen for this purpose because of its relative simplicity and ease of implementation. The flow field results of a first set of accelerated simulations showed a close correspondence to the benchmark data, especially in terms of secondary flow structures. A second set of simulations at the lower experimental Mach number did however reveal a worrisome result: PowerFLOW consistently predicts an unphysical jet at the inlet boundary. Additional investigations are required in order to determine the reason(s) behind this discrepancy, but in the meantime the acoustic spectra from the first set of simulations provided some meaningful insights. Most importantly, it was shown that patients with a critical level of SGS present with an increase in broadband pressure levels, which indicates that it is possible to distinguish between different models based on the acoustic spectra.

During the second stage a Realistic Upper Airway Model (RUAM) was simulated at both experimental and accelerated Mach numbers. As opposed to the SUAM case, the flow fields of these simulations showed a close resemblance. On the other hand, their acoustic spectra exhibited marked differences in terms of shape and absolute pressure levels. Nonetheless, both cases indicated a clear distinction between healthy and stridorous spectra in the order of 20 - 30 dB, which is much more pronounced compared to the simplified models.

Due to the lack of experimental reference data it was impossible to determine the accuracy of the SUAM and RUAM spectra, an issue which once more emphasizes the need for a more fundamental research that focuses on obtaining comprehensive benchmark results. As long as these are not available, all simulations are essentially ‘shots in the dark’.

Overall, it can be concluded that the LBM offers a viable alternative for conventional Computational Fluid Dynamics techniques in the simulation of respiratory airflows, provided that the aforementioned issues are resolved.

---

# Chapter 11

---

## Recommendations

This work established the potential value of using the stridor signal of a patient as a means to determine the size and location of his or her obstruction. Nonetheless, it merely presents the first step, albeit an important one, in the development of a non-invasive diagnostic tool for Upper Airway Obstructions (UAOs). Section 11.1 therefore describes a possible sequence of next steps that should be taken in order to achieve that goal. Section 11.2 then gives a detailed overview of the possible improvements in the geometrical model. Because there were still some unresolved issues pertaining to the numerical methodologies, Section 11.3 discusses how these may be resolved.

### 11.1 Towards a Non-Invasive Diagnostic Tool: Next Steps

The acoustic spectra derived from the upper airway models seem promising. Nevertheless, their accuracy remains uncertain as long as they have not been validated with experimental data. The proper next step would therefore be to *design an experiment* that measures the acoustic signal that is generated by the airflow through both healthy and obstructed airways. Fluid flow data should be acquired simultaneously by means of Particle Image Velocimetry (PIV) as a means to extend the database of benchmark results, which is currently restricted to the experimental results of [Brouns et al. \(2006\)](#) and [Jayaraju et al. \(2008\)](#).

The obstruction would ideally be replaceable so that multiple degrees and types of constrictions can be assessed. The Simplified Upper Airway Model (SUAM) is best suited for this purpose because it allows identical set-ups of the numerical and experimental test cases, i.e., there are no simplifications from one test case to another, nor are there any unknown model parameters. In terms of picking an appropriate UAO it was already mentioned in Chapter 8 that Subglottic Stenosis (SGS) is a suitable candidate because it occurs in a rigid form and in different degrees of severity (see the Myer-Cotton grading system in Figure (2.12)). It is also important to develop the constrictions as such that they represent stenoses

that actually occur within the human upper airway. It is therefore recommended to consult both medical textbooks and a medical expert as to obtain a comprehensive overview of the pathophysiology of SGS.

Once the Lattice Boltzmann Method (LBM) is validated with this experimental data it can be considered opportune to switch to more realistic models. This should be done in a stepwise and organized fashion, where the model complexity is increased by only one additional feature for each consecutive model upgrade. There are two reasons why this particular approach should be adopted.

- If the simulation turns out to be erroneous the error source can be found in the implementation of the latest model feature.
- Because the number of variables in a Realistic Upper Airway Model (RUAM) are almost unlimited it would be unwise to switch to such model directly. It should first be investigated what model attributes have a dominant influence on the acoustic spectrum. Those that can be proven to have a negligible impact can then be discarded from the eventual analysis of a RUAM in order to accelerate the simulations.

Although each additional model attribute should essentially be validated by comparing the results with experimental data, it is acknowledged that this might be too time-consuming given the degree of complexity of some of the model features. Therefore it is advised that the features are first tested in combination with simplified geometries for which benchmark data is readily available. This is similar to the procedure followed in this thesis in which both periodic hills and a diaphragm were simulated prior to the upper airway models.

Given the long list of potential model improvements (Section 11.2), it might also be difficult to pick a sensible starting point. Fortunately, [van der Velden et al. \(2015\)](#) gave some direction by accounting for the fluid-structure interaction between the airflow and the airway walls. In their paper it was indicated that the tonal noise which is typically generated by SGS stems from the vibration of the airway walls. Therefore, a logical next step would be to model monopole acoustic sources by adding a structural solver to the overall simulation set-up.

When these model features are partitioned (subdivided) according to their relative impact on the acoustic spectrum, it is possible to switch to the simulation of a RUAM. One set of aeroacoustic results for a RUAM has already been included in this thesis, but that was mainly to show that the PowerFLOW software is able to perform such computation. The actual results are once again not trustworthy because they have not been validated against experimental data. Therefore, prior to performing any RUAM simulations, a realistic model should be acquired from a patient who suffers from (preferably) SGS, both before and after the surgical intervention. Acoustic measurements should also be performed on the same patient. This experimental data would then be a sufficient basis to validate the numerical model.

Subsequently, once it has been shown that the numerical model can correctly identify the aeroacoustic characteristics of fluid flow through a RUAM, it is time to shift the focus towards the simulation of different UAOs. Similar to the case of SGS, the actual simulations



should be preceded by a further investigation of the pathophysiology of the most common UAOs (including, amongst others, vocal cord paralysis and laryngomalacia). Given the wide variety of UAOs it is deliberately advised to start with the most common ones. There is yet another issue that should be considered. Several UAOs, even amongst the common ones, are very flexible, i.e., they experience strong non-linear deformations throughout the respiratory cycle. As a consequence, the Fluid-Structure Interaction (FSI)-techniques that were applied in modeling the movement of the airway walls may no longer be suitable to model the non-linear deformation of the UAO. An additional validation step should therefore be executed prior to dealing with such flexible UAOs. The aim of this procedure is to prove that UAOs indeed have a unique acoustic footprint.

A final important aspect in the development of the non-intrusive diagnostic tool is to investigate the inter-subject variability of the acoustic spectrum. To that end, the same UAO should be simulated in combination with different geometries. A thorough analysis of these simulation results should then lead to either of the possibilities mentioned in the introduction to this thesis. They are repeated here for the convenience of the reader: *When it is confirmed that stridor is indeed largely independent of patient-specific anatomy, efforts can be aimed at the development of a look-up table which unambiguously relates acoustic features to upper airway disorders. This approach would not require physicians to have knowledge of the underlying numerical methodologies. On the other hand, when patient-specific anatomical detail does play a role of importance in the simulation results, this information should be used in the attempt to solve the inverse numerical problem. Following this approach, a combination of in vivo acoustic measurement data and imaging data of the patient's upper airway anatomy would be used to determine the type of fluid flow, and hence the type of obstruction, which might have caused the stridor. This requires a study of time-reversal methods and causes an additional burden for physicians. Moreover, computational time becomes of crucial importance due to the required urgency of the diagnosis.*

This entire discussion is summarized in the schematic overview of Figure (11.1).

### **Other Applications: Virtual Surgery**

Next to being a potentially non-invasive diagnostic tool for UAOs, there might be other applications for this method. Once it is shown that it can accurately predict the fluid flow through the upper airway, it can be applied to simulate the outcome of a surgical intervention. In other words, it would become possible to determine the post-operative flow field, thereby allowing the physician to assess the influence of any intervention prior to performing real surgery (i.e., the physician can perform virtual surgery to assess the outcome). This is a very promising thought, because the physician would then be able to optimize the intervention as to maximize the benefit to the patient. When the acoustic characteristics can also be assessed reliably, a similar procedure can be followed to investigate the impact of a surgical intervention on the patient's stridor.

Due to the time requirement which is often involved in clinical situations, these computations should be performed within a timespan of 24 hours (optimization today, surgery tomorrow). The LBM is especially attractive for these purposes because it can be efficiently parallelized.

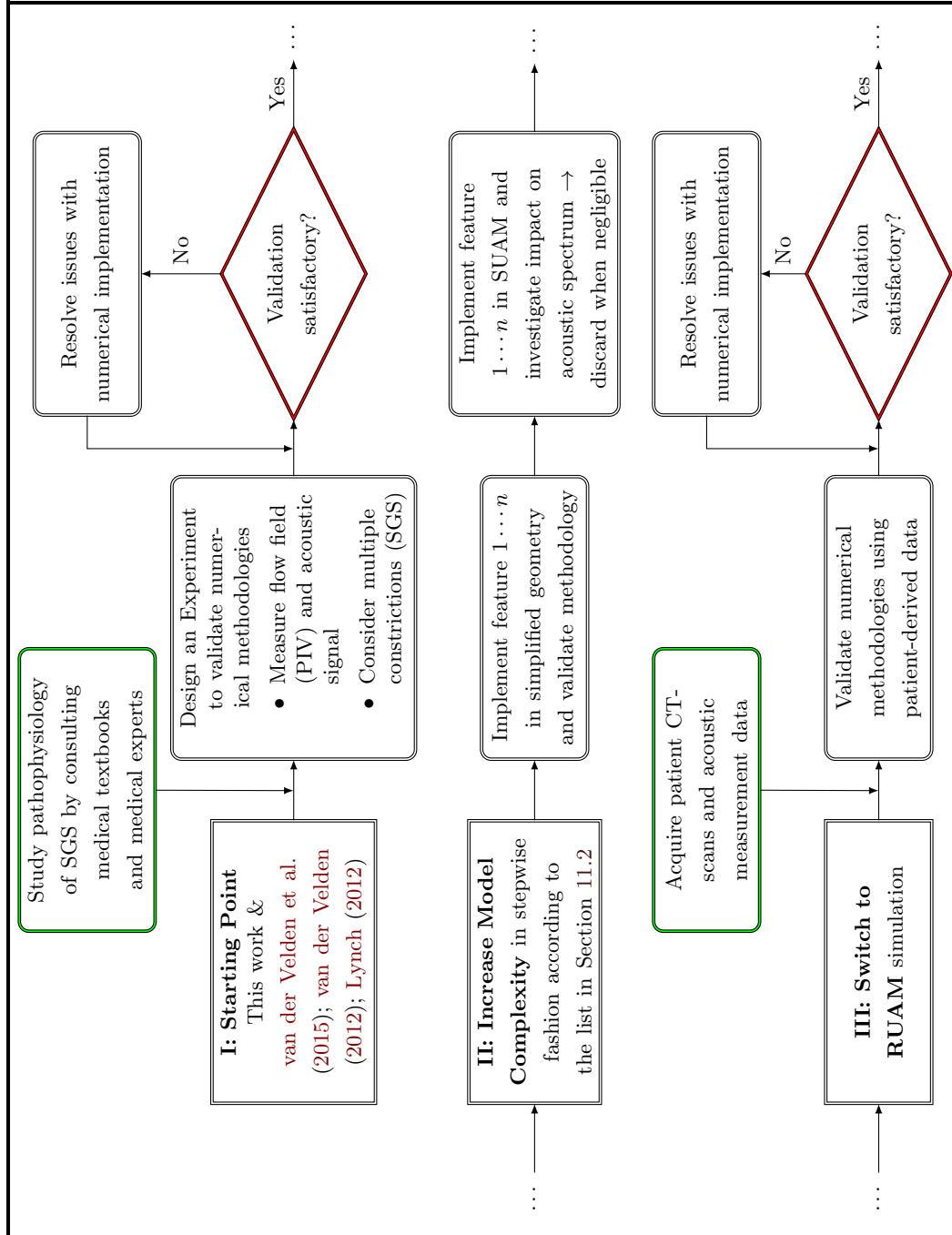
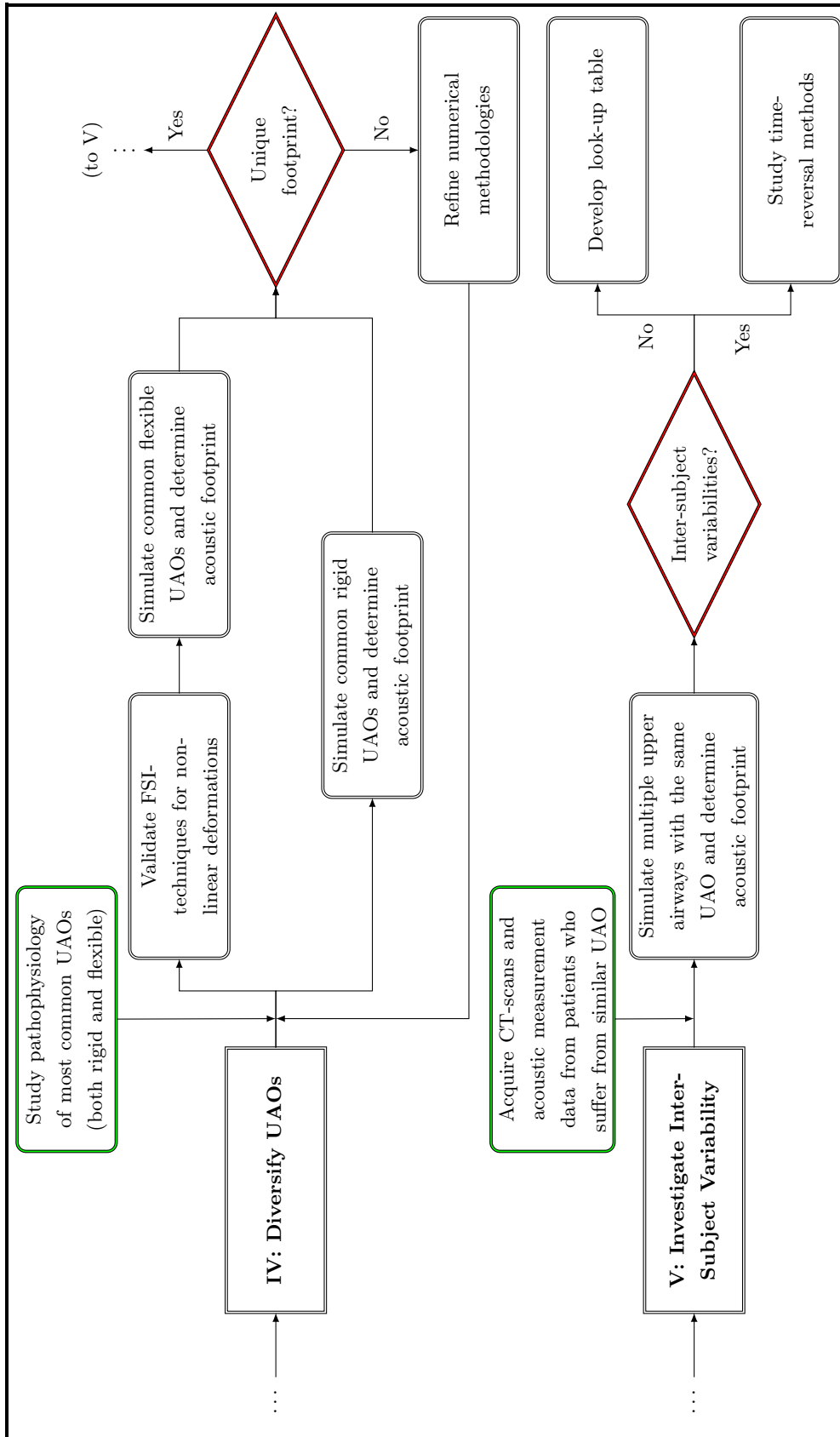


Figure 11.1: Overview of the sequence of steps that should be taken in the development of a noninvasive diagnostic tool for Upper Airway Obstructions.



**Figure 11.1:** Overview of the sequence of steps that should be taken in the development of a noninvasive diagnostic tool for Upper Airway Obstructions. (cont.)

## 11.2 Upper Airway Model

Needless to say that the upper airway has a very complex geometry. On top of that many physical and biological processes occur within the upper airway, each of which might influence the fluid flow and, by extension, the noise-generating mechanisms. It is therefore important to account for these processes in the aeroacoustic simulations.

In terms of the geometry itself the most accurate models can be derived from Computed Tomography (CT)-images. While the RUAM used in this thesis started at the oropharynx, it is important to include both oral and nasal cavities because they change the aeroacoustic characteristics of the fluid flow. In later stages more intricate features such as the tongue, the uvula, the oropharyngeal isthmus, a realistic epiglottis and the vocal cords should also be included in the geometry (note that these terms are clarified in Chapter 2).

Some important physical and biological processes are summarized in Table (11.1). Extensive discussions on each of these topics can be found in the accompanying literature study Foucart (2014). It should be emphasized that this list is by no means extensive and should be completed in collaboration with a medical expert in the field of otorhinolaryngology.

**Table 11.1:** Overview of most important physical and biological processes that are active in the upper airway.

Process	Explanation
<i>Wall Movement (FSI)</i>	The airway walls are compliant which means that they will continuously deform throughout a respiration cycle due to the varying wall pressure. More importantly, this wall movement introduces monopole sound sources which were proven to have a major impact on the acoustic spectrum van der Velden et al. (2015).
Mucociliary clearance	The airway walls are covered with a dynamic micron-sized layer of mucus that assists in the partial removal of inhaled micro- and nanosized particles. This removal process introduces a net movement of the mucus layer towards the laryngeal/pharyngeal regions at a rate between 50 - 200 $\mu\text{m/s}$ .
Acoustic Impedance	The airway walls absorb part of the acoustic wave energy which causes a frequency-dependent reduction of the pressure levels. Moreover, the amount of energy that is absorbed depends on local tissue properties which vary throughout the airway.
Temperature variations	During inspiration ambient air is inhaled which is likely to be at a different temperature than the human core temperature. Upon contact with the airway walls the inlet flow gradually reaches the body temperature, and the rate at which this happens is different for oral and nasal breathing.

A final issue that should be addressed here concerns the boundary conditions. In general small differences in the inlet velocity profile will not have a major impact on the fluid flow further downstream. Regardless thereof, Taylor et al. (2010) and Doorly et al. (2008) showed that a significantly more accurate inlet velocity profile can be obtained by including part of the external face in the geometry. With regard to the outlet boundary condition it should be noted that adopting a constant mass flow is acceptable but certainly not an ideal reflection of the intrathoracic pressure changes. Two alternatives are discussed by Huang et al. (2013, 2011).

Independent of the way in which the inlet and outlet boundary conditions are specified, a full respiration cycle should be simulated in order to determine a fully accurate acoustic spectrum. This is especially important when considering UAOs that present with biphasic stridor. In those cases an analysis of both inspiratory and expiratory acoustic spectra might prove to be an essential prerequisite for distinguishing them from other UAOs. Further information on how to specify the fluctuating boundary conditions can be found in [Lee et al. \(2010\)](#); [Shi et al. \(2008\)](#); [Jin et al. \(2007\)](#); [Zhang and Kleinstreuer \(2004\)](#); [Zhang et al. \(2002b\)](#). Again, more information concerning the general topic of boundary conditions can be found in [Foucart \(2014\)](#).

### 11.3 Numerical Methodology

With regard to the PowerFLOW software four important questions have been raised throughout this thesis but they remain as yet unresolved.

- The simplified upper airway simulations revealed the interesting fact that PowerFLOW is sometimes unable to accurately model the flow field at very low Mach numbers ( $\sim 0.007$ ). It should be further investigated why the simulation converges to a non-physical flow field at the inlet, and how this issue can be resolved in an elegant way.
- Preliminary research indicated that it might be possible to scale acoustic results that have been acquired at an accelerated Mach number. It was however impossible to derive the exact scaling factor, which is possibly frequency-dependent. The bottleneck in this analysis was the limited availability of information regarding the way in which PowerFLOW achieves a higher Mach number, and concerning the scaling that is potentially already performed by the program itself. Besides, it would be interesting to figure out how the acoustic dipole sources can be extracted from PowerFLOW such that their relative importance with respect to quadrupoles (and in a later stage monopoles) can be assessed.
- In relation to the previous item it was postulated that a large increase in Mach number might impact the Reynolds number at which the flow is simulated. If this statement is valid, it implies that the low Reynolds number flow through the upper airways can only be simulated at its experimental Mach number in order to arrive at a correct acoustic spectrum. It is therefore advised to analyze this statement very carefully by comparing the acoustic spectra of simulations that are executed at integral multiples of the experimental Mach number. The statement is positively verified if it can be shown that the spectra diverge above a certain threshold Mach number. All simulations should then be carried out at a Mach number that is smaller than this threshold value.
- Currently the upper airway simulations did not include any Nonreflecting Boundary Conditions (NRBCs). It should be determined how they can be inserted in the case definition without influencing the flow field.



---

# Bibliography

- L. Adewale. Anatomy and assessment of the pediatric airway. *Pediatric Anesthesia*, 19(Suppl. 1):1–8, July 2009.
- V. Agnirothi, G. Ghorbaniasl, S. Verbanck, and C. Lacor. An eddy interaction model for particle deposition. *Journal of Aerosol Science*, 47:39–47, May 2012.
- S.M. Ahmad and A.M.S. Soliman. Congenital anomalies of the larynx. *Otolaryngologic Clinics of North America*, 40(1):177–191, February 2007.
- C.K. Aidun and J.R. Clausen. Lattice-Boltzmann Method for complex flows. *Annual Review of Fluid Mechanics*, 42:439–472, 2010.
- G.P. Almeida, D.F.G. Durão, and M.V. Heitor. Wake flows behind two-dimensional model hills. *Experimental Thermal and Fluid Science*, 7(1):87–101, July 1993.
- N. Bailie, B. Hanna, J. Watterson, and G. Gallagher. An overview of numerical modeling of nasal airflow. *Rhinology*, 44(1):53–57, March 2006.
- C. Bailly, P. Lafon, and S. Candel. Computation of noise generation and propagation for free and confined turbulent flows. *2nd AIAA/CEAS Aeroacoustics Conference*, 96-1732, May 1996. State College, Pennsylvania.
- C.G. Ball, M. Uddin, and A. Pollard. Mean flow structures inside the human upper airway. *Flow, Turbulence and Combustion*, 81(1-2):155–188, July 2008.
- A. Belanger, M. Meskine, B. Caruelle, and K. Debatin. Aero-acoustic simulation of a double diaphragm using lattice Boltzmann method. *11th AIAA/CEAS Aeroacoustics Conference*, AIAA 2005-2917, May 2005. Monterey, California.
- D.J. Brenner and E.J. Hall. Computed tomography - an increasing source of radiation exposure. *The New England Journal of Medicine*, 357(22):2277–2284, November 2007.
- G.A. Brès, F. Pérot, and D. Freed. Properties of the lattice-Boltzmann method for acoustics. *15th AIAA/CEAS Aeroacoustics Conference*, AIAA 2009-3395, May 2009. Miami, Florida.
- M. Breuer, N. Peller, C. Rapp, and M. Manhart. Flow over periodic hills - numerical and experimental study in a wide range of Reynolds numbers. *Computer & Fluids*, 38(2): 433–457, February 2009.

- L. Brodsky. Structure and development of the upper respiratory system in infants and children. In B.P. Fuhrman and J.J. Zimmerman, editors, *Pediatric Critical Care*, chapter 35, pages 485–489. Elsevier, 4th edition, 2011.
- M. Brouns, S. Verbanck, J. Van Beek, S. Vanlanduit, J. Vanherzeele, and C. Lacor. PIV on the flow of a simplified upper airway model. *13th International Symposium on Applications of Laser Techniques to Fluid Mechanics*, June 2006. Paper 1120.
- M. Brouns, S.T. Jayaraju, C. Lacor, J. De Mey, M. Noppen, W. Vincken, and S. Verbanck. Tracheal stenosis: a flow dynamics study. *Journal of Applied Physiology*, 102(3):1178–1184, March 2007.
- H. Chen. Volumetric formulation of the lattice Boltzmann method for fluid dynamics: Basic concept. *Physical Review E*, 58(3):3955–3963, September 1998.
- H. Chen, S. Chen, and W.H. Matthaeus. Recovery of the Navier-Stokes equations using a lattice-gas Boltzmann method. *Physical Review A*, 45(8):5339–5342, April 1992.
- H. Chen, C. Teixeira, and K. Molvig. Realization of fluid boundary conditions via discrete Boltzmann dynamics. *International Journal of Modern Physics C*, 9(8):1281–1292, December 1998.
- H. Chen, O. Filippova, J. Hoch, K. Molvig, R. Shock, C. Teixeira, and Zhang R. Grid refinement in lattice Boltzmann methods based on volumetric formulation. *Physica A*, 362(1):158–167, March 2006.
- J. Chen and E. Gutmark. Numerical investigation of airflow in an idealized human extrathoracic airway: a comparison study. *Biomechanics and Modeling in Mechanobiology*, 13(1):205–214, January 2014.
- Y. Cheng, Y. Zhou, and B.T. Chen. Particle deposition in a cast of human oral airways. *Aerosol Science and Technology*, 31(4):286–300, October 1999.
- S.S. Chikatamarla and I.V. Karlin. Lattices for the lattice Boltzmann method. *Physical Review E*, 79(046701), April 2009.
- S. Chung and S.K. Kim. Digital particle image velocimetry studies of nasal airflow. *Respiratory Physiology and Neurobiology*, 163(1-3):111–120, November 2008.
- J. Claes, A. Boudewyns, P. Deron, V. Vander Poorten, and H. Hoeve. Management of stridor in neonates and infants. *B-ENT*, 1:Suppl. 1, 113–125, 2005.
- B. Crouse, S. Senthoran, D. Freed, G. Balasubramanian, M. Gleason, M. Puskarz, P. Lew, and L. Mongeau. Experimental and numerical investigation of a flow-induced cavity resonance with application to automobile buffeting. *12th AIAA/CEAS Aeroacoustics Conference*, AIAA 2006-2494, May 2006. Cambridge, Massachusetts.
- N. Curle. The influence of solid boundaries upon aerodynamic sound. *Proceedings of the Royal Society A*, 231(1187):505–514, September 1955.



- A. de Alarcon, R.T. Cotton, and M.J. Rutter. Laryngeal and tracheal airway disorders. In R.W. Wilmott, V. Chernick, T.F. Boat, R.R. Deterding, A. Bush, and F. Ratjen, editors, *Kendig and Chernick's disorders of the respiratory tract in children*, chapter 69, pages 969–975. Elsevier, 8th edition, 2012.
- J.W. De Backer, W.G. Vos, C.D. Gorlé, P. Germonpré, B. Partoens, F.L. Wuyts, P.M. Parizel, and W. De Backer. Flow analyses in the lower airways: Patient-specific model and boundary conditions. *Medical Engineering & Physics*, 30(7):872–879, September 2008a.
- J.W. De Backer, W.G. Vos, S.L. Verhulst, and W. De Backer. Novel imaging techniques using computer methods for the evaluation of the upper airway in patients with sleep-disordered breathing: A comprehensive review. *Sleep Medicine Reviews*, 12(6):437–447, December 2008b.
- A.T. de Jong, H. Bijl, A. Hazir, and J. Wiedemann. Aeroacoustic simulation of slender partially covered cavities using a lattice Boltzmann method. *Journal of Sound and Vibration*, 332(7):1687–1703, April 2013.
- D.J. Doorly, D.J. Taylor, A.M. Gambaruto, R.C. Schroter, and N. Tolley. Nasal architecture: form and flow. *Phil. Trans. R. Soc. A*, 366(1879):3225–3246, September 2008.
- R.L. Drake, A.W. Vogl, and A.W.M. Mitchell. *Gray's anatomy for students*. Elsevier, 2nd edition, 2009.
- B. Duda, E. Fares, and R. Kotapati. Application of the lattice Boltzmann method to shear layer flows. *53rd AIAA Aerospace Sciences Meeting*, AIAA 2015-1970, January 2015. Kissimmee, Florida.
- G. Eitel, R.K. Freitas, A. Lintermann, M. Meinke, and W. Schröder. Numerical simulation of nasal cavity flow based on a Lattice-Boltzmann Method. In A. Dillmann, G. Heller, M. Klaas, H.-P. Kreplin, W. Nitsche, and W. Schröder, editors, *New Results in Numerical and Experimental Fluid Mechanics VII*, volume 112 of *Notes on Numerical Fluid Mechanics and Multidisciplinary Design*, pages 513–520. Springer Berlin Heidelberg, 2010.
- M. Escobar. *Finite element simulation of flow-induced noise using Lighthill's acoustic analogy*. PhD thesis, University of Erlangen-Nürnberg, April 2007.
- J.E. Ffowcs Williams and D.L. Hawkings. Sound generation by turbulence and surfaces in arbitrary motion. *Philosophical Transactions of the Royal Society A*, 264(1151):321–342, May 1969.
- M. Finck, D. Hänel, and I. Wlokas. Simulation of nasal flow by lattice Boltzmann methods. *Computers in Biology and Medicine*, 37(6):739–749, June 2007.
- S. Fleming, M. Thompson, R. Stevens, C. Heneghan, A. Plüddemann, I. Maconochie, L. Tarassenko, and D. Mant. Normal ranges of heart rate and respiratory rate in children from birth to 18 years: a systematic review of observational studies. *The Lancet*, 377(9770):1011–1018, 2011.
- M. Foucart. Fluid-acoustic interaction simulation of a stridor patient's upper respiratory system using the Lattice Boltzmann Method: Literature Study. Master's thesis, TU Delft University of Technology, Kluyverweg 1, 2629HS Delft, July 2014.

- R.K. Freitas and W. Schröder. Numerical investigation of the three-dimensional flow in a human lung model. *Journal of Biomechanics*, 41(11):2446–2457, August 2008.
- J. Fröhlich, C.P. Mellen, W. Rodi, L. Temmerman, and M.A. Leschziner. Highly resolved large-eddy simulation of separated flow in a channel with streamwise periodic constrictions. *Journal of Fluid Mechanics*, 526:19–66, March 2005.
- A.M. Gambaruto, D.J. Taylor, and D.J. Doorly. Modelling nasal airflow using a Fourier descriptor representation of geometry. *International Journal for Numerical Methods in Fluids*, 59(11):1259–1283, April 2009.
- I. Garcia-Lopez, J. Peñorrocha Teres, M. Perez-Ortin, M. Cerpa, I. Rabanal, and J. Gavilan. Paediatric vocal fold paralysis. *Acta Otorrinolaringologica (English edition)*, 64(4):283–288, July-August 2013.
- P.F. Ghalati, E. Keshavarzian, O. Abouali, A. Faramarzi, J. Tu, and A. Shakibafard. Numerical analysis of micro- and nano-particle deposition in a realistic human upper airway. *Computers in Biology and Medicine*, 42(1):39–49, January 2012.
- M.L. Gillison, L. Alemany, P.J.F. Snijders, A. Chaturvedi, B.M. Steinberg, S. Schwartz, and X. Castellsagué. Human papillomavirus and diseases of the upper airway: head and neck cancer and respiratory papillomatosis. *Vaccine*, 30(Suppl. 5):F34–F54, November 2012.
- X. Gloerfelt and B. Lafon. Direct computation of the noise induced by a turbulent flow through a diaphragm in a duct at low Mach number. *Computers & Fluids*, 37(4):388–401, May 2008.
- L. Gray, J.C. Denny III, H. Carvajal, and R. Jahrsdoerfer. Fourier analysis of infantile stridor: preliminary data. *International Journal of Pediatric Otorhinolaryngology*, 10(2):191–199, November 1985.
- B. Grgic, W.H. Finlay, P.K.P. Burnell, and A.F. Heenan. In vitro intersubject and intrasubject deposition measurements in realistic mouth-throat geometries. *Journal of Aerosol Science*, 35(8):1025–1040, August 2004.
- G. Grisar-Soen, O. Komisar, O. Aizenstein, M. Soudack, D. Schwartz, and G. Paret. Retropharyngeal and parapharyngeal abscess in children - epidemiology, clinical features and treatment. *International Journal of Pediatric Otorhinolaryngology*, 74:1016–1020, 2010.
- J.J. Haapaniemi. Adenoids in school-aged children. *The Journal of Laryngology and Otology*, 109(3):196–202, March 1995.
- R. Haberman. *Applied partial differential equations with Fourier series and boundary value problems*. Pearson Prentice Hall, 4th edition, 2004.
- K. Habibi, H. Gong, A. Najafi-Yazdi, and L. Mongeau. Numerical simulations of sound radiated from internal mixing nozzles with forced mixers using the lattice Boltzmann method. *19th AIAA/CEAS Aeroacoustics Conference*, AIAA 2013-2143, May 2013. Berlin, Germany.
- X. He and L.-S. Luo. Theory of the lattice Boltzmann method: From the Boltzmann equation to the lattice Boltzmann equation. *Physical Review E*, 56(6):6811–6817, December 1997.

- A.F. Heenan, E. Matida, A. Pollard, and W.H. Finlay. Experimental measurements and computational modeling of the flow field in an idealized human oropharynx. *Experiments in Fluids*, 35(1):70–84, July 2003.
- F.J. Higuera and J. Jiménez. Boltzmann approach to lattice gas simulations. *Europhysics Letters*, 9(7):663–668, August 1989.
- J. Hirschberg. Acoustic analysis of pathological cries, stridor and coughing sounds in infancy. *International Journal of Pediatric Otorhinolaryngology*, 2(4):287–300, November 1980.
- W. Hofmann. Modelling inhaled particle deposition in the human lung - A review. *Journal of Aerosol Science*, 42(10):693–724, October 2011.
- R.G. Hooper. Forced inspiratory nasal flow-volume curves: a simple test of nasal airflow. *Mayo Clinic Proceedings*, 76(10):990–994, October 2001.
- L.M. Hopkins, J.T. Kelly, A.S. Wexler, and A.K. Prasad. Particle image velocimetry measurements in complex geometries. *Experiments in Fluids*, 29(1):91–95, 2000.
- I. Hörschler, W. Schröder, and M. Meinke. On the assumption of steadiness of nasal cavity flow. *Journal of Biomechanics*, 43(6):1081–1085, April 2010.
- J. Huang, L. Zhang, and S. Yu. Modeling micro-particle deposition in human upper respiratory tract under steady inhalation. *Particuology*, 9(1):39–43, February 2011.
- J. Huang, H. Sun, C. Liu, and L. Zhang. Moving boundary simulation of airflow and micro-particle deposition in the human extra-thoracic airway under steady inspiration. part i: Airflow. *European Journal of Mechanics B/Fluids*, 37:29–41, January 2013.
- K. Inthavong, A.P. Mouritz, J. Dong, and J.Y. Tu. Inhalation and deposition of carbon and glass composite fibre in the respiratory airway. *Journal of Aerosol Science*, 65:58–68, November 2013.
- R.R. Jain and M.F. Rabb. The difficult pediatric airway. In C.A. Hagberg, editor, *Benumof's and Hagberg's airway management*, chapter 36, pages 723–760. Elsevier, 3rd edition, 2012.
- S. Jakirlić, R. Jester-Zürker, and C. Tropea, editors. *9th ERCOFTAC/IAHR/COST workshop on refined turbulence modelling*, October 4-5 2001. Darmstadt University of Technology.
- D. Jardine, O.J. Bhutta, and A. Inglis. Specific diseases of the respiratory system: upper airway. In B.P. Fuhrman and J.J. Zimmerman, editors, *Pediatric Critical Care*, chapter 44, pages 561–574. Elsevier, 4th edition, 2011.
- S.T. Jayaraju, M. Brouns, C. Lacor, B. Belkassen, and S. Verbanck. Large eddy and detached eddy simulations of fluid flow and particle deposition in a human mouth-throat. *Journal of Aerosol Science*, 39(10):862–875, October 2008.
- H.H. Jin, J.R. Fan, M.J. Zeng, and K.F. Cen. Large eddy simulation of inhaled particle deposition within the human upper respiratory tract. *Journal of Aerosol Science*, 38(3): 257–268, March 2007.

- A. Johnstone, M. Uddin, A. Pollard, A. Heenan, and W.H. Finlay. The flow inside an idealised form of the human extra-thoracic airway. *Experiments in Fluids*, 37(5):673–689, November 2004.
- A. Keating, P. Dethioux, R. Satti, and S. Noelting. Computational aeroacoustics validation and analysis of a nose landing gear. *15th AIAA/CEAS Aeroacoustics Conference*, AIAA 2009-3154, May 2009. Miami, Florida.
- F. Krause, A. Wenk, C. Lacor, W.G. Kreyling, W. Möller, and S. Verbanck. Numerical and experimental study on the deposition of nanoparticles in an extrathoracic oral airway model. *Journal of Aerosol Science*, 57:131–143, March 2013.
- P. Lallemand and L.-S. Luo. Theory of the Lattice Boltzmann Method: Dispersion, dissipation, isotropy, Galilean invariance, and stability. ICASE Report 2000-17, National Aeronautics and Space Administration, Hampton, Virginia, April 2000.
- N. Leboulanger, B. Louis, R. Fodil, P.-Y. Boelle, A. Clément, E.-N. Garabedian, and B. Fauroux. Analysis of the pharynx and the trachea by the acoustic reflection method in children: A pilot study. *Respiratory Physiology & Neurobiology*, 175(2):228–233, February 2011.
- N. Leboulanger, B. Louis, H. Corvol, A. Ramirez, R. Fodil, F. Lofaso, and B. Fauroux. Evaluation of the trachea and intrathoracic airways by the acoustic reflection method in children with cystic fibrosis. *Respiratory Physiology & Neurobiology*, 181(1):74–78, April 2012.
- N. Leboulanger, B. Louis, and B. Fauroux. The acoustic reflection method for the assessment of paediatric upper airways. *Paediatric Respiratory Reviews*, 15(1):38–41, March 2014.
- J. Lee, Y. Na, S. Kim, and S. Chung. Unsteady flow characteristics through a human nasal airway. *Respiratory Physiology and Neurobiology*, 172(3):136–146, July 2010.
- A. Lieberman, A. Cohen, and A. Tal. Digital signal processing of stridor and snoring in children. *International Journal of Pediatric Otorhinolaryngology*, 12(2):173–185, December 1986.
- Y. Li, R. Satti, P.-T. Lew, R. Shock, and S. Noelting. Computational aeroacoustic analysis of flow around a complex nose landing gear configuration. *14th AIAA/CEAS Aeroacoustics Conference*, AIAA 2008-2916, May 2008. Vancouver, British Columbia Canada.
- D.E. Lieberman, R.C. McCarthy, K.M. Hiiemae, and J.B. Palmer. Ontogeny of postnatal hyoid and larynx descent in humans. *Archives of Oral Biology*, 46(2):117–128, February 2001.
- M.J. Lighthill. On sound generated aerodynamically. I: General theory. *Proceedings of the Royal Society A*, 211(1107):564–587, March 1952.
- D.K. Lilly. A proposed modification of the Germano subgrid-scale closure method. *Physics of Fluids A*, 4(3):633–635, March 1992.
- C. Lin, M.H. Tawhai, G. McLennan, and E.A. Hoffman. Characteristics of the turbulent laryngeal jet and its effect on airflow in the human intra-thoracic airways. *Respiratory Physiology and Neurobiology*, 157(2-3):295–309, August 2007.

- A. Lintermann, M. Meinke, and W. Schröder. Investigations of human nasal cavity flows based on a Lattice-Boltzmann Method. In M. Resch, X. Wang, W. Bez, E. Focht, H. Kobayashi, and S. Roller, editors, *High Performance Computing on Vector Systems 2011*, pages 143–158. Springer Berlin Heidelberg, 2012.
- A. Lintermann, G. Eitel-Amor, M. Meinke, and W. Schröder. Lattice-Boltzmann solutions with local grid refinement for nasal cavity flows. In A. Dillmann, G. Heller, H.-P. Kreplin, W. Nitsche, and I. Peltzer, editors, *New Results in Numerical and Experimental Fluid Mechanics VIII*, volume 121 of *Notes on Numerical Fluid Mechanics and Multidisciplinary Design*, pages 583–590. Springer Berlin Heidelberg, 2013a.
- A. Lintermann, M. Meinke, and W. Schröder. Fluid mechanics based classification of the respiratory efficiency of several nasal cavities. *Computers in Biology and Medicine*, 43(11): 1833–1852, November 2013b.
- C.T. Lynch. The numerical acoustic and fluid flow analysis on a CT-scan derived upper airway model of a stridor patient. MSc thesis, TU Delft University of Technology, Kluyverweg 1, 2629HS Delft, March 2012.
- B. Ma and K.R. Lutchen. CFD simulation of aerosol deposition in an anatomically based human large-medium airway model. *Annals of Biomedical Engineering*, 37(2):271–285, February 2009.
- R. Manceau, J.P. Bonnet, M.A. Leschziner, and F. Menter, editors. *10th Joint ERCOF-TAC(SIG-15)/IAHR/QNET-CFD workshop on refined turbulence modelling*, October 10-11 2002. Université de Poitiers.
- S. Marié, D. Ricot, and P. Sagaut. Comparison between lattice Boltzmann method and Navier-Stokes high order schemes for computational aeroacoustics. *Journal of Computational Physics*, 228(4):1056–1070, March 2009.
- A. McConnell. Anatomy and physiology of the respiratory system. In A. McConnell, editor, *Respiratory Muscle Training - Theory and Practice*, chapter 1, pages 3–36. Churchill Livingstone Elsevier, 1st edition, 2013.
- G.R. McNamara and G. Zanetti. Use of the Boltzmann equation to simulate lattice-gas automata. *Physical Review Letters*, 61(20):2332–2335, November 1988.
- C.P. Mellen, J. Fröhlich, and W. Rodi. Large eddy simulation of the flow over periodic hills. In M. Deville and R. Owens, editors, *Proceedings of 16th IMACS world congress*, Lausanne, Switzerland, 2000. Pages CD-ROM.
- M. Mihaescu, S. Murugappan, M. Kalra, S. Khosla, and E. Gutmark. Large Eddy Simulation and Reynolds-Averaged Navier-Stokes modeling of flow in a realistic pharyngeal airway model: an investigation of obstructive sleep apnea. *Journal of Biomechanics*, 41(10):2279–2288, July 2008.
- T. Miki, X. Wang, T. Aoki, Y. Imai, T. Ishikawa, K. Takase, and T. Yamaguchi. Patient-specific modelling of pulmonary airflow using GPU cluster for the application in medical practice. *Computer Methods in Biomechanics and Biomedical Engineering*, 15(7):771–778, July 2012.

- M.R. Miller, J. Hankinson, V. Brusasco, F. Burgos, R. Casaburi, A. Coates, R. Crapo, P. Enright, C.P.M. van der Grinten, P. Gustafsson, R. Jensen, D.C. Johnson, N. MacIntyre, R. McKay, D. Navajas, O.F. Pedersen, R. Pellegrino, G. Viegi, and J. Wanger. Standardisation of spirometry. *European Respiratory Journal*, 26(2):319–338, August 2005.
- M. Miyamoto, Y. Ito, K. Takahashi, T. Takami, T. Kobayashi, A. Nishida, and M. Aoyagi. Numerical study on sound vibration of an air-reed instrument with compressible LES. *arXiv preprint arXiv:1005.3413*, 2010.
- A.M. Modrykamien, R. Gudavalli, K. McCarthy, X. Liu, and J.K. Stoller. Detection of upper airway obstruction with spirometry results and the flow-volume loop: a comparison of quantitative and visual inspection criteria. *Respiratory Care*, 54(4):474–479, April 2009.
- A.A. Mohamad. *Lattice Boltzmann Method: Fundamentals and engineering applications with computer codes*. Springer-Verlag London, 1st edition, 2011.
- A.E. Muñiz. Stridor in infancy. In J.M. Baren, S.G. Rothrock, J. Brennan, and L. Brown, editors, *Pediatric Emergency Medicine*, chapter 34, pages 306–318. Elsevier, 2008.
- G. Mylavaram, S. Murugappan, M. Mihaescu, M. Kalra, S. Khosla, and E. Gutmark. Validation of computational fluid dynamics methodology used for human upper airway flow simulations. *Journal of Biomechanics*, 42(10):1553–1559, July 2009.
- G. Mylavaram, M. Mihaescu, L. Fuchs, G. Papatziomos, and E. Gutmark. Planning human upper airway surgery using computational fluid dynamics. *Journal of Biomechanics*, 46(12):1979–1986, August 2013.
- L. Nicolaou and T.A. Zaki. Direct numerical simulations of flow in realistic mouth-throat geometries. *Journal of Aerosol Science*, 57:71–87, March 2013.
- P. Nithiarasu, O. Hassan, K. Morgan, N.P. Weatherill, C. Fielder, H. Whittet, P. Ebdon, and K.R. Lewis. Steady flow through a realistic human upper airway geometry. *International Journal for Numerical Methods in Fluids*, 57(5):631–651, June 2008.
- S. Noelting, M. Wessels, and D. Freed. Prediction of aeroacoustic noise from a simplified landing gear using a lattice Boltzmann scheme. *46th AIAA Aerospace Sciences Meeting and Exhibit*, AIAA 2008-20, January 2008. Reno, Nevada.
- S. Noelting, G.A. Brès, P. Dethioux, T. Van de Ven, and R. Vieito. A hybrid lattice-Boltzmann/FW-H method to predict sources and propagation of landing gear noise. *16th AIAA/CEAS Aeroacoustics Conference*, AIAA 2010-3976, June 2010. Stockholm, Sweden.
- M.P. Norton and D.G. Karczub. *Fundamentals of noise and vibration analysis for engineers*. Cambridge University Press, 2007. Digital Edition.
- J. Peiró, L. Formaggia, M. Gazzola, A. Radaelli, and V. Rigamonti. Shape reconstruction from medical images and quality mesh generation via implicit surfaces. *International Journal for Numerical Methods in Fluids*, 53(8):1339–1360, March 2007.
- F. Pérot, M.S. Kim, D.M. Freed, D. Lee, K.D. Ih, and M.S. Kim. Direct aeroacoustics prediction of ducts and vents noise. *16th AIAA/CEAS Aeroacoustics Conference*, AIAA 2010-3724, June 2010. Stockholm, Sweden.

- F. Pérot, M. Meskine, F. Gille, and S. Vergne. Aeroacoustics prediction of simplified and production automotive HVAC ducts and registers. *17th AIAA/CEAS Aeroacoustics Conference*, AIAA 2011-2935, June 2011. Portland, Oregon.
- M. Piellard and C. Bailly. Validation of a hybrid CAA method. Application to the case of a ducted diaphragm at low Mach number. *14th AIAA/CEAS Aeroacoustics Conference*, AIAA 2008-2873, May 2008. Vancouver, British Columbia Canada.
- M. Piellard and C. Bailly. Several computational aeroacoustics solutions for the ducted diaphragm at low Mach number. *16th AIAA/CEAS Aeroacoustics Conference*, AIAA 2010-3996, 2010. Stockholm, Sweden.
- U. Piomelli. Wall-layer models for large-eddy simulations. *Progress in Aerospace Sciences*, 44(6):437–446, August 2008.
- S.B. Pope. *Turbulent flows*. Cambridge University Press, 2000.
- N.B. Powell, M. Mihaescu, G. Mylavarapu, E.M. Weaver, C. Guillemineault, and E. Gutmark. Patterns in pharyngeal airflow associated with sleep-disordered breathing. *Sleep Medicine*, 12(10):966–974, December 2011.
- K.N. Premnath, M.J. Pattison, and S. Banerjee. Large-eddy simulation of self-sustained flow instabilities in cavities using the lattice-Boltzmann method. *AIAA Journal*, 47(1):229–243, January 2009.
- Y.H. Qian, D. d’Humières, and P. Lallemand. Lattice BGK models for Navier-Stokes equation. *Europhysics Letters*, 17(6):479–484, January 1992.
- Ch. Rapp, F. Pfeleger, and M. Manhart. New experimental results for a LES benchmark case. In V. Armenio, B. Geurts, and J. Fröhlich, editors, *Direct and Large-Eddy Simulation VII: proceedings of the seventh international ERCOFTAC workshop on direct and large-eddy simulation*, ERCOFTAC Series 13, pages 69–74. Springer, January 2010.
- J. Rosell and P. Cabras. A three-stage method for the 3D reconstruction of the tracheo-bronchial tree from CT scans. *Computerized Medical Imaging and Graphics*, 37(7-8): 430–437, October 2013.
- J. Sandeau, I. Katz, R. Fodil, B. Louis, G. Apiou-Sbirlea, G. Caillibotte, and D. Isabey. CFD simulation of particle deposition in a reconstructed human oral extrathoracic airway for air and helium-oxygen mixtures. *Journal of Aerosol Science*, 41(3):281–294, March 2010.
- M. Sanjosé, C. Méon, V. Masson, and S. Moreau. Direct numerical simulation of acoustic reduction using serrated trailing-edge on an isolated airfoil. *20th AIAA/CEAS Aeroacoustics Conference*, AIAA 2014-2324, June 2014. Atlanta, Georgia.
- R. Satti, Y. Li, R. Shock, and S. Noelting. Aeroacoustics analysis of a high-lift trapezoidal wing using a lattice Boltzmann method. *14th AIAA/CEAS Aeroacoustics Conference*, AIAA 2008-3048, May 2008. Vancouver, British Columbia Canada.
- E. Seeram. *Computed tomography: physical principles, clinical applications, and quality control*. Elsevier, 3rd edition, 2009.

- H. Shi, C. Kleinstreuer, and Z. Zhang. Dilute suspension flow with nanoparticle deposition in a representative nasal airway model. *Physics of Fluids*, 20:013301, 2008.
- A.M. Shinneeb and A. Pollard. Investigation of the flow physics in the human pharynx/larynx region. *Experiments in Fluids*, 53(4):989–1003, October 2012.
- E.B. Slawinski and D.G. Jamieson. Studies of respiratory stridor in young children: acoustical analyses and tests of a theoretical model. *International Journal of Pediatric Otorhinolaryngology*, 19(3):205–222, August 1990.
- R.S. Snell. *Clinical anatomy by regions*. Lippincott Williams & Wilkins, 9th edition, 2011.
- S. Standring, N.R. Borley, P. Collins, A.R. Crossman, M.A. Gatzoulis, J.C. Healy, D. Johnson, V. Mahadevan, R.L.M. Newell, and C.B. Wigley. *Gray's anatomy: The anatomical basis of clinical practice*. Elsevier, 40th edition, 2009.
- K.W. Stapleton, E. Guentsch, M.K. Hoskinson, and W.H. Finlay. On the suitability of  $k - \epsilon$  turbulence modeling for aerosol deposition in the mouth and throat: a comparison with experiment. *Journal of Aerosol Science*, 31(6):739–749, 2000.
- H.L. Stone. Iterative solution of implicit approximations of multidimensional partial differential equations. *SIAM Journal of Numerical Analysis*, 5(3):530–558, September 1968.
- S. Succi. *The Lattice Boltzmann Equation for fluid dynamics and beyond*. Clarendon Press, Oxford, 1st edition, 2001.
- D.J. Taylor, D.J. Doorly, and R.C. Schroter. Inflow boundary profile prescription for numerical simulation of nasal airflow. *J. R. Soc. Interface*, 7(44):515–527, March 2010.
- C.M. Teixeira. Incorporating turbulence models into the lattice-boltzmann method. *International Journal of Modern Physics*, 9(8):1159–1175, 1998.
- L. Temmerman, M.A. Leschziner, C.P. Mellen, and J. Fröhlich. Investigation of wall-function approximations and subgrid-scale models in large eddy simulation of separated flow in a channel with streamwise periodic constrictions. *International Journal of Heat and Fluid Flow*, 24(2):157–180, April 2003.
- C. Testa. *Acoustic formulations for aeronautical and naval rotorcraft noise prediction based on the Ffowcs Williams and Hawkings equation*. PhD thesis, Delft University of Technology, February 2008.
- D.M. Thompson, J.P. Willging, and R.T. Cotton. Lesions of the larynx, trachea, and upper airway. In A.G. Coran, N.S. Adzick, T.M. Krummel, J. Laberge, R.C. Shamberger, and A.A. Caldamone, editors, *Pediatric Surgery*, chapter 65, pages 837–854. Elsevier, 2012.
- W.C.P. van der Velden. Numerical investigation of an upper airway in a patient suffering from stridor - A fluid-structure-acoustic interaction simulation in OpenFOAM. MSc thesis, TU Delft University of Technology, Kluyverweg 1, 2629HS Delft, November 2012.
- W.C.P. van der Velden, A.H. van Zuijlen, A.T. de Jong, C.T. Lynch, L.J. Hoeve, and H. Bijl. Acoustic simulation of a patient's obstructed airway. *Computer Methods in Biomechanics and Biomedical Engineering*, 2015. DOI: 10.1080/10255842.2014.996877.



- F. Van Herpe. *Computational Aeroacoustics for Turbulent duct flow*. PhD thesis, University of Cambridge, 1994.
- F. Van Herpe, S. Vergne, and E. Gaudard. Wavenumber-frequency analysis of the wall pressure fluctuations in the wake of a rear view mirror using a lattice Boltzmann model. *Proceedings of the Acoustics 2012 Nantes Conference*, pages 1851–1856, April 2012.
- S. Verbanck, T. de Keukeleire, D. Schuermans, M. Meysman, W. Vincken, and B. Thompson. Detecting upper airway obstruction in patients with tracheal stenosis. *Journal of Applied Physiology*, 109(1):47–52, July 2010.
- S. Verbanck, H. Kalsi, M. Biddiscombe, V. Agnirothi, B. Belkassam, C. Lacor, and O. Usmani. Inspiratory and expiratory aerosol deposition in the upper airway. *Inhalation Toxicology*, 23:104–111, 2011.
- E.M. Vigen. *The lattice Boltzmann method: Fundamentals and acoustics*. PhD thesis, Norwegian University of Science and Technology (NTNU), Trondheim, February 2014.
- C.A. Wagner, T. Hüttl, and P. Sagaut. *Large-eddy simulation for acoustics*, volume 20 of *Cambridge Aerospace Series*. Cambridge University Press, 2007.
- D.Y. Wang, H.P. Lee, and B.R. Gordon. Impacts of fluid dynamics simulation in study of nasal airflow physiology and pathophysiology in realistic human three-dimensional nose models. *Clinical and Experimental Otorhinolaryngology*, 5(4):181–187, December 2012.
- Y. Wang and S. Elghobashi. On locating the obstruction in the upper airway via numerical simulation. *Respiratory Physiology & Neurobiology*, 193:1–10, March 2014.
- Y. Wang, Y. Liu, X. Sun, S. Yu, and F. Gao. Numerical analysis of respiratory flow patterns within human upper airway. *Acta Mechanica Sinica*, 25(6):737–746, December 2009.
- M. Wheeler, C.J. Coté, and I.D. Todres. The pediatric airway. In C.J. Coté, J. Lerman, and I.D. Todres, editors, *A practice of anesthesia for infants and children*, chapter 12, pages 237–278. Elsevier, 4th edition, 2009.
- J. Xi, X. Si, J.W. Kim, and A. Berlinski. Simulation of airflow and aerosol deposition in the nasal cavity of a 5-year-old child. *Journal of Aerosol Science*, 42(3):156–173, March 2011.
- J. Xi, A. Berlinski, Y. Zhou, B. Greenberg, and X. Ou. Breathing resistance and ultrafine particle deposition in nasal-laryngeal airways of a newborn, an infant, a child, and an adult. *Annals of Biomedical Engineering*, 40(12):2579–2595, December 2012.
- J. Xi, J. Kim, X.A. Si, and Y. Zhou. Diagnosing obstructive respiratory diseases using exhaled aerosol fingerprints: A feasibility study. *Journal of Aerosol Science*, 64:24–36, October 2013.
- X. Xu, J. Sang Lee, and R.H. Pletcher. A compressible finite volume formulation for large eddy simulation of turbulent pipe flows at low Mach number in Cartesian coordinates. *Journal of Computational Physics*, 203(1):22–48, February 2005.
- V. Yakhot and S.A. Orszag. Renormalization group analysis of turbulence. i. basic theory. *Journal of Scientific Computing*, 1(1):3–51, 1986.

- Z. Zhang and C. Kleinstreuer. Airflow structures and nano-particle deposition in a human upper airway model. *Journal of Computational Physics*, 198(1):178–210, July 2004.
- Z. Zhang and C. Kleinstreuer. Computational analysis of airflow and nanoparticle deposition in a combined nasal-oral-tracheobronchial airway model. *Journal of Aerosol Science*, 42(3): 174–194, March 2011.
- Z. Zhang, C. Kleinstreuer, and C.S. Kim. Micro-particle transport and deposition in a human oral airway model. *Journal of Aerosol Science*, 33(12):1635–1652, December 2002a.
- Z. Zhang, C. Kleinstreuer, and C.S. Kim. Cyclic micron-size particle inhalation and deposition in a triple bifurcation lung airway model. *Journal of Aerosol Science*, 33(2):257–281, February 2002b.
- J.W. Zwartenkot. Fast Fourier spectral analysis of inspiratory stridor in children. Technical report, Department of Otorhinolaryngology Erasmus Medical Centre, Sophia Children's Hospital Rotterdam, 2010.
- J.W. Zwartenkot, H.L.J. Hoeve, and J. Borgstein. Inter-observer reliability of localization of recorded stridor sounds in children. *International Journal of Pediatric Otorhinolaryngology*, 74(10):1184–1188, October 2010.

---

# Appendix A

---

## Hill Geometry

Between  $x = 0$  and  $x = 9$ :

$$h(x) = \min(28, 2.800000000000 \times 10^1 + 0.000000000000 \times 10^0 x \\ + 6.775070969851 \times 10^{-3} x^2 - 2.124527775800 \times 10^{-3} x^3)$$

Between  $x = 9$  and  $x = 14$ :

$$h(x) = 2.507355893131 \times 10^1 + 9.754803562315 \times 10^{-1} x \\ - 1.016116352781 \times 10^{-1} x^2 + 1.889794677828 \times 10^{-3} x^3$$

Between  $x = 14$  and  $x = 20$ :

$$h(x) = 2.579601052357 \times 10^1 + 8.206693007457 \times 10^{-1} x \\ - 9.055370274339 \times 10^{-2} x^2 + 1.626510569859 \times 10^{-3} x^3$$

Between  $x = 20$  and  $x = 30$ :

$$h(x) = 4.046435022819 \times 10^1 - 1.379581654948 \times 10^0 x \\ + 1.945884504128 \times 10^{-2} x^2 - 2.070318932190 \times 10^{-4} x^3$$

Between  $x = 30$  and  $x = 40$ :

$$h(x) = 1.792461334664 \times 10^1 + 8.743920332081 \times 10^{-1} x \\ - 5.567361123058 \times 10^{-2} x^2 + 6.277731764683 \times 10^{-4} x^3$$

Between  $x = 40$  and  $x = 54$ :

$$h(x) = \max(0, 5.639011190988 \times 10^1 - 2.010520359035 \times 10^0 x \\ + 1.644919857549 \times 10^{-2} x^2 + 2.674976141766 \times 10^{-5} x^3)$$

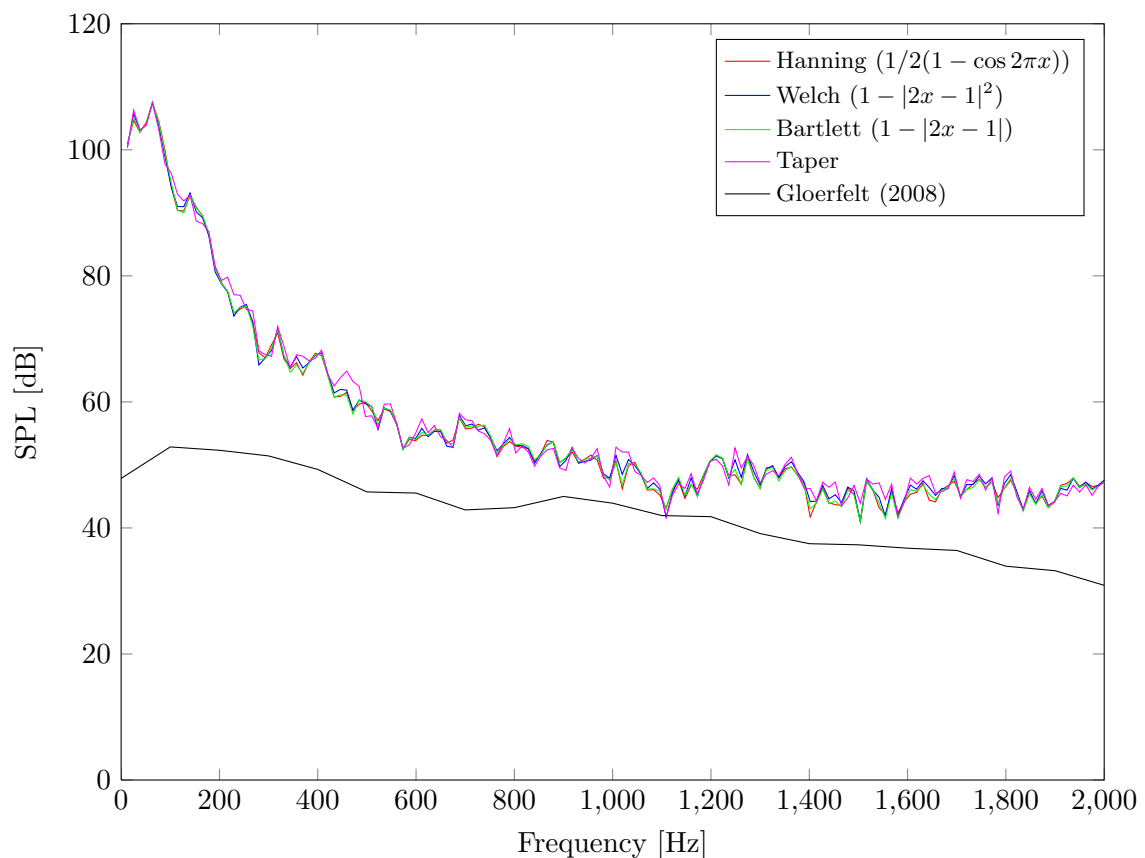


---

## Appendix B

---

# Influence of Window Functions on Acoustic Spectrum



**Figure B.1:** Comparison of four different window functions used to calculate the acoustic spectrum of Probe # 8, fine mesh, Mach Number Same as Experiment.

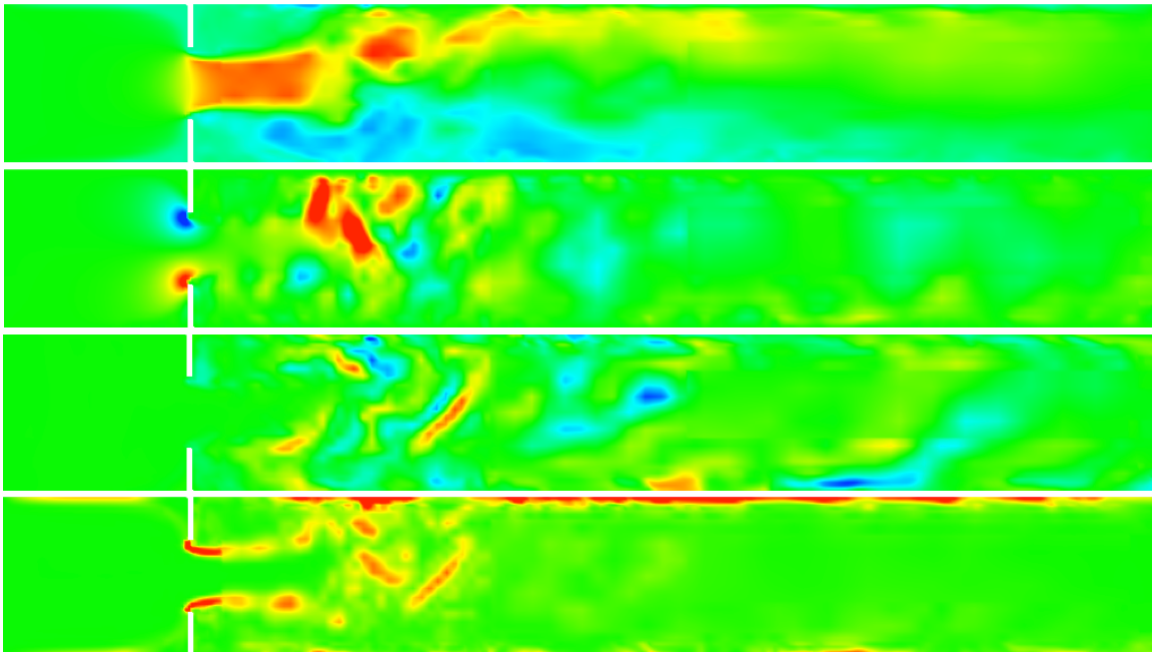


---

## Appendix C

---

### Coarsest Mesh: Instantaneous Flow Fields



**Figure C.1:** Overview of the instantaneous flow fields obtained with the coarsest mesh. From top to bottom: longitudinal velocity  $u$  (levels between -15 and 28 m/s), crossflow velocity  $v$  (levels between -10 and 10 m/s), spanwise velocity  $w$  (levels between -10 and 10 m/s), vorticity magnitude  $||\omega||$  (levels between -5,000 and 5,000 s<sup>-1</sup>).



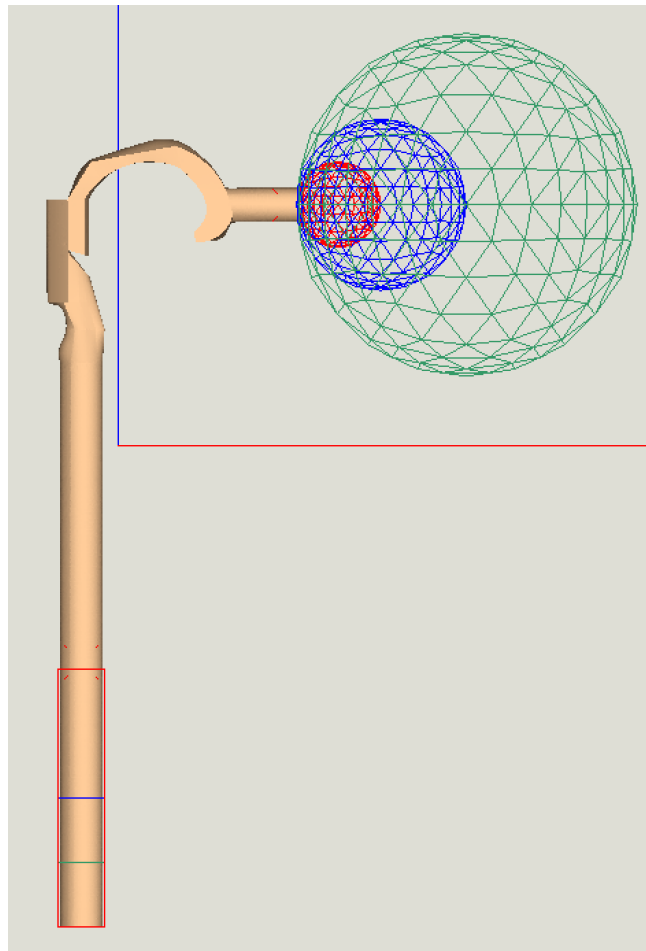


---

## Appendix D

---

### SUAM - Possible Implementation of NRBC



**Figure D.1:** Possible implementation of a Nonreflecting Boundary Condition in the Simplified Upper Airway Model. The colors indicate regions of increased voxel size.



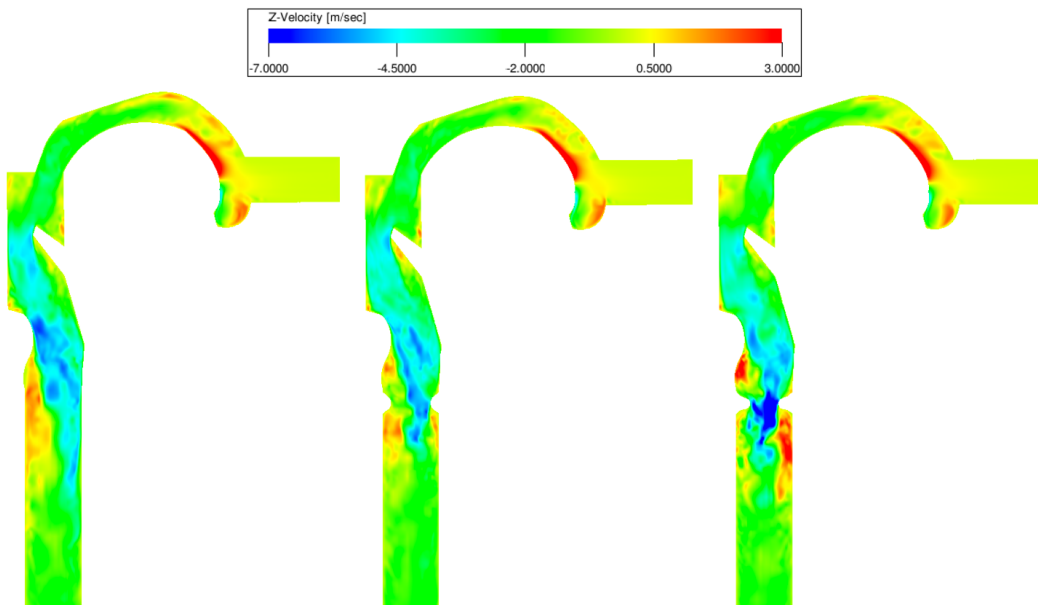
---

## Appendix E

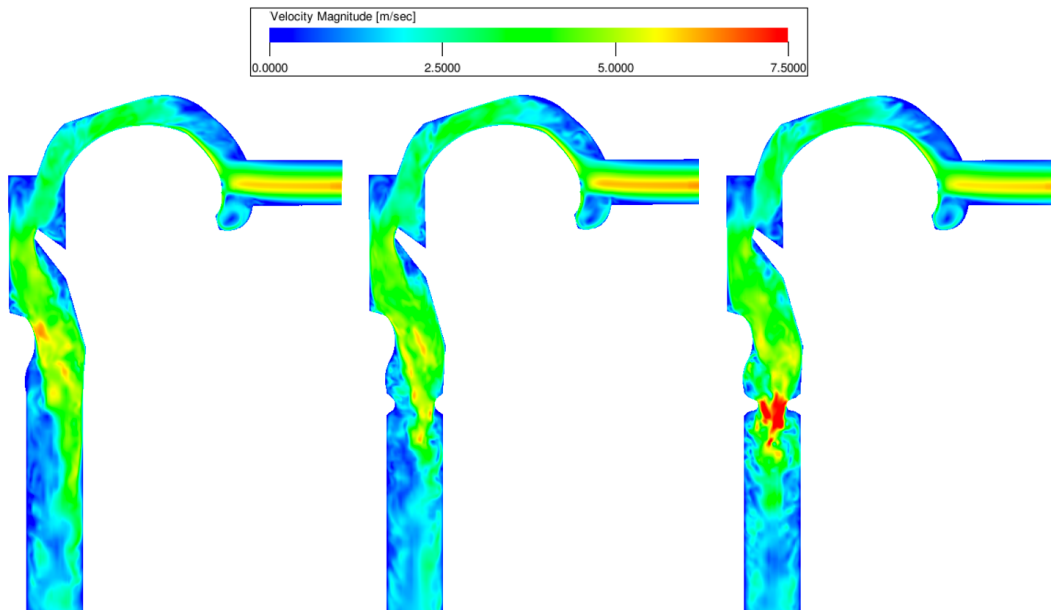
---

# SUAM - Fluid Flow Results

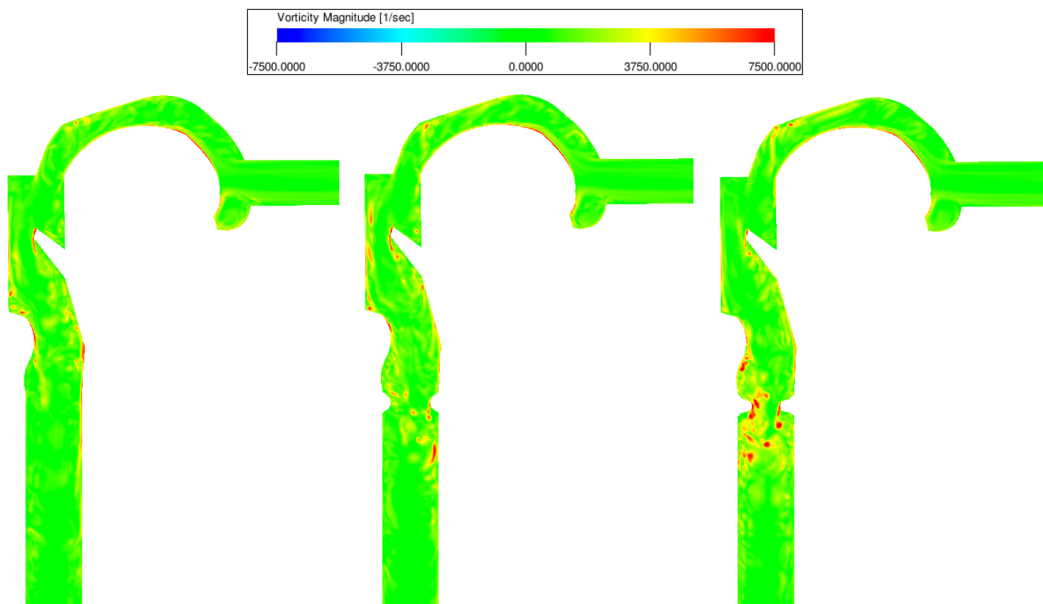
### E.1 Mach Number Chosen by PowerFLOW: Acoustic Mesh



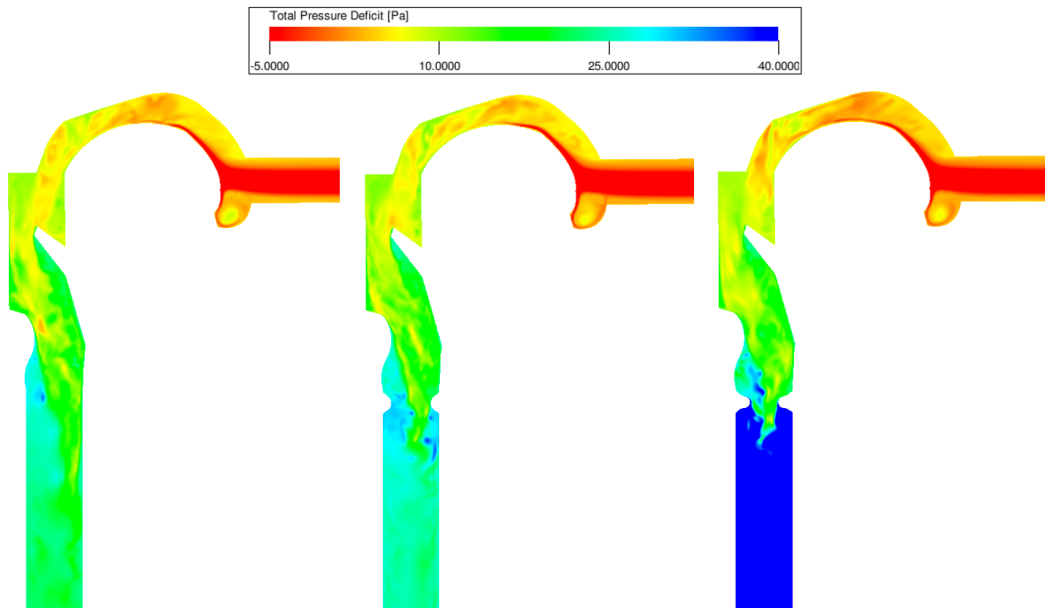
**Figure E.1:** Snapshot of the instantaneous vertical velocity  $u_z$  (levels between -7 and 3 m/s) in the central sagittal plane, acoustic mesh (6 cells/mm). From left to right: healthy model, 50% constriction, 75% constriction.



**Figure E.2:** Snapshot of the instantaneous velocity magnitude  $\|\mathbf{u}\|$  (levels between 0 and 7.5 m/s) in the central sagittal plane, acoustic mesh (6 cells/mm). From left to right: healthy model, 50 % constriction, 75 % constriction.

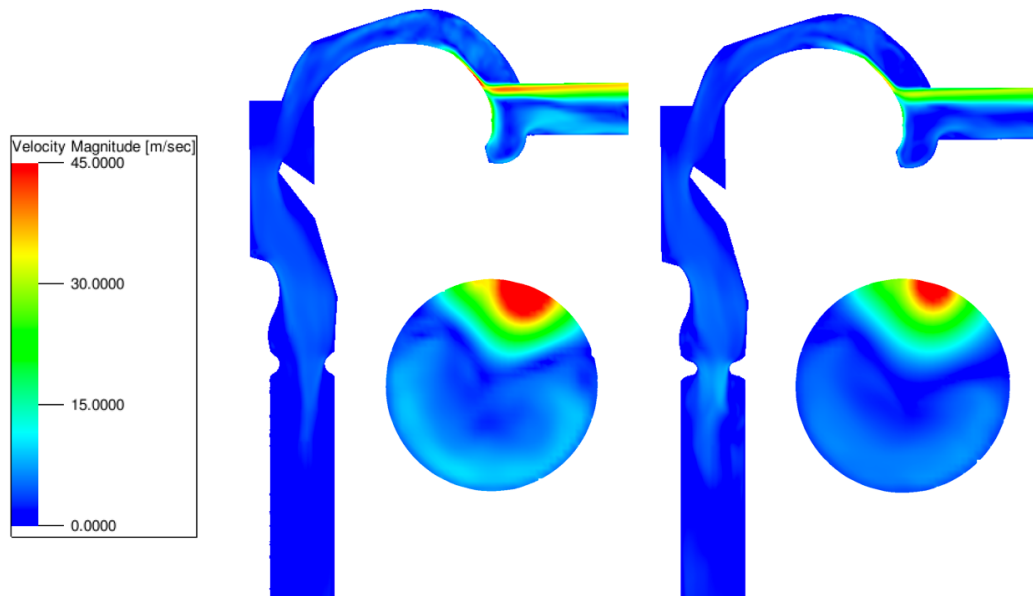


**Figure E.3:** Snapshot of the instantaneous vorticity magnitude  $\|\boldsymbol{\omega}\|$  (levels between -7,500 and 7,500  $\text{s}^{-1}$ ) in the central sagittal plane, acoustic mesh (6 cells/mm). From left to right: healthy model, 50 % constriction, 75 % constriction.



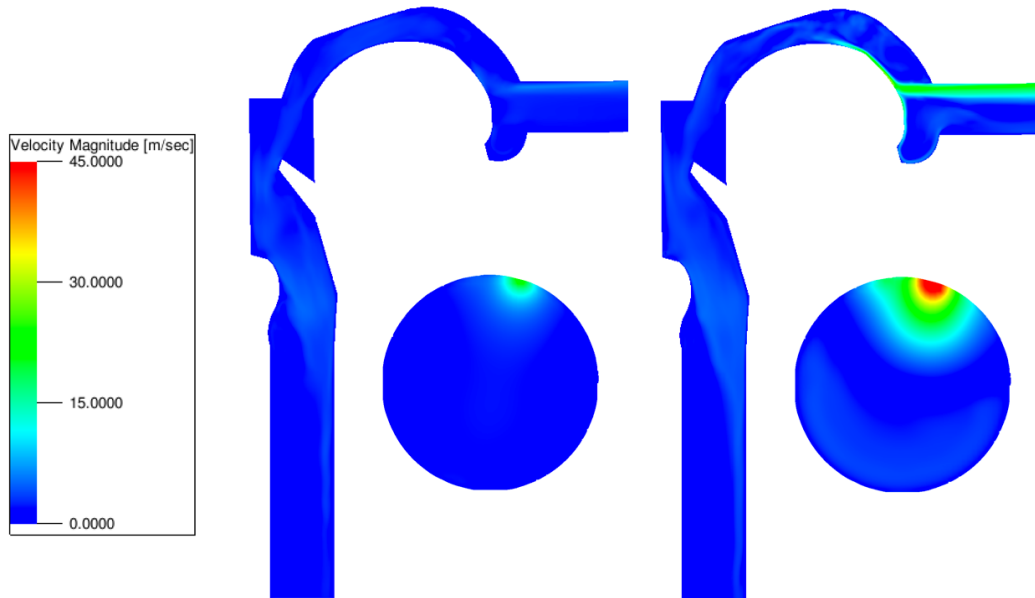
**Figure E.4:** Snapshot of the instantaneous pressure deficit  $p'$  (levels between -5 and 40 Pa) in the central sagittal plane, acoustic mesh (6 cells/mm). From left to right: healthy model, 50 % constriction, 75 % constriction.

## E.2 Mach Number Same as Experiment: Acoustic Mesh

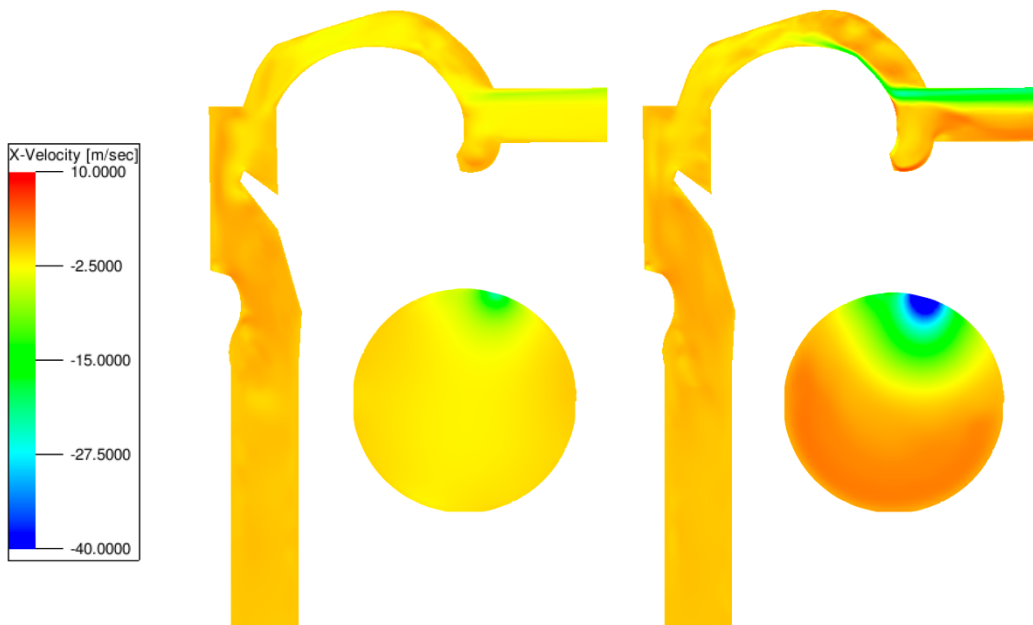


**Figure E.5:** Snapshot of the averaged velocity magnitude  $\|u\|$  (levels between 0 and 45 m/s) in the central sagittal plane, acoustic mesh (6 cells/mm). The front views are taken within 1 mm from the inlet boundary. From left to right: 50 % constriction (0.29s), 75 % constriction (0.19s).

### E.3 Mach Number Same as Experiment: Fine Mesh

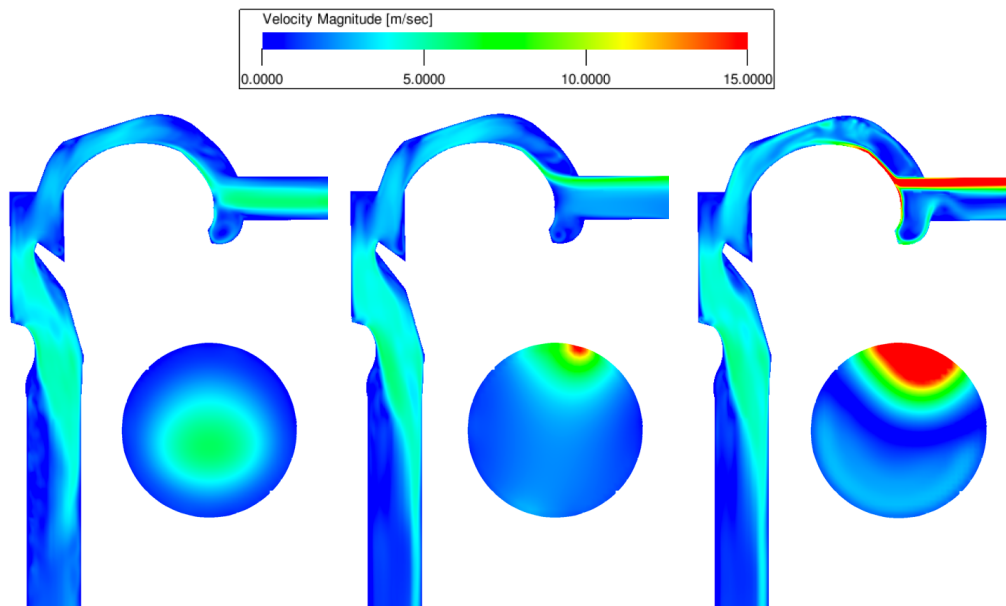


**Figure E.6:** Temporal evolution of the averaged velocity magnitude  $\|\mathbf{u}\|$  (levels between 0 and 45 m/s), Mach Number Same as Experiment, healthy model, fine mesh (8 cells/mm). The front views are taken within 1 mm from the inlet boundary. From left to right: 0.05 s, 0.1 s.

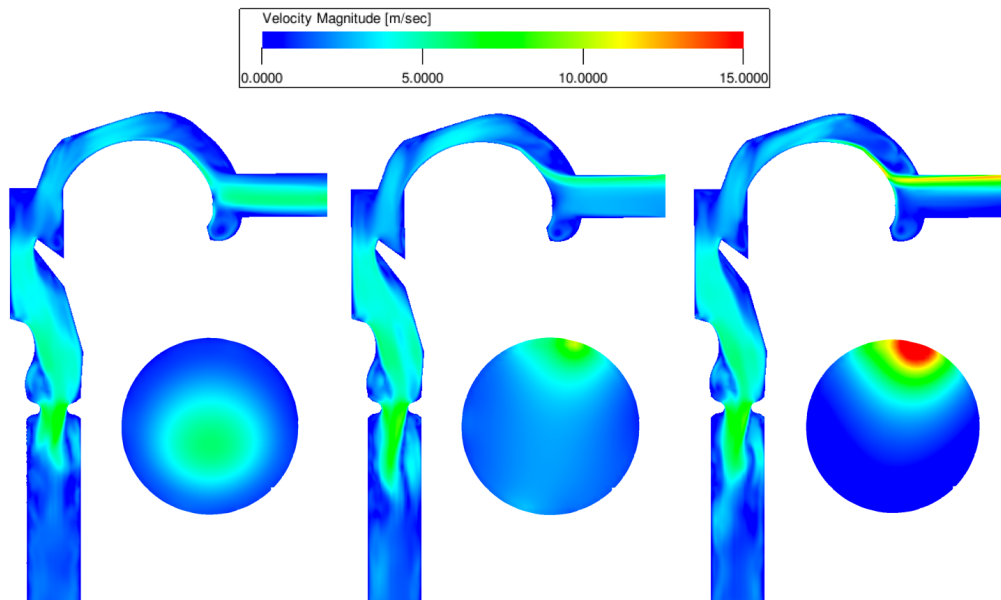


**Figure E.7:** Temporal evolution of the averaged horizontal velocity  $u_x$  (levels between -40 and 10 m/s), Mach Number Same as Experiment, healthy model, fine mesh (8 cells/mm). The front views are taken within 1 mm from the inlet boundary. Note the strong backflow in the cylindrical inlet region. From left to right: 0.05 s, 0.1 s.

## E.4 Mach Number Same as Experiment: Acoustic Mesh, Seeded

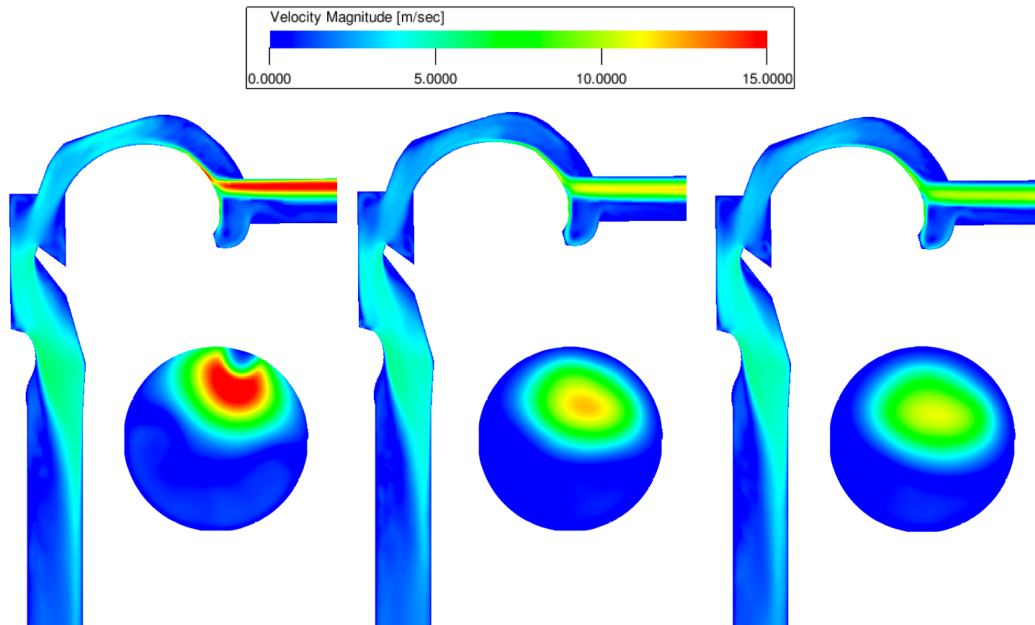


**Figure E.8:** Effect of CbP initial condition on the temporal evolution of the averaged velocity magnitude  $\|\mathbf{u}\|$  (levels between 0 and 15 m/s), Mach Number Same as Experiment, healthy model, acoustic mesh (6 cells/mm). The front views are taken within 1 mm from the inlet boundary. From left to right: 0s, 0.1s, 0.15s.



**Figure E.9:** Effect of CbP initial condition on the temporal evolution of the averaged velocity magnitude  $\|\mathbf{u}\|$  (levels between 0 and 15 m/s), Mach Number Same as Experiment, 75% constriction, acoustic mesh (6 cells/mm). The front views are taken within 1 mm from the inlet boundary. From left to right: 0s, 0.1s, 0.15s.

### E.5 Mach Number Chosen by PowerFLOW: Acoustic Mesh, Seeded

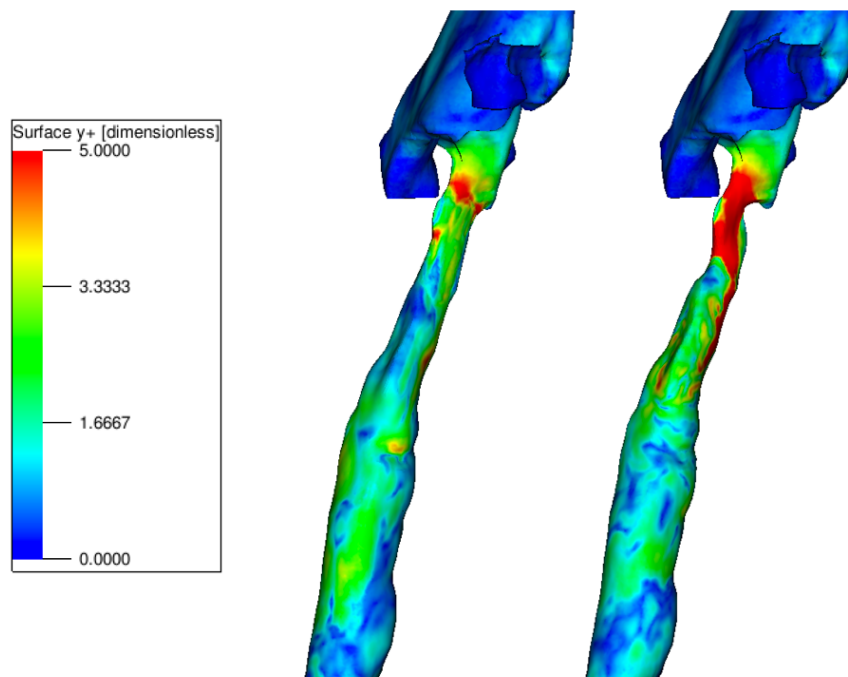


**Figure E.10:** Effect of SaE initial condition on the temporal evolution of the averaged velocity magnitude  $\|\mathbf{u}\|$  (levels between 0 and 15 m/s), Mach Number Chosen by PowerFLOW, healthy model, acoustic mesh (6 cells/mm). The front views are taken within 1 mm from the inlet boundary. From left to right: 0.026 s, 0.133 s, 0.24 s.



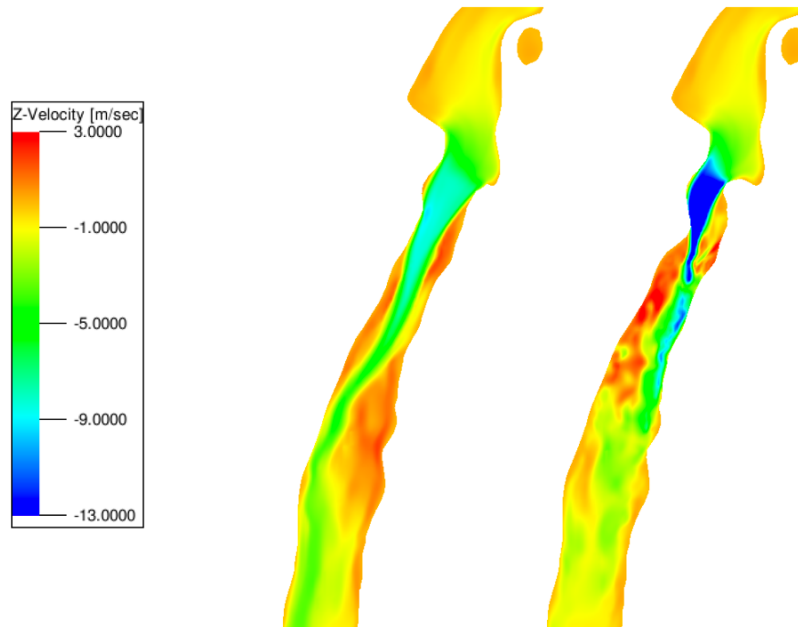
## RUAM - Fluid Flow Results

### F.1 Boundary-Layer Resolution

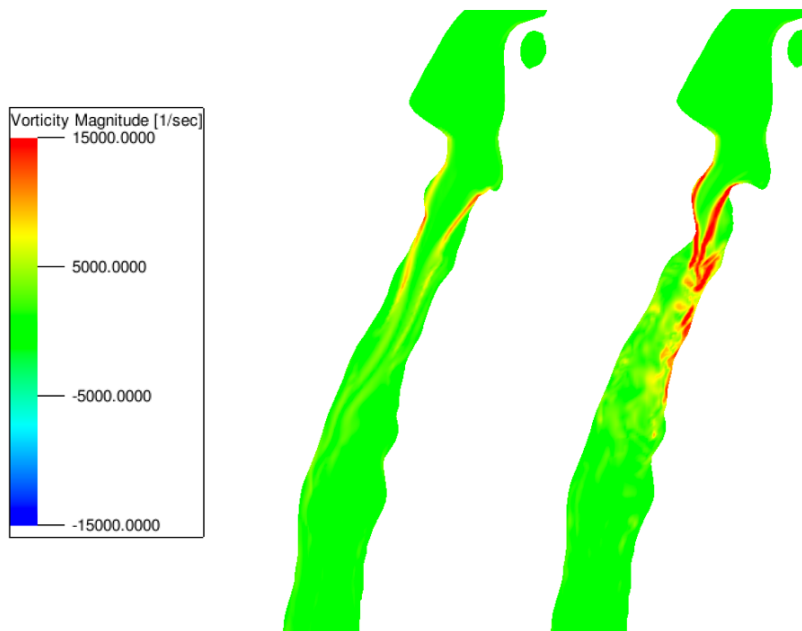


**Figure F.1:** Instantaneous snapshot of  $y^+$  (levels between 0 and 5), a measure for the near-wall resolution, acoustic mesh, Mach Number Chosen by PowerFLOW. From left to right: healthy model, stridorous model.

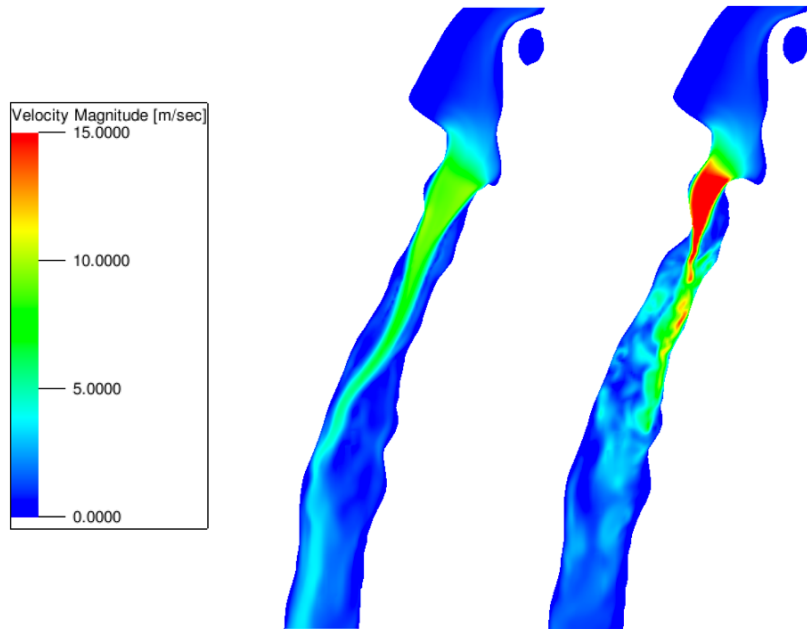
## F.2 Instantaneous Flow Fields



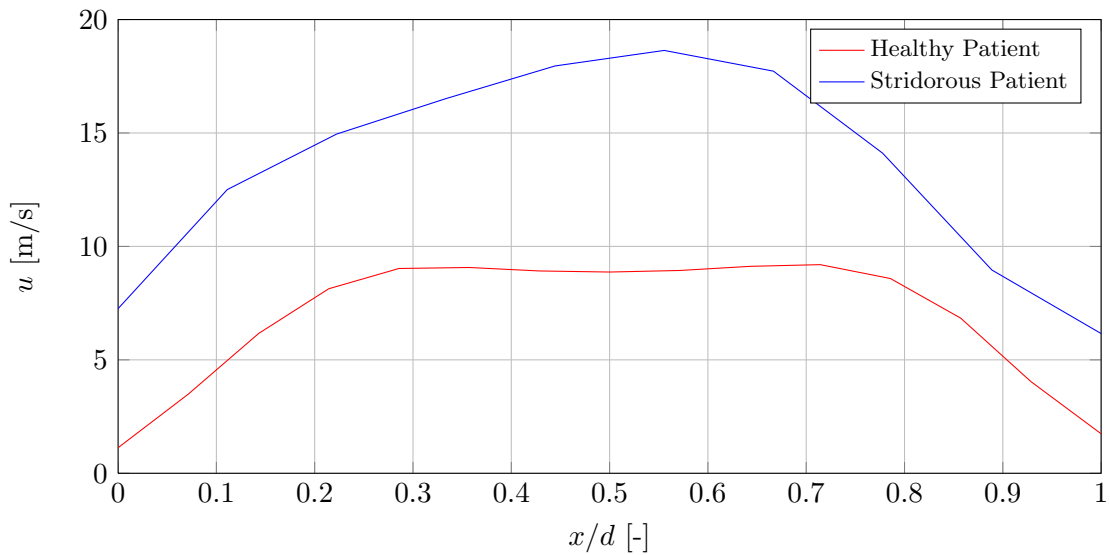
**Figure F.2:** Snapshot of the instantaneous vertical velocity  $u_z$  (levels between -13 and 3 m/s) in the central sagittal plane, Mach Number Same as Experiment, acoustic mesh (6 cells/mm). From left to right: healthy model, stridorous model.



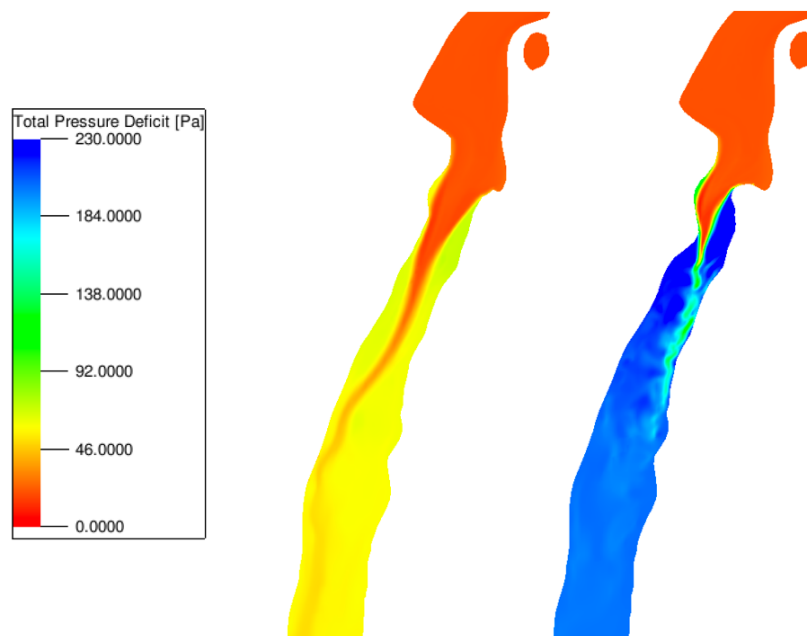
**Figure F.3:** Snapshot of the instantaneous vorticity magnitude  $\|\omega\|$  (levels between -15,000 and 15,000  $s^{-1}$ ) in the central sagittal plane, Mach Number Same as Experiment, acoustic mesh (6 cells/mm). From left to right: healthy model, stridorous model.



**Figure F.4:** Snapshot of the instantaneous velocity magnitude  $\|\mathbf{u}\|$  (levels between 0 and 15 m/s) in the central sagittal plane, Mach Number Same as Experiment, acoustic mesh (6 cells/mm). From left to right: healthy model, stridorous model.

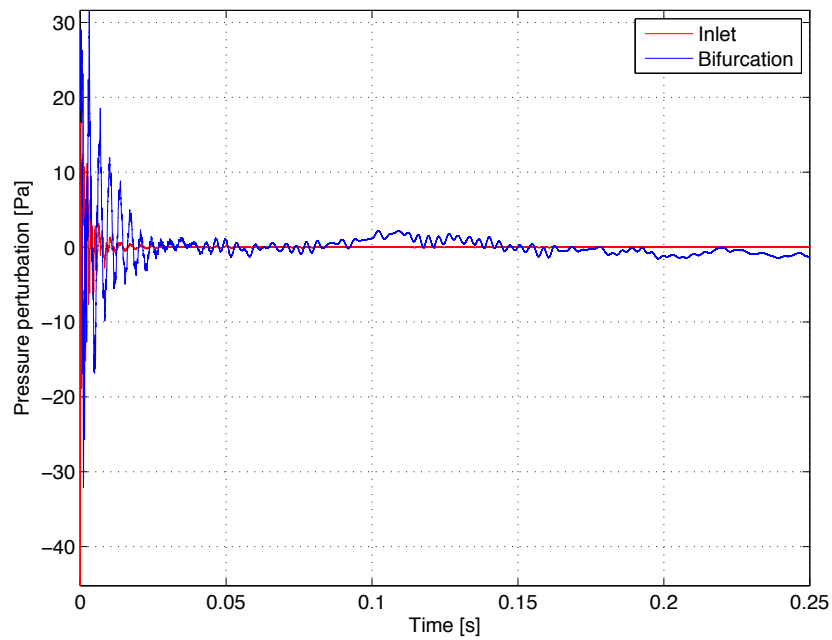


**Figure F.5:** Comparison of the averaged velocity magnitude  $\|\mathbf{u}\|$  at the end of the constriction in the central sagittal plane, Mach Number Same as Experiment, acoustic mesh (6 cells/mm).



**Figure F.6:** Snapshot of the instantaneous pressure deficit  $p'$  (levels between 0 and 230 Pa) in the central sagittal plane, Mach Number Same as Experiment, acoustic mesh (6 cells/mm). From left to right: healthy model, stridorous model.

### F.3 Temporal Evolution of Pressure Signal



**Figure F.7:** Pressure perturbation as measured by the acoustic probes, healthy model, Mach Number Same As Experiment. Note the transient start-up prior to  $t = 0.05$  s.





